Single cell dielectrophoretic trapping for the analysis of cellular membrane dynamics

By

Fabrice Matthieu Gielen

A thesis submitted in partial fulfillment of the requirement for the degree of Doctor of Philosophy

Department of Chemistry, Imperial College London
November 2011

Abstract

Cellular membrane dynamics has been subject to an ever-growing research interest since the introduction of the fluid mosaic model in the early seventies. The recognition that individual components of a cell membrane are able to diffuse in a two-dimensional matrix led to the crucial questioning of the structure-function relationship. The stunning diversity of lipid or proteins making up the plasma membrane of mammalian cells prevents theoretical treatment to apprehend membrane organization and dynamics. For this reason, membrane dynamics has remained up to now predominantly an experimental field of study. The presence of membrane micro-domains including lipid rafts and the co-existence of several phases has for instance been recently confirmed using single-molecule fluorescence detection methods. These domains as well as overall membrane fluidity are thought to be essential in many key cellular processes such as signal transduction, pathogen entry or trafficking.

This thesis focuses on the development, characterization and applications of novel microfluidic tools for probing cellular plasma membrane structure and dynamics. We successfully demonstrated dielectrophoretic trapping of single mammalian cells (typically 10μm in diameter) as a means to facilitate time-resolved studies on living cell membranes for timescales of minutes.

Firstly, microfluidic devices embedding micro-electrodes have been fabricated. These dielectrophoretic (DEP) traps were characterized to assess their potential as a tool for performing in-vitro membrane bio-assays. DEP traps have been subsequently used to trap single-cells near a defined surface and reagents were introduced via microfluidic channels. Incorporation of a Förster Resonance Energy transfer (FRET) acceptor dye within a donor labelled cellular membrane allowed for time-resolved observation of colocalization events using a scanning confocal microscope and fluorescence lifetime imaging. The presence of cholesterol was shown to influence probes localization.

Such microfluidic devices coupled with high-resolution imaging of single cells can potentially be used to study the organization dynamics of individual molecules on the membrane of live cells.

Acknowledgments

I wish to express my gratitude to Dr. Joshua Edel for his invaluable guidance throughout the whole length of the project, his availability in all matters and passionate enthusiasm for scientific questioning. I would also like to stress the role played by Prof. Andrew deMello and Prof. Antony Cass for their insightful feedbacks, critical reading and support at many stages of this work.

Thank you to the members of both Edel's and deMello's research groups for their cheerful dynamic and insightful comments. Among them, special thanks to Dr. Xize Niu for the sharing of his profound expertise during the whole length of our collaborations, Kalpana Vijayakumar and Benjamin White for initially teaching me cell culturing, Fiona Pereira for her help in apprehending biological concepts, Margarita Stapountzi for patiently building and co-testing the scanning confocal rig.

I wish to thank the members and organizers of the Institute of Chemical Biology, giving me the opportunity to open my mind to a world originally far remote from my education, to discuss new ideas with fellow PhD students and to allow me participating in numerous conferences, seminars and transferable skills programs.

Eventually, I wish to thank my family for their constant love and support, to my daughter for her extraordinary joie de vivre and foremost to my friend, wife and mother of my future children. Gintarė, ačiū!

Contents

Abstract ..... *ii*

Acknowledgments ..... *iii*

Contents ..... *iv*

List of figures ..... *x*

List of tables ..... *xx*

List of Abbreviations ..... *xxii*

Chapter I. Introduction *1*

I.1. The plasma membrane: structure and organization **2**

I.1.1. Cell plasma membrane composition 2

I.1.2. Fluidity of the lipid bilayer 5

I.1.2.1. The fluid mosaic model 5

I.1.2.2. Membrane micro-domains 6

I.1.2.3. Cytoskeleton partitioning 7

I.1.3. The presence of different lipid orders in the plasma membrane 8

I.1.3.1. The influence of temperature on membrane fluidity and order 9

I.1.3.2. Lipid rafts nanodomains 10

I.1.3.3. Example of Jurkat T-cell signalling 10

I.1.3.4. Tumour cell membranes and fluidity 12

I.2. Membrane order studies using fluorescence **12**

I.2.1. Single molecule techniques 13

I.2.1.1. Fluorescence Correlation Spectroscopy 13

I.2.1.2. Single Particle Tracking 15

I.2.2. Fluorescence measurements on ensemble of molecules 16

I.2.2.1. Fluorescence Lifetime Imaging (FLIM) 16

I.2.2.2. Order sensitive fluorescent dyes used in FLIM 18

I.2.2.3. FLIM- Förster Resonance Energy Transfer (FLIM-FRET) 20

I.2.2.4. Colocalization studies with FRET 21

I.3. Alternative tools to study membrane dynamics **22**

I.4. Cellular trapping for membrane analysis in a microfluidic environment **22**

I.4.1. Analyses based on single cells versus cell ensemble studies 23

I.4.2. Single cell patterning in a microfluidic environment 23
I.4.2.1. Single cell trapping techniques and membrane analysis 24
I.4.3. The dielectrophoretic force as a route to cell patterning 27
I.4.3.1. Description and trap geometry 27
I.4.3.2. Potential hurdles to manipulating cells in DEP traps 28
I.5. Project aim 29
I.6. References 31
Chapter II. Methodology 35
II.1. Fabrication of microfluidic devices 36
II.1.1. Designs used in this work and dimensions 36
II.1.2. Gold patterning on glass 38
II.1.3. Making of the SU-8 master mould used for soft lithography 41
II.1.4. Making and bonding of a PDMS micro-chip 42
II.1.4.1. PDMS replica 42
II.1.4.2. Chip bonding 43
II.1.5. Packaging 43
II.2. Materials 44
II.2.1. Fluidics and particles 44
II.2.2. Cells 44
II.2.3. Fluorescent lipid analogs 45
II.2.3.1. Absorption spectrum of a conjugated dye 45
II.2.3.2. Absorption spectrum of a dialkylcarbocyanine dyes 46
II.2.4. Cell labelling 48
II.2.5. Electrical excitation 50
II.3. The laser scanning detection platform 50
II.3.1. The overall setup 50
II.3.2. Light Source 51
II.3.3. The scanning unit 53
II.3.4. The objective and confocal volume 54
II.3.5. The detection path 56
II.3.5.1. The pinhole 56
II.3.5.2. Towards the APDs 56
II.3.6. Overview of the scanning confocal microscope 57
II.3.7. Integrating microfluidic chips with optics 58
II.3.8. Time correlated single photon counting setup 59

II.3.8.1. Time-Tagged Time-Resolved Mode (TTTR) 60

II.4. FLIM analysis procedure 61

II.4.1. FLIM histogramming 61

II.4.1.1. IRF correction 61

II.4.1.2. Fitting algorithm 63

II.4.2. FLIM maps 64

II.4.3. Screening algorithm for cell populations 64

II.5. FRET analysis between multiple lipid analogues in a 2D fluid 66

II.6. References 69

Chapter III. Dielectrophoretic cell trapping: theory and characterization 70

III.1. Governing equation for the dielectrophoretic force 71

III.1.1. Implications of the expression of the DEP force 72

III.1.2. Dielectric model for a particle with conductive losses 73

III.1.3. Mammalian cell dielectric model 73

III.1.3.1. The three frequency regions for Re(CM) in the single-shell model 75

III.2. The force balance for a cell within a DEP trap in a microchannel 79

III.3. Simulations 81

III.3.1. Design rules 81

III.3.2. 2D DEP cage 82

III.3.3. Effect of geometrical confinement on electric field distribution 85

III.3.3.1. Lateral exclusion of other cells 87

III.3.3.2. Electric potential wells 89

III.3.4. 3D Visualization 90

III.4. Characterization of nDEP traps 91

III.4.1. Mapping XY non-uniformities 91

III.4.2. Mapping Z confinement force in nDEP traps 92

III.4.2.1. Example: confinement of 1µm particles 93

III.5. Single cell trapping 96

III.5.1. Influence of trapping voltage 96

III.5.2. Influence of cell density 97

III.6. Resistance to flows for trapped particles 100

III.7. Cell viability in permanent electric fields 101

III.8. References 103

Chapter IV. Temperature mapping in nDEP traps 105

IV.1. Introduction 106

IV.2. Theory 108

IV.2.1. Heating with planar micro-electrodes 108

IV.3. Calibration 109

IV.4. High-resolution temperature mapping 113

IV.4.1. Setup 113

IV.4.2. Spatial distribution of heat 114

IV.4.3. Transient temperature rise and cooling of the microsystem 115

IV.4.4. Temperature map from intensity 117

IV.4.5. Temperature map from FLIM 119

IV.4.6. Discussion 120

IV.5. Comparison with theory 122

IV.6. Summary 123

IV.7. References 124

Chapter V. Dielectric cell response in highly conductive buffers 125

V.1. Introduction 126

V.2. Theoretical frequency response in high conductive buffers 127

V.2.1. High frequencies 127

V.2.2. Intermediate frequencies 128

V.2.3. Low frequencies 128

V.3. In-flow cell identification 131

V.3.1. Microfluidic design 131

V.3.2. Theoretical balance of forces 132

V.3.3. Cell viability upon heating 134

V.3.4. Slowing down factors 135

V.4. Summary 140

V.5. References 141

Chapter VI. Mapping lateral heterogeneities of cellular membranes using time-resolved fluorescence spectroscopy 142

VI.1. FLIM of membrane micro-domains 143

VI.1.1. Spatial and temporal resolution 143
VI.1.1.1. Spatial resolution 143
VI.1.1.2. Temporal resolution 144
VI.1.2. Example of FLIM use 147
VI.2. Probe distribution 148
VI.2.1. Importance of labelling conditions 148
VI.2.2. Minimizing photobleaching 151
VI.3. FLIM mapping of labelled U937 cells 152
VI.4. 3D mapping 157
VI.5. Fluorescence lifetime and fluidity 159
VI.6. Colocalization of identical dyes in the membrane 160
VI.6.1. Colocalization after cholesterol extraction 164
VI.7. FLIM-FRET 165
VI.7.1. 2D unlinked FRET in a cell membrane 165
VI.7.2. Membrane FRET in U937 cells using DiO/DiD 168
VI.8. Summary 170
VI.9. References 172
Chapter VII. Membrane FRET assays for membrane dynamics 173
VII.1. Methodology for membrane assays 174
VII.2. Effect of electric field on fluorescence lifetime measurements 175
VII.2.1. Excluding electrode contributions 175
VII.2.2. Fluorescence lifetime and electric fields 176
VII.3. DiO/DiD FRET colocalization assay on Jurkat cell membranes 178
VII.3.1. Initial state 178
VII.3.2. Acceptor dye incorporation 179
VII.3.3. Discussion 185
VII.4. FRET exclusion assay in U937 cell membrane 186
VII.4.1. Experiment 186
VII.4.2. Results & discussion 190
VII.5. Summary 190
VII.6. References 192

Chapter VIII. Conclusions and outlook 193

VIII.1. Summary of achievements 194

VIII.2. Suggested improvements 196

VIII.3. Outlook 197

VIII.4. References 198

List of figures

Chapter I. Introduction

Figure I-1. Schematic of a phospholipid 3

Figure I-2. A phospholipid bilayer 3

Figure I-3. Schematic of the cell membrane composition(reproduced from [14]). 4

Figure I-4. Progressive diffusion in the fluid mosaic model with increasing time from A to C..... 6

Figure I-5. Diffusion and domain formation: If the exchange resulting in two like pairs is energetically favourable, domains can form. At thermodynamic equilibrium, molecules still diffuse inside and outside the domains, and some of them are transiently trapped in domains (reproduced from [19]). ... 7

Figure I-6. The models of the membrane-skeleton "fence" (A) and the anchored-transmembrane protein "pickets" (B) that together are thought to partition the entire plasma membrane into small compartments (reproduced from [23]). 8

Figure I-7. Structure of the gel phase, liquid-disordered phase and liquid-ordered phase containing cholesterol (adapted from [26]). 8

Figure I-8. Melting properties of the membrane of E.Coli grown at 37ºC and 15 ºC (reproduced from [28]). 9

Figure I-9. Jurkat T-cell signalling cascade from [33] 11

Figure I-10. Cancerous cell membranes undergo various alterations (reproduced from [37]). 12

Figure I-11. Principles of Fluorescence Correlation Spectroscopy. A. The sample is illuminated by focusing the laser beam with an objective. The emitted photons are then spectrally filtered and detected (e.g. with an avalanche photodiode). A pinhole before the detector limits the detection volume in the z-direction, so that the light from upper and lower planes is eliminated. B. The emission of photons diffusing in and out the focal volume induces fluctuation in the signal intensity. The fluorescence trace recorded during a given period of time is auto-correlated. C. The graph shows the values obtained for the auto-correlated fluorescence signal (white circles). The diffusion coefficient, binding kinetics parameters or particle concentration can be determined by fitting the experimental values to the autocorrelation function (solid line) (reproduced from [47]). 14

Figure I-12. Analysis of single particle trajectories. On the left, the trajectories of free-diffusing (A) and confined (B) particles are shown. The graph on the right depicts the corresponding mean-square-displacement (MSD) versus lag time for the same particles (reproduced from [23]). 16

Figure I-13. Jablonski diagram for the phenomenon of fluorescence. 17

Figure I-14. Jablonski diagram illustrating the FRET process 20

Figure I-15. kinetics of colocalization (A) and exclusion(B) for two fluorescently labelled molecules. 21

Figure I-16. The most common cell-trapping techniques in microfluidic platforms (reproduced from [69]) 24

Figure I-17. Cell trapping tools based on hydrodynamic flows and passive structures. A. A microwell array filled with rat basophilic leukemia cells. B. Arrayed pillar structures. C. Schematic of a hydrodynamic trap. Scale bars for A and B are 100µm and 20µm.(adapted from [74-76]). 26

Figure I-18. A. Single HeLa cell trapped by negative dielectrophoresis. B. Corticol rat neurons trapped in a quadrupole geometry. C. U937 cells trapped between line electrodes using positive DEP (reproduced from [87-89]). 28

Figure II-1. A. Dimensions of the patterned electrodes for the square geometry (in microns). B. A 7 x 4 array with total footprint less than 1mm^2. C. Schematic of a microfluidic chip with integrated planar micro-electrodes and a micro-channel. 37

Chapter II. Methodology

Figure II-2. Lift-off process steps for Cr/Au patterning on glass 39

Figure II-3. A. 2D AFM scan of a gold electrode on a borosilicate glass slide showing the square trap. B. An optical picture of the same trap with the other line electrode 40

Figure II-4. Cross-section showing the height profile of a DEP trap. The inset indicates the line used for the cross-section. 40

Figure II-5. Chemical structure of a fluorosilane film on a silicon wafer surface (adapted from [3]). 42

Figure II-6. Example of an SU-8 master mould with etched PDMS window over the area comprising patterned microstructures. 42

Figure II-7. Photograph of a packaged device together with a 1 penny coin 43

Figure II-8. Bright field picture of Jurkat T-cells as seen through a 60x objective of an inverted microscope. 44

Figure II-9. Chemical structure of 1,1 diethyl-2,2-carbocyanine iodide and the schematic boundaries of the 1D box used for theoretical treatment. 45

Figure II-10. Chemical structure of the carbocyanines phospholipid analogs. A. DiI, B. DiO, C. DiD. 47

Figure II-11. Normalized absorption (dashed lines) and emission (full lines) spectra of DiO, DiI and DiD inserted into phospholipid bilayer membranes (spectra from www.invitrogen.com) 47

Figure II-12. Insertion of a carbocyanine dye within a DPPC bilayer (adapted from [10]). 48

Figure II-13. Pelleted labelled Jurkat cells in PBS with 5µM DiD. 49

Figure II-14. A. Fluorescent intensity picture of DiO labelled Jurkat cells spread on a coverslip. B. Superimposed bright field and fluorescence picture from a single T-cell. The dye is specifically labelling the plasma membrane. 49

Figure II-15. Schematic optical setup for FLIM acquisition. SM: Scanning Mirrors, DM: Dichroic Mirror, LPF: Long-Pass Filter, PH: Pinhole (100 µm diameter), BPF: Band-Pass Filter, L: Converging Lens 51

Figure II-16. Original pump beam and resulting supercontinuum beam after propagation through a crystal fiber (www.fianum.com). 52

Figure II-17. High-speed scanning mirrors are deflected by galvanometer motors to produce the scanning pattern 53

Figure II-18. The different scanning modes. A. XY mode. B. XZ mode and C. XYZ mode. 53

Figure II-19. The confocal volume with cylindrical and curved components 54

Figure II-20. The home-built detection path (DM: dichroic mirror, M: mirror, LPF: long pass filter, PH: pinhole, BPF: band pass filter, L: lens, APD: avalanche photodiode detector) 57

Figure II-21. Photograph of the scanning confocal setup 58

Figure II-22. The microfluidic chip with electrical connections and capillary connections on the microscope stage 59

Figure II-23. The principle of TCSPC. 60

Figure II-24. The Symphotime interface for reading TTTR files and fitting fluorescence decay curves. 61

Figure II-25. Decay curve for a solution of 1mM Rose Bengal in water and characteristic FWHM. 62

Figure II-26. A. Raw intensity map for the green channel. B. Lifetime map for the green channel C. Raw intensity map for the red channel. D. Lifetime map for the red channel. E. Cell identification and labelling. F. Extraction of lifetime histograms for each cell with Gaussian fits. G. Global lifetime histograms for all the cells present in the map with Gaussian fits. 65

Figure II-27. Relationship between transfer efficiency and donor-acceptor distance 67

Chapter III. Dielectrophoretic cell trapping: theory and characterization

Figure III-1. The effective dipole and non-uniformities of the electric field create a net force on a neutral particle (reproduced from [3]). 71

Figure III-2. The smeared-out schematic used towards the effective dielectric properties of a mammalian cell (adapted from [16]). 74

Figure III-3. Parameters used in the dielectric model of a mammalian cell. 74

Figure III-4. Real part of the CM factor for a mammalian cell immersed in a dielectric medium. The red curve represents a low conductivity buffer (conductivity 50mS/m) while the blue one represents a high conductivity buffer like a physiological fluid (1.6S/m). Cell radius was 5.1µm, membrane thickness 7nm, membrane conductivity 10^{-7}S/m, membrane permittivity $16\varepsilon_0$, cytoplasmic permittivity $78\varepsilon_0$ and conductivity 0.7S/m. 77

Figure III-5. Comparison between live cell (blue) and PS bead (red) responses in a high conductivity buffer. Parameters for the live cells are the ones explicated in Figure III.4. Parameters for the bead were permittivity $2.5\varepsilon_0$ and conductivity 10^{-4}S/m. 78

Figure III-6. Relative amplitude response as a function of applied electric field frequency (red curve) corresponding to the imaginary part of the CM factor. The dashed blue curve is the real-part of the CM factor. Medium conductivity is set at 50mS/m.The dielectric parameters are the ones given in the caption of Figure III.4. 79

Figure III-7. The main forces on a single cell within a microchannel in a planar DEP trap: DEP force, ElectroHydrodynamic (EHD) forces, lift force and drag force with main directions are schematically represented. The Poiseuille parabolic flow velocity is also shown. 80

Figure III-8. Schematic of the simulated geometry and projection to 3 planar parallel electrodes. 82

Figure III-9. The geometry and associated mesh with increased resolution close to the electrodes. 83

Figure III-10. Electric field norm associated with the simulated model 84

Figure III-11. Normalized DEP force direction associated with three line electrodes. 84

Figure III-12. Electric field norm simulated for a channel of height 30µm (A) and 120µm (B) showing the effect of geometrical confinement on electric field distribution. The scale has been adapted to highlights differences in the DEP trapping region. 86

Figure III-13. Highlight of the confinement strength of an nDEP trap in a three lines electrode geometry. Negative component of the projection on the vertical axis of $\left|\nabla_z \vec{E}^2\right|$ in a deep channel

(here 120 µm) (A) and a shallow channel 30µm deep (B). Blue regions correspond to strong gradients while red regions correspond to weak gradients. Both simulations have the same colour map. 87

Figure III-14. Normalized DEP barrier height (upwards DEP force) over the first line electrode as a function of channel height at constant voltage. A. for a 30µm deep channel and B. for a 120 µm deep channel. 88

Figure III-15. Normalized barrier height as a function of channel height. 88

Figure III-16. Electric energy density 5 microns above the surface are aligned with the traps. The scale has been adapted to highlight the low potential well regions. 89

Figure III-17. 3D model representing $\left|\nabla_z \vec{E}^2\right|$ with z slices every 5 microns. The parameters are the same as in Figure III.10. The square dimensions are 20 x 20 µm. 90

Figure III-18. Comparison of 3D shapes of nDEP traps. A. With three line electrodes. B. with a round trapping electrode and C. with a square trap with quadrupole electrodes 91

Figure III-19. A. E.Coli randomly distributed on top of electrodes. B. E.Coli. repelled and aligned with the electric field lines 92

Figure III-20. A. Dipole-electric field alignment in E.Coli for complex electrode geometries. B. COMSOL simulated electric field lines for the same geometry. 92

Figure III-21. Fluorescence picture of trapped 1µm beads imaged with a 60x water immersion objective with their trajectory overlaid for a 10 seconds recording. The trap edges are shown as a red full line. 94

Figure III-22. Comparison between DEP restricted displacement under 3Vpp-20MHz (red curve) and freely floating bead (blue curve). The curves represent the average for 4 beads as shown in Figure III.18. 94

Figure III-23. Snapshot of trapped bead fluorescence intensity seen as 3D Gaussian peaks as a function of applied voltage at a constant frequency of 20MHz. A for 3Vpp and B. for 6Vpp 95

Figure III-24. DEP titerplate for assessing single cell trapping capabilities for a given electrode geometry. 96

Figure III-25. Number of traps having 0, 1 or more than 2 cells trapped depending on trapping voltage. A. at 3Vpp B. at 8Vpp. 97

Figure III-26. Snapshots showing trapped cells at different cell density. A. 4.10^4 cells/mL, B. 8.10^4 cells/mL and C. 5.10^5 cells/mL. Red circles indicate single cells. 98

Figure III-27. Cell trapping capability as a function of cell density. 99

Figure III-28. Holding force as a function of flow velocity near a trapped PS bead. The red line shows the quadratic fit associated. 100

Figure III-29. Snapshots of 2 trapped Jurkat cells, one of them undergoing division. The five snapshots correspond to different times: A. initially, B. after 14min, C. after 24min, D. after 30min and E. after 36min. 102

Chapter IV. Temperature mapping in nDEP traps

Figure IV-1. Heat capacity profile as a function of temperature for the membrane of E.Coli. The grey area corresponds to lipid melting and the peaks at 60ºC and above to protein denaturation events (adapted from [7]). 107

Figure IV-2. Schematic of the calibration chamber with a rhodamine B solution. P1.Peltier element, T1 and T2 are thermocouples linked to Peltier and calibration solution respectively. 110

Figure IV-3. Schematic of the calibration setup. 110

Figure IV-4. Recorded lifetime (A) and temperature (B) as a function of time for a temperature ramp from RT to 90 degrees C. 111

Figure IV-5. Calibration plot for measuring temperature with rhodamine B: intensity and fluorescence lifetime decay with temperature at a rate 1.12%/°C and 1.07 %/°C respectively. 112

Figure IV-6. A. Schematic of the microfluidic device including gold electrodes patterned on glass and the fluidic chamber; B. bright field picture of a single nDEP trap 114

Figure IV-7. Lifetime map over electrodes energized at $5V_{pp}$-1MHz. 114

Figure IV-8. Reconstituted heat profiles at the vicinity of the microelectrodes in the presence and absence of field. 115

Figure IV-9. Transient increase in temperature upon a voltage step. The focal plane was adjusted at 5 µm above the surface of the device. 116

Figure IV-10. Data treatment to obtain temperature variation from intensity measurements. A. raw data B. after thresholding C. after applying the median filter D. after division of intensity maps 'on'/'off'. 118

Figure IV-11. Temperature map from intensity measurements. 119

Figure IV-12. FLIM pictures before (A) and after (B) applying the median filter of size 5x5 and converting lifetime to temperature rise. 120

Figure IV-13. Fluorescence lifetime distributions before (in blue) and after (in red) switching on the electric field..... 121

Figure IV-14. Relationship between temperature rise and applied voltage: the blue curve corresponds to experimental data while the red one is based on Eq. IV-3..... 123

Chapter V. Dielectric cell response in highly conductive buffers

Figure V-1. Theoretical frequency response of cells based on the effective single-shell model. Vertical dashed lines indicate 1MHz and 40MHz. A. The cell cytoplasm conductivity changes from 0.3S/m to 1.1S/m for a set membrane conductivity of 10^{-7}S/m and membrane capacitance 13mF/m^2. B. The cell membrane conductivity changes from 10^{-5}S/m to 10^{-3}S/m for a set cytoplasm conductivity of 1.2S/m and membrane capacitance 13mF/m^2.C. Theoretical frequency response when varying the cell membrane capacitance from 5 to 20mF/m^2 for live and heat-treated cells (cytoplasmic conductivity of 0.3S/m and 0.9S/m respectively) immersed in a high conductivity buffer (1.65S/m).Cytoplasm dielectric constant was 80, membrane thickness 7nm, cell radius 5.1µm for all plots..... 131

Figure V-2. A. Schematic of the microfluidic flow cell with embedded planar electrodes. B. Corresponding cell velocity as a function of travelling time. C. Bright field snapshot of a live T-cell approaching the electrodes. 132

Figure V-3. Percentage of dead cells as a function of heating time at 65ºC. 135

Figure V-4. Position versus time for a single cell as extracted from the image analysis software. Incoming velocity and minimum velocity were measured as the slopes of the red dashed lines. 136

Figure V-5. Slowing down factor versus incoming velocity at 1MHz (A) and 40MHz (B) exhibit the presence of two distinct populations. The probability ellipses for both distributions correspond to 1σ. 138

Chapter VI. Mapping lateral heterogeneities of cellular membranes using time-resolved fluorescence spectroscopy

Figure VI-1 A.Intensity map for a DiI labelled Jurkat cell. The white square indicates the scanning area for figures B and C. B. Membrane close-up showing the spatial resolution limit for a single frame C. for an accumulated 50 frames 144

Figure VI-2. Membrane close-up showing the FLIM map of a membrane close-up. A. for a single frame B. for an accumulated 50 frames. C. Fluorescence decay curves for a single frame and 50 accumulated frames show a decrease in statistical noise. 146

Figure VI-3. Schematic analysis of membrane domains using FLIM. I. A model membrane with 2 rigid regions represented as grey patches. II. Fluorescence decay curves corresponding to regions A, B and C of schematic I. III. Corresponding lifetime histograms. 147

Figure VI-4. Quantitative incorporation of DiO depending on labelling conditions. A. RT for 15 minutes. B. 37ºC for 3 minutes and C. 37ºC for 15 minutes. 149

Figure VI-5. Average fluorescence from each cell based on different labelling conditions. 150

Figure VI-6. Photobleaching rate of a single DiO labelled Jurkat cell at different illumination powers. 151

Figure VI-7. Normalized lifetime decay histogram (blue curve) obtained from the TCSPC electronics for a DiI labelled U937 cell and corresponding fit (black line). The Instrument Response Function measured from the dye Rose Bengal in water is shown in red. The residuals plot reflects the goodness of the fit. 153

Figure VI-8. (A) Intensity map for a DiI labelled U937 cells. (B) lifetime map of DiI incorporated in the membrane..... 154

Figure VI-9. Example of average lifetime distribution for DiI in a U937 cell membrane. 154

Figure VI-10. Fluorescence Lifetime histograms for 5µM DiI in ethanol. The Gaussian fit of the same dye in a U937 membrane is given for comparison. 155

Figure VI-11. Normalized pre-exponential factor map representing the weight of the short lifetime component. The map was weighted by intensity..... 156

Figure VI-12. 2D slices of a DiI labelled U937 cell with focus moved upwards by steps of 2 microns from 0 to 10µm. Series i label intensity pictures, series l label FLIM maps..... 158

Figure VI-13. Lifetime histograms corresponding to each slice.0µm represents picture 1 in Figure VI.12. 158

Figure VI-14. Chemical structure of beta-cyclodextrin. 159

Figure VI-15. Exposure to MBCD reduces the average fluorescence lifetime of DiI in U937 plasma membranes. 160

Figure VI-16. Absorption and emission spectra of DiO in ethanol. The spectral overlap is hatched. 161

Figure VI-17. Example of a DiO labelled Jurkat cell with hot spots. A. Intensity map. B. Average lifetime map for the green channel. 162

Figure VI-18. Lifetime histogram for the green channel highlighting the bimodal distribution..... 162

Figure VI-19. Scatter plot of intensity versus lifetime for each pixel analyzed in a FLIM map. A. for a cell having hot spots. B. for a cell without hot spots. 163

Figure VI-20. Intensity (A and B) and lifetime maps (C and D) when labelling at RT native cells and cells without cholesterol respectively. The same number of scans has been taken for comparison purposes 164

Figure VI-21. Lifetime histogram with and without cholesterol extraction corresponding to the cells in Figure VI.20 165

Figure VI-22. A. Random mix of donors and acceptors. B. Donors and acceptors in the same phase. C. donors and acceptors in different phases. 166

Figure VI-23. A. Schematic snapshot of lipid diffusion with no colocalization resulting in a random distribution of donors (green) and acceptors (red). B. Schematic snapshot in the presence of lipid colocalization. 167

Figure VI-24. Simulated FRET intensity as a function of donor/acceptor initial density and colocalization events 168

Figure VI-25. Emission spectrum of DiO and absorption spectrum of DiD shows the hatched spectral overlap needed for FRET. 169

Figure VI-26. Average lifetime of DiO as a function of labelling conditions. 170

Chapter VII. Membrane FRET assays for membrane dynamics

Figure VII-1.Single cell membrane assays in DEP traps were performed by following 6 steps. 1. Incubation of cells at high density. 2. DEP trapping. 3. Imaging of selected cells. 4. Addition of reagent. 5. Incubation 6. End-point imaging of selected cells. 175

Figure VII-2. A. Intensity picture of a Jurkat cell in a square nDEP trap. Electrode contribution is apparent. The rounded square highlights the electrode edges while the dashed circle shows the pixels used to produce figure C. B. FLIM map including the contribution of the electrodes in the overall fluorescence decay fit. C. FLIM map excluding electrode contributions. 176

Figure VII-3. Qualitative motion of a cell showing superimposed fluorescence snapshots before and after trapping. The edge of the trap is highlight by a red square. 177

Figure VII-4. Lifetime histograms for DiO in absence and presence of an electric field. 177

Figure VII-5. Intensity map for a DiO-labelled Jurkat cell in the green (A) and red (B) channel. C. FLIM map for the green channel. 179

Figure VII-6. Intensity map after 1 minute incubation in a 5µM DiD solution for the green (A) and red (B) channels. C-D. FLIM maps for the green and red channel respectively. 180

Figure VII-7. Normalized lifetime histograms for the green channel at different times during DiD incorporation. 181

Figure VII-8. Lifetime histograms for the red channel at different times of DiD labelling 183

Figure VII-9. FRET efficiency as a function of labelling time. 184

Figure VII-10. A. FRET efficiency versus relative acceptor concentration fitted with a hyperbolic function. B. Quenching of FRET donor DiO-C18 as a function of acceptor DiI-C16 concentration in RBL cells as published in [2] for a similar FRET pair. 185

Figure VII-11. A. Fluorescence intensity map of trapped U937 cells in 5 individual traps B. cells labelled from 1 to 5. 187

Figure VII-12. Lifetime maps (1a,1b)and FRET intensity maps (2a,2b) before (series a) and after 15 minutes incubation in 3mM MBCD (series b). 188

Figure VII-13. Lifetime histograms in the green channel for individual cells show a shift towards higher lifetimes. 189

List of tables

Chapter I. Introduction

Table I.1. Review of fluorescent dyes used for membrane domains studies 19

Table I.2. Suitability matrix for given requirements set for single cell membrane analysis 25

Chapter II. Methodology

Table II.1. Properties of the confocal volume and diffraction-limited resolution 55

Chapter III. Dielectrophoretic cell trapping: theory and characterization

Table III.1. Dielectric parameters of human leukocytes extracted from the single-shell model. Reproduced from 18 75

Chapter IV. Temperature mapping in nDEP traps

Table IV.1. Fitting parameters for temperature and lifetime calibration measurements 111

Table IV.2. Fitting parameters for the Gaussian curves obtained from lifetime probability distribution 122

Chapter V. Dielectric cell response in highly conductive buffers

Table V.1. Number of cells screened for each frequency and fitting parameters with mean μ and standard deviation σ for the Gaussian fits of histograms of slowing down factors at 1MHz and 40MHz 139

Chapter VI. Mapping lateral heterogeneities of cellular membranes using time-resolved fluorescence spectroscopy

Table VI.1. DiI lifetime depending on its local lipid environment: average lifetime increases with order (from 10) 152

Table VI.2. Fitting parameters for the lifetime histogram of DiI in the membrane of a U937 cell 153

Table VI.3. Fitting parameters for the lifetime histograms of Figure VI.21 165

Chapter VII. Membrane FRET assays for membrane dynamics

Table VII.1. Gaussian fitting parameters for the lifetime histograms of Figure VII.4. 178

Table VII.2. One component Gaussian fitting parameters: average lifetimes and variances for the green channel at different times of labelling..... 182

Table VII.3. Mean and variance of Gaussian fits for the lifetime histogram at different FRET acceptor labelling times 183

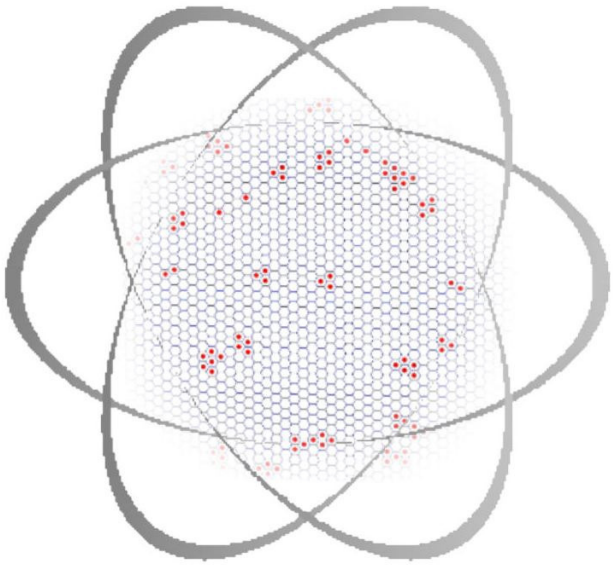
Table VII.4. Difference in average lifetime extracted from single component Gaussian fits before and after treatment with MBCD. 189

List of Abbreviations

Symbol	Meaning	Unit
GUV	Giant Unilamellar Vesicle	
DOPE	DiOleoylPhosphatidylEthanolamine	
GPI	GlycosylPhosphatidylInositol	
PS	PolyStyrene	
DSC	Differential Scanning Calorimetry	
FCS	Fluorescence Correlation Spectroscopy	
SPT	Single Particle Tracking	
FLIM	Fluorescence Lifetime Imaging	
FRET	Förster Resonance Energy Transfer	
TCSPC	Time-Correlated Single Photon Counting	
TTTR	Time-Tagged Time Resolved	
τ	Fluorescence lifetime	s
RT	Room Temperature	ºC
CW	Continuous-Wave	
IRF	Instrument Response Function	
ROI	Region Of Interest	
APD	Avalanche PhotoDiode	
CCD	Charge Coupled Device	
PMT	Photomultiplier Tube	
NA	Numerical Aperture	
EHD	ElectroHydroDynamic (flow)	
AC-EOF	Alternative Current Electro-Osmosis	
nDEP	Negative Dielectrophoresis	
pDEP	Positive Dielectrophoresis	
R	Radius of a cell or particle	m
v	Flow velocity	m/s
D	Diffusion coefficient	m^2/s
W	Power generation per unit volume of the media	W

$\vec{E}$	Applied electric field	V/m
ε	Absolute dielectric constant	F/m
σ	Electrical conductivity	S/m
$\underline{\varepsilon}$	Complex permittivity	
CM	Clausius-Mossotti factor	
PDMS	PolyDiMethylSiloxane	
IPA	IsoPropyl Alcohol	
SU-8	Negative photoresist	
ITO	Indium Tin Oxide	
DiI	Fluorescent lipid analog (1,1'-dioctadecyl-3,3,3',3'-tetramethylindocarbocyanine perchlorate)	
DiD	Fluorescent lipid analog (1,1'-dioctadecyl-3,3,3',3'-tetramethylindodicarbocyanine, 4-chlorobenzenesulfonate salt)	
DiO	Fluorescent lipid analog (3,3'-dioctadecyloxacarbocyanine, perchlorate)	
U937	Human leukemic monocyte lymphoma cell line	
Jurkat cell	Human T cell lymphoblast-like cell line	

Chapter I. Introduction



This introduction chapter aims at giving general insight into the relevant background of cellular membrane dynamics studies with primary focus on the plasma membrane of mammalian cells. It is essential to first review the generally accepted model of a two-dimensional fluid. Based on this model, cellular membrane structure and organization are discussed and the functional importance and clinical significance of lipid/protein domains and lipid rafts are highlighted.

Fluorescence spectroscopy techniques for studying membrane order are subsequently introduced with emphasis on detecting events relevant to membrane dynamics at high spatio-temporal resolution.

Finally, the various tools which are commonly employed for single cell trapping within a microfluidic environment are reviewed, showing the benefits of using dielectrophoretic trapping for facilitating membrane studies.

I.1. The plasma membrane: structure and organization

The plasma membrane of mammalian cells contains hundreds of different lipid species and one of the major challenges in contemporary molecular biology and biophysics is to understand the functional significance of this molecular diversity.[1-3] Besides its structural function, cell membranes are involved in the transport of energy, matter and information into and out of the cell.[4] The lipid bilayer, originally envisaged as merely a matrix for embedding membrane proteins, is now recognized as a main contributor to a number of membrane functions via its effect on protein conformation, stability, assembly and distribution and recent years have seen increased interest in lipid rafts which are believed to be key elements in membrane-related processes.[3]

I.1.1. Cell plasma membrane composition

Cell membranes are non-covalent, supra-molecular assemblies of lipids and proteins that form self-contained volumes. They define cellular compartments by acting as permeability barriers to polar molecules. The main components of which cell membranes are made up are reviewed hereafter.

Phospholipids are major components of the cell membrane. They are made of a polar head group and two hydrophobic hydrocarbon tails (**Figure I-1**). Tails are generally fatty acids of variable length where cis-conformed bonds (unsaturated) can be found. The four main phospholipids present in mammalian plasma membranes are phosphotidylcholine, phosphatidyethanolamine, phosphatidylserine and sphingomyelin.

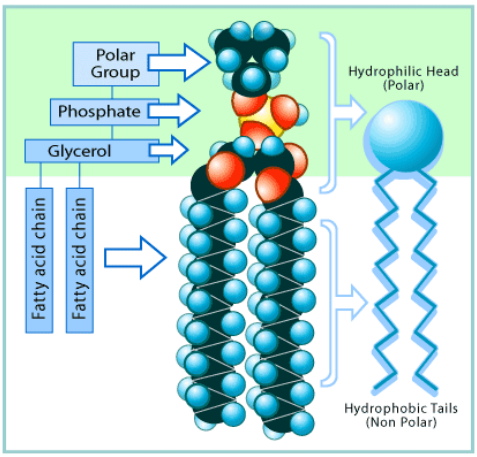


***Figure I-1**. Schematic of a phospholipid*

Phospholipids are described as being amphipathic, having both a hydrophobic and a hydrophilic region. Because of their structure, lipids immersed in water will self-assemble so that the phosphate heads make contact with the water and the hydrophobic hydrocarbon tails are restricted to water-free areas.[5] Self-assembled structures include micelles, liposomes or phospholipid bilayers (**Figure I-2**). The typical thickness of a mammalian plasma membrane is 5-8nm.[6]

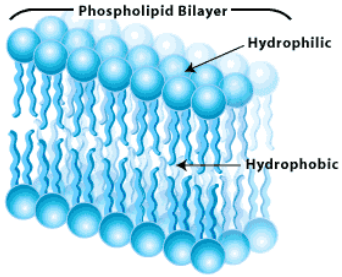


***Figure I-2**. A phospholipid bilayer*

Secondly, **membrane proteins** represent approximately 0.5-1mol% of the overall membrane. They accomplish various functions such as signal transduction, transport or adhesion. Membrane proteins are classified into two major categories: integral proteins and peripheral proteins. Integral proteins are generally transmembrane proteins, with hydrophobic regions that completely span the hydrophobic interior of the membrane. The hydrophilic ends of the molecule are exposed to the aqueous solutions on either side of the membrane. An example of integral protein includes G protein-coupled receptors having 7 transmembrane domains. Peripheral proteins are not embedded in the lipid bilayer but rather loosely bound to the

surface of the membrane, often to the exposed parts of integral proteins. They include desmosomes, clathrin-coated pits, caveolaes, and different structures involved in cell adhesion.

Thirdly, **membrane carbohydrates** exist usually in the form of branched oligosaccharides with fewer than 15 sugar units.[7] Some of these oligosaccharides are covalently bound to lipids, forming molecules called **glyco-lipids.** Glycolipids account for 5 percent of all lipid molecules in the external monolayer. Most are covalently bonded to proteins, which are thereby **glyco-proteins**. The oligosaccharides on the external side of the plasma membrane vary from species to species, among individuals of the same species, and even from one cell type to another in a single individual. The diversity of the molecules and their location on the cell surface enable oligosaccharides to function as markers that distinguish one cell from another.

Cholesterol is a common steroid in animal cell membranes and contribute to stabilizing the membrane.[8-11] It is believed (together with sphingolipids) to lie at the root of particular membrane domains formation, which is referred to as lipid rafts (see **I.1.3**). The plasma membranes of eukaryotic cells contain a large quantity of cholesterol (typically 30-50 mol%).[12] Cholesterol reduces the mobility of some CH_2 groups of hydrocarbon chains. The region thus becomes less prone to deformation and also less permeable to small hydrophilic molecules.[13] **Figure I-3** illustrates a schematic of the cell membrane with its main constituents.

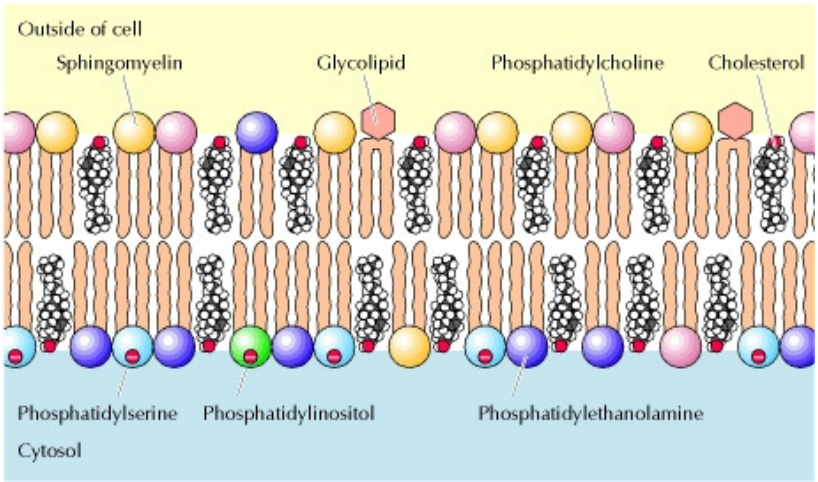


***Figure I-3**. Schematic of the cell membrane composition(reproduced from [14]).*

The **cytoskeleton** consisting roughly of filaments networks (actin filaments, intermediate filaments, microtubules) is anchored to the membrane via anchor proteins which ensure stability of the cell.[15]

It is worth pointing out that membranes are asymmetric structures.[16] They have distinct inside and outside faces with the two lipid layers differing in lipid composition, and individual proteins having directional orientation in the membrane. For instance, in human red blood cells, nearly all lipidic molecules containing choline in their head group (phosphatidylcholine and sphingomyelin) are located on the outside monolayer whereas phospholipids having a primary amine terminal group are located on the inner monolayer.[17] This asymmetrical distribution of proteins, lipids, and carbohydrates depends on lipid production in the endoplasmic reticulum.

I.1.2. Fluidity of the lipid bilayer

I.1.2.1. The fluid mosaic model

The two layers of a membrane bilayer are held together primarily by hydrophobic interactions. This is an entropy-driven mechanism by which the hydrophobic system tends to exclude water. The effective force it provides is sufficient to trigger self-assembly of lipid bilayers. However, membrane components are still able to drift laterally.

The fluid mosaic model (Singer and Nicolson, 1972) as a representation of the cell membrane by Singer and Nicolson has long been accepted.[18] It states that the biological membranes can be considered as an unstructured two-dimensional fluid into which individual proteins are embedded. **Figure I-4** represents a simplified schematic membrane with arbitrary molecules labeled as rod dots progressively diffusing in the absence of any lateral organization effects.

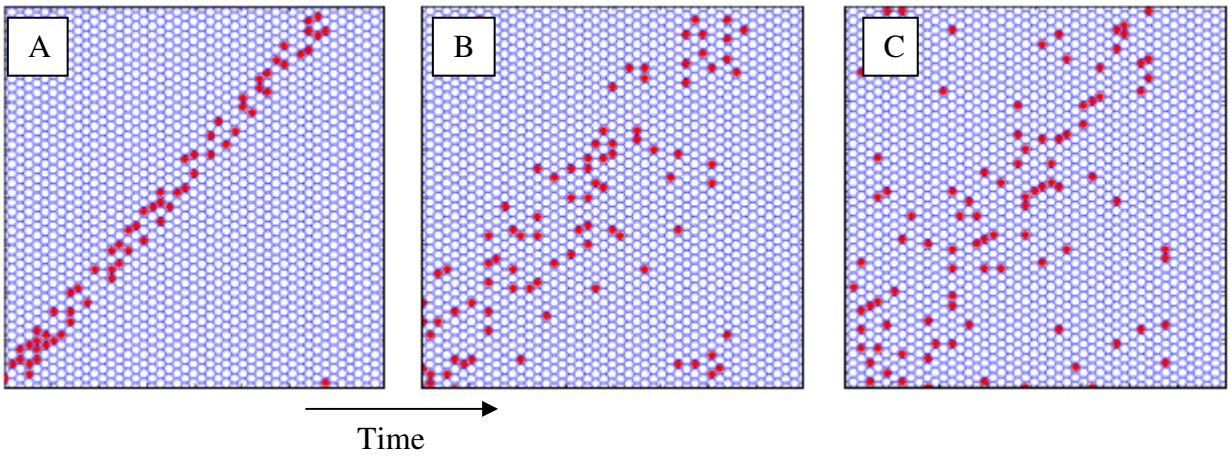


Figure I-4**. Progressive diffusion in the fluid mosaic model with increasing time from **A** to **C

Relying solely on thermodynamics forces, most lipids are randomly mobile in the plane of the membrane, with thermodynamic intensive variables like temperature or pressure also affecting the fluidity of the membrane.[19-21] Saffman and Delbrück further related the diffusant size to the translational diffusion coefficient in a two-dimensional continuum fluid. [22]

This model has however recently proven to be incomplete.[23] Specifically, diffusion coefficients for both proteins and lipids in the plasma membrane were found to be smaller than those found in artificially reconstituted membranes such as Giant Unilamellar Vesicles (GUVs) or liposomes by factors of 5 to 50. Various models have been proposed to explain this large difference in macroscopic diffusion coefficients including membrane micro-domains. [24]

I.1.2.2. Membrane micro-domains

Membrane micro-domains can be classified as either protein-based or lipid-based. [24] In both cases, differential interactions between components are the main driving force responsible for the segregation of components into domains. Mismatches between the hydrophobic thicknesses of molecular components, cohesive forces (Van der Waals interactions) and the lipid chain entropy are thought to result in a wide range of differential interactions among membrane components. In the simplest mixture of two distinct lipids, domain formation will result from the favoured exchanges occurring at the microscopic level between similar components. This is illustrated by **Figure I-5**.

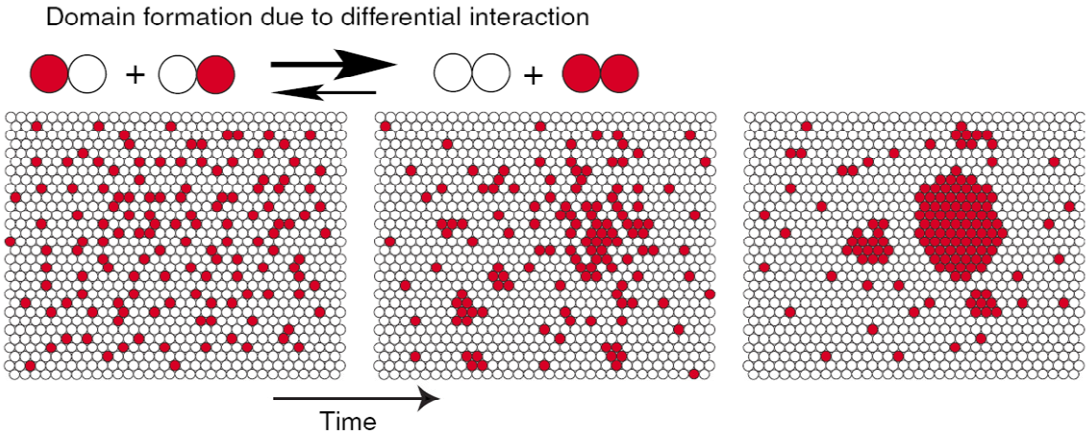


***Figure I-5**. Diffusion and domain formation: If the exchange resulting in two like pairs is energetically favourable, domains can form. At thermodynamic equilibrium, molecules still diffuse inside and outside the domains, and some of them are transiently trapped in domains (reproduced from [19]).*

Resulting from these differential interactions, the plasma membranes of mammalian cells contain many heterogeneities or domains embedded in the phospholipid bilayer such as protein-protein complexes, lipid rafts, pickets and fences (formed by the actin-based filaments of the cytoskeleton) and large immobilized structures (such as synapses or desmosomes). Membrane undulation has also been shown to help protein hopping between these micro-domains.[25]

I.1.2.3. Cytoskeleton partitioning

Cytoskeleton-dependent membrane domains have also been hypothesized. DiOleoylPhosphatidylEthanolamine (DOPE) molecules were found to undergo short-term confined diffusion within a compartment and long-term hop movement between the compartments (anomalous or hop diffusion).[23] This led to the hypothesis that the plasma membrane is partitioned with regards to molecular diffusion. Compartmentalization could be caused by the fence (corralling) effects of the membrane skeleton as well as the hydrodynamic slowing effects of transmembrane-protein pickets anchored on the membrane-skeleton fence as schematically represented in **Figure I-6**.

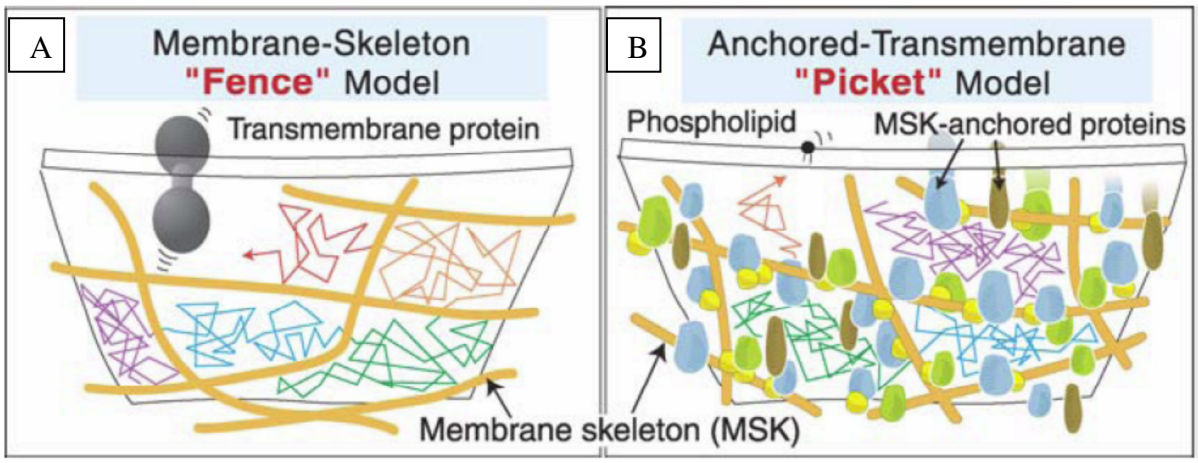


***Figure I-6**. The models of the membrane-skeleton "fence" (**A**) and the anchored-transmembrane protein "pickets" (**B**) that together are thought to partition the entire plasma membrane into small compartments (reproduced from [23]).*

I.1.3. The presence of different lipid orders in the plasma membrane

Several phases co-exist within a mammalian cell membrane. Pure phospholipid bilayers below melting temperature T_m form a solidified gel phase, which melts above the T_m to a fluid phase (liquid-disordered (L_d)). The presence of cholesterol (hatched ovals in Fig. 4) orders the acyl chains of the latter phase, and is referred to as an intermediate liquid-ordered state (L_o). These three phases are represented in **Figure I-7**.

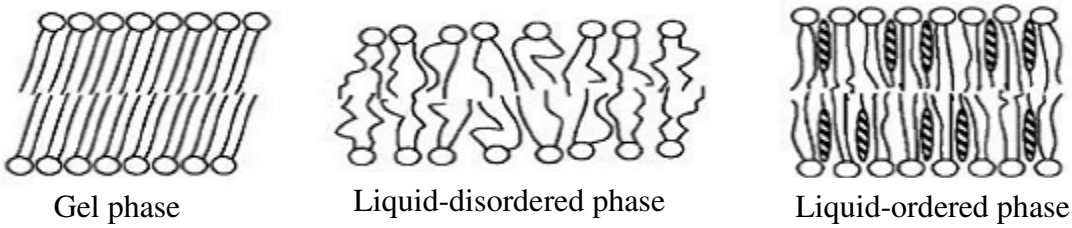


***Figure I-7**. Structure of the gel phase, liquid-disordered phase and liquid-ordered phase containing cholesterol (adapted from [26]).*

A typical cell membrane at physiological temperatures (around 37ºC) is made of coexisting L_o and L_d phases. The presence of different phases within the same plasma membrane further contributes to micro-domain or cluster formations.

I.1.3.1. The influence of temperature on membrane fluidity and order

The composition and thermodynamic properties of a cell membrane strongly depends on the intensive thermodynamics variables. These include pressure, temperature, chemical potential or electrostatic interactions. Depending on these parameters, individual lipids as well as the membrane as a whole undergo phase transitions. Phase transitions can be studied using Differential Scanning Calorimetry (DSC). It is a commonly employed technique in the field of drug-membrane interactions.[27] DSC measures the amount of heat needed to increase the temperature of a sample and reference as a function of temperature.

Figure I-8 illustrates a DSC plot highlighting the temperature window for which lipids start melting when E.Coli are grown at 37ºC and 15 ºC respectively.

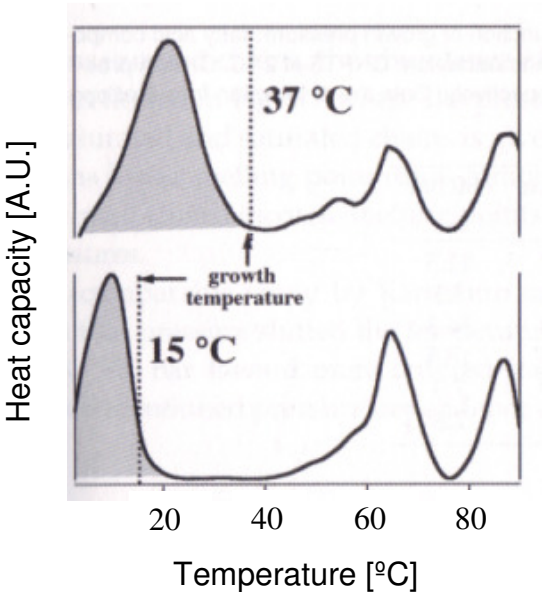


***Figure I-8**. Melting properties of the membrane of E.Coli grown at 37ºC and 15 ºC (reproduced from [28]).*

The melting temperature is in both cases found right below the growth temperature which suggests membrane fluidity is always preserved. The composition of the membrane as produced by the endoplasmic reticulum is therefore actively controlled by temperature changes. This phenomenon has implications when cells are taken out of their growth temperature: membrane order is directly increasing with decreasing temperatures. The discrepancy between growth temperature and experimental temperatures (for instance RT) therefore plays an important role when evaluating membrane dynamics.

I.1.3.2. Lipid rafts nanodomains

The existence of lipid rafts was first hypothesized in 1988.[29] These are temporary phase separation domains of the fluid bilayer thought to be 10-200nm in diameter, enriched in both sphingolipids and cholesterol.[11] The original concept of rafts was used as an explanation for the transport of cholesterol from the trans face of the Golgi network to the plasma membrane. The idea was more formally developed in 1997 by Simons and Ikonen.[30]

Despite much evidence supporting the existence of raft domains, the definition, size and function of these domains are still under debate.[31] The controversy mainly arises because these domains are too small to be optically resolved. Recently, lipid rafts have been defined as ‘‘*small (10–200nm), heterogeneous, highly dynamic, sterol- and sphingolipid-enriched domains that compartmentalize cellular processes. Small rafts can sometimes be stabilized to form larger platforms through protein–protein and protein–lipid interactions*”.[32]

I.1.3.3. Example of Jurkat T-cell signalling

One key aspect triggering the response of an adaptive immune system is the binding of a T cell antigen receptor (TCR) to a cognate peptide-Major Histocompatibility Complex (MHC) ligand presented on the surface of an antigen-presenting cell.[31] TCR signaling cascade is initiated by the phosphorylation of tyrosines of the TCR/CD3 complex by Lck kinases anchored in the cytoplasmic leaflet of the T cell plasma membrane. The phosphorylations of membrane-associated signaling proteins trigger the formation of signaling domains made of protein complexes held together by protein-protein interactions. The cascade chain initiated by domain formation is represented schematically in **Figure I-9**.

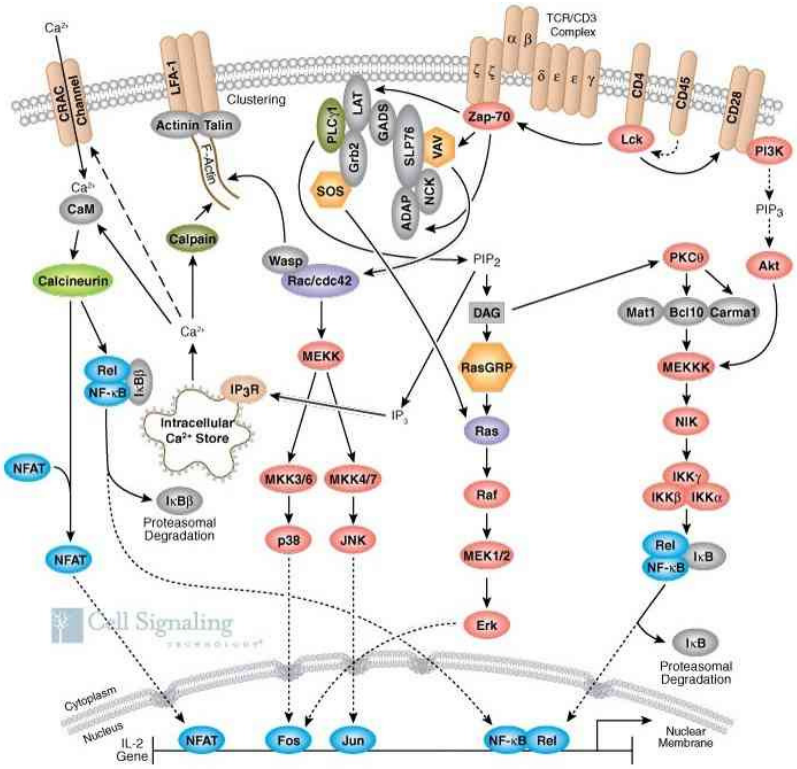


***Figure I-9**. Jurkat T-cell signalling cascade from* [33]

TCR signaling domains have been shown to accumulate cholesterol, sphingomyelin and saturated phosphatidylcholine species referred to as lipid rafts. The stabilisation of these rafts results from cross-linking of raft-membrane proteins.

Fluorescence techniques have recently been used to refine the definition of lipid rafts including Fluorescence Correlation Spectroscopy (FCS) and FRET. FCS is able to distinguish raft markers like cholera toxin B subunit bound to gangliosode (GM1) from non-raft markers via their lateral mobility.[34] FRET analysis helped detail the distribution of GPI-anchored fluorescent proteins in the plasma membrane of live cells before and after Jurkat cell stimulation.[35]

The existence of lipid rafts is now widely recognized as nanoscopic domains serving as platforms for TCR early signalling events involving protein complexes. Membrane dynamics therefore lies at the core of T-cell response.

I.1.3.4. Tumour cell membranes and fluidity

The composition and properties of tumour cells is the subject of intensive research. Alterations to membrane compositions, over-expression of receptors and charge densities have been reported. This is illustrated in **Figure I-10**. In a study by Sok *et al.*, the membranes of lung tumour cells have been found to possess a higher degree of fluidity than membranes of non-tumour cells. The authors argue this might constitute a complementary prognostic method.[36]

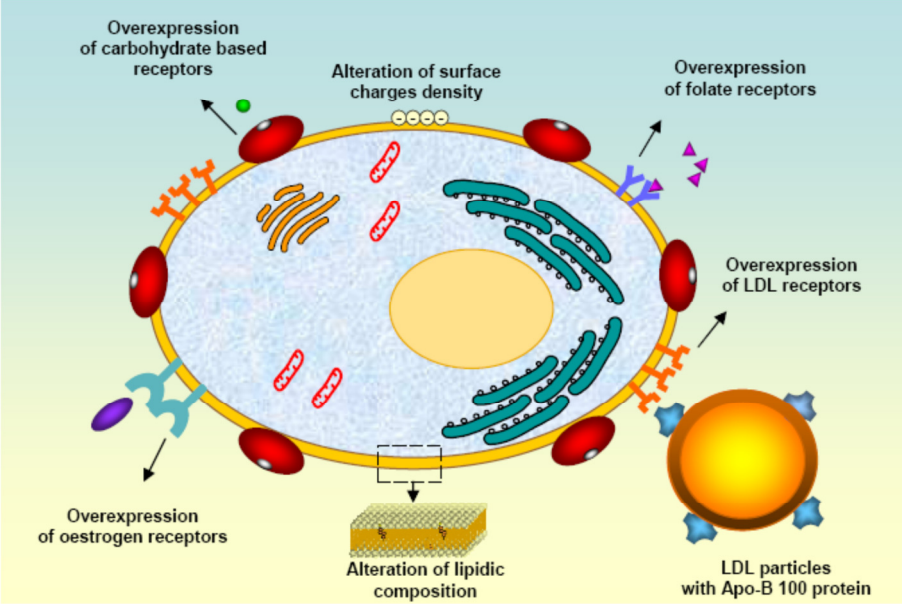


***Figure I-10**. Cancerous cell membranes undergo various alterations (reproduced from [37]).*

A better understanding of lipid and proteins membrane dynamics is thought to have important functional implications on the activity of signaling protein complexes or the identification of cancerous cells and is thus highly relevant for fundamental research.[38-41]

To conclude, the motion of individual molecules as well as domain dynamics is a complex topic and subject to extensive research. Unsurprisingly, it is far from being fully understood.

I.2. Membrane order studies using fluorescence

The challenge of modern biology is to study individual components of a cell membrane with minimum perturbations. To this aim, optical detection techniques based on fluorescence

contrast has brought a wide range of tools able to interrogate membranes in physiological conditions.[20] Seeing and tracking individual molecules has historically been possible through the introduction of single molecule detection techniques such as Fluorescence Correlation Spectroscopy (FCS) and Single Particle tracking (SPT).[42, 43] These techniques allow direct access to the diffusivity of a labelled tag and can be related to the presence of phase heterogeneity within a membrane. They give highly localized information at very high resolution (down to tens of nanometers). However, measuring diffusion over the whole membrane has proven so far too difficult due to the low data acquisition rates. This can lead to problems of data extrapolation from small portions of a membrane and can represent a significant hurdle in the data analysis and further interpretations.[44]

On the other hand, ensemble measurements such as Fluorescence Lifetime Imaging (FLIM) probing the full length of a membrane at diffraction-limited resolution reflect the general state of a membrane while preserving access to heterogeneity measurements.[45] Indeed, the latter technique can be adapted to reach sub-diffraction resolution thanks to the use of Förster Resonance Energy Transfer (FLIM-FRET) between acceptor and donor dyes.[46] The combination of FLIM and FLIM-FRET techniques therefore retains the capability of scanning a wide area of a membrane while detecting nanoscopic events such as colocalization of fluorescent molecules.

I.2.1. Single molecule techniques

I.2.1.1. Fluorescence Correlation Spectroscopy

The theory of FCS was developed first by Magde *et al.* in 1972.[43] FCS characterizes the fluctuations in fluorescence intensity of a system at equilibrium.[47]

A schematic of a typical FCS setup is shown in **Figure I-11A**. It usually employs a microscope objective with high numerical aperture to focus the laser and achieve efficient detection of emitted photons. The photons emitted within the focal volume pass through a pinhole, which reduces the detection volume in the z-direction. As a result, the measurement volume is confined down to the femtoliter level. Then, the photons pass through optical filters and are detected by a high-sensitivity avalanche photodiode. The diffusion of fluorophore molecules through the focal volume or changes in their emission properties due to chemical

reactions, association/dissociation events, photodynamic processes or conformational changes produce fluctuations in fluorescence intensity that can be quantified and auto-correlated as a function of time (**Figure I-11B**). The characteristic decay time of the autocorrelation function is related to the time that the fluorophore spends within the focal volume, which in turn depends on the mobility of the particle: the larger the diffusion coefficient, the faster the decay (**Figure I-11C**).

FCS averages thousands of single-diffusion events seen as fluorescence peaks, allowing precise estimate of diffusion coefficients and particle concentrations in relatively short acquisition times (in the timescale of a minute). It thus can be used to investigate not only molecule mobility, transport, and diffusion processes but also rate constants of inter- or intra-molecular reactions or binding.[48]

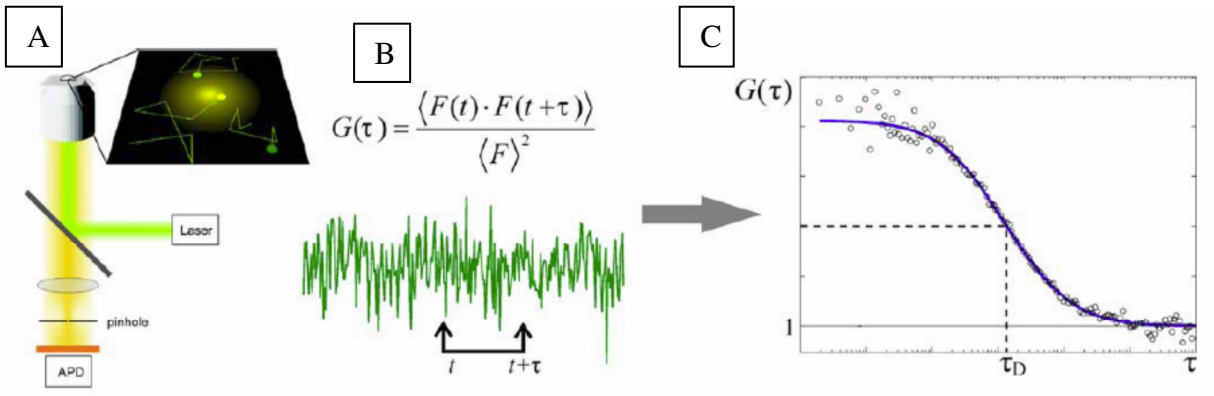


***Figure I-11**. Principles of Fluorescence Correlation Spectroscopy. **A**. The sample is illuminated by focusing the laser beam with an objective. The emitted photons are then spectrally filtered and detected (e.g. with an avalanche photodiode). A pinhole before the detector limits the detection volume in the z-direction, so that the light from upper and lower planes is eliminated. **B**. The emission of photons diffusing in and out the focal volume induces fluctuation in the signal intensity. The fluorescence trace recorded during a given period of time is auto-correlated. **C**. The graph shows the values obtained for the auto-correlated fluorescence signal (white circles). The diffusion coefficient, binding kinetics parameters or particle concentration can be determined by fitting the experimental values to the autocorrelation function (solid line) (reproduced from [47]).*

The organization of the cell membrane has been intensively investigated by FCS and one of the main advances in cell membrane understanding has been the evidence for micro-domains,

which have been of large interest for over 30 years.[49] Diffusion measurements at different spatial scales gave rise to the so-called FCS diffusion law. This provides information about the confinement parameters of micro-domains in cell membranes. For instance, the diffusion properties of GFP proteins bound to the cell membrane by different tags were affected by the disruption of lipid-based or cytoskeleton-based micro-domains, revealing the importance of these factors in membrane organization.[50] Hindered or 'anomalous' diffusion with different regimes in the diffusivity of molecules have been explained by the hopping of dyes in and out more rigid regions.[51, 52] Dual-colour fluorescence cross-correlation spectroscopy has also been used to analyze two reporters diffusing in the probe volumes, especially for binding kinetics studies.[53]

I.2.1.2. Single Particle Tracking

SPT uses video microscopy combined with digital computer processing to monitor the motion of single proteins or lipids in the plane of the membrane.[54] The molecules of interest are often labelled with sub-micrometer particles (e.g. colloidal gold of 40–100nm in diameter) coated with specific antibodies or ligands. These particles give rise to a diffraction airy disc pattern allowing determination of the centroid position with around 10 nm precision. [43] Total Internal Reflection Fluorescence (TIRF) microscopy can also be used for SPT, as only a thin plane of the sample is illuminated such that the background fluorescence is strongly reduced.[55] SPT is a powerful technique to detect deviations from Brownian diffusion, such as confined diffusion, anomalous diffusion, or directed flow of particles. A typical analysis of single particle trajectories is shown on **Figure I-12**.

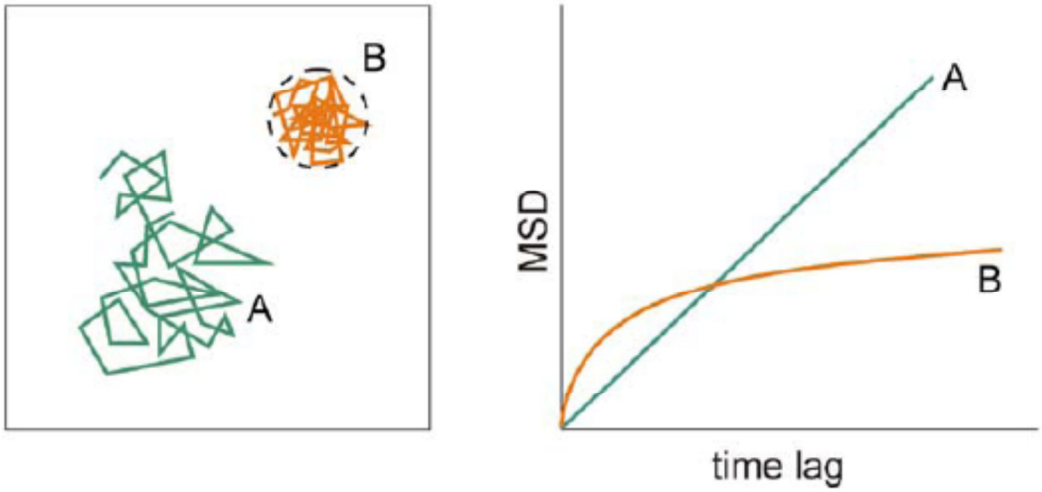


***Figure I-12**. Analysis of single particle trajectories. On the left, the trajectories of free-diffusing (A) and confined (B) particles are shown. The graph on the right depicts the corresponding mean-square-displacement (MSD) versus lag time for the same particles (reproduced from [23]).*

On the whole, FCS detects fluorescence photons emitted from different molecules and is used to find the average diffusion at a constant position on a membrane while SPT tracks a single particle over a small area of a membrane and therefore extract true single-molecule information.

I.2.2. Fluorescence measurements on ensemble of molecules

I.2.2.1. Fluorescence Lifetime Imaging (FLIM)

The phenomenon of fluorescence and fluorescence lifetime can be explained with the use of a Jablonski diagram as the one shown in **Figure I-13**.

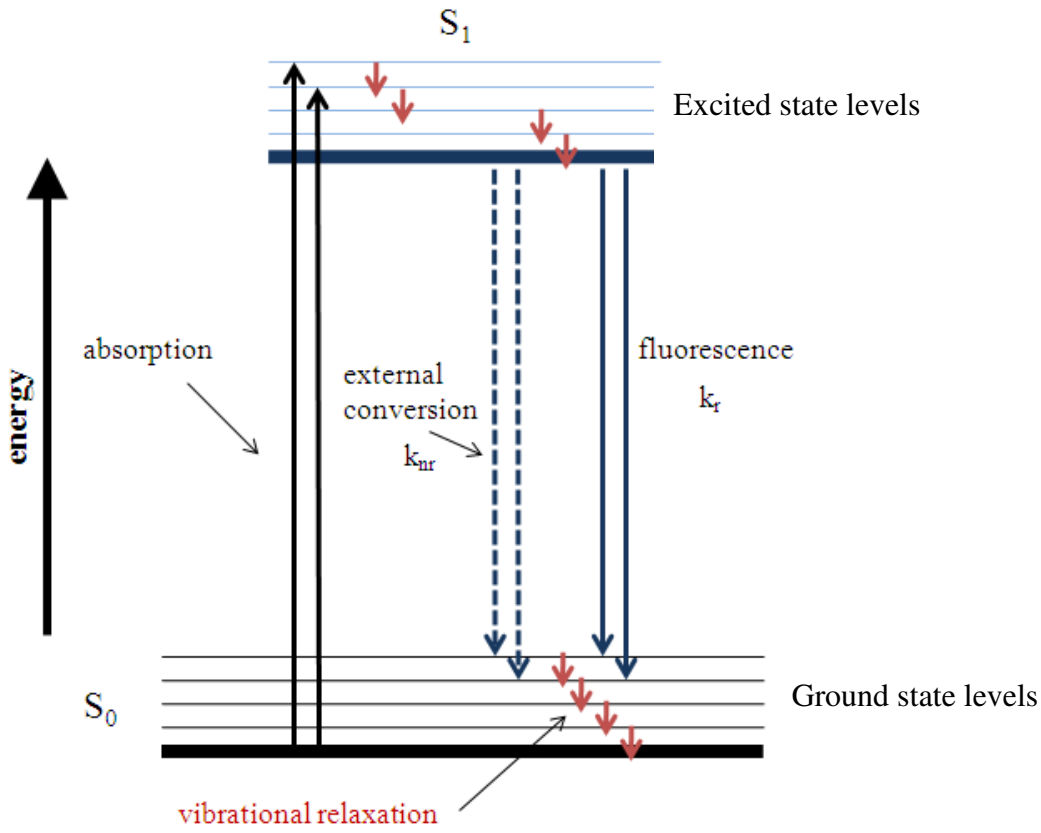


***Figure I-13**. Jablonski diagram for the phenomenon of fluorescence.*

A fluorophore can absorb a photon and be excited to either the so-called S_1 state or higher singlet electronic states. The molecule will lose energy to the surrounding environment as it returns to the Boltzmann distribution so rapid relaxation by internal conversion into the lowest vibrational level of S1 will usually occur. The molecule will then return to the ground state (S_0) either radiatively with the emission of a photon or non-radiatively. This radiative emission of a photon is known as fluorescence.

The fluorescence of a fluorophore can be further characterized by its fluorescence lifetime. The fluorescence lifetime (τ) is the time taken for the fluorescence intensity to decay exponentially to 1/e of the intensity at the time zero of excitation. Fluorescence lifetime can be expressed using the following equation:

$$\tau = \frac{1}{k_r + k_{nr}}$$ **Eq. I-1**

The radiative decay rate k_r is dependent on the intrinsic properties of a fluorophore while the non-radiative decay rate k_{nr} is dependent on the local environment. Lifetime can therefore be used as a tool to resolve various fluorophores and probe the nature of their chemical environment. Importantly, measurements of fluorescence lifetimes are ratiometric meaning that they are independent of the concentration of fluorophores. Also, unlike intensity measurements where dyes are prone to photobleaching, lifetime allows artefact-free quantification.

In this thesis, the words 'lifetime' and 'fluorescence lifetime' are used interchangeably.

I.2.2.2. Order sensitive fluorescent dyes used in FLIM

The partitioning of lipids can be looked at using fluorescence detection techniques. The most popular approaches make use of mimetic membranes of known compositions with clearly distinct L_o/L_d domains. The general tendency of lipids to partition in each phase have been evaluated in many such studies.[44, 52] It has been found that lipid analogs with long alkyl chain length such as the carbocyanine dye DiI-C18(3) significantly tend to localize into more ordered regions than those with short alkyl chain length. These studies are important for the development of specific reporters of membrane domains. However, it has to be pointed out that fluorescent lipids placed in an artificial phospholipid mixture exhibit a very different behaviour than in the plasma membrane of a cell and therefore any interpretations has to be done with care.

Among other techniques, membrane order has been examined using fluorescence lifetime spectroscopy. The photo-physical sensitivity to membrane phase has for instance been demonstrated using carbocyanine, AminoNaphthylEthenylPyridinium (di-4-ANEPPDHQ) or Nitro-2-1,3-BenzoxaDiazol-4-yl (NBD) dyes.[32, 56, 57] **Table I.1** summarizes the properties of these dyes used with FLIM for membrane order.

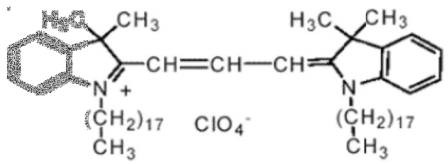
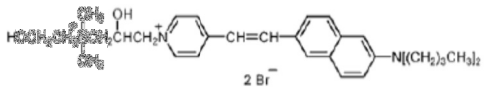
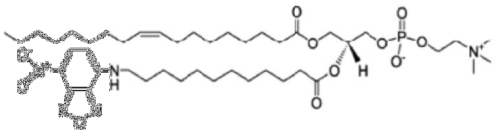
Phospholipid analog	Chemical structure	Excitation wavelength of maximum absorption	Original use	Lifetime in Ld regions	Lifetime in Lo regions	Remarks
Alkyl chain coupled carbocyanine dyes	 Linear structure of DiI	DiO - 488nm DiI - 552nm DiD - 647nm	Originally used as a membrane stain. Was also found to be dependent on membrane fluidity	1ns	1.5ns	Localized in both Ld and Lo regions depending on hydrocarbon chain length.[56] Probes with long alkyl-chain found predominantly in cholesterol rich regions.[58]
di-4-ANEPPDHQ		473nm	Transmembrane potential measurements Also employed for fluidity studies	1.85ns	3.5ns	Very sensitive dye but photo-physical properties vary with the presence of an electric potential.[32] Its lifetime also depends on the presence of cholesterol
18:1-12:0 NBD PC		467nm	Mainly used for membrane organization	7ns	11ns	Actual phospholipid as opposed to phospholipid analog. Lifetimes are not sensitive to variation of cholesterol concentration.[57]

Table I.1. *Review of fluorescent dyes used for membrane domains studies*

Overall, the lifetime of these dyes increases with higher degree of ordering of a membrane. This is believed to be due to steric hindrance or restricted decay routes.[57] The sensitivity highly varies from dye to dye and di-4-ANEPPDHQ, which was originally designed for measuring electrical potential has been so far found the most sensitive to membrane order.[32] However, in the framework of this study using DEP, di-4-ANEPPDHQ was not found appropriate due to the application of electric fields in the cell trapping process.

I.2.2.3. FLIM- Förster Resonance Energy Transfer (FLIM-FRET)

FRET is a distance-dependent interaction between the electronic excited states of two dye molecules in which excitation is transferred from a donor molecule to an acceptor molecule without emission of a photon.[59] The efficiency of FRET is dependent on the inverse sixth power of the intermolecular separation, making it useful over distances comparable with the dimensions of biological macromolecules. As a result, FRET is often referred to as a `spectroscopic ruler´. FRET is an important technique for investigating a variety of biological phenomena that produce changes in molecular proximity.[59] Membrane dynamics with microscopic or nanoscopic domains is particularly suited for examination by FRET. In particular, colocalization of proteins and other molecules can be imaged with spatial resolution beyond the limits of conventional optical microscopy. The Jablonski diagrams illustrating the energy transfer between donor dye and acceptor dye is shown in **Figure I-14**.

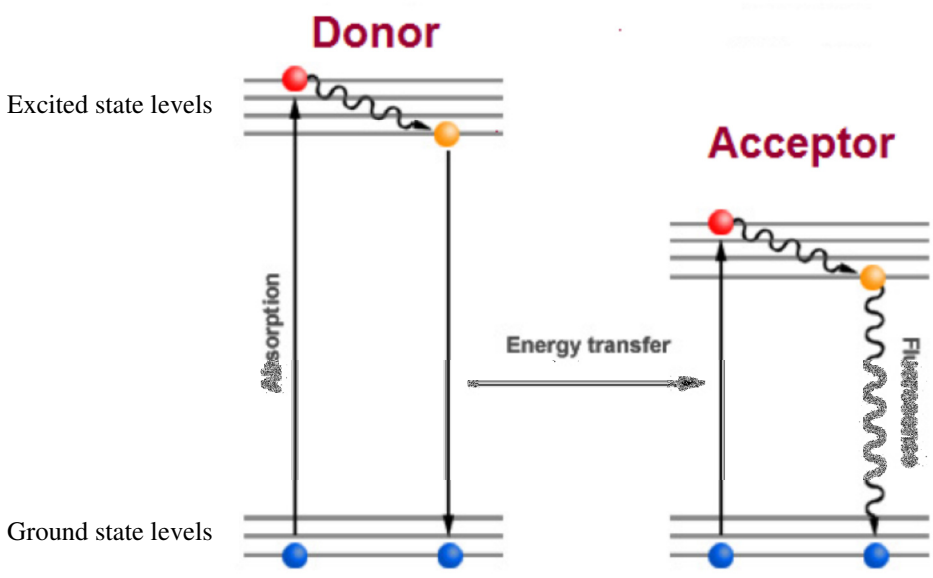


***Figure I-14**. Jablonski diagram illustrating the FRET process*

There are conditions for the existence of FRET which are:

1 - Donor and acceptor molecules must be in close proximity (typically 10–100 Å).

2 - The absorption spectrum of the acceptor must overlap the fluorescence emission spectrum of the donor

3 - Donor and acceptor transition dipole orientations must be approximately parallel.

If the aforementioned conditions are met, FRET can be studied in conjunction with FLIM as the characteristic donor quenching effect of FRET is detected as a decrease in the fluorescence lifetime of donor molecules. The combination is referred to as FLIM-FRET.

I.2.2.4. Colocalization studies with FRET

Lipid-lipid recognition and nearest-neighbour experiments are recognized as being very important to probing membrane organization.[60, 61] **Figure I-15** schematically represents the kinetics of colocalization between two fluorescent reporters. k_{on} represents the effective colocalization rate constant within shared micro-domains, k_{off} is the effective exclusion rate constant.

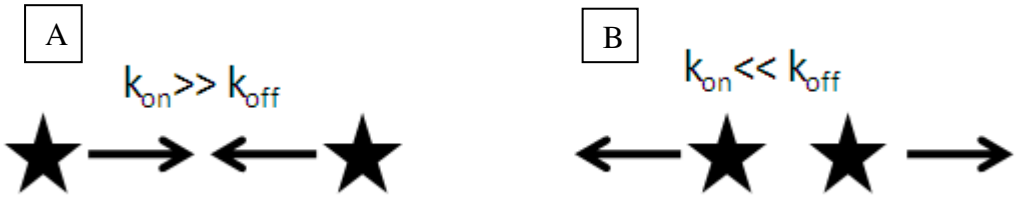


***Figure I-15**. kinetics of colocalization (**A**) and exclusion(**B**) for two fluorescently labelled molecules.*

Nearest-neighbour recognition measurements take 'molecular-level snapshots' of lipid organization in fluid bilayers by detecting and quantifying the thermodynamic tendency of two lipids or proteins to become nearest-neighbours. It gives access to the equilibrium constant k_{on}/k_{off}. The nanometric spatial resolution of FRET has greatly contributed to this field by measuring lateral distribution at the single molecule level. Both homo-FRET between identical probes and hetero-FRET have been found useful for studies involving lateral segregation and the identification of ordered/disordered phases. Nanoscopic heterogeneities have for example been confirmed in RBL-2H3 cells using FRET. Colocalization between raft markers has shown the presence of different raft types, exclusion of non-raft proteins and strong local cholesterol content in COS-7 cells.[62] These studies are

likely to have a great impact on our understanding of supra-molecular structure-function relationship in biological membranes.

As a conclusion, there are a range of mature tools based on fluorescence detection for high-resolution imaging giving a clear picture of both microscopic and nanoscopic molecular dynamics.[63] FLIM and FLIM-FRET are particularly suited to detect membrane order, colocalization and binding events. Single-molecule techniques, on the other hand, can prove very useful tools to probe the fundamental ordering and dynamics of cellular membranes by studying a very low number of molecules at a time.

I.3. Alternative tools to study membrane dynamics

Aside from fluorescence approaches, new tools to study membrane dynamics are still under development. A powerful example is the photothermal interference contrast method which can resolve individual receptors labeled with gold nanoparticles and track them for several minutes on cell surfaces.[64] Label-free techniques such as Raman microscopy techniques can monitor molecular vibrations with minimum perturbation to the biosystem. It has already been applied to lipid-lipid interactions.[65]

All these novel techniques will prove extremely useful to provide novel measurements and generate complementary pieces of information to fluorescence-based methods.

I.4. Cellular trapping for membrane analysis in a microfluidic environment

In this section, we present cell trapping techniques with emphasis on trapping suspension cells. Suspension cells naturally live without attachment to a substrate such as cells present in blood (hematopoietic cells). On the contrary, adherent cell lines from tissues do require an attachment matrix as a culture flask surface where they grow in monolayers. The possibility of trapping adherent cells stably by only surface adhesion forces bypass the need to design complicated trapping strategies unless for special prerequisites. As such, the work presented

in this thesis was performed with a monocyte cell line (U937) and a lymphocyte cell line (Jurkat cell) both able to live in suspension buffers.

I.4.1. Analyses based on single cells versus cell ensemble studies

Conventional cell assays are performed by pipetting cells suspended in a buffer into the wells of a microtiter plate where assaying reagents are then introduced. These traditional cell studies rely on the averaging of a large number of cell responses (typically >3000). The random positioning of cells on a substrate implies the impossibility to assess the local environment experienced by each cells, for instance the number of neighbouring cells. This may introduce poor reproducibility when analyzing ensemble responses. This has in some cases led to misinterpretation due to molecular heterogeneities.[66] Other drawbacks include a very large volume consumption of reagents (in the range of 100µL), the cost and limited versatility of the detection instruments.

Second, these methods are unable to acquire quantitative cell responses having fast timescales (less than 5 minutes). This includes ion channel activity, intracellular transport or quick diffusion effects at the surface of a membrane.[67]

I.4.2. Single cell patterning in a microfluidic environment

In this work, we are aiming at the combination of three factors: accurate cell positioning, control over the cell micro-environment and fast, quantitative high-resolution fluorescence imaging of single cell response to environment changes.

• The control over cell location is essential for being able to track the same cell with high spatio-temporal accuracy or study multiple cells simultaneously. The knowledge of their trapping location also facilitates pre-assaying calibration steps. The development of single cell trapping arrays has been largely eased by the development of miniaturization technologies from the microelectronics industry which offers the possibility of creating single cell arrays within microfluidic networks through the patterning of micron sized structures or electrodes.[68]

• Cellular behaviour is hugely influenced by its extracellular environment. The use of microfluidic technologies gives the possibility to deliver reagents to single cells and allows fine control of the cells micro-environment. This will eventually lead to a better understanding of single cell responses to uniform environment changes as well as enable the study of their transient responses.

• Fluorescence and fluorescence lifetime imaging provide the collection of information-rich data with diffraction-limited resolution. This contrasts with established techniques like flow cytometry where a large number of cells can be screened at single cell level but with no spatial information and are limited to specific labelling conditions. The integration of cell trapping and fluorescence imaging imposes constraints on fabrication materials (low auto-fluorescence, transparency, short cell to objective distance). However this has been addressed by the versatility of materials available for the fabrication of microfluidic components.

I.4.2.1. Single cell trapping techniques and membrane analysis

Cell trapping methods can be classified as either surface contact or contact-less as shown in **Figure I-16**.[69-71] They also correspond to either passive trapping approaches (contacting forces) or using active trapping mechanisms (contact-less forces).

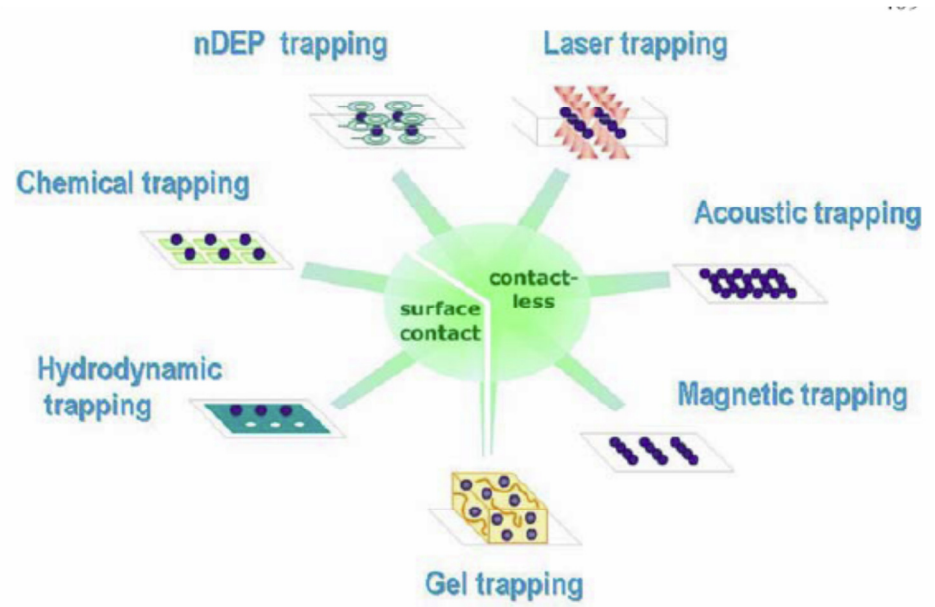


***Figure I-16**. The most common cell-trapping techniques in microfluidic platforms (reproduced from [69])*

The need to perform membrane analyses of single cells at high resolution for a timescale of minutes defines a set of specific requirements which ultimately dictate the choice of the trapping method. They include:

1 - Preserved long term cell viability
2 - Easy integration and coupling with high–resolution optics
3 - Possibility to array single cells
4 - Minimum cell-to-objective lens distance
5 - Minimum unwanted interactions with surfaces prone to inducing stress to the membrane

Table I.1 summarizes the suitability of selected cell trapping techniques with regards to membrane analysis. In this table, '+' indicates good suitability with respect to the quoted criteria while '-' indicates the criteria is not met or difficult to achieve.

Criteria number / Trapping method	1	2	3	4	5
DEP	+	+	+	+	+
Optical trapping	+	-	-	+	+
Hydrodynamic trapping	+	+	+	-	-
Gel trapping	+	+	-	-	-
Chemical trapping	-	+	+	+	-

***Table I.1**. Suitability matrix for given requirements set for single cell membrane analysis*

Chemical trapping introduces physical contact altering local membrane properties, for instance using "nanofiber carpets" made of stretchable polymer chains able to bind cell adhesion receptors.[72] Biocompatible hydrogels for cell trapping are randomly holding cells in a matrix and as such can difficultly create well defined single cell arrays.[73]

Among hydrodynamic trapping techniques, microwell arrays, pillar structures or hydrodynamic traps have been introduced.[74-76] Snapshots of these systems are shown in **Figure I-17**.

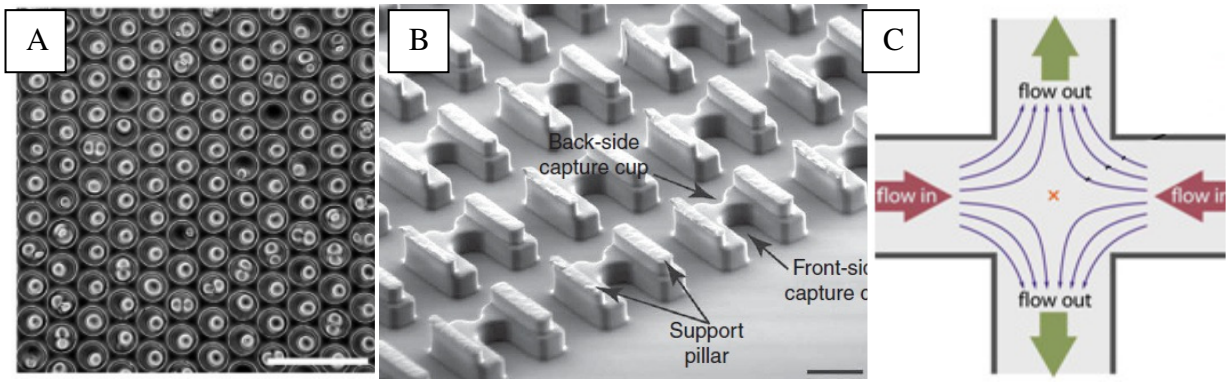


***Figure I-17**. Cell trapping tools based on hydrodynamic flows and passive structures. **A**. A microwell array filled with rat basophilic leukemia cells. **B**. Arrayed pillar structures. **C**. Schematic of a hydrodynamic trap. Scale bars for A and B are 100µm and 20µm.(adapted from [74-76]).*

All the aforementioned techniques confine cells in predefined locations. However cells will be loosely bound to a substrate or unstably confined as in the case of hydrodynamic trapping. In all cases, introduction of a flow will change their exact location and most likely induce rotations. This is a limiting factor for single cell imaging. The presence of structure boundaries also affects fluorescence signals which are not easily deconvoluted.

Magnetic trapping makes use of magnetic micro or nanobeads which directly tag the cell membrane and move it under strong magnetic fields. Their interest therefore appears more for studies which do not involve membrane dynamics processes.[77]

The use of acoustic standing waves requires complex integration of transducers for wave production. Furthermore, this technique cannot easily achieve single cell trapping.[78]

One of the main drawbacks of optical trapping is that the number of traps is normally limited by the available laser power because each trap requires an equal power portion. As the technique already requires a laser for trapping, analysis based on laser light absorption require at least one supplementary optical pathway which makes the overall integration more difficult.

On the other hand, DEP meets all the criteria set out for efficient membrane analysis. It is presented in more depth in the next paragraph.

Alongside the single cell trapping methods presented in **Figure I-16**, hybrid methods can also be designed to achieve efficient trapping. For instance, electro-mechanical traps have been designed and built.[79]

Although cell trapping techniques have been successfully demonstrated academically, they still need adoption by the biologist community. Among many hurdles are the questioning of the exact confinement effects introduced by microfluidic and microflows on cell behaviour. This will have to be clarified quantitatively in the future.

I.4.3. The dielectrophoretic force as a route to cell patterning

I.4.3.1. Description and trap geometry

Dielectrophoresis (DEP) is based on the action of a non-uniform electric field exerting dipolar forces on neutral dielectric objects such as cells or micro-beads.[80, 81] Polarizability depends on field frequency. If the medium is more polarizable than the cell, the force brings the cell towards low field regions: this is referred to as negative DEP (repulsion). If the cell is more polarizable than the surrounding medium, the cell is pushed to high field regions: this is referred to as positive DEP (attraction).

DEP presents many advantages as a cell-patterning technique. Because DEP traps consist of scalable electrode arrays, they can be designed to pattern thousands of cells on a single glass slide and can be made small enough to ensure single-cell resolution.[82, 83] DEP offers the advantage of predefined single cell trapping location and exclusion of other cells. The external function generator allows fast reconfiguration of the trapping domain. The integration with high-resolution optics is achieved thanks to the patterning of electrodes on thin coverslip glass, reducing the cell-to-objective distance.

One further advantage of the DEP trapping technique is that the integrated microfluidic chip environment allows facile assaying and control over the aqueous buffers of interest.

Prior geometries for DEP trapping include nDEP octopoles or nDEP cages. [84, 85, 86] They are created using electrodes on the top and bottom of a chamber. Both geometries trap cells in the centre of the channel, rather than on the surface, making them unstable under flow

conditions. In addition, the nDEP octopole [85] has strict packaging needs, requiring alignment of the quadrupoles on the top and bottom of the channel. Planar electrodes, on the contrary have been found powerful for immobilizing single cells close to the surface where electrodes are patterned. They include round electrodes, quadrupole geometry or line electrodes.[87-89] **Figure I-18** shows snapshots of cells trapped using various electrode geometries.

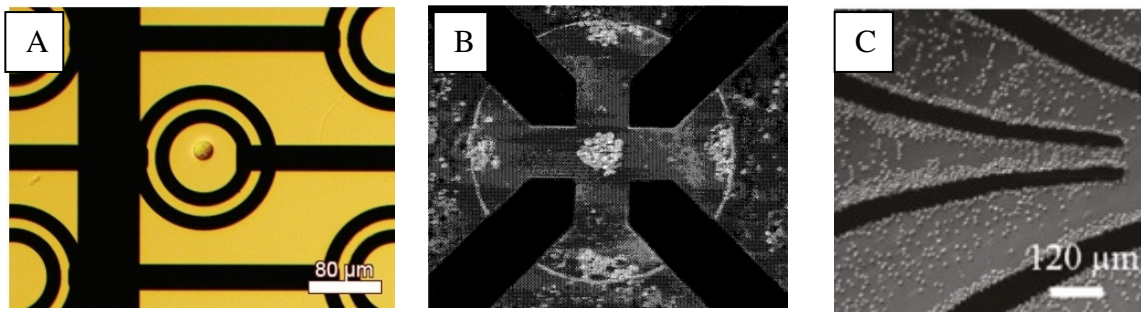


***Figure I-18**. **A**. Single HeLa cell trapped by negative dielectrophoresis. **B**. Corticol rat neurons trapped in a quadrupole geometry. **C**. U937 cells trapped between line electrodes using positive DEP (reproduced from [87-89]).*

As above-mentioned, DEP traps can use either negative DEP (nDEP)—pushing cells away from the electrodes—or positive DEP (pDEP)—pulling cells toward the electrodes. The choice of the working regime directly affects the design of the trapping electrodes.

Cells immersed in physiological buffers will always exhibit nDEP behaviour, being less polarizable than buffer over the typical frequency range of DEP. In addition, when studying live cells, it is preferable to keep them away from potentially harmful high field regions. This is why numerous studies focus on the use of negative DEP traps.[83, 86, 87]

I.4.3.2. Potential hurdles to manipulating cells in DEP traps

When it comes to testing DEP traps, most published studies focus on polymer beads having a similar size to cells. Although transitioning from beads to cells has been demonstrated repeatedly, there are several issues that arise when using DEP to pattern cells. Specifically, cells can be damaged from cell heating or transmembrane loading.[90-92]

When electric fields are present in a conductive medium, heating through Joule heating of the medium occurs. This can increase the temperature of the cell and create irreversible damage.[93] This subject is treated in-depth in **Chapter IV** of this thesis.

Transmembrane loading occurs when the induced cell membrane potential exceeds a critical value, possibly causing electroporation or disruption of cell-cycle dynamics. Because the membrane acts like an electrical high-pass filter, operating at applied signal frequencies in the MHz range and limiting the applied signal voltage will both help to minimize transmembrane loading.

Another possible issue is electrode fouling, caused by reactions between the electrodes and the surrounding cell-culture media. Thoroughly cleaning the electrodes after each experiment can limit this effect.

As a conclusion, the viability of cells in nDEP cages has been reported several times using practical electric field conditions and, as such, has paved the way towards performing cellular assays within nDEP traps.[94-96]

I.5. Project aim

The development of microfluidic tools for studying biological processes such as membrane dynamics is an essential step towards a better comprehension of complex biological systems. More specifically, combining cell trapping and microfluidic reagent delivery can prove extremely versatile in interrogating single cell membrane properties. These tools will eventually lead to a clearer understanding of single cell response to environmental changes. Amongst the various detection techniques developed for membrane dynamics, fluorescence detection seems to be the more mature, partly because of its high sensitivity and the possibility to interrogate single molecules. The use of such fluorescence detection platforms with high spatial/temporal resolution, sometimes compromised by the lack of integration with cell trapping techniques, has yet to be fully leveraged.

In this thesis, we demonstrate dielectrophoretic trapping of single mammalian cells (typically 10μm in diameter) as a means to facilitate time-resolved studies on living cell membranes. Microfluidic networks consisting of integrated micro-electrodes have been fabricated. These devices have been used to trap single-cells near a defined surface within a flowing stream or in a plate format. Once trapped, the live mammalian cells are assayed for timescales of minutes.

First simulations are performed to help designing efficient trapping devices (**Chapter II**). They are subsequently characterized to assess the potential of DEP as a tool for performing cellular membrane assays (**Chapter III**). When assaying a membrane, it is very important to keep track of temperature rises within each trap. This is studied in-depth in **Chapter IV**.

The cell dielectric response to a non-uniform AC electric field is highly dependent on the presence of the cell membrane and this can be fruitfully exploited for applications in cell separation, trapping or identification. **Chapter V** examines a method to identifying a simple mixture of cells immersed in their physiological buffer.

Finally we use the fluorescent lipid analogs DiO and DiD to perform colocalization FRET assays. Addition of the acceptor dye within the microfluidic network allows for real time observation of FRET events from the cellular membrane using scanning confocal lifetime imaging. Cholesterol depletion is subsequently shown to influence probe localization. (**Chapter VII**)

Such microfluidic devices can potentially be used to study both lipid organization dynamics as well as lipid lateral diffusion on the membrane surface when combining fluorescence detection formats. Their adoption by the biological community has yet to be done to ensure they achieve their full potential.

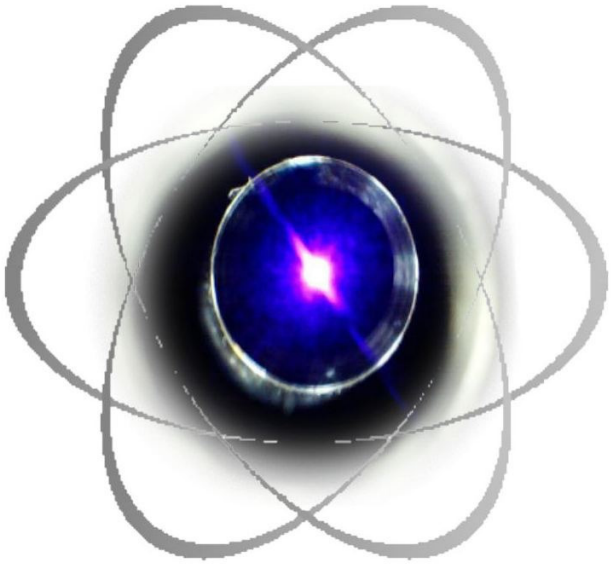
I.6. References

(1) Dowhan, W. *Annual Review of Biochemistry* **1997**, *66*, 199-232.
(2) Bevers, E. M.; Comfurius, P.; Dekkers, D. W. C.; Zwaal, R. F. A. *Biochimica Et Biophysica Acta-Molecular and Cell Biology of Lipids* **1999**, *1439*, 317-330.
(3) Brown, D. A.; London, E. *Annual Review of Cell and Developmental Biology* **1998**, *14*, 111-136.
(4) Alberts, B. Molecular Biology Of The Cell, 4th edition, *New-york:Garland Science* **2002**.
(5) Tanford, C., The Hydrophobic Effect, 2nd edition, *New-York: Wiley* **1980**.
(6) Marra, J.; Israelachvili, J. *Biochemistry* **1985**, *24*, 4608-4618.
(7) Spector, A. A.; Yorek, M. A. *Journal of Lipid Research* **1985**, *26*, 1015-1035.
(8) Pucadyil, T. J.; Chattopadhyay, A. *Biochimica Et Biophysica Acta-Biomembranes* **2007**, *1768*, 655-668.
(9) Pralle, A.; Keller, P.; Florin, E. L.; Simons, K.; Horber, J. K. H. *Journal of Cell Biology* **2000**, *148*, 997-1007.
(10) Orr, G.; Hu, D. H.; Ozcelik, S.; Opresko, L. K.; Wiley, H. S.; Colson, S. D. *Biophysical Journal* **2005**, *89*, 1362-1373.
(11) Scherfeld, D.; Kahya, N.; Schwille, P. *Biophysical Journal* **2003**, *85*, 3758-3768.
(12) Hao, M. M.; Mukherjee, S.; Maxfield, F. R. *Proceedings of the National Academy of Sciences of the United States of America* **2001**, *98*, 13072-13077.
(13) Pucadyil, T. J.; Chattopadhyay, A. *Chemistry and Physics of Lipids* **2006**, *143*, 11-21.
(14) Cooper, G. M. *Sinauer Associates Inc.* **2009**.
(15) Bennett, V.; Gilligan, D. M. *Annual Review of Cell Biology* **1993**, *9*, 27-66.
(16) Rothman, J. E.; Lenard, J. *Science* **1977**, *195*, 743-753.
(17) Yeagle, P. L. *Faseb Journal* **1989**, *3*, 1833-1842.
(18) Singer, S. J.; Nicolson, G. L. *Science* **1972**, *175*, 720-&.
(19) Marguet, D.; Lenne, P. F.; Rigneault, H.; He, H. T. *Embo Journal* **2006**, *25*, 3446-3457.
(20) Chapman, D.; Benga, G. In *Chapman, D.*, 1984, pp 1-56.
(21) Kornberg, R. D.; McConnel.Hm *Proceedings of the National Academy of Sciences of the United States of America* **1971**, *68*, 2564-&.
(22) Saffman, P. G.; Delbruck, M. *Proceedings of the National Academy of Sciences of the United States of America* **1975**, *72*, 3111-3113.
(23) Kusumi, A.; Nakada, C.; Ritchie, K.; Murase, K.; Suzuki, K.; Murakoshi, H.; Kasai, R. S.; Kondo, J.; Fujiwara, T. *Annual Review of Biophysics and Biomolecular Structure* **2005**, *34*, 351-U354.
(24) Lindner, R.; Naim, H. Y. *Experimental Cell Research* **2009**, *315*, 2871-2878.
(25) Brown, F. L. H. *Biophysical Journal* **2003**, *84*, 842-853.
(26) Munro, S. *Cell* **2003**, *115*, 377-388.
(27) Mavromoustakos, T. M. In *Methods in Molecular Biology*; Humana Press Inc, 999 Riverview Dr, Ste 208, Totowa, Nj 07512-1165 USA, 2007; Vol. 400, pp 587-600.
(28) Heimburg, T., Thermal Biophysics of Membranes, *Wiley* **2007**.
(29) Simons, K.; Vanmeer, G. *Biochemistry* **1988**, *27*, 6197-6202.
(30) Simons, K.; Ikonen, E. *Nature* **1997**, *387*, 569-572.
(31) Harder, T.; Sangani, D. *Cell Commun Signal* **2009**, *7*, 21.
(32) Owen, D. M.; Lanigan, P. M. P.; Dunsby, C.; Munro, I.; Grant, D.; Neil, M. A. A.; French, P. M. W.; Magee, A. I. *Biophysical Journal* **2006**, *90*, L80-L82.
(33) Robinson, T.; Schaerli, Y.; Wootton, R.; Hollfelder, F.; Dunsby, C.; Baldwin, G.; Neil, M.; French, P.; Demello, A. *Lab Chip* **2009**, *9*, 3437-3441.

(34) Bacia, K.; Scherfeld, D.; Kahya, N.; Schwille, P. *Biophysical Journal* **2004**, *87*, 1034-1043.
(35) Glebov, O. O.; Nichols, B. J., Glasgow, Scotland, Jul 18-22 2004; Portland Press; 673-675.
(36) Sok, M.; Sentjurc, M.; Schara, M. *Cancer Letters* **1999**, *139*, 215-220.
(37) Makky, A., analyse des mecanismes de penetration intramembranaire de porphyrines glycoconjuguees utilisables en therapie photodynamique des cancers, PhD dissertation, **2010**.
(38) Sheets, E. D.; Simson, R.; Jacobson, K. *Current Opinion in Cell Biology* **1995**, *7*, 707-714.
(39) Viola, A.; Gupta, N. *Nature Reviews Immunology* **2007**, *7*, 889-896.
(40) Christova, Y.; James, P. S.; Cooper, T. G.; Jones, R. *Journal of Andrology* **2002**, *23*, 384-392.
(41) Bates, I. R.; Hebert, B.; Luo, Y. S.; Liao, J.; Bachir, A. I.; Kolin, D. L.; Wiseman, P. W.; Hanrahan, J. W. *Biophysical Journal* **2006**, *91*, 1046-1058.
(42) Chen, Y.; Muller, J. D.; So, P. T. C.; Gratton, E. *Biophysical Journal* **1999**, *77*, 553-567.
(43) Magde, D.; Webb, W. W.; Elson, E. *Physical Review Letters* **1972**, *29*, 705-&.
(44) Kim, S. A.; Heinze, K. G.; Schwille, P. *Nature Methods* **2007**, *4*, 963-973.
(45) Davey, A. M.; Walvick, R. P.; Liu, Y. X.; Heikal, A. A.; Sheets, E. D. *Biophysical Journal* **2007**, *92*, 343-355.
(46) Chen, Y.; Mills, J. D.; Periasamy, A. *Differentiation* **2003**, *71*, 528-541.
(47) Schwille, P.; Korlach, J.; Webb, W. W. *Cytometry* **1999**, *36*, 176-182.
(48) Ries, J.; Yu, S. R.; Burkhardt, M.; Brand, M.; Schwille, P. *Nature Methods* **2009**, *6*, 643-U631.
(49) Kahya, N.; Scherfeld, D.; Bacia, K.; Schwille, P. *Journal of Structural Biology* **2004**, *147*, 77-89.
(50) Engelke, H.; Heinrich, D.; Radler, J. O. *Physical biology*, *7*, 046014.
(51) Weiss, M.; Hashimoto, H.; Nilsson, T. *Biophysical Journal* **2003**, *84*, 4043-4052.
(52) Garcia-Saez, A. J.; Schwille, P. *Methods* **2008**, *46*, 116-122.
(53) Bacia, K.; Majoul, I. V.; Schwille, P. *Biophysical Journal* **2002**, *83*, 1184-1193.
(54) Saxton, M. J.; Jacobson, K. *Annual Review of Biophysics and Biomolecular Structure* **1997**, *26*, 373-399.
(55) Ewers, H.; Smith, A. E.; Sbalzarini, I. F.; Lilie, H.; Koumoutsakos, P.; Helenius, A. *Proceedings of the National Academy of Sciences of the United States of America* **2005**, *102*, 15110-15115.
(56) Packard, B. S.; Wolf, D. E. *Biochemistry* **1985**, *24*, 5176-5181.
(57) Stockl, M.; Plazzo, A. P.; Korte, T.; Herrmann, A. *Journal of Biological Chemistry* **2008**, *283*, 30828-30837.
(58) Sengupta, P.; Holowka, D.; Baird, B. *Biophysical Journal* **2007**, *92*, 3564-3574.
(59) Jares-Erijman, E. A.; Jovin, T. M. *Nature Biotechnology* **2003**, *21*, 1387-1395.
(60) Krisovitch, S. M.; Regen, S. L. *Journal of the American Chemical Society* **1991**, *113*, 8175-8177.
(61) Regen, S. L. *Current Opinion in Chemical Biology* **2002**, *6*, 729-735.
(62) Nichols, B. J. *Current Biology* **2003**, *13*, 686-690.
(63) Baumgart, T.; Hess, S. T.; Webb, W. W. *Nature* **2003**, *425*, 821-824.
(64) Lasne, D.; Blab, G. A.; Berciaud, S.; Heine, M.; Groc, L.; Choquet, D.; Cognet, L.; Lounis, B. *Biophysical Journal* **2006**, *91*, 4598-4604.
(65) Schultz, Z. D.; Levin, I. W. *Annual review of analytical chemistry (Palo Alto, Calif.)* **2011**, *4*, 343-366.

(66) Wouters, F. S.; Verveer, P. J.; Bastiaens, P. I. H. *Trends in Cell Biology* **2001**, *11*, 203-211.
(67) Anselmetti, D. Single Cell Analysis, *Wiley* **2009**.
(68) Wang, Z. H.; Kim, M. C.; Marquez, M.; Thorsen, T. *Lab on a Chip* **2007**, *7*, 740-745.
(69) Johann, R. M. *Analytical and Bioanalytical Chemistry* **2006**, *385*, 408-412.
(70) Tabeling, P., Introduction to Microfluidics, *Oxford University Press* **2005**.
(71) Price, A. K.; Culbertson, C. T. *Anal Chem* **2007**, *79*, 2614-2621.
(72) Helmke, B. P.; Minerick, A. R. *Proceedings of the National Academy of Sciences of the United States of America* **2006**, *103*, 6419-6424.
(73) Braschler, T.; Johann, R.; Heule, M.; Metref, L.; Renaud, P. *Lab on a Chip* **2005**, *5*, 553-559.
(74) Tanyeri, M.; Johnson-Chavarria, E. M.; Schroeder, C. M. *Applied Physics Letters* **2010**, *96*, 3.
(75) Skelley, A. M.; Kirak, O.; Suh, H.; Jaenisch, R.; Voldman, J. *Nature Methods* **2009**, *6*, 147-152.
(76) Rettig, J. R.; Folch, A. *Analytical Chemistry* **2005**, *77*, 5628-5634.
(77) Koschwanez, J. H.; Carlson, R. H.; Meldrum, D. R. *Review of Scientific Instruments* **2007**, *78*, 5.
(78) Hammarstrom, B.; Evander, M.; Barbeau, H.; Bruzelius, M.; Larsson, J.; Laurell, T.; Nillsson, J. *Lab on a Chip* **2010**, *10*, 2251-2257.
(79) Le, D. V.; Rosales, C.; Khoo, B. C.; Peraire, J. *Lab on a Chip* **2008**, *8*, 755-763.
(80) Foster, K. R.; Schwan, H. P. *Critical Reviews in Biomedical Engineering* **1989**, *17*, 25-104.
(81) Pohl, H. A.; Crane, J. S. *Biophysical Journal* **1971**, *11*, 711-&.
(82) Frenea, M.; Faure, S. P.; Le Pioufle, B.; Coquet, P.; Fujita, H. *Materials Science & Engineering C-Biomimetic and Supramolecular Systems* **2003**, *23*, 597-603.
(83) Yu, Z.; Xiang, G. X.; Pan, L. B.; Huang, L. H.; Yu, Z. Y.; Xing, W. L.; Cheng, J. *Biomedical Microdevices* **2004**, *6*, 311-324.
(84) Albrecht, D. R.; Sah, R. L.; Bhatia, S. N. *Biophysical Journal* **2004**, *87*, 2131-2147.
(85) Korlach, J.; Reichle, C.; Muller, T.; Schnelle, T.; Webb, W. W. *Biophysical Journal* **2005**, *89*, 554-562.
(86) Rosenthal, A.; Voldman, J. *Biophysical Journal* **2005**, *88*, 2193-2205.
(87) Thomas, R. S.; Morgan, H.; Green, N. G. *Lab on a Chip* **2009**, *9*, 1534-1540.
(88) Heida, T.; Rutten, W. L. C.; Marani, E. *Ieee Transactions on Biomedical Engineering* **2001**, *48*, 921-930.
(89) Khoshmanesh, K.; Akagi, J.; Nahavandi, S.; Skommer, J.; Baratchi, S.; Cooper, J. M.; Kalantar-Zadeh, K.; Williams, D. E.; Wlodkowic, D. *Analytical Chemistry* **2011**, *83*, 2133-2144.
(90) Docoslis, A.; Kalogerakis, N.; Behie, L. A. *Cytotechnology* **1999**, *30*, 133-142.
(91) Fuhr, G.; Glasser, H.; Muller, T.; Schnelle, T. *Biochimica Et Biophysica Acta-General Subjects* **1994**, *1201*, 353-360.
(92) Archer, S.; Li, T. T.; Evans, A. T.; Britland, S. T.; Morgan, H. *Biochemical and Biophysical Research Communications* **1999**, *257*, 687-698.
(93) Arnold, W. M.; Franich, N. R. *Current Applied Physics* **2006**, *6*, 371-374.
(94) Arnold, W. M.; Franich, N. R., Queenstown, New Zealand, Feb 06-11 2005; *Elsevier Science Bv*; 371-374.
(95) Heida, T.; Rutten, W. L. C.; Marani, E. *Journal of Physics D-Applied Physics* **2002**, *35*, 1592-1602.
(96) Chuang, C. H.; Lee, Y. C.; Huang, H. S.; Hsiao, F. B.; Hsu, Y. M.; Wang, K. H.; Dinj, L.; Hsu, H. J., Zhuhai, People's Rep. of China, Jan 18-21 2006; *Ieee*; 1207-1210.

Chapter II. Methodology



This section details the methodology adopted throughout this work and expounds on the use of microfluidic devices for single-cell analyses. The materials, fabrication processes and packaging procedures are first detailed. High-sensitivity optical detection is achieved using scanning confocal microscopy acquiring time-resolved fluorescence events. The full optical setup is hereby described. Eventually, the FLIM and FRET analysis algorithms are given.

II.1. Fabrication of microfluidic devices

Material choice is of primary importance when it comes to building and using microfluidic platforms. As the surface-to-volume ratio increases, surface properties have an increasing clout on the overall device performance and function. For instance, wetting, roughness or transparency have to be carefully considered in line with the specifics and goals of a particular experiment. The optical detection employed in this work also sets harsh requirements such as high transparency of substrates at defined wavelengths, minimum auto-fluorescence and very small distance (<210µm) between microscope objective and objects under analysis. Here, a thin hydrophobic borosilicate glass surface ensures minimum non-specific binding of cells and readily allows integration with the optical stage of commercial microscopes.

Dielectrophoretic platforms require integration of metallic electrodes. The selected metal should not affect cell viability or interfere with any of its functions (cell cycle, expression,…). In this thesis, we used gold which has been long known as biocompatible and is widely used for dental operations or in-vivo drug delivery. It was deposited on a thin adhesion layer made of chromium. Non-specific binding of cells can be kept to a minimum by using dielectrophoretic repulsion.

The microfluidic channels built atop the glass have to be shallow (<200µm) to maximize confinement. For easy replication purposes, the polymer polydimethylsiloxane (PDMS) has been a favorite choice in the microfluidic research community. It can be easily fabricated in various geometries and using several layers using soft lithography.[1] As a soft material, its integration with fluidic connectors is also relatively simple. Its permeability to gas is beneficial for cell cultures which require gas exchange. Drawbacks include the uncontrolled formation of air bubbles affecting the chip operation and the stability of microflows.

II.1.1. Designs used in this work and dimensions

The electrode design used in this work was mainly based on the square electrode geometry first described by Rosenthal *et al* in 2005 and which has been thoroughly characterized based

on geometrical parameters.[2] The dimensions adapted to trapping mammalian cells of the order of 10µm in diameter are summarized in **Figure II-1a**. This design has several practical advantages when it comes to cell patterning. First, the square opening area can be tuned to trap single cells based on the match with cell diameter. This requires optimizing the electrode dimensions for a given cell type. Second, the nature of the geometry creates a strong vertically confining force that can hold cells against micro-flows created by fluid injection. Third, the possibility to massively parallelize the unit trap makes it attractive for high-throughput studies. In **Figure II-1b**, we show an array of square traps with a total footprint of less than 1mm^2. Trapping arrays are usually needed in cell type assays to obtain statistical data. **Figure II-1c** shows how the design can be combined with a microfluidic channel to achieve a functional platform.

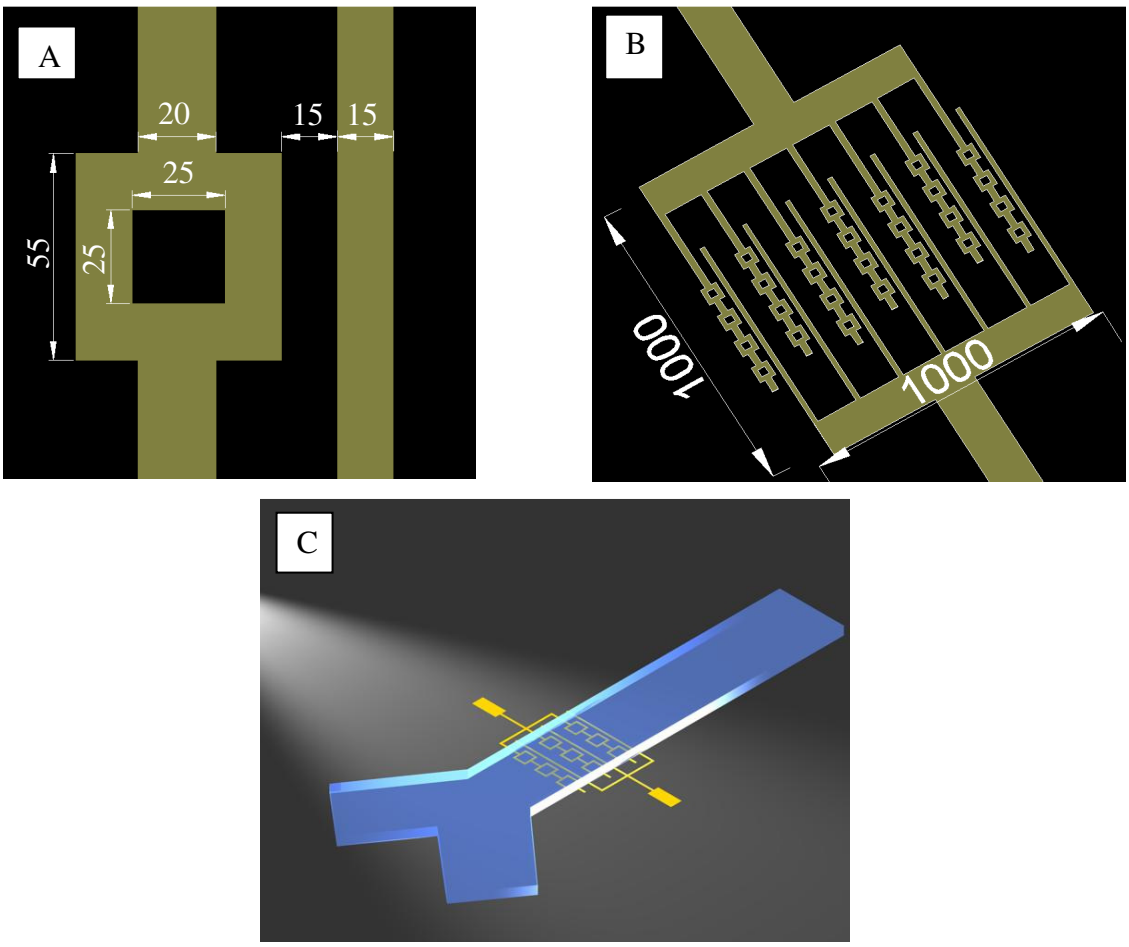


***Figure II-1**. **A**. Dimensions of the patterned electrodes for the square geometry (in microns). **B**. A 7 x 4 array with total footprint less than 1mm^2. **C**. Schematic of a microfluidic chip with integrated planar micro-electrodes and a micro-channel.*

II.1.2. Gold patterning on glass

The microchip fabrication process was done in a class 1000 cleanroom (less than 1000 particles of diameter 0.5µm or more per cubic meter).

Gold electrodes were patterned by following a lift-off process as illustrated in **Figure II-2**. In this process, a photoresist was first patterned with lithographic techniques, gold was deposited on specific areas defining electrodes and the remaining photoresist finally removed (it is usually referred to as a sacrificial material).

Specifically, the photoresist AZ® 1512HS (MicroChemicals) was spin-coated on thin glass (borosilicate glass, 150 µm thickness, 2.2 x 2.2cm). For this process, the glass was first dehydrated at 110°C on a hot plate for 10 minutes before being allowed to cool down (step 1). The liquid photoresist was spin-coated on top of the glass by depositing a few drops at the centre of the glass. Next the spin-coater ran at 500 rotations per minute for 10 seconds allowing spreading of the solution followed by 3000 rotations per minute for 30 seconds. The deposited resist was then allowed to cure for 2 minutes on a hot plate set at 90ºC. The final theoretical thickness of the cured resist was 1.4µm (step 2).

A lithographic emulsion mask designed by AutoCAD® (JD Phototools) was produced to selectively absorb UV light and sandwiched between the cured photoresist and a thick glass slide. This ensured close contact between mask and substrate and increases the fidelity of the transferred pattern. The UV exposure dose was adapted to the resist thickness, here 50mJ/cm^2. The exposed regions of the resist were then developed with a 1 minute immersion in a developer solution made of AZ® 400K (Clariant) diluted 1:4 in de-ionized (DI) water. The glass was subsequently washed in DI water, blown dry with N_2 and stored at Room Temperature (RT) (step 3).

Next, a 25 nm chromium adhesion layer was deposited using a sputter coater (Emitech, K575X) followed by the deposition of 40 nm of gold (Emitech, K550) (step 4). The photoresist carrying unbound chromium/gold was then stripped off by dissolution in an acetone bath. The detachment of gold was facilitated by placing the acetone-filled container

in an ultrasonication bath for a few seconds (step 5). The devices were further cleaned in isopropyl alcohol (IPA) and DI water, blown-dry with N_2 and stored at RT (step 6).

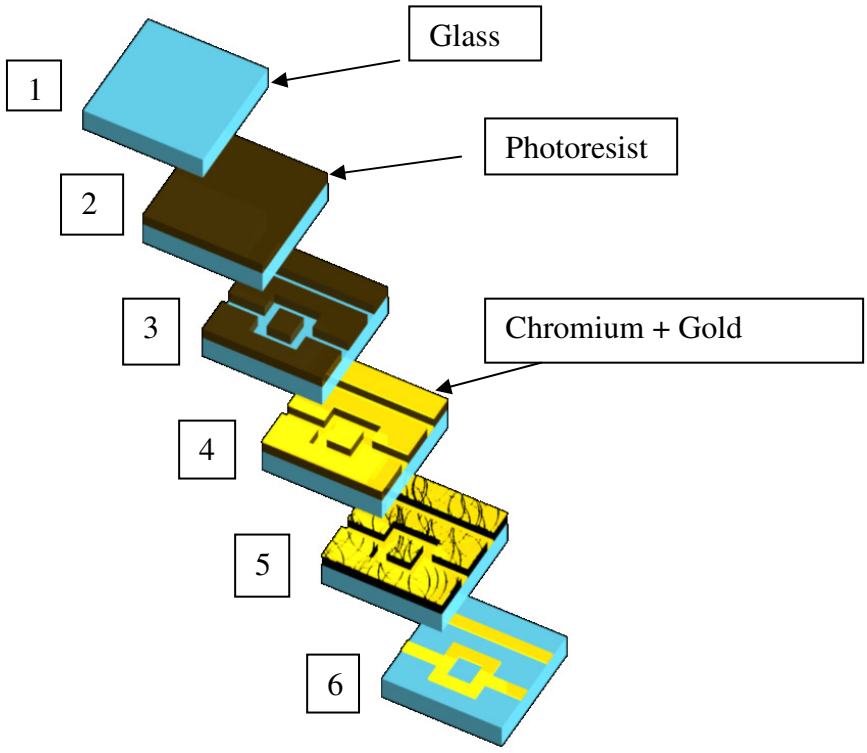


***Figure II-2**. Lift-off process steps for Cr/Au patterning on glass*

The actual thickness of the gold layer was examined using Atomic Force Microscope (AFM) measurements. **Figure II-3** shows a 2D AFM scan of the trapping area. The AFM scan provides insight into the morphology and fine structure of the electrodes. It is seen that the roughness of the deposited gold layer is not higher than the one of the glass and that dimensions match the design fairly well. It is worth pointing out that the edges of the gold electrodes have a high roughness due to incomplete detachment of gold.

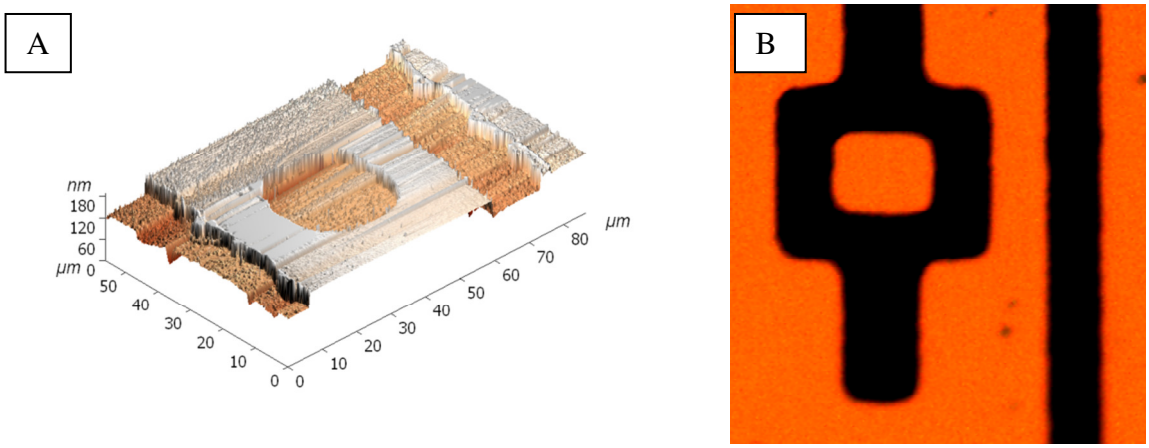


***Figure II-3**. **A**. 2D AFM scan of a gold electrode on a borosilicate glass slide showing the square trap. **B**. An optical picture of the same trap with the other line electrode*

The cross-section in the middle of the trap shows that the average gold thickness was 40nm. This is illustrated in **Figure II-4**.

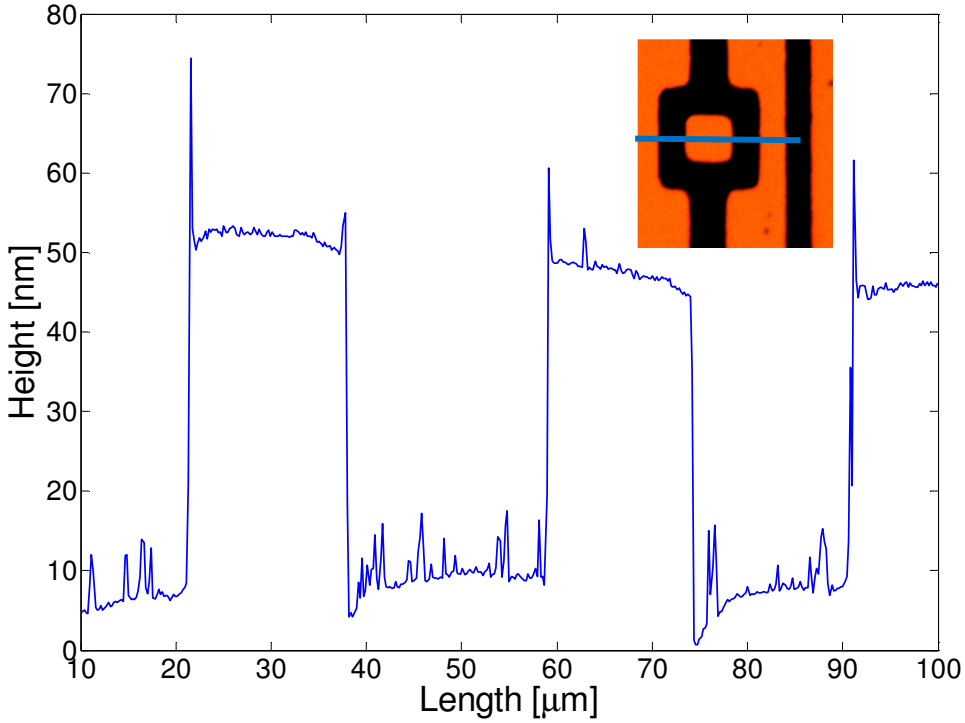


***Figure II-4**. Cross-section showing the height profile of a DEP trap. The inset indicates the line used for the cross-section.*

II.1.3. Making of the SU-8 master mould used for soft lithography

Given the high aspect ratio of the microchannels and microstructures commonly found in microfluidic chips, the very viscous epoxy-based SU-8 photoresist has been historically used for building master moulds where PDMS can be cast and replicated.
This negative-tone master mould was produced by photolithography on a 4-inch silicon wafer of orientation <100>. In the same way as described in the previous paragraph, the silicon wafer was uniformly coated with SU-8 50 photoresist (Michrochem, Chestech Ltd, UK) using spin-coating. The final thickness of the photoresist layer is primarily dictated by the viscosity of the solution (12550 cSt for SU-8 50) and the spinning speed. Following the protocol provided by manufacturers, the typical conditions to theoretically obtain a uniform 50µm deep layer of resist were 500 rpm for 15 seconds followed by a ramp to 3000 rpm for 30 seconds. The wafer was then soft baked on a hot plate for 15 min at 65 ºC and 30 min at 95ºC to evaporate the solvent present in the stock solution. UV light irradiation followed the soft bake. With the emulsion film mask in close contact with the SU-8 layer, the wafer was introduced in a closed chamber and UV-irradiated over its whole area with high collimation. The exposure time (energy deposited) had to be adapted to the SU-8 thickness and was typically 50s (equivalent of 500mJ/cm^2). After the polymerization process has been initiated by irradiation, the cross-linking is further enhanced through a hard-bake step of 5 minutes at 95 ºC.

After allowing the wafer to cool down, it was plunged into a developer solution made of 2-methoxy-1-methylethyl acetate (Microposit EC solvent, Chestech, UK). The 2 minutes immersion allowed the non-exposed parts of the wafer to be dissolved into the solution and the wafer was subsequently washed with clean developer, IPA, DI water and blown dry with nitrogen.

The patterned SU-8 master was further washed in an n-hexane, methanol and water baths before being blown dry again. Finally trichloro(1,1,2,2-perfluooctyl)silane was evaporated onto the wafer inside a vacuum chamber. Briefly, a few drops of concentrated silane were dropped into a glass flask and put inside the dessicator together with the wafer for 30 minutes. This silanization step creates an ultrathin hydrophobic coating which facilitates the desorption of PDMS in the subsequent chip making process (**Figure II-5**).

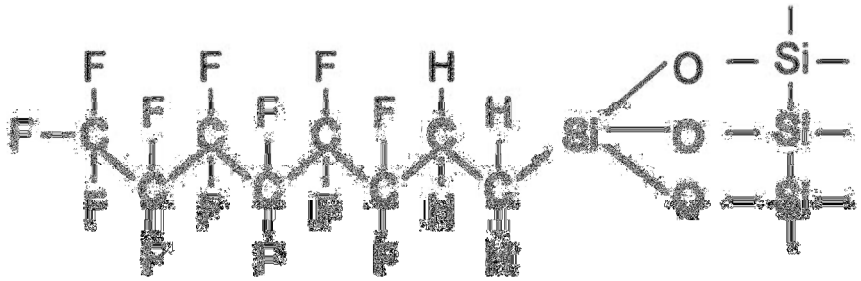


***Figure II-5**. Chemical structure of a fluorosilane film on a silicon wafer surface (adapted from [3]).*

II.1.4. Making and bonding of a PDMS micro-chip

II.1.4.1. PDMS replica

A PDMS pre-polymer (SYLGARD 184 Silicone Elastomer Kit, Dow Corning, Midland, MI) was fully mixed with the curing agent and degassed in a vacuum chamber for 30 minutes to remove any air bubbles. The polymer was then poured onto the master mould in a Petri dish. It was cured for 12 hours at 65ºC on a hotplate. After curing, the PDMS replica was carefully peeled off from the master mould and cut into individual chips. Fluidic inlets and outlets were punched through the PDMS channel using truncated syringe needles of suitable diameters. An example SU-8 mould with PDMS having been sampled is shown in **Figure II-6**.

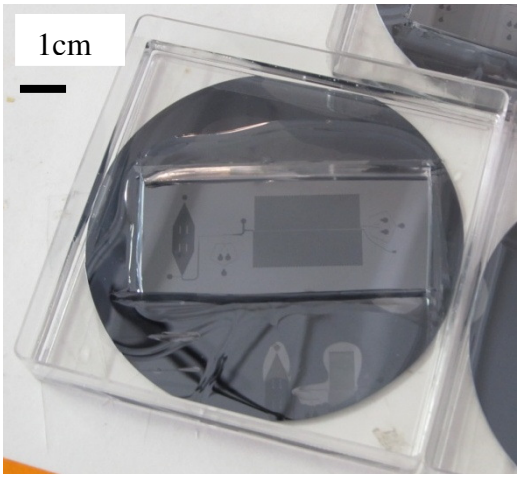


***Figure II-6**. Example of an SU-8 master mould with etched PDMS window over the area comprising patterned microstructures.*

II.1.4.2. Chip bonding

Before PDMS bonding on the Cr/Au patterned glass, the latter was rinsed in 0.5 M KOH solution followed by DI water and nitrogen blowing. The PDMS channel was cleaned using a N_2 gun. Both were placed inside an oxygen plasma chamber for 1 minute (Harrick Plasma,USA) to clean and oxidize the surfaces. Alignment and bonding was done using a standard stereo microscope as feedback. The bonded chip was left on a hot plate at 90ºC for 10 minutes to promote adhesion.

II.1.5. Packaging

Once fabricated, the metal pads were covered with silver glue (RS) and electric wires (RS, 0.25 sq.mm) were pressed on it. After curing for a minimum of four hours at room temperature, a two-part epoxy (ITW Devcon) was deposited to strengthen the bond between the connectors and microfluidic chip. After full curing of the epoxy at 65 ºC overnight, PTFE tubes (200 µm in diameter) were inserted into the punched holes and sealed using PDMS. After fast curing of the PDMS at 100 ºC on a hot plate, the chip was stored at room temperature until use. **Figure II-7** shows a fully packaged microfluidic device.

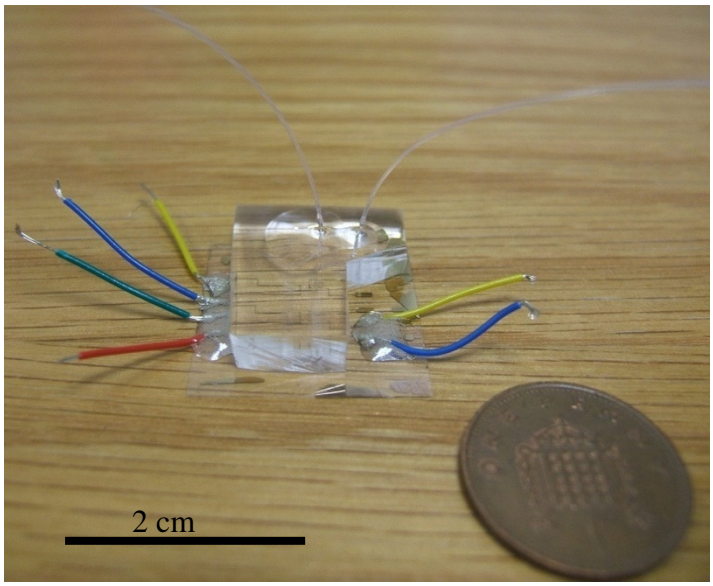


***Figure II-7**. Photograph of a packaged device together with a 1 penny coin*

II.2. Materials

II.2.1. Fluidics and particles

Microflows were created with a precision syringe pump (PHD 2000, Harvard Apparatus) using a 1mL Becton-Dickinson syringe. Typical flow rates ranged from 0.05 to 3µL/min. For testing purposes, polystyrene beads (PolySciences) of diameter 10 µm with density of 1.062 g/cm3, packaged as 2.5% solids in water were used. Bead stock solutions were made with appropriate conductivity by combining appropriate volumes of 18.2 MΩ-cm de-ionized water containing 0.1% Triton X-100 and phosphate buffered saline (PBS, Sigma Aldrich). Conductivities were measured using a Dist 5 conductivity meter (VWR).

II.2.2. Cells

Jurkat T-cells (suspension human T-cell line) and U937 monocyte cells were cultured in a 37ºC incubator with 5 % CO_2 inside a suspending growth solution of RPMI (Gibco) containing 10% Fetal Bovine Serum and 1% L-Glutamine. For experiments, they were resuspended in Ca^{2+}/Mg^{2+}-free Dulbecco's PBS 1x at pH 7.4. The exact buffer composition was 2.6mM KCl, 1.4mM KH2PO4, 136mM NaCl and 8.1mM Na2HPO4 (Sigma Aldrich). A few milliliters of cells at high density (>10^6cells/mL) were centrifuged at 1280 rotations per minute for 5 minutes and the supernatant was replaced by fresh PBS. **Figure II-8** is a bright-field picture of a few Jurkat cells suspended in PBS through a 60x microscope objective.

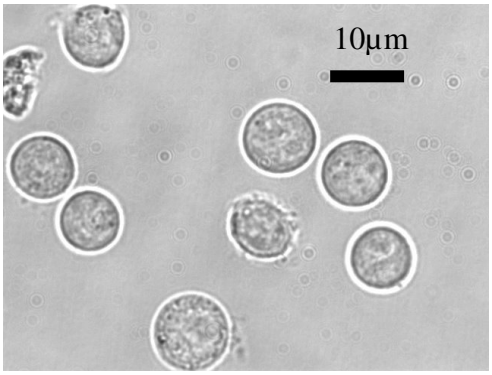


***Figure II-8**. Bright field picture of Jurkat T-cells as seen through a 60x objective of an inverted microscope.*

Using a home-built image analysis software written with Matlab, the average diameter of live Jurkat cells was determined 10.2 ±3.5µm from bright field pictures such as the one shown in **Figure II-8**.

II.2.3. Fluorescent lipid analogs

The fluorescent dyes chosen in this work are carbocyanine phospholipid analogs. They are conjugated dyes exhibiting specific spectral properties as described below.

II.2.3.1. Absorption spectrum of a conjugated dye

Absorption of light by chemical substances can result in electronic transitions from the ground state to an excited state. For many compounds including polymethine dyes, this is due to the presence of weakly bound delocalized electrons. The characteristic absorption bands of the visible region of the spectrum make these dyes typically colourful. The visible bands for polymethine dyes arise from electronic transitions involving π electrons along the polymethine chain. The wavelength of the absorption bands depends on the spacing of the electronic energy levels. This has been studied theoretically by Kuhn who based his work on a quantum mechanical model known as the particle-in-the-box or 'free-electron' model.[4] It considers the dye molecule as a one dimensional box in which delocalized electrons are free to move. This is represented schematically in **Figure II-9**.

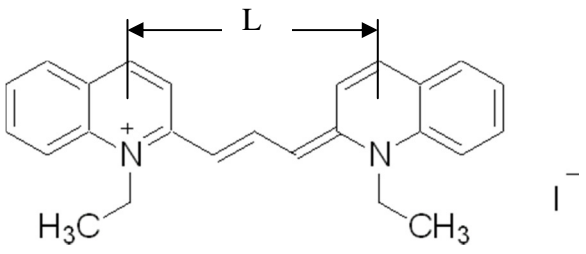


***Figure II-9**. Chemical structure of 1,1 diethyl-2,2-carbocyanine iodide and the schematic boundaries of the 1D box used for theoretical treatment.*

The boundaries of the 1D box are the nitrogen atoms after which the potential is assumed to rise to infinite. The quantum mechanical solution for the energy levels based on the free electron model is:

$$E = \frac{n^2 h^2}{8mL^2} \qquad \textit{Eq. II-1}$$

Here m is the mass of the electron, h is the Planck's constant, L the length of the box and n is the quantum number identifying the state of the electron. Using Pauli exclusion principle and the fact that $\Delta E = hc/\lambda$, with c the speed of light in vacuum, one can show that the wavelength of maximum absorption is given by **Eq. II-2**.

$$\lambda_{\max} = \frac{8mc}{h}\frac{L^2}{N+1} \qquad \textit{Eq. II-2}$$

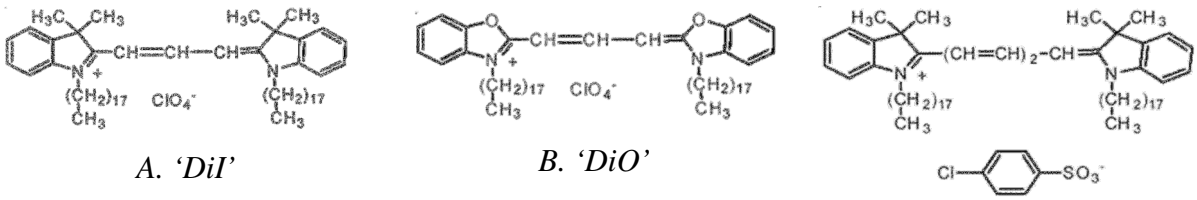
Here N is the number of π electrons along the chain. **Eq. II-2** shows that as the conjugation length increases, the wavelength of maximum absorption also increases which is consistent with experimental observations.

II.2.3.2. Absorption spectrum of a dialkylcarbocyanine dyes

Carbocyanine dyes can be coupled to alkyl chains on the nitrogen atoms marking the boundaries of the 1D box. This is performed via an N-alkylation reaction of the azaheterocycle, for instance under microwave irradiation.[5] The resulting dye has a structure similar to phospholipids and this structural similarity means they can incorporate readily into a lipid bilayer. The fact they are cations probably increases the incorporation rate within a negatively charged bilayer.[6]

The three dialkylcarbocyanine dyes used in this work were DiI-C_{18}(3) or 1,1'-dioctadecyl-3,3,3',3'-tetramethylindocarbocyanine perchlorate (DiI), DiO-C_{18}(3) or 3,3'-dioctadecyloxacarbocyanine, perchlorate (DiO) and DiIC_{18}(5) or 1,1'-dioctadecyl-3,3,3',3'-tetramethylindodicarbocyanine, 4-chlorobenzenesulfonate salt (DiD). The subscript is the number of carbon atoms in each alkyl tail and the number in brackets corresponds to the

length of the conjugation between the indoline and benzoazole ring systems. DiI, DiO and DiD have respectively a red, yellow and blue colour. Their chemical structure is displayed in **Figure II-10**.



A. 'DiI' *B. 'DiO'* *C. 'DiD'*

***Figure II-10**. Chemical structure of the carbocyanines phospholipid analogs. A. DiI, B. DiO, C. DiD*

They all possess two saturated 18 carbon-long alkyl chains perpendicular to the dipole axis of the fluorophore. They differ in their absorption spectra as illustrated in

Figure II-11.

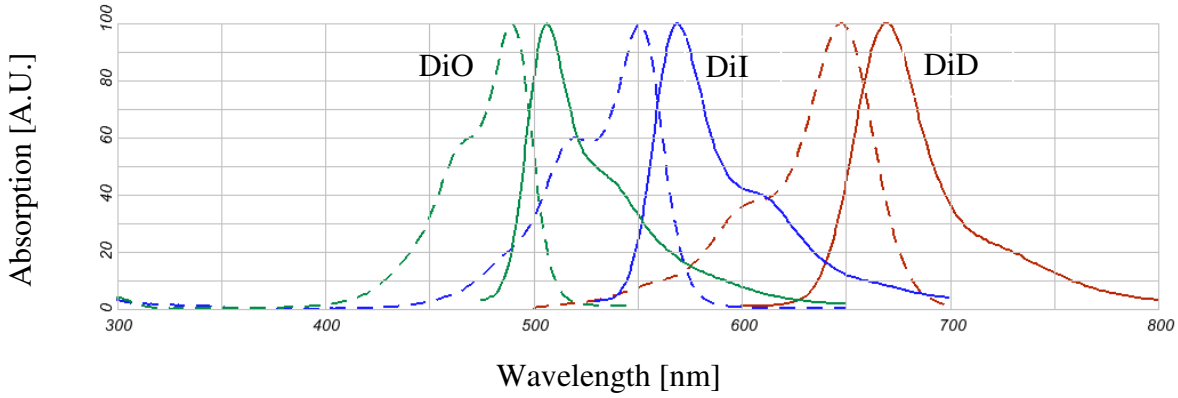


***Figure II-11**. Normalized absorption (dashed lines) and emission (full lines) spectra of DiO, DiI and DiD inserted into phospholipid bilayer membranes (spectra from www.invitrogen.com)*

Further to studies focusing on carbocyanines, the spectral properties of dialkylcarbocyanines have been found independent of the length of the alkyl chains but dependent on conjugation length and the nature of the heteroatoms in the terminal ring systems.[7] The absorption/emission spectra for dialkylcarbocyanine dyes are therefore easily tunable which finds numerous applications in the design of fluorescence or absorbance based assays. For

instance, they have been employed as potential sensors, neuronal tracers, in the analysis of membrane structure and dynamics.[8, 9]

Their physical insertion and distribution inside a lipid bilayer has been studied in model systems.[10] **Figure II-12** shows how DiI inserts into a DPPC lipid bilayer.

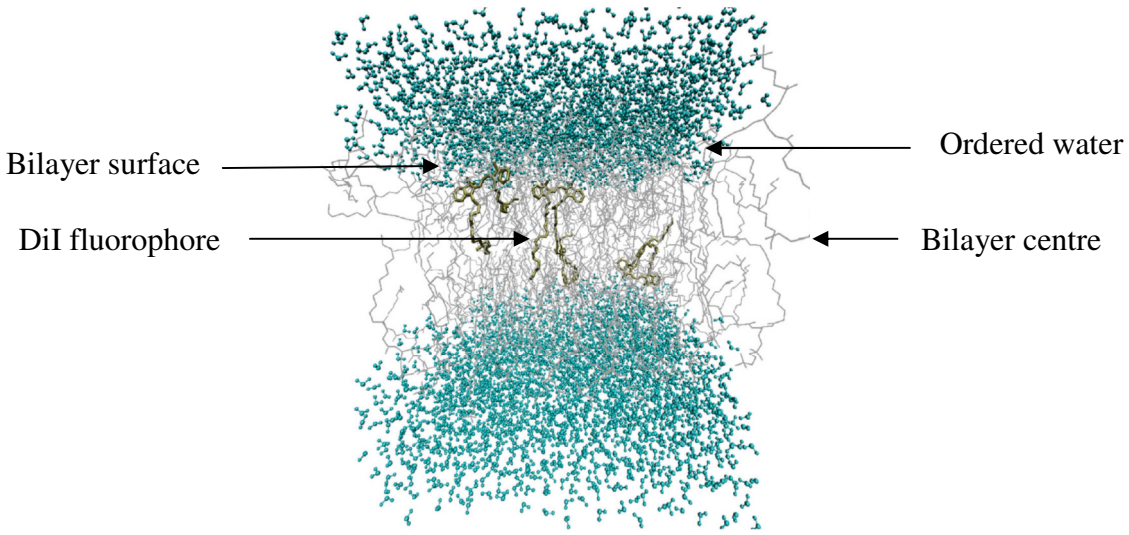


***Figure II-12**. Insertion of a carbocyanine dye within a DPPC bilayer (adapted from [10]).*

DiI appears as buried within the core of lipid bilayer and can be present on either leaflet of the membrane. DiO, DiI and DiD are intercalating dyes which exhibit high fluorescence when inserted in a lipid bilayer compared to fluorescence of the freely floating dyes.

II.2.4. Cell labelling

Jurkat or U937 cells were labelled with fluorescent dyes with protocols depending on the type of experiments. Typically, cells in PBS were incubated for 15 minutes at 37ºC together with 1-5µM of dye. The added volume of dye dissolved in ethanol is such that the final solution contains less than 1% solvent. The Falcon tube containing cells was placed in the cell incubator to facilitate probe incorporation. Second, cells were washed extensively in PBS by successive centrifugations (5 minutes at 1280 RPM) and re-suspension in fresh PBS buffer.

This ensured the final solution had a minimum amount of freely floating dyes. **Figure II-13** shows the blue coloured pellet formed by DiD labelled Jurkat cells after centrifugation.

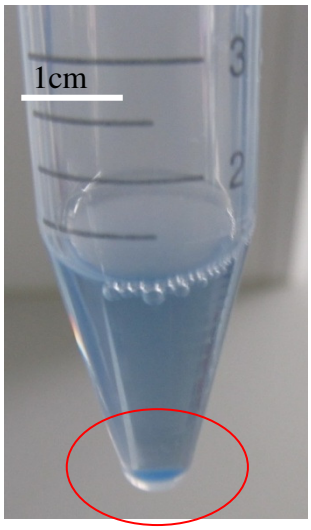


***Figure II-13**. Pelleted labelled Jurkat cells in PBS with 5µM DiD.*

For double labelling of cells in the carbocyanine FRET assays, cells were incubated with DiO first, washed, divided and subsequently labelled or not with DiD. This is because DiD has been found to have a higher incorporation rate in membranes.[11] **Figure II-14** displays the qualitative intensity distribution after DiO labelling of Jurkat cells.

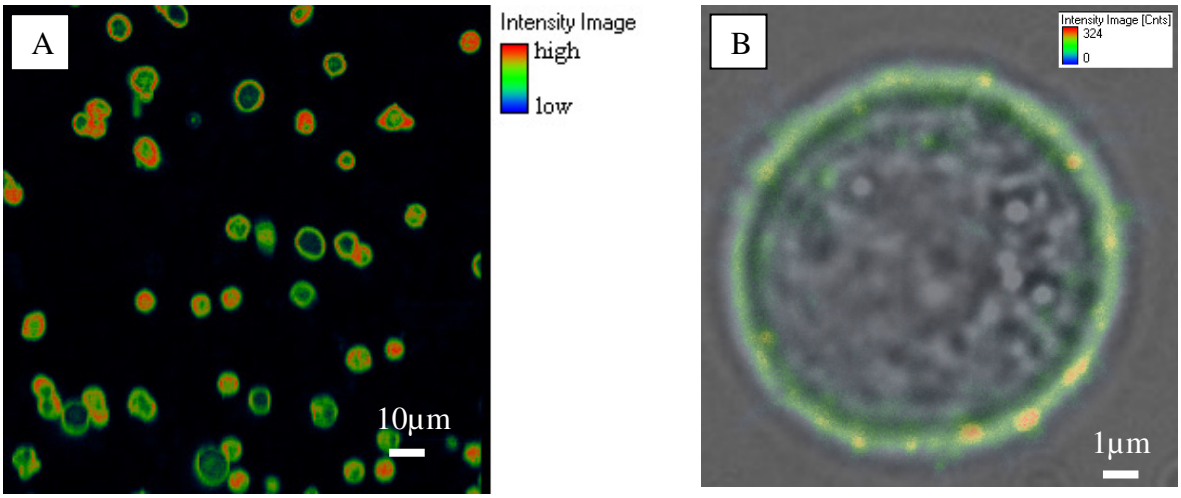


***Figure II-14**. **A**. Fluorescent intensity picture of DiO labelled Jurkat cells spread on a coverslip. **B**. Superimposed bright field and fluorescence picture from a single T-cell. The dye is specifically labelling the plasma membrane.*

II.2.5. Electrical excitation

For the electrical signal, a function generator (TG2000, Thurlby Thandar Instruments) was connected to the electrodes via BNC cables with adapted wire grip leads gripping the conducting wires of the contact pads to the microelectrodes. A sinusoidal signal with voltage chosen between 1 $V_{peak\text{-}to\text{-}peak}$ to 20 V_{pp} and a frequency in the range [100 kHz - 20MHz] was subsequently applied to the microelectrodes.

II.3. The laser scanning detection platform

II.3.1. The overall setup

The detection platform used in this work was an inverted scanning laser confocal microscope (FV300, Olympus) modified with a custom-built detection path. In the context of cell membrane imaging, the acquisition of optical sections is highly valuable. The use of a confocal microscope ensures out-of-plane light rejection limiting the effective excitation depth. The customized path maximizes sensitivity as required for performing measurements involving low concentrations of molecules. A schematic representation of the overall setup is given in **Figure II-15**. Details of each component of the setup are given below.

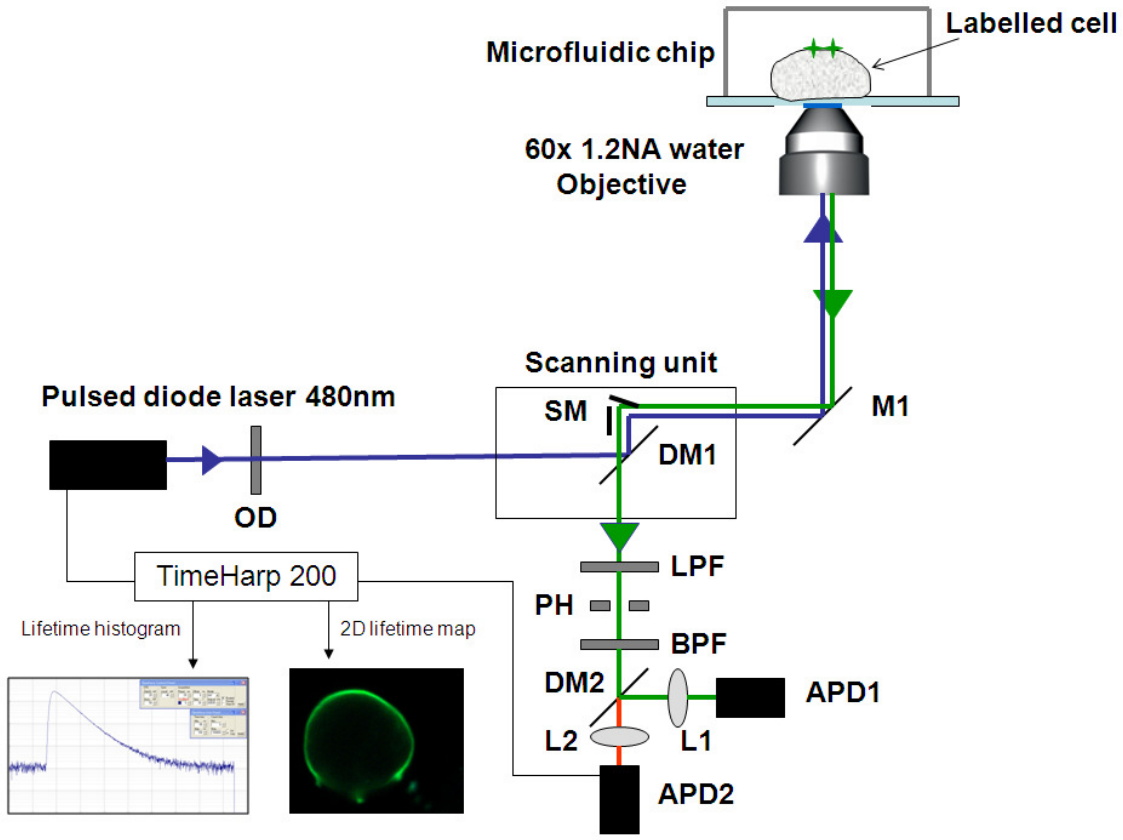


***Figure II-15**. Schematic optical setup for FLIM acquisition. SM: Scanning Mirrors, DM: Dichroic Mirror, LPF: Long-Pass Filter, PH: Pinhole (100 µm diameter), BPF: Band-Pass Filter, L: Converging Lens*

II.3.2. Light Source

The excitation source for all measurements in this work was a spectrally filtered supercontinuum laser source (SC450, Fianum). Supercontinuum spectra are produced by sending an original pump beam into a photonic crystal fiber. Spectral broadening arises from the interactions of several non-linear processes as illustrated in **Figure II-16**.

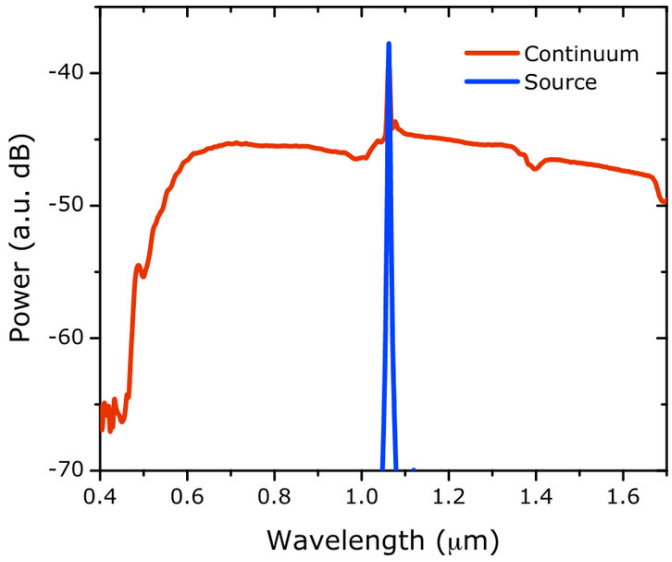


***Figure II-16**. Original pump beam and resulting supercontinuum beam after propagation through a crystal fiber (www.fianum.com).*

The output laser light produced was unpolarized. The wavelength was chosen 488nm via an Acousto-Optic Tunable Filter (AOTF) system directly coupled to the laser output thanks to an optical fiber. The AOTF functions as an electronically tunable excitation filter to simultaneously modulate the intensity and wavelength of multiple laser lines from one or more sources.[12] Devices of this type rely on a specialized bi-refringent crystal whose optical properties vary upon interaction with an acoustic wave. The bandwidth at a wavelength of 488nm was 2-5nm; this is equivalent to classical laser diodes. The laser can be used in either Continuous-Wave (CW) or pulsed mode. The pulsed mode is especially useful for experiments such as time-resolved fluorescence spectroscopy. Unlike intensity measurement where the sample is continuously illuminated, time-resolved measurements like fluorescence lifetime require that the sample be excited by a laser pulse with a width that is typically shorter than the decay to allow measurements of the fluorescence decay. Here the laser was producing 5ps pulses at a rate 20MHz. For each wavelength chosen, the intensity of the beam can be digitally chosen which is useful for experiments requiring precise control over excitation energy. This is in contrast to usual neutral density filters providing only predefined attenuation factors. The power produced at the output of the AOTF at full power was typically 150µW.

II.3.3. The scanning unit

Once generated, the laser beam was directed towards the laser-scanning unit of an inverted laser scanning confocal microscope (FV300, Olympus).

The beam was first sent towards a 488nm dichroic filter (FV3 DM488-2, Olympus). This separates excitation light from fluorescence signal and correct for the finite bandwidth of laser emission. The filtered laser pulses are subsequently deflected by scanning mirrors. The core element of the scanning unit, displayed in **Figure II-17**, are the galvanometer scanning mirrors able to deflect the beam over a given area with a mechanical angular resolution of 15µrad providing a 10nm step control and a scan frequency of 100Hz (www.thorlabs.com).

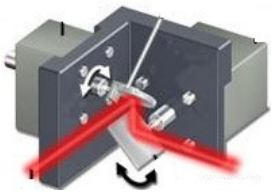


***Figure II-17**. High-speed scanning mirrors are deflected by galvanometer motors to produce the scanning pattern*

The programming of the scanning unit in combination with the piezo-actuation of the microscope objective allows 2D as well as 3D acquisitions. For cell imaging, XY slices were acquired at a median plane of the cell. A typical scanning acquisition allowed 512 x 512 pixels to be scanned in 1.12 seconds repeatedly. By scanning for different axial depths, the 3D cell membrane morphology could be reconstituted. The different scanning modes are represented in **Figure II-18**.

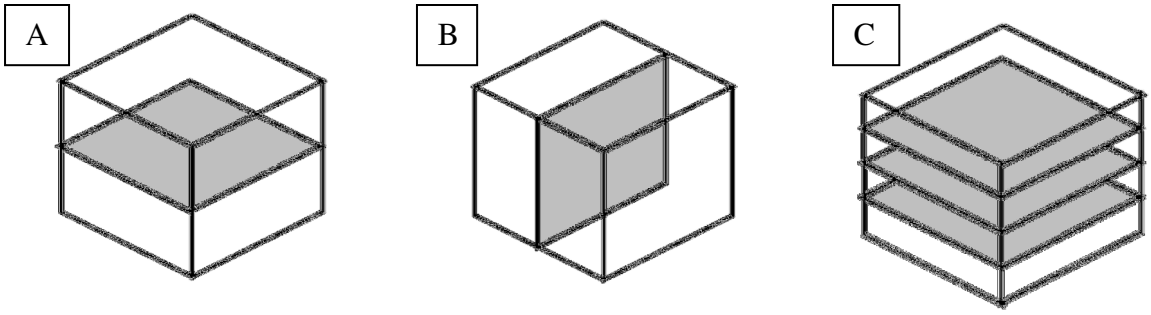


***Figure II-18**. The different scanning modes. **A**. XY mode. **B**. XZ mode and **C**. XYZ mode*

II.3.4. The objective and confocal volume

Micronic and submicronic imaging require that the highest spatial resolution be obtained at the focal plane. This is done by using a diffraction limited microscope with a high Numerical Aperture (NA) objective.

The intensity of a focused laser beam can be described mathematically using:

$$I = I_0 e^{-2(x^2+y^2+\frac{z^2}{\kappa^2})/w^2} \qquad \textit{Eq. II-3}$$

where I_0 is the intensity at the centre, w is the beam radius in the XY plane and κ is a geometric factor usually equal to the optical resolution in the Z direction divided by the optical resolution in the XY plane. These properties define the confocal volume to be an elongated cylinder with a curved contour (**Figure II-19**).

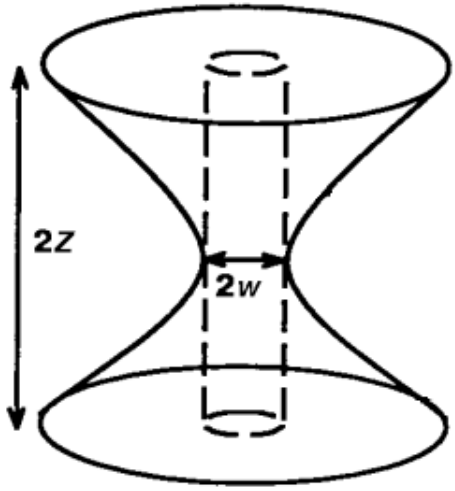


***Figure II-19**. The confocal volume with cylindrical and curved components*

The confocal volume is given by the following relationship:[13]

$$V_c = \frac{2\lambda^2 f^2}{\pi n^2 w^2} z + \frac{2\pi n^2 w^2}{3 f^2} z^3 \qquad \textit{Eq. II-4}$$

Here z is the depth of focus and is generally estimated to be 1.0µm depending on the spherical aberration of the objective [14], f is the focal length of the objective, n is the refractive

index of the medium and λ is the wavelength of excitation. Fluorescence Correlation Spectroscopy (FCS) measurements have been made using 100pM fluorescein to quantify the detection volume. The waist radius of the Gaussian probe volume has been found 470nm. Using this value and ***Eq. II-4***, the total confocal volume was around 1.3fL.

Resolution for a diffraction-limited optical microscope in the XY plane can be described as the minimum detectable distance between two closely spaced specimen points. It is known as the Rayleigh limit:

$$R = \frac{0.61\lambda}{NA}, NA = n.\sin(\vartheta) \qquad \textit{Eq. II-5}$$

Here R is the separation distance, λ is the illumination wavelength, n is the refractive index between the lens and the sample, and θ is one-half of the objective angular aperture. It is seen from **Eq. II-5** that resolution can be increased by increasing NA. The 60x water-immersion objective chosen (UPLSAPO 60x/1.2 NA, f=3.0mm water immersion, Olympus) had a working distance of 0.28mm with a cover slip correction collar between 0.13 and 0.21 mm. Although oil immersion objective have higher NA values, the poor matching between the refractive index of oil (n ≈1.5) and water samples (n≈1.33) creates aberration problems, which are detrimental to resolution. In addition to increasing axial resolution, the use of a high NA objective minimizes the depth-of-field that is needed for confocal imaging.

Table II.1 below summarizes the confocal volume and estimated resolution in the *XY* and Z planes.

Experimental confocal volume	**Estimated resolution in the *XY* plane**	**Estimated resolution in the Z plane**
1.3fL	248nm	500nm

Table II.1*. Properties of the confocal volume and diffraction-limited resolution*

II.3.5. The detection path

Instead of using the original PhotoMultiplier Tube (PMT) included in the scanning unit of the FV300 microscope, the detection path was modified to allow integration of sensitive Avalanche PhotoDiodes (APDs) and double channel detection needed for FRET type experiments. A photograph is shown in **Figure II-20**. To this aim, a mirror (Thorlabs) was placed inside the scanning unit at 45° with respect to the incoming fluorescence signal in order to direct the fluorescence vertically upwards. A 1" hole was drilled in the top plate of the scanning unit to allow the fluorescence signal to exit the box. The fluorescence light was then directed onto a second mirror (ME1-P01, Thorlabs) mounted in a cage system. The angle of the mirror with respect to the fluorescence signal was precisely adjusted thanks to x-y screws included in the mounting system. Subsequently, the fluorescent signal was filtered with a high quality 488 nm long pass filter (LP02-488RU-25, RazorEdge ®, Semrock, Laser 2000). This ensures filtering all excitation light that might have been reflected back to the detection path.

II.3.5.1. The pinhole

The detection beam was subsequently focused onto the 100 µm pinhole (P100S, Thorlabs). Only light collected from regions very close to the focal plane is transmitted through the pinhole, thus improving the signal-to-noise ratio. Accordingly, the smaller the pinhole, the better the discrimination against scattered light from outside the focal probe volume. However, less light can pass through the detector as the pinhole diameter is reduced. Therefore, high efficiency detectors such as APDs are essential in confocal fluorescence measurements. Here the pinhole had a diameter of 100µm which matches the 60x objective for optimum light rejection.

II.3.5.2. Towards the APDs

At this point, the fluorescence photons were split using a dichroic mirror. This separates photons into two channels based on their wavelength (energy). The channel with photons having a wavelength in the range [488nm-630nm] is referred to as the 'green channel' where as the photons having wavelengths above 630nm constitute the 'red channel'. Photons were

focused through a plano-convex lens (LA1805-A, Thorlabs) towards APD detectors operating in single photon counting mode (SPCM-AQRH-13, PerkinElmer Optoelectronics). The whole detection path was carefully covered with black cloths to ensure minimum background signal.

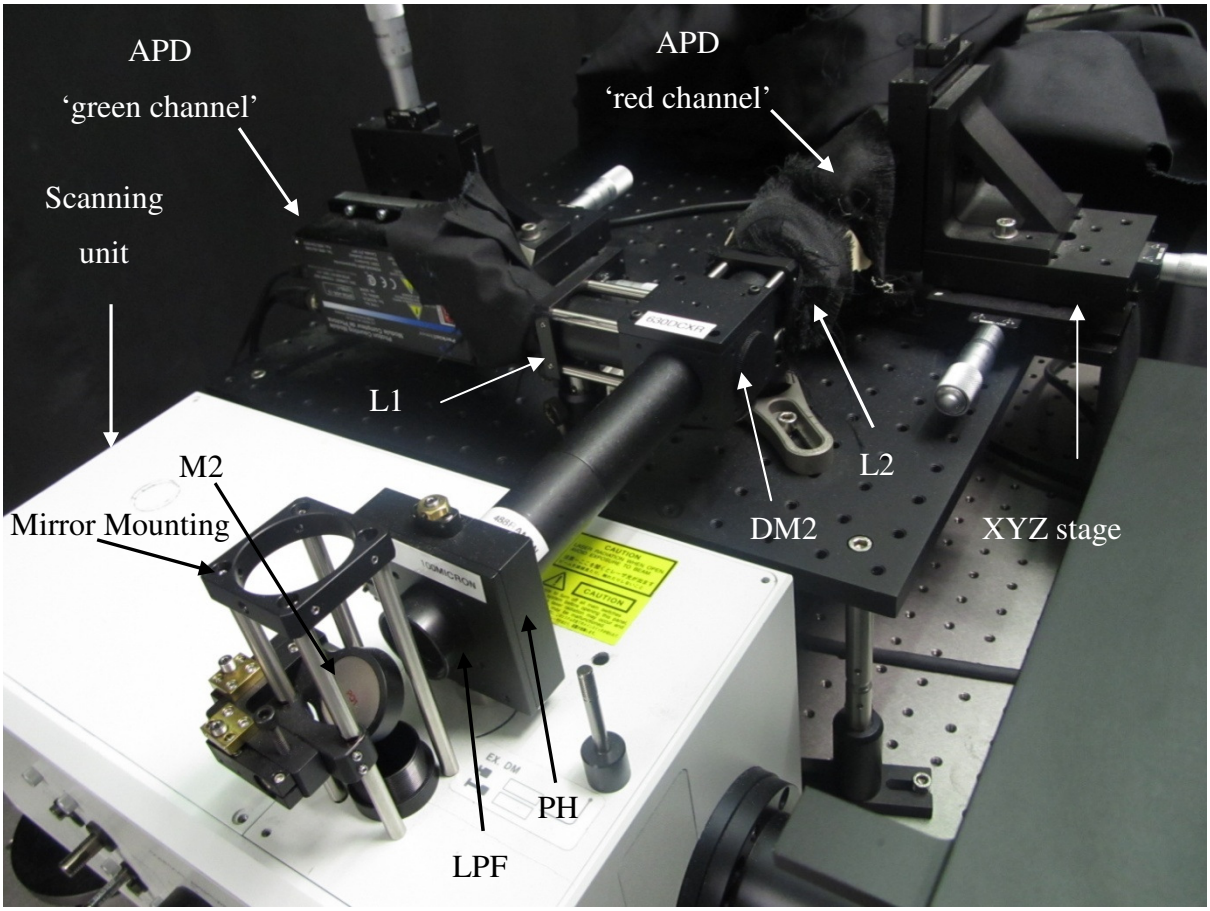


***Figure II-20**. The home-built detection path (DM: dichroic mirror, M: mirror, LPF: long pass filter, PH: pinhole, BPF: band pass filter, L: lens, APD: avalanche photodiode detector).*

II.3.6. Overview of the scanning confocal microscope

A travel microscope stage (H117 Stage, Prior Scientific) was controlled manually to align objective and regions of interest. A CCD camera (Drangonfly Express™, Point Grey Research) was giving visual feedback for laser focusing or cell trapping. **Figure II-21** is a photograph of the 'scanning confocal' microscope setup.

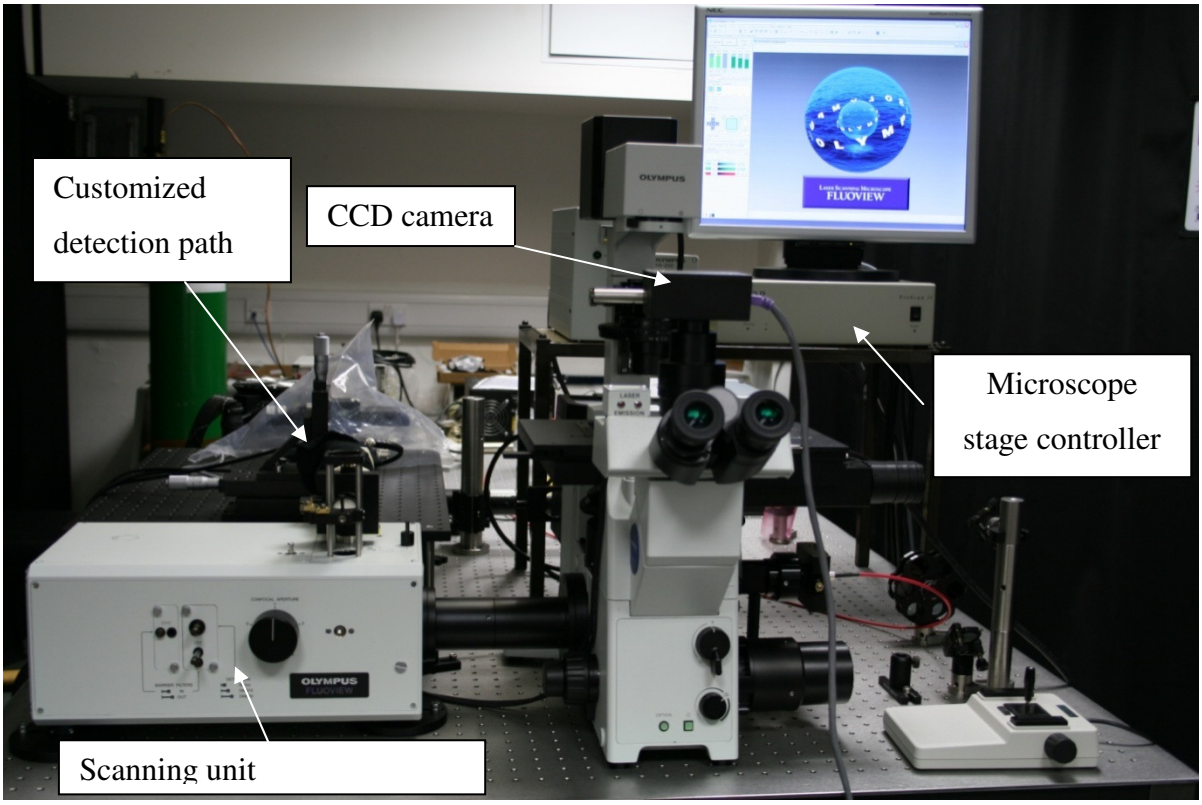


***Figure II-21**. Photograph of the scanning confocal setup*

II.3.7. Integrating microfluidic chips with optics

The overall experimental setup brings together fluidics (syringe pump, tubing and microfluidic chip) with electrical excitation (function generator) and optics (microscope, bright-field camera).

The microfluidic device is placed above the 60x water objective on the microscope stage by adhesion of a large coverslip (borosilicate glass, thickness 1) with the chip. Water is added in between the two glass slides for improved adhesion and refractive index matching. **Figure II-22** is a photograph of the chip sitting over the objective on the microscope stage.

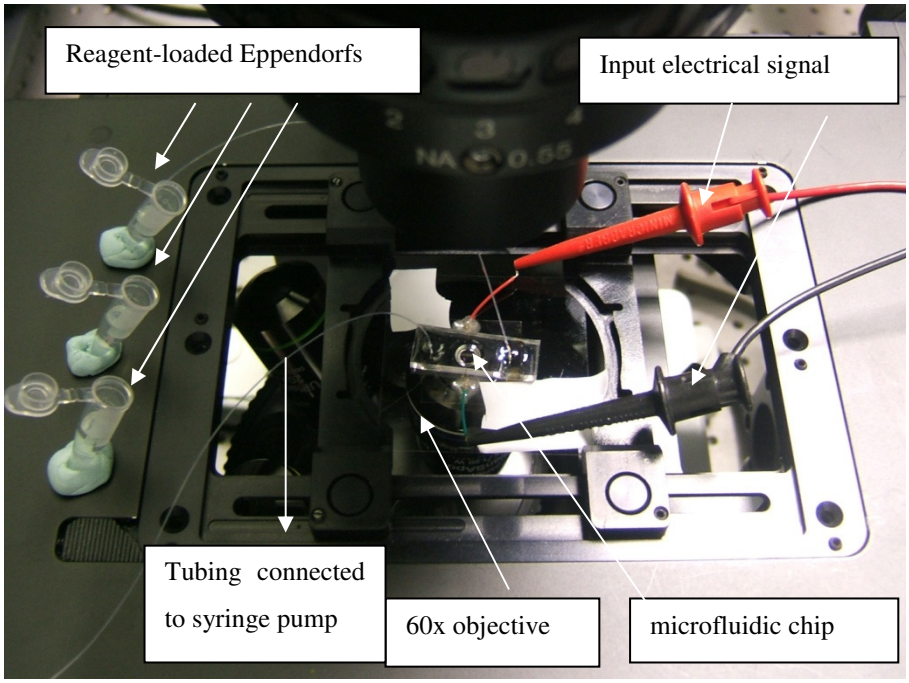


Figure II-22. *The microfluidic chip with electrical connections and capillary connections on the microscope stage*

II.3.8. Time correlated single photon counting setup

Fluorescence lifetime acquisition was performed with a Time Correlated Single Photon Counting (TCSPC) system comprising a TimeHarp 200 PCI board and software (TimeHarp 200, v. 6.0, PicoQuant).

The main principle of TCSPC is illustrated in **Figure II-23**. The electrical signal obtained from the APDs is fed to the TimeHarp board START input via a router and the electric SYNC signal provided by the laser driver is fed to the board via a SYNC pulse adapter. The relative times between the laser excitation pulse and the corresponding fluorescence photon arrivals, termed start-stop-times, are collected with a time resolution of 29 ps. Experimentally, times are measured by recording the time lapse between photon arrival and the next laser pulse. This is to keep conversion rates as low as the actual fluorescence counts as most of the time periods between laser pulses will have no photon events. The memory cell holds the photon counts for one corresponding time bin (time channel). When statistically sufficient counts have been collected, the start-stop-times obtained from multiple cycles can be used to form a histogram representing the fluorescence decay.

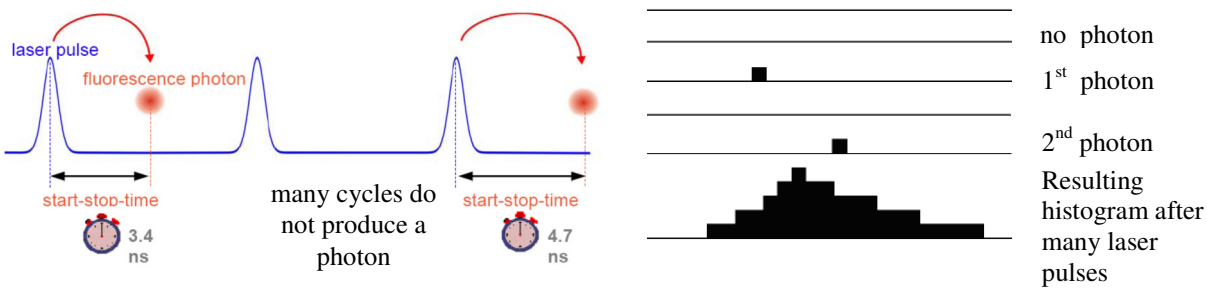


***Figure II-23**. The principle of TCSPC.*

Due to detector dead time and dead time in the acquisition board, if the number of photons occurring in one excitation cycle is more than 1, the system only registers the first photon and misses the following ones. This leads to an over-representation of early photons in the histogram (pile-up). It is therefore crucial to keep the probability of cycles with more than one photon as low as possible by adjusting the laser power and repetition frequency. The practical solution is to keep the average count rate at the detector at most 1-5 % of the excitation rate.

II.3.8.1. Time-Tagged Time-Resolved Mode (TTTR)

In the TTTR mode of the TimeHarp 200, the start-stop timing of each photon event is recorded together with a time-tag from an independent digital counter running with a period of 100 ns. In order to determine the spatial origin of the photon events when scanning with the FV300 microscope, the TimeHarp 200 board also provides inputs for synchronization of the signal derived from the scan controller. These external markers are treated as regular TTTR photon records with a special flag which distinguishes between a true photon and marker records.

Thanks to the time-tagging format and the scan markers, each photon can be allocated to one pixel of the scanned image. The fluorescence lifetime for all photons at a given pixel is extracted from the start-stop times recorded. A histogram can then be reconstructed at pixel

level. The SymphoTime software (Picoquant) provides the visual interface to draw fluorescence lifetime maps and export the fitting data (**Figure II-24**).

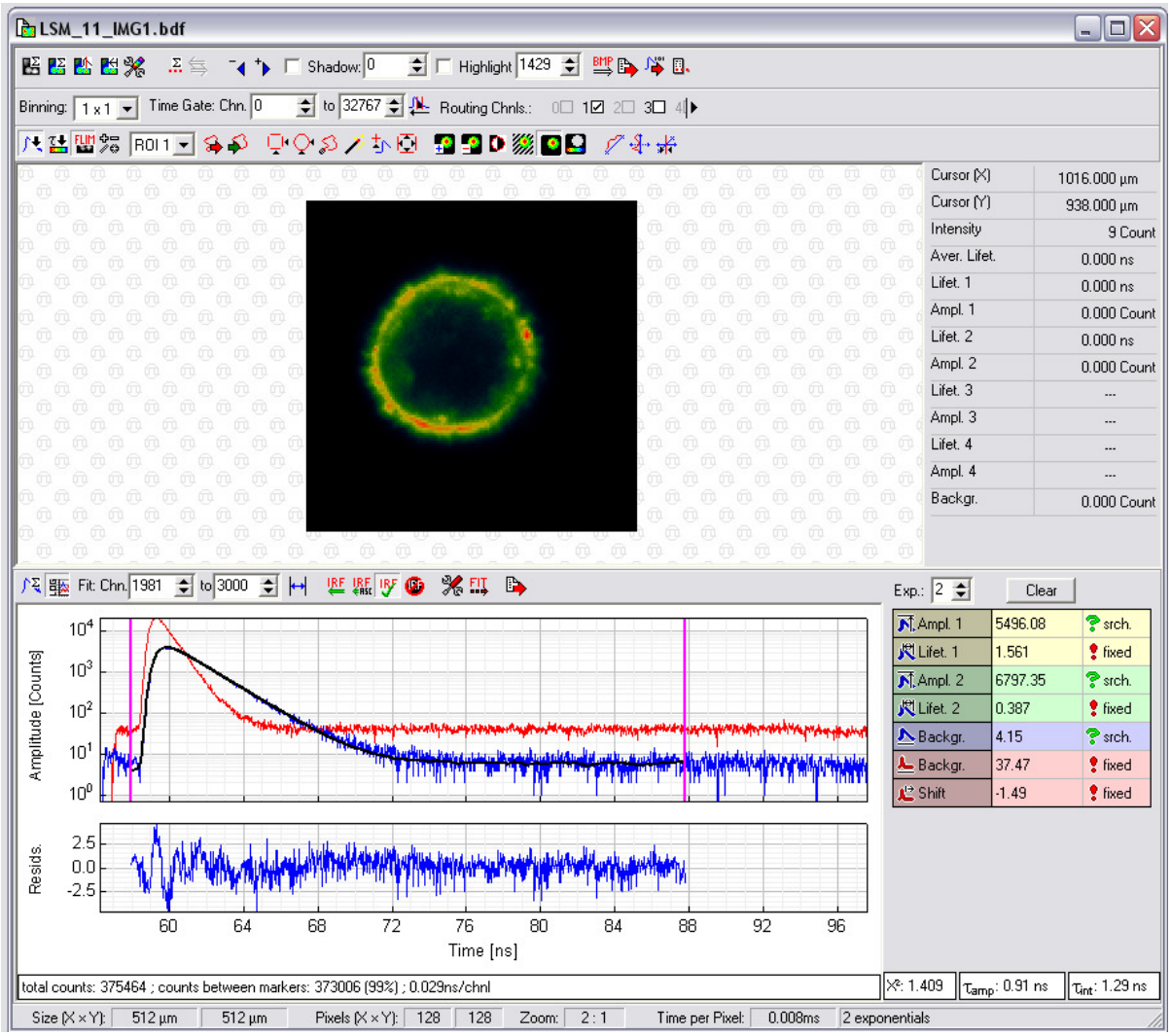


***Figure II-24**. The Symphotime interface for reading TTTR files and fitting fluorescence decay curves.*

II.4. FLIM analysis procedure

II.4.1. FLIM histogramming

II.4.1.1. IRF correction

To correct for the excitation pulse having a finite width and the detectors having a finite response time, the Instrument Response Function (IRF) has to be acquired. Although the IRF does not significantly affect the measurement of long lifetimes but with short lifetime measurements it is essential. The decay curve acquired after TTTR processing is a convolution of IRF and theoretical decay curve:

$$I_{th}(t) = IRF(t) \otimes I_{\exp}(t) \qquad \textit{Eq. II-6}$$

Here I_{th} and I_{exp} are the theoretically and experimental decay curves respectively. In practice, the IRF was recorded using a Rose Bengal solution in water having a fluorescence lifetime of 91ps.[15] This was compared to Auramine O in water with a lifetime of 3ps but no significant differences were found.

As a rule of thumb, lifetimes down to 1/10 the IRF widths can be recovered. In the setup presented in this work, the IRF had a fluorescent decay with Full Width Half-Maximum (FWHM) characteristic time 800ps as shown in **Figure II-25**. This translates into lifetime accuracies down to 80ps.

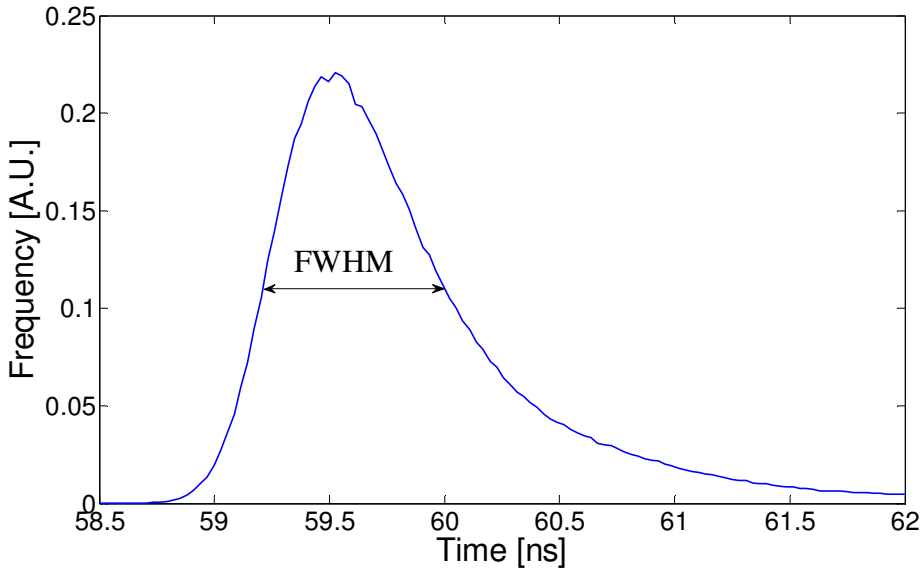


***Figure II-25**. Decay curve for a solution of 1mM Rose Bengal in water and characteristic FWHM.*

II.4.1.2. Fitting algorithm

Only photons corresponding to membrane probes should be processed for the fitting algorithm. To that aim, intra-cellular fluorescence and background were excluded manually, defining a region-of-interest (ROI) along the high intensity membrane. The overall fluorescence decay curve was subsequently generated automatically by the software by summing up the registered photons.

When fitting to fluorescence decay curve careful consideration should be made as to what model is appropriate. In many cases a fluorescence decay curve can be approximated to a single exponential. But if two or more fluorophore populations or fluorescence decay routes are present then a multiple exponential format should be used:[16]

$$I(t) = \sum_{0}^{n} I_{0n} e^{-\frac{t}{\tau_n}} \qquad \textbf{Eq. II-7}$$

Here I_{0n} is the measured intensity corresponding to the n-th component (also called pre-exponential factor) and τ_n the n-th lifetime component. The number of components depends on the sample under investigation. It is usually 2 or more in complex environments such as membranes. The program uses a least squares algorithm to fit the chosen decay at pixel level to the data and works to iteratively reduce the measure of the difference between them. The parameter chi-squared in ***Eq. II-8*** is used to minimise this difference,

$$\chi^2 = \sum_{n} \frac{(I(t_n) - I_{fit}(t_n))^2}{I(t_n)} \qquad \textbf{Eq. II-8}$$

Here $I(t_n)$ is the measured intensity and $I_{fit}(t_n)$ is the fitted decay. The decay which has the minimum chi-squared is then chosen. Finally, the average lifetime is computed as the weighted sum of lifetimes τ_n by the corresponding pre-exponential factors.

$$\tau_{av} = \frac{\sum_{n} I_{0n}\tau_n}{\sum_{n} I_{0n}} \qquad \textbf{Eq. II-9}$$

II.4.2. FLIM maps

A FLIM map was built by accumulating an average of 50-70 frames. The fluorescence lifetime components of 2D maps were assumed constant and taken from the fit of the overall fluorescence decay. Only pre-exponential factors were extracted pixel-by-pixel using the same least squares fitting approach. This gave a 2-dimensional map of average lifetimes. In many cases, the number of photons in one pixel bin is insufficient to determine the lifetime parameters accurately enough. If this constitutes a ROI, statistics have then to be increased by applying a binning factor. A typical binning employed was 4 x 4 with a photon count per pixel of more than 100. Eventually, the average brightness for each pixel is weighted by its intensity so as to obtain an intensity-weighted FLIM map. To obtain lifetime histograms, the intensity weighted lifetimes were used.

II.4.3. Screening algorithm for cell populations

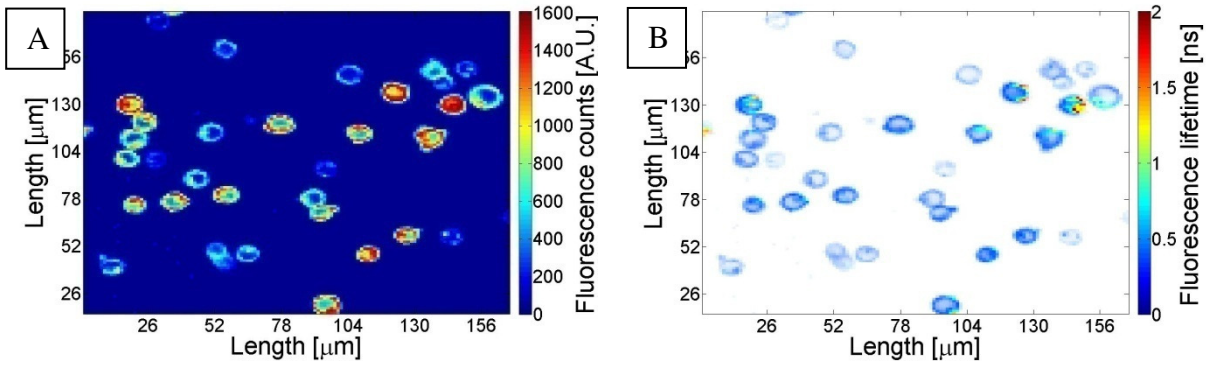
If a FLIM map contains a patchwork of cells rather than a single cell, each cell defines a specific ROI from which lifetime histograms can be plotted. In order to extract the signal content from each individual cell, a home-made algorithm was written in Matlab. It includes three main steps:

1 - Reading of raw intensity/lifetime maps.

2 - Intensity based thresholding of images and recognition of cell envelopes. Labelling of individual areas of the original image (also referred to as image segmentation).

3 - Extraction of intensity-weighted lifetime histograms and global lifetime histograms for the detected cells.

Figure II-26 gives a succession of pictures generated by the analysis program.



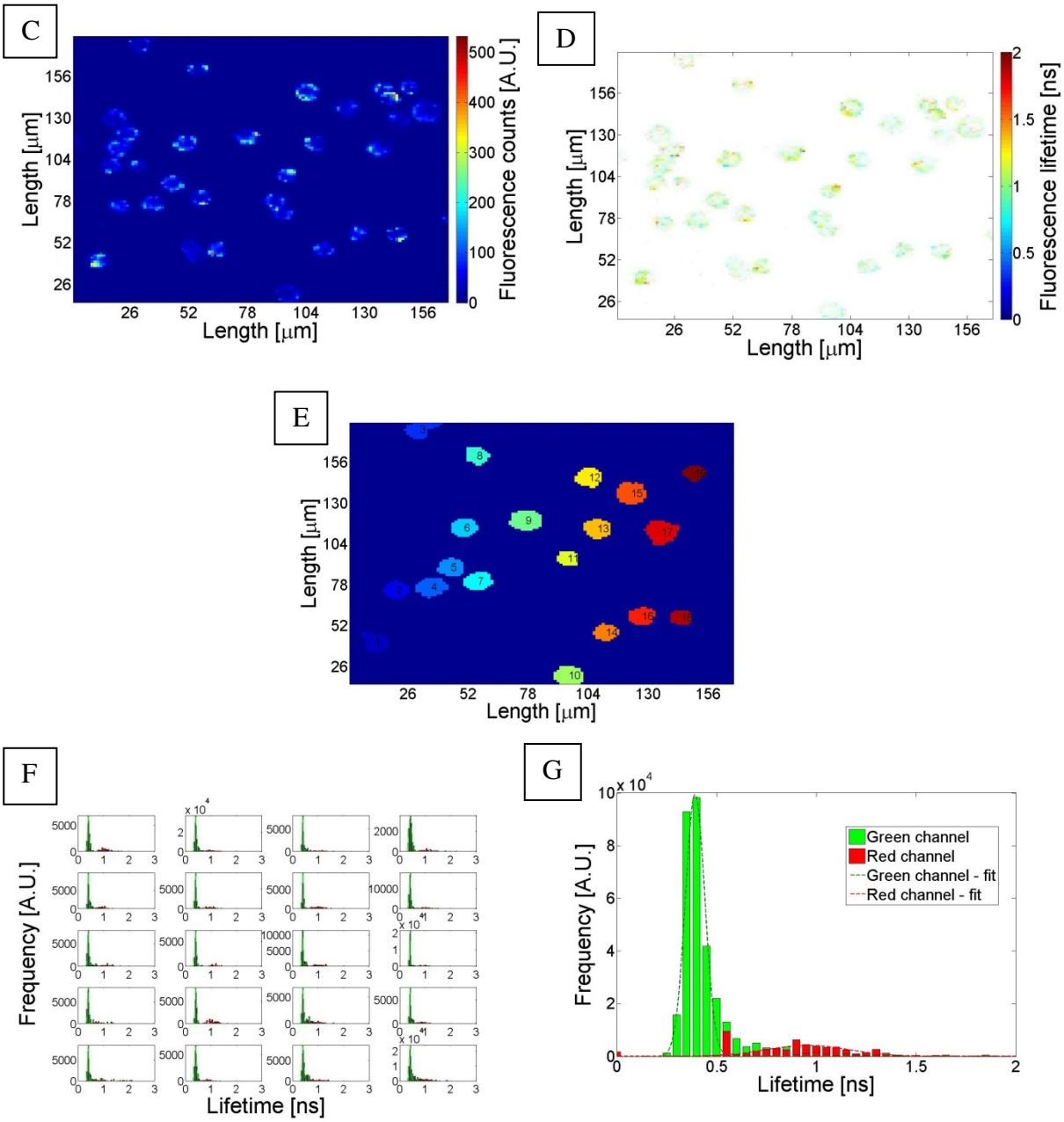


***Figure II-26**. **A**. Raw intensity map for the green channel. **B**. Lifetime map for the green channel **C**. Raw intensity map for the red channel. **D**. Lifetime map for the red channel. **E**. Cell identification and labelling. **F**. Extraction of lifetime histograms for each cell with Gaussian fits. **G**. Global lifetime histograms for all the cells present in the map with Gaussian fits.*

For statistical analyses, only Gaussian fits for which the R^2 coefficient was over 0.95 were selected for further data processing.

II.5. FRET analysis between multiple lipid analogues in a 2D fluid

Contrary to a classical FRET assay format, where donor and acceptor diffuse homogeneously and randomly in a 3D volume, FRET events between unlinked dyes in a cellular membrane present certain characteristics:

1 - Donors and acceptors are unlinked
2 - There are random, multiple donor-acceptor distances at a given time
3 - Donor and acceptors are restricted to diffuse in a 2D plane

In these conditions, the intensity of the donor dye in the presence of acceptor has been found to take the expression:[17]

$$I_{DA}(t) = I_0 \exp(-\frac{t}{\tau_D}) \exp(-\gamma(\frac{t}{\tau_D})^{\frac{1}{3}}) \qquad \textit{Eq. II-10}$$

$$\gamma = \Gamma(2/3) n_A . \pi R_0^{\,2} \qquad \textit{Eq. II-11}$$

Here τ_D is the lifetime of the donor in the absence of acceptor, Γ is the complete Gamma function, n_A is the number of acceptor present within an area $\pi R_0^{\,2}$ around the donor molecule. The Förster radius R_0 is the distance at which the energy transfer efficiency is 50%.

$$R_0^{\,6} = \frac{9 Q_0 \ln 10 \kappa^2 J}{128 \pi^5 n^4 N_A} \qquad \textit{Eq. II-12}$$

Here Q_0 is the fluorescence quantum yield of the donor in the absence of acceptor, n is the refractive index of the medium, N_A the Avogadro's number. The Förster radius depends on the amount of overlap between donor emission spectrum and acceptor absorption spectrum via the overlap integral J. The orientation of the dyes has also to be considered although the κ^2 coefficient is often taken 2/3 if both dyes undergo fast isotropic motions.

In practice, the lifetime-based evaluation of FRET efficiency for multiple donors is expressed by:

$$E = 1 - \frac{\int \frac{I_D(t)}{I_D^0} dt}{< \tau_D >} \qquad \textit{Eq. II-13}$$

The minimum distance between donor and acceptor R_{da} can be subsequently inferred from FRET efficiency measurements using:

$$R_{da} = \left(\frac{1-E}{E} \right)^{\frac{1}{6}} R_0 \qquad \textit{Eq. II-14}$$

This equation lies at the root of the expression 'spectroscopic ruler' employed for FRET based assays as the donor-acceptance distance can be directly inferred from FRET efficiency calculations. The relationship between FRET efficiency versus donor-acceptor distance based on ***Eq. II-14*** is plotted in **Figure II-27**.

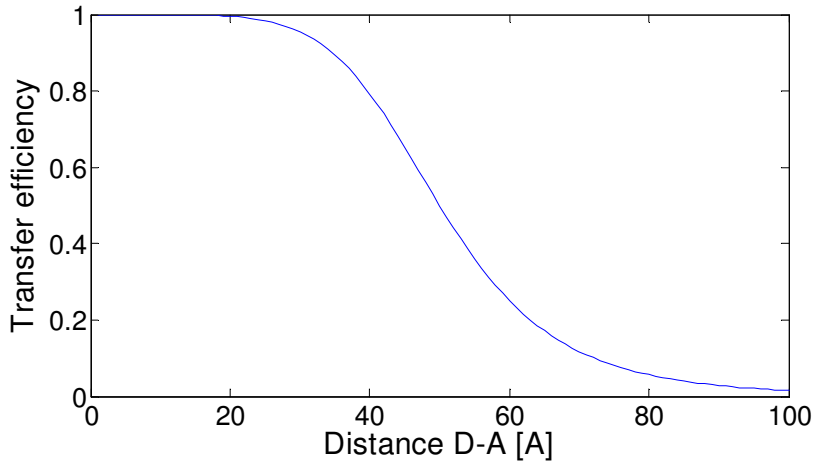


Figure II-27*. Relationship between transfer efficiency and donor-acceptor distance*

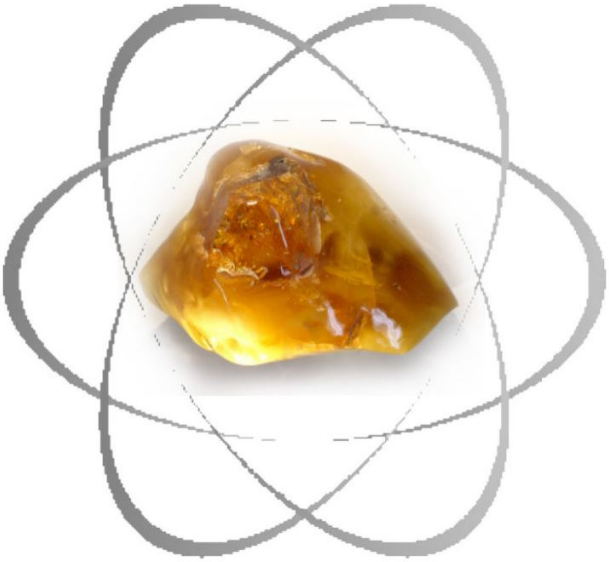
In the context of 2D FRET with multiple acceptors, multiple donor-acceptor distances will be found and interpretation should be carefully considered. FRET efficiencies can be used to probe the existence of excluded volumes around donors.[16] In that case, FRET events will be

rarer than for randomly distributed probes. Inversely, FRET pairs with strong colocalization will have a high FRET efficiency due to their proximity.

II.6. References

(1) Xia, Y. N.; Whitesides, G. M. *Annual Review of Materials Science* **1998**, *28*, 153-184.
(2) Rosenthal, A.; Voldman, J. *Biophysical Journal* **2005**, *88*, 2193-2205.
(3) Bhushan, B.; Hansford, D.; Lee, K. K. *Journal of Vacuum Science & Technology A* **2006**, *24*, 1197-1202.
(4) Kuhn, *Journal of chemical physics* **1949**, *17*.
(5) Bogdal, D.; Pielichowski, J.; Jaskot, K. *Heterocycles* **1997**, *45*, 715-722.
(6) Godin, D. V.; Garnett, M. *Journal of Membrane Biology* **1976**, *28*, 143-168.
(7) Packard, B. S.; Wolf, D. E. *Biochemistry* **1985**, *24*, 5176-5181.
(8) Honig, M. G.; Hume, R. I. *Trends in Neurosciences* **1989**, *12*, 333-&.
(9) Loura, L. M. S.; Fedorov, A.; Prieto, M. *Biochimica Et Biophysica Acta-Biomembranes* **2000**, *1467*, 101-112.
(10) Gullapalli, R. R.; Demirel, M. C.; Butler, P. J. *Physical Chemistry Chemical Physics* **2008**, *10*, 3548-3560.
(11) Sengupta, P.; Holowka, D.; Baird, B. *Biophysical Journal* **2007**, *92*, 3564-3574.
(12) Kim, H. S.; Yun, S. H.; Kwang, I. K.; Kim, B. Y. *Optics Letters* **1997**, *22*, 1476-1478.
(13) Hill, E. K.; de Mello, A. J. *Analyst* **2000**, *125*, 1033-1036.
(14) Nie, S. M.; Chiu, D. T.; Zare, R. N. *Analytical Chemistry* **1995**, *67*, 2849-2857.
(15) Chen, R. F. *Archives of Biochemistry and Biophysics* **1977**, *179*, 672-681.
(16) Lakowicz, J. R., Principles of Fluorescence Spectroscopy, *Springer*, **2006**.
(17) Koppel, D. E.; Fleming, P. J.; Strittmatter, P. *Biochemistry* **1979**, *18*, 5450-5457.

Chapter III. Dielectrophoretic cell trapping: theory and characterization



This chapter introduces the main forces present within dielectrophoretic traps and expounds on the conditions needed to create a dielectrophoretic cage with strong confinement. COMSOL Multiphysics® simulations were used to examine the shape and exclusion capability of those traps. These simulations are valuable for facilitating the design of real devices. Experimental testing of the traps demonstrates these confinement effects and the potential of DEP for cell assaying.

III.1. Governing equation for the dielectrophoretic force

Dielectrophoresis (DEP) uses non-uniform AC electric fields (10 kHz to 100 MHz) to manipulate and position cells or particles.[1] DC-dielectrophoresis also exists as a complementary tool.[2] In DEP, the electric field polarizes a particle (even electrically neutral) by creating an effective dipole moment. The field non-uniformities subsequently exert a net force on this dipole. This is illustrated in **Figure III-1**.

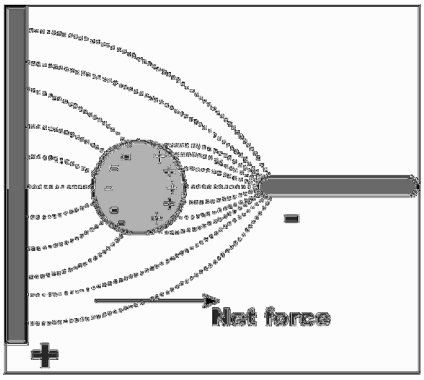


***Figure III-1**. The effective dipole and non-uniformities of the electric field create a net force on a neutral particle (reproduced from [3]).*

TheDEP force is derived from:

$$\vec{F} = \vec{p}.\nabla\vec{E} \qquad \textit{Eq. III-1}$$

Here p is the induced dipole moment and $\vec{E}$ (r, w) is theapplied electric field. It can be shown that the time-averaged DEP force for the dipolar approximation of the DEP force takes the form:

$$\overrightarrow{<F_{DEP}>} = \pi\varepsilon_m R^3 \,\mathrm{Re}[\underline{CM}(\omega)]\nabla\vec{\underline{E}}^2(r,\omega) \qquad \textit{Eq. III-2}$$

Here ε_m is the absolute dielectric permittivity of the surrounding medium, R is the radius of the cell, where r is the spatial coordinate of the cell and ω is the frequency of the applied field. CM is the Clausius-Mossotti (CM) factor representing polarization difference between the particle and the suspension medium.

III.1.1. Implications of the expression of the DEP force

The sign of the CM factor dictates the global behaviour of the particle. Physically, the effective induced dipole is either aligned with the field if the polarization of the particle is greater than that of the medium or aligned against the field in the opposite case. A positive CM factor indicates that the DEP force pushes cells toward an electric field maximum (pDEP) whereas a negative CM factor indicates that the DEP force pushes cells away from the electrodes to an electric field minimum (nDEP).

One of the most significant implications of the expression of the DEP force from ***Eq. III-2*** is that it is extremely dependent on geometry through the gradient term $\nabla\vec{E}^2$. Careful design of complex geometries can thus lead to more control over cells.[4, 5] 3D electrodes designs have been investigated [6, 7] but are ultimately limited by fabrication and packaging complexity. Dynamic programmable electrodes formed on a photoconductive material constitute an elegant alternative to real metallic electrodes but the approach also requires complex fabrication.[8]

As already mentioned, the expression of the time-averaged DEP force is based on the dipolar approximation. Higher order moments may also contribute to the global DEP force. As a matter of fact, in the case of a complex geometry, when non-uniformities in the electrode pattern are commensurate with the size of the cell, higher order moments are likely to be induced. However, in the case of nDEP, cells are pushed out of high gradient regions: the influence of the high order moments is therefore diminished. The influence of higher order moments for the square electrode design represent approximately half of the DEP response [9]

The electric field gradient term in ***Eq. III-2*** has a dimension V^2/m^3. This means the DEP force decays quickly with distance away from electrodes. Therefore, particles of interest have to be in the vicinity of strong electric fields in order to get trapped. Another consideration derived from ***Eq. III-2*** is that the DEP force is very amenable to scaling down as the voltage practical for cell trapping with electrode gap of 10µm becomes less than 1V. Typical forces experienced by cells suspended in water in a DEP traps are 10-200pN depending on particle-electrodes distance.

The general expression for the CM factor relates to the polarization states of both medium and suspended object which are strongly frequency dependent.

$$\underline{CM} = \frac{\underline{\varepsilon}_p - \underline{\varepsilon}_m}{\underline{\varepsilon}_p + 2\underline{\varepsilon}_m} \qquad \textit{Eq. III-3}$$

Here $\underline{\varepsilon_m}$ and $\underline{\varepsilon_p}$ are the complex permittivities of the medium and cell respectively. From the expression given in ***Eq. III-3***, the CM factor has a value varying between -0.5 and +1 which define the maximum responses in nDEP and pDEP respectively.

The real part of the CM factor determines the magnitude of the DEP force. The imaginary part reflects the torque which can be seen in rotating electric fields experiments such as travelling-wave DEP or electro-rotation studies.[10, 11]

III.1.2. Dielectric model for a particle with conductive losses

The complex permittivity of the medium for a particle with conductive losses can be further developed as:[12]

$$\underline{\varepsilon}_m = \varepsilon_0 \varepsilon_m + \frac{\sigma_m}{j\omega} \qquad \textit{Eq. III-4}$$

Here ε_0 is the absolute permittivity of vacuum, ε_m is the relative permittivity of the medium, σ_m is the electric conductivity of the medium and j is $\sqrt{-1}$. ***Eq. III-4*** assumes that the object is purely spherical and constitutes a homogeneous dielectric material. These assumptions are rarely met in practice and the generalization of ***Eq. III-4*** for use with biological objects such as cells has been the subject of numerous studies.[13, 14]

III.1.3. Mammalian cell dielectric model

A mammalian cell is in its simplest approximation a sphere containing a conductive fluid enclosed by a very thin membrane. The overall charge of the membrane is negative but this does not affect the DEP response at frequencies over 100kHz.[15] An analytical treatment of cell impedance model has been recently found and is referred to as the effective single-shell

model. In this model, the cell is progressively smeared-out and finally approximated as a sphere with a single wall (**Figure III-2**).

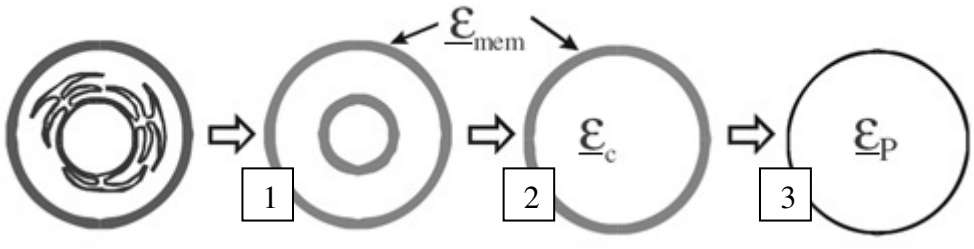


***Figure III-2**. The smeared-out schematic used towards the effective dielectric properties of a mammalian cell (adapted from [16]).*

In this model, the endoplasmic reticulum is effectively modifying the capacitance of the nuclear envelope described as an encapsulated shell (step 1). The plasma and nuclear membranes are then merged into a single one (step 2) with effective permittivities of the membrane and cytoplasm being $\underline{\varepsilon}_{mem}$ and $\underline{\varepsilon}_c$ respectively. The final cell with an effective single-shell has a complex permittivity $\underline{\varepsilon}_p$ (step 3).

This approach allows estimation of the frequency-dependent polarization status for heterogeneous multi-shell spherical objects and has been applied to mammalian cells as well as yeast cells.[11] The different parameters to model mammalian cells properties are exhibited in **Figure III-3**.

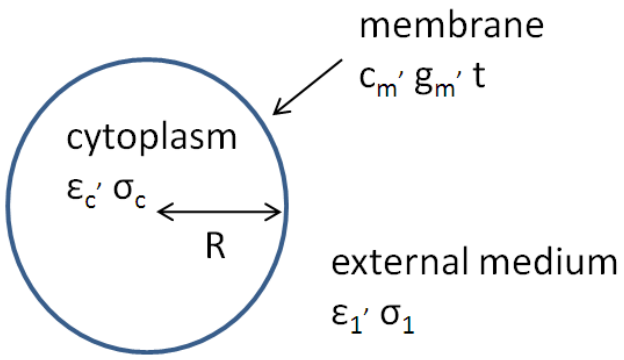


***Figure III-3**. Parameters used in the dielectric model of a mammalian cell.*

Membranes are characterized by an effective capacitance c_m and conductance g_m per unit surface area. It has a finite thickness t, usually assumed 5-7nm. The external buffer medium

is assumed to have a dielectric permittivity ε_1 and conductivity σ_1; the cytoplasm, although containing many organelles, is assumed to be a homogeneous sphere of dielectric permittivity ε_c and conductivity σ_c. The spherical cell has an equivalent outer radius R.

Based on this model, the effective permittivity of a cell has been found analytically:[17]

$$\underline{\varepsilon}_p = \underline{\varepsilon}_m \frac{\left[\gamma^3 + 2\frac{\underline{\varepsilon}_c - \underline{\varepsilon}_{mem}}{\underline{\varepsilon}_c + 2\underline{\varepsilon}_{mem}}\right]}{\left[\gamma^3 - \frac{\underline{\varepsilon}_c - \underline{\varepsilon}_{mem}}{\underline{\varepsilon}_c + 2\underline{\varepsilon}_{mem}}\right]}, \gamma = \frac{R}{R-t} \qquad \textit{Eq. III-5}$$

Examples of dielectric parameters of some human leukocytes are given in **Table III.1**. Surface conductance is often considered negligible.

Cell type	Radius (μm)	C_m (mF/m^2)	σ_c (S/m)	ε_c
T-lymphocytes	3.29 ± 0.35	10.5 ± 3.1	0.65 ± 0.15	103.9 ± 24.5
B-lymphocytes	3.29 ± 0.26	12.6 ± 3.5	0.73 ± 0.18	154.4 ± 39.9
Monocytes	4.63 ± 0.36	15.3 ± 4.3	0.56 ± 0.10	126.8 ± 35.2
Granulocytes	4.71 ± 0.23	11.0 ± 3.2	0.60 ± 0.13	150.9 ± 39.3

Table III.1. *Dielectric parameters of human leukocytes extracted from the single-shell model (reproduced from [18]).*

III.1.3.1. The three frequency regions for Re(CM) in the single-shell model

The presence of the plasma membrane in the single-shell model dictates the frequency response. Three well-defined regions exist:

a. $\omega \rightarrow 0$

At low frequencies, conduction currents dominate. The membrane of a mammalian cell acts as a very low-loss capacitor: it blocks DC electric current from the interior of the cell and therefore protects the cytoplasm. The membrane conductivity is often assumed negligible for live cells and has been measured close to 10^{-7}S/m.[19]

b. ω → ∞

The high-frequency regime is dominated by dielectric polarization currents. The membrane becomes transparent to the electric field and the cell behaves as a dielectric sphere of permittivity ε_c.

The transition between conductivity dominated and permittivity-dominated regimes depends on the relaxing time of Maxwell-Wagner-Sillars interfacial polarization. This corresponds to charges created at the particle-medium interface to maintain continuity of current density across the interface. This transitional frequency is given by:

$$f_{MW} = 1/2\pi \frac{\sigma_c + 2\sigma_m}{\varepsilon_c + 2\varepsilon_m} \qquad \textit{Eq. III-6}$$

The corresponding frequency is over 250MHz for cells in physiological buffers but can be tuned by resuspension into a low conductivity medium. Above this value, the cell response is given by:

$$\mathrm{Re}(CM) \approx \frac{\varepsilon_c - \varepsilon_m}{\varepsilon_c + 2\varepsilon_m} \qquad \textit{Eq. III-7}$$

For the cytoplasm, the dielectric constant for a mammalian cell is typically close to the one of water.[14] As a result, the cell response becomes close to zero when the cell is suspended in water ($78\varepsilon_0$).

c. Intermediate frequencies

In the effective single shell model, the frequency spectrum of cells possesses an intermediate region, typically in the MHz range, where the voltage drops almost entirely across the cell membrane. For these frequencies, the cytoplasm actually becomes a perfect conductor: the potential drop is entirely across the cell membrane.

From ***Eq. III-5***, it is possible to analytically infer Re(CM) as a function of frequency. **Figure III-4** shows this factor for a typical cell of radius 5µm immersed in a high conductivity buffer (the physiological situation) and in a low conductivity buffer of 50mS/m.

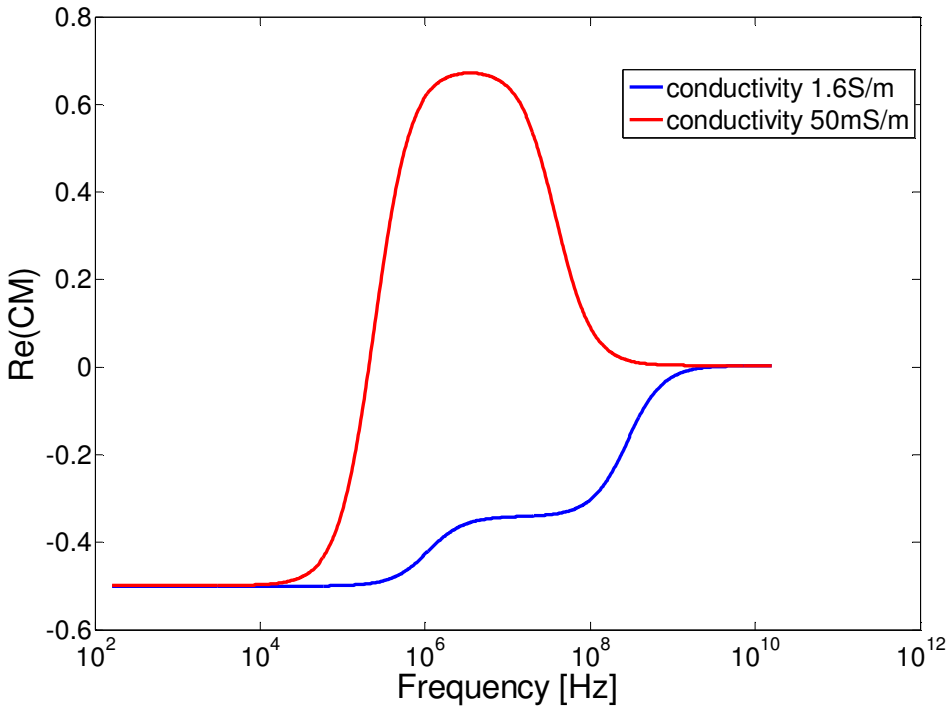


Figure III-4. Real part of the CM factor for a mammalian cell immersed in a dielectric medium. *The red curve represents a low conductivity buffer (conductivity 50mS/m) while the blue one represents a high conductivity buffer like a physiological fluid (1.6S/m). Cell radius was 5.1µm, membrane thickness 7nm, membrane conductivity 10^{-7}S/m, membrane permittivity $16\varepsilon_0$, cytoplasmic permittivity $78\varepsilon_0$ and conductivity 0.7S/m.*

The inversion between nDEP and pDEP behaviour in low conductivity media is largely exploited for separation of live/dead cells or cells with different dielectric parameters.[20] Importantly, a polystyrene (PS) bead of radius similar to the cell under study is a good model to simulate DEP cell response in a high-conductivity buffer as the factor Re(CM) stays also negative throughout the typical frequency range. For comparison purposes, the factor Re(CM) is plotted in **Figure III-5** for a live cell and a PS bead as a function of input signal frequency.

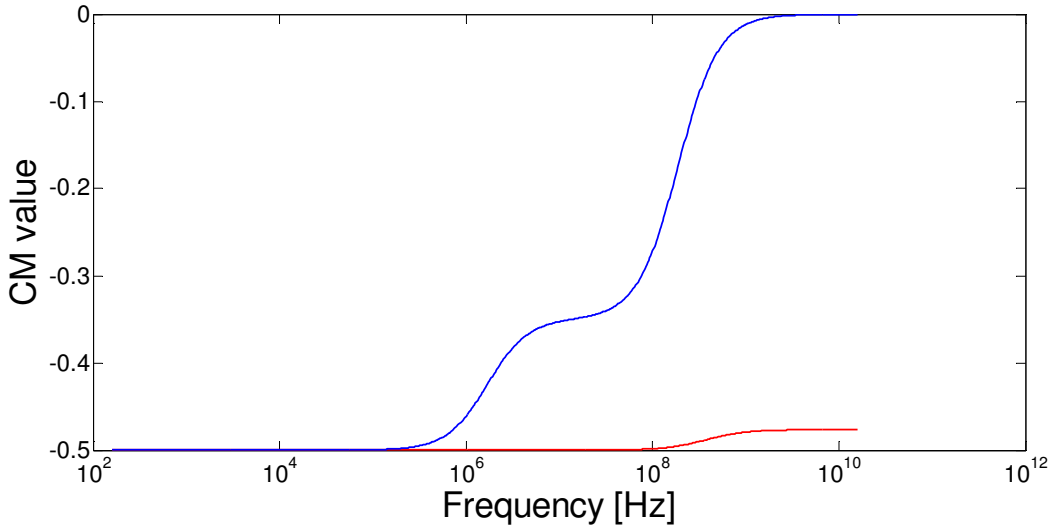


***Figure III-5**. Comparison between live cell (blue) and PS bead (red) responses in a high conductivity buffer. Parameters for the live cells are the ones explicated in **Figure III.4.** **Parameters for the bead were permittivity 2.5**ε_0 and conductivity 10^{-4}S/m.*

Apart from the global displacement brought about by DEP, a torque can also be exerted on a cell if the electric field is not aligned with the effective dipole of the cell any longer. The torque is the cross-product of the effective dipole with the electric field.

A torque exists if the electric field is rotating faster than dipole time-response in a quadrupole electrode design (electro-rotation) or over phase-shifted interdigitated electrodes (traveling-wave DEP). In this case, the rotation of cells can be measured as a function of frequency. A typical frequency-dependent rotation amplitude in a low conductivity buffer is given in **Figure III-6**.

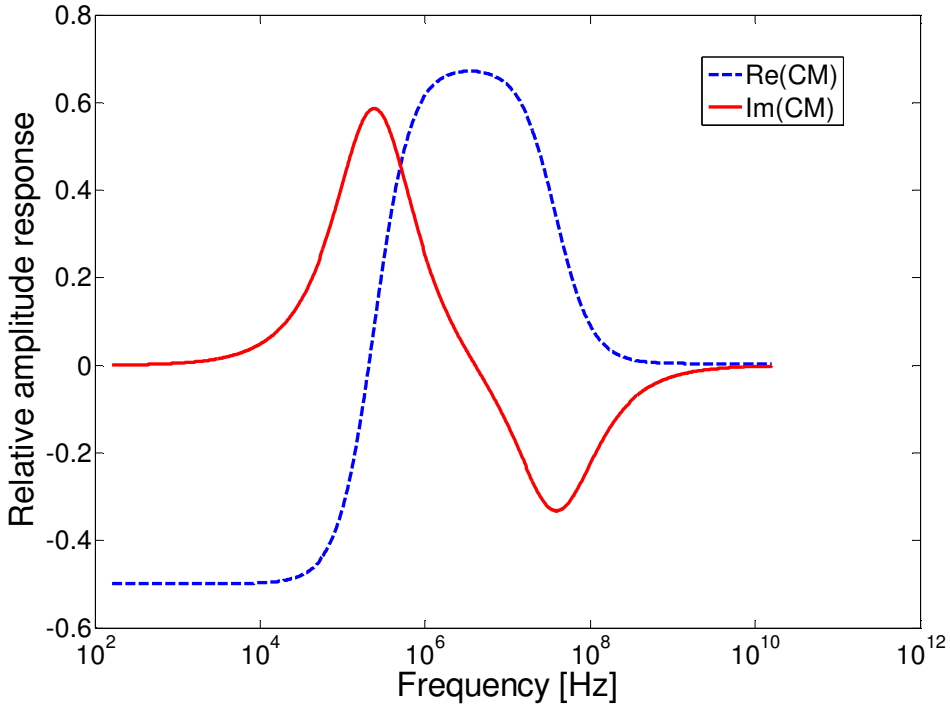


***Figure III-6**. Relative amplitude response as a function of applied electric field frequency (red curve) corresponding to the imaginary part of the CM factor. The dashed blue curve is the real-part of the CM factor. Medium conductivity is set at 50mS/m.The dielectric parameters are the ones given in the caption of Figure III.4.*

Experimentally, measuring rotation rates is practical because rotation does not depend on the original location of cells with respect to electrodes whereas the magnitude of the DEP force does. However rotation is only seen within rotating fields, which are created with phase-shifted signals in multi-electrode systems.

III.2. The force balance for a cell within a DEP trap in a microchannel

The DEP trapping and holding of a cell requires careful understanding of the force balance at the micro-scale. The three main contributions in addition to DEP force are hydrodynamic drag force, gravity and lift of the cells.[21] **Figure III-7** schematically represent the forces and their predominant directions.

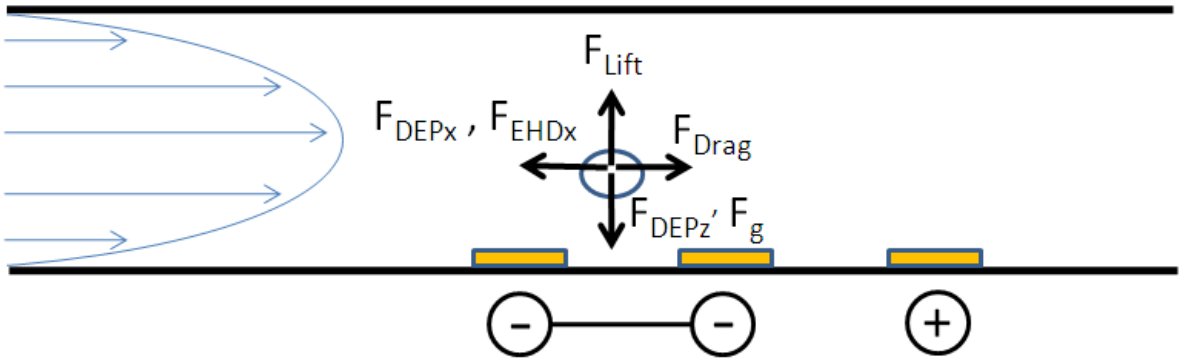


***Figure III-7**. The main forces on a single cell within a microchannel in a planar DEP trap: DEP force, ElectroHydrodynamic (EHD) forces, lift force and drag force with main directions are schematically represented. The Poiseuille parabolic flow velocity is also shown.*

The hydrodynamic drag force can be expressed as:

$$\vec{F}_{drag} = 6\pi\mu R k \vec{v}_p \qquad \textbf{Eq. III-8}$$

Here μ is the dynamic viscosity of the buffer, $\vec{v}_p$ the velocity field at the centre of the cell, k is a non-dimensional correction factor for the wall effect. For instance, a cell in contact with a wall has a k factor of approximately 1.7.[22] In turn, a cell of diameter 10μm near a wall with a flow velocity of 100μm/s at the vicinity undergoes a hydrodynamic force of 16pN.

The expression of the gravitational force is:

$$\vec{F}_g = \frac{4}{3}\pi R^3(\rho_p - \rho_m)\vec{g} \qquad \textbf{Eq. III-9}$$

Here ρ_p and ρ_m respectively the densities of cell and medium and $\vec{g}$ the local gravitational acceleration. This force is 0.6pN for a cell of radius 10μm in water of density 1125kg/m^3.[23]

The hydrodynamic lifting force has been found by Williams *et al.* to be:[24]

$$\overrightarrow{F_{lift}} \approx 0.153R^3\mu\frac{1}{(z-R)}\frac{d\overrightarrow{v_p}}{dz}\bigg|_{z=0} \qquad \textit{Eq. III-10}$$

Here a cell is located at (z-R) above a substrate. The force tends to push cells in a direction perpendicular to the fluid flow and is high in near-wall regions. Using a typical parabolic flow profile of average velocity 100µm/s, an estimate of the hydrodynamic force 1µm above substrate is 0.1pN. It is therefore much lower than the DEP confinement forces.

EHD flows are created by local temperature rise close to the electrodes giving rise to both conductivity and permittivity gradients. They contribute to the buoyancy force, pushing cells away from the DEP trap. The time-average force has been approximated by Ramos.[25]

$$<\vec{F}_{EHD}>=-\frac{1}{2}\left[\left(\frac{\vec{\nabla}\sigma_m}{\sigma_m}-\frac{\vec{\nabla}\varepsilon_m}{\varepsilon_m}\right)\frac{\varepsilon_m\vec{E}^2}{1+(\omega\tau)^2}+\frac{1}{2}\vec{E}^2\vec{\nabla}\varepsilon_m\right] \qquad \textit{Eq. III-11}$$

Here τ is the thermal relaxation time. This force become significant when temperatures rise significantly (>10ºC) (for instance when using high conductivity buffers) or when large electric fields are applied.

Other factors that can influence the behaviour of cells include mechanical forces (contacts), Brownian motion, AC electro-osmosis (AC-EOF) and temperature gradients leading to ElectroHydroDynamic forces.[9, 26, 27] AC-EOF is observed at frequencies lower than 50kHz and thus has a limited influence at DEP-operating frequencies.

III.3. Simulations

III.3.1. Design rules

Here we consider a planar DEP trap such as a square trapping geometry. The cross-section is made of 3 parallel line electrodes as represented in **Figure III-8**.[28]

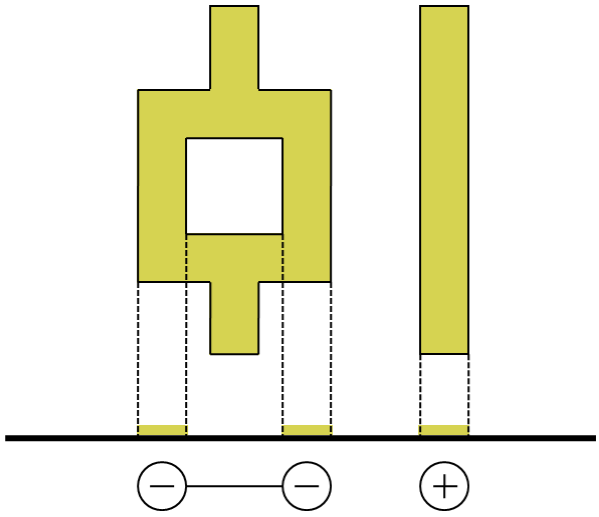


***Figure III-8**. Schematic of the simulated geometry and projection to 3 planar parallel electrodes.*

The design rules adapted here from Rosenthal's original study are based on the idea that the spacing between electrodes should be at least bigger than the cell diameter in order to trap them.[29] This critical dimension can be fruitfully tuned to obtain size selective trapping. Additionally, a too large gap between cathodes translates into decreased electric gradients. Given the heterogeneities of a cell population such as T-cell, the spacing of 15-20µm is a good compromise. Direct contact with electrodes must be avoided to prevent direct charging effects. The spacing between the anode and first cathode should be as close as possible to generate high gradients. Here again, 20µm seems realistic. The width of the electrodes should ensure that fields are not too strongly localized which could lead to cell damage but also not too low to ensure efficient trapping. 10µm is a practical value comparable to reported geometries.[29]

III.3.2. 2D DEP cage

The following simulations have been performed using COMSOL package. They include electric field simulations using the Finite Element Method (FEM). FEM is a numerical technique for finding approximate solutions of partial differential equations over a meshed domain. It is especially useful when analytical solutions do not exist for a given problem. For

all simulations, the Laplace equation was equation was used (no space charges) and the time-dependent solver was used.

In the two-dimensional model simulated, the geometry chosen is an nDEP trap based on only three planar line electrodes embedded in a shallow channel. The channel height is chosen to be 30µm. Three line electrodes of width 10µm have a spacing of 20µm. The two left electrodes represented the ground while the right electrode was set at $+5V_{rms}$. Bound conditions for the other surfaces was electrical insulation. The dielectric fluid parameters are those of water with dielectric permittivity $78\varepsilon_0$ and conductivity 10^{-7}S/m.

The non-uniform mesh was made of triangular elements with minimum sizes down to 0.1µm close to the electrodes and sizes increasing up to 1µm away from the electrodes. **Figure III-9** is a visual representation of the mesh.

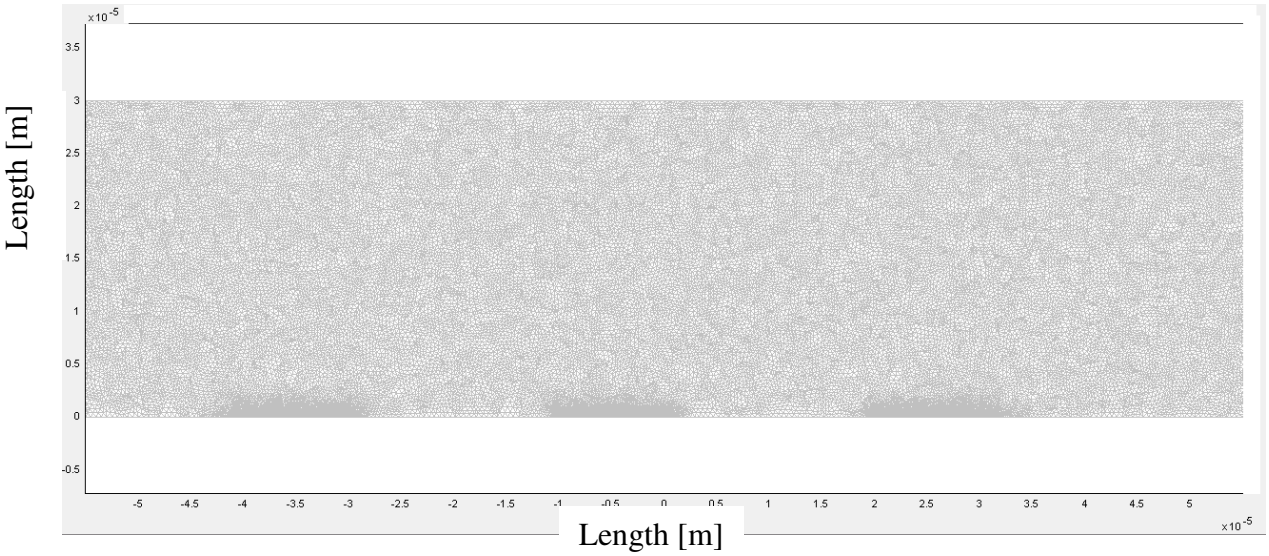


***Figure III-9**. The geometry and associated mesh with increased resolution close to the electrodes.*

The electric field associated to the same geometry can subsequently be mapped as shown in **Figure III-10**. It highlights hotspots present at the edges of the electrodes.

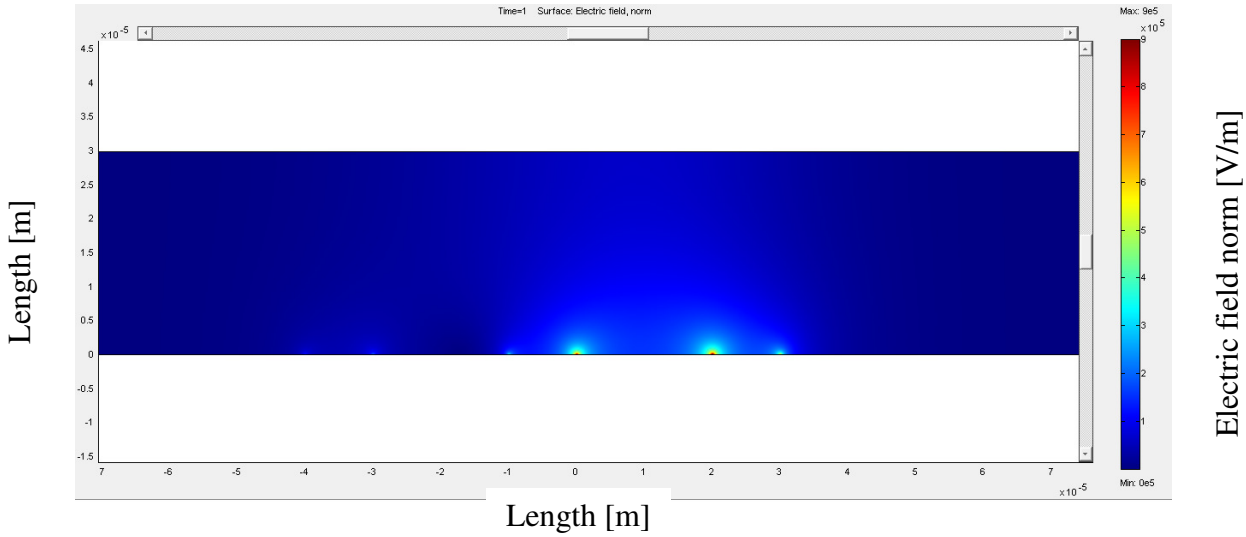


***Figure III-10**. Electric field norm associated with the simulated model*

DEP force can be mapped when plotting the gradient of the square of the electric field norm. The direction of this force for a particle under nDEP is shown in**Figure III-11**.

Figure III-11 shows the normalized DEP force direction in close proximity to the electrodes and highlights the DEP trapping and DEP levitation regions.

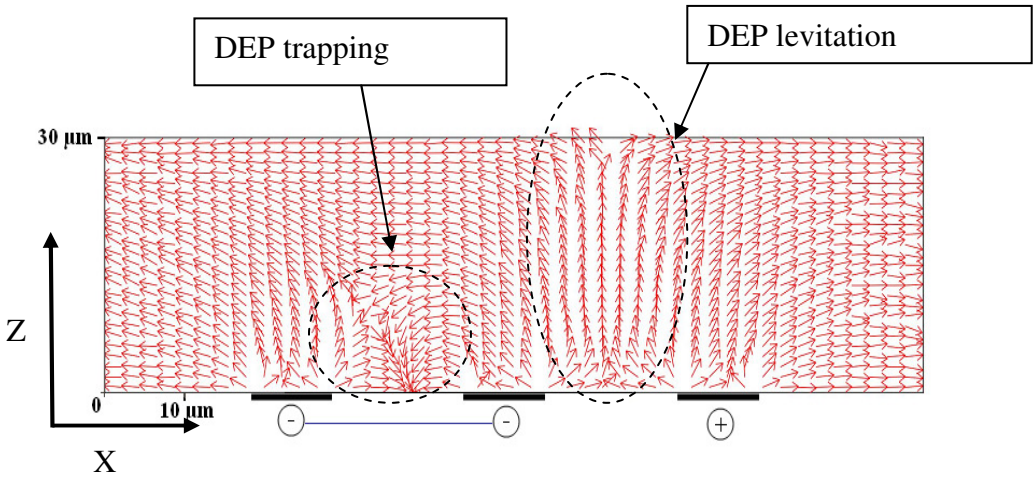


***Figure III-11**. Normalized DEP force direction associated with three line electrodes.*

Depending on the location of the cell, the force is directed differently:

• Between the two right electrodes, a strong electric field exists and the DEP force is directed upwards: the cell will be therefore be lifted up. This phenomenon is known as DEP levitation.

• Between the left electrodes the force is directed downwards and pushes cells towards the middle of the electrodes: this region defines the nDEP trap.

• Outside the outer left electrode (the left side in

Figure III-11), cells are weakly pushed away (due to the low gradient far from the electrode gap)

• Outside the right electrode (the right side in

Figure III-11), cells are strongly pushed forward away from electrodes.

A DEP cage exists when a cell is forced to go back to a single location when slightly moved away from its equilibrium. In addition, the strength of the cage can be quantified and mapped.

III.3.3. Effect of geometrical confinement on electric field distribution

The depth of the micro-channel plays an important role in shaping the electric field distribution. To demonstrate that, we simulated the geometry introduced in the previous paragraph for 2 different channel heights of 30µm and 120µm respectively. The electric field norm is seen to adopt a different distribution as shown in **Figure III.12**.

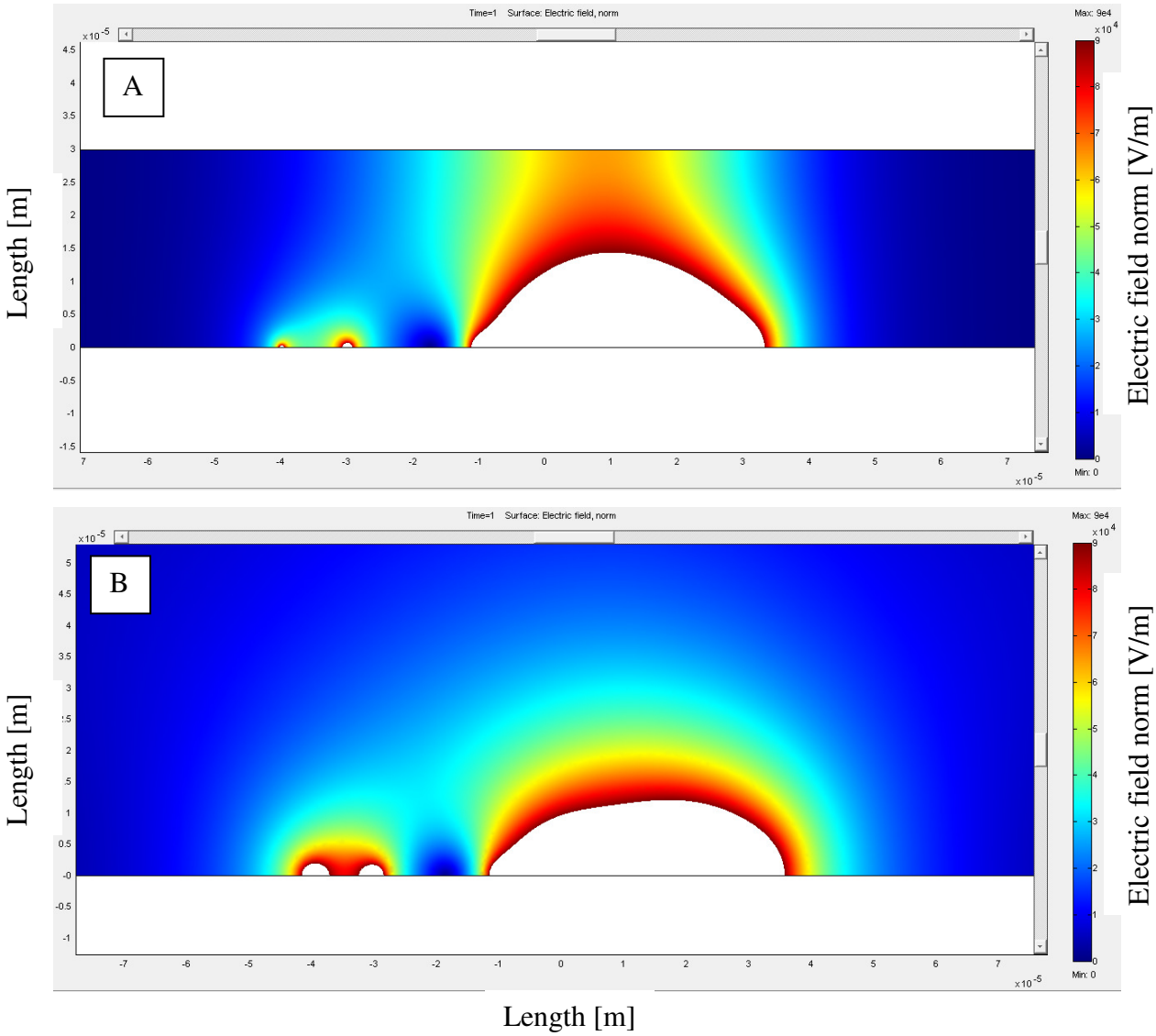


***Figure III-12**. Electric field norm simulated for a channel of height 30µm (A) and 120µm (B) showing the effect of geometrical confinement on electric field distribution. The scale has been adapted to highlights differences in the DEP trapping region.*

In terms of trapping capability, the vertical component of the DEP force $\left|\nabla_z \vec{E}^2\right|$ is a pertinent parameter and is represented in **Figure III-13**.

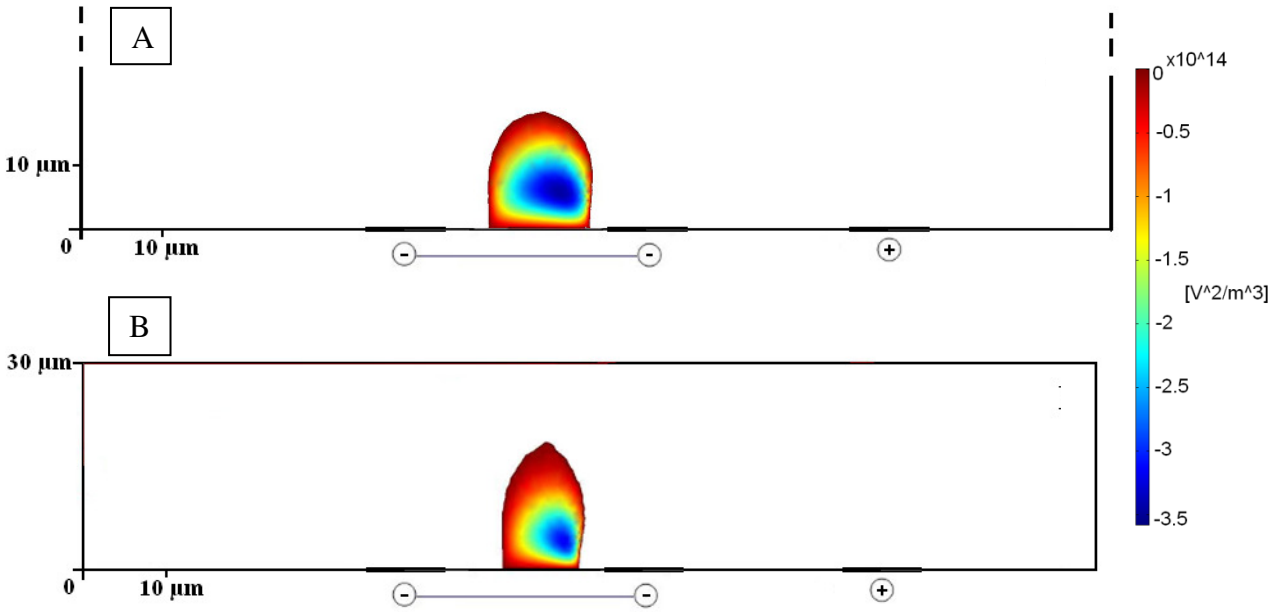


***Figure III-13**. Highlight of the confinement strength of an nDEP trap in a three lines electrode geometry. Negative component of the projection on the vertical axis of* $\left|\nabla_z \vec{E}^2\right|$ *in a deep channel (here 120 µm) (**A**) and a shallow channel 30µm deep (**B**). Blue regions correspond to strong gradients while red regions correspond to weak gradients. Both simulations have the same colour map.*

In the case of a shallow channel, the shape of the DEP cage is seen vertically elongated with high gradients close to the edge of the elctrodes. The cage extends up to half the total depth of the channel which translates into higher probability of trapping nearby cells. Given the high density of the mesh, the differences seen cannot be due to numerical noise.

III.3.3.1. Lateral exclusion of other cells

Any cells flowing towards the third electrode line (the left electrode in **Figure III-13**) will be lifted up as long as the electric field is left turned on. The magnitude of this exclusion effect directly depends from the channel height. Here again, we compared a 30µm and 120µm channel. It is worthwhile pointing out that the exclusion is only lateral due to the planar nature of the electrodes. Cells can still access the trap from above as has been shown.[30] **Figure III-14** illustrates the gradient term projected on the vertical z-axis. It highlights the fact that lateral exclusion increases with increasing channel depth.

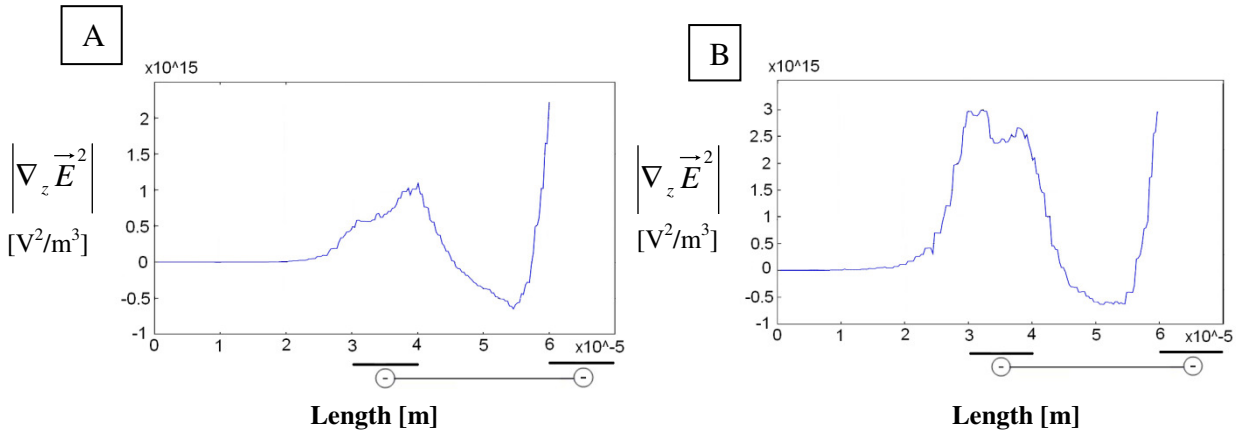


***Figure III-14**. Normalized DEP barrier height (upwards DEP force) over the first line electrode as a function of channel height at constant voltage. **A**. for a 30µm deep channel and **B**. for a 120 µm deep channel.*

The effective barrier height seen by incoming cells can be plotted as a function of channel height as shown in **Figure III-15**.

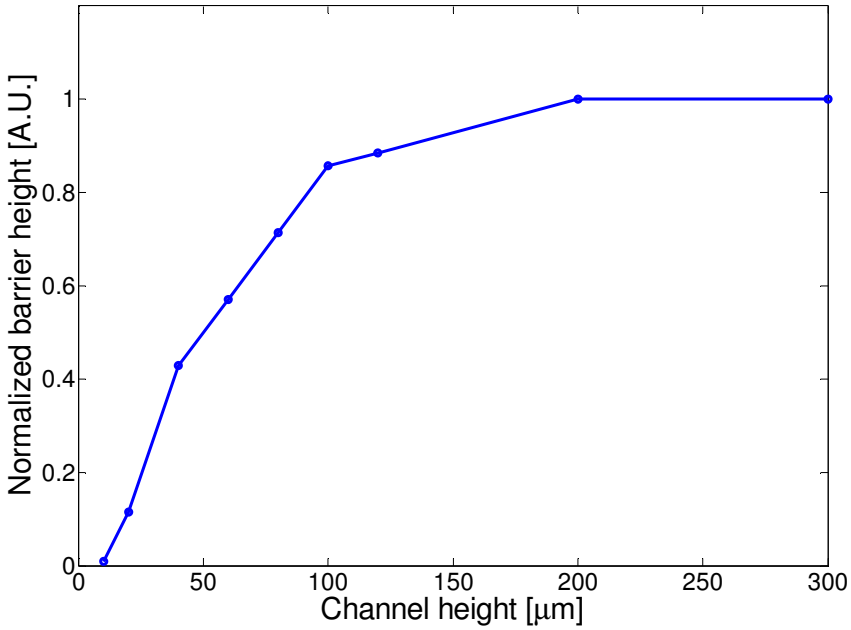


***Figure III-15**. Normalized barrier height as a function of channel height.*

From **Figure III-15**, it is seen that to ensure strong lateral exclusion, it is preferable to work with channels having a depth over 100µm. On the other hand, applications such as in-flow trapping can be achieved more easily in shallow channels, allowing cells to pass the outer cathode.

III.3.3.2. Electric potential wells

If a cell is floating above the planar patterned electrodes, it will tend to settle down due to their density being higher than water and fall into electric potential wells. In a conservative force field, the energy density seen by a particle will be proportional to $\left|\vec{E}^2\right|$.

These wells of lower energy density can be quantitatively mapped as in **Figure III-16**. Here we simulated an array of 3 x 3 traps surrounded by line electrodes and plotted the energy density 5 microns above the surface.

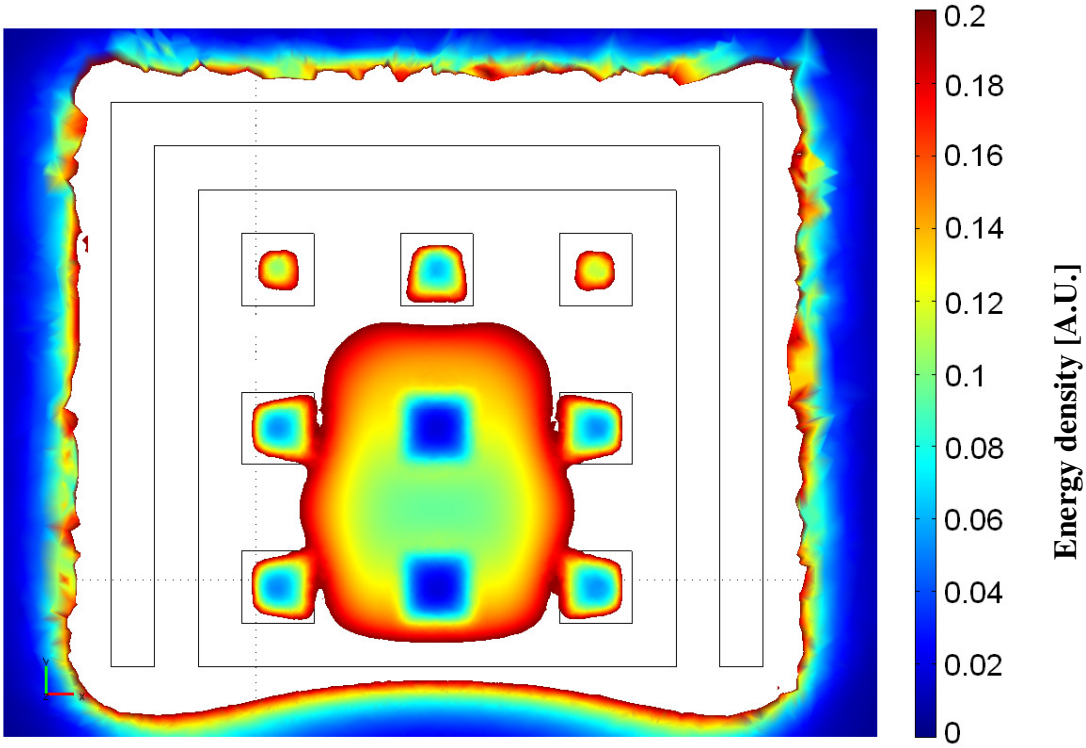


***Figure III-16**. Electric energy density 5 microns above the surface are aligned with the traps. The scale has been adapted to highlight the low potential well regions.*

Local potential wells are seen aligned with traps. This implies cells will tend to fall towards the centre of each trap. Energy density is decreasing away from the electrode gap. This means, experimentally, that cells will tend to accumulate in these regions.

III.3.4. 3D Visualization

3D visualization gives insight into the physical extension of the DEP trap. **Figure III-17** depicts a square electrode geometry with slices representing $\left|\nabla_z \vec{E}^2\right|$ every 5µm.

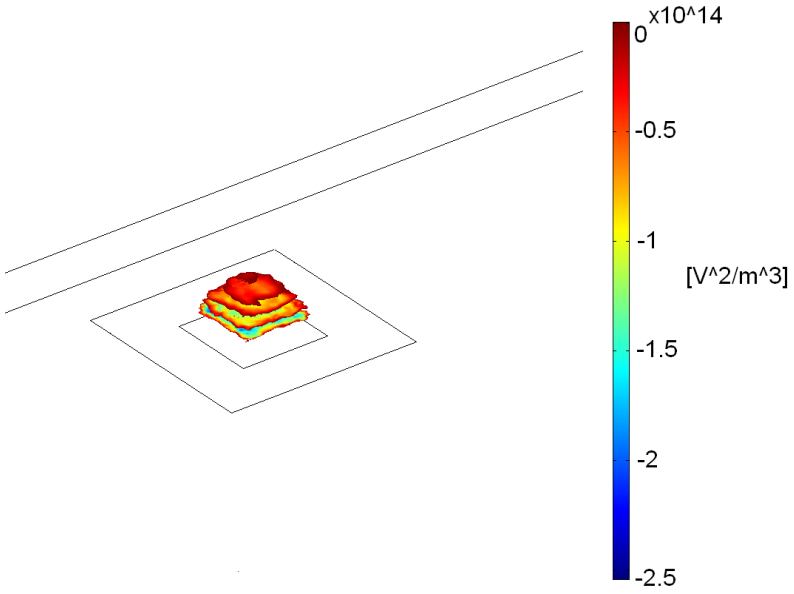


***Figure III-17**. 3D model representing $\left|\nabla_z \vec{E}^2\right|$ with z slices every 5 microns. The parameters are the same as in **Figure III-13**. The square dimensions are 20 x 20 µm.*

In **Figure III-17**, the vertical extension of the nDEP confinement zone is approximately 25µm, consistent with the 2D simulations. These simulations stress the capability of confinement of such nDEP traps and can be used for fine-tuning of trap geometries. Several examples are given in **Figure III-18**.

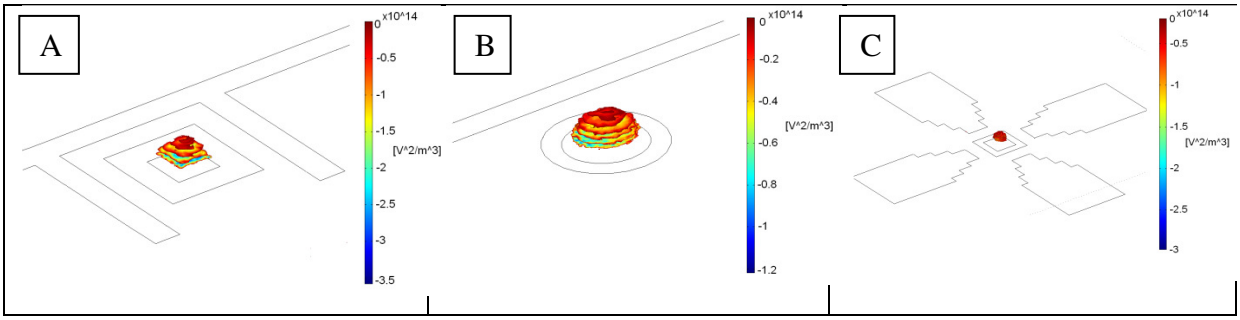


***Figure III-18**. Comparison of 3D shapes of nDEP traps. **A**. With three line electrodes. **B**. with a round trapping electrode and **C**. with a square trap with quadrupole electrodes*

The square trap surrounded on 3 sides by line electrodes (**Figure III-18A**) has the strongest confinement potential due to the additive nature of the gradient term. **Figure III-18B** shows a semi-spherical cage with lower trapping strength than its square counterpart due to larger electrode-trap gap. In **Figure III-18C**, a quadrupole electrode with centred square trap is shown to have very small vertical extension (up to 10µm).

III.4. Characterization of nDEP traps

III.4.1. Mapping XY non-uniformities

nDEP square traps are versatile trapping tools provided the size of the object to trap is commensurate with the dimension of the square. For testing or characterization purposes, one can examine the reaction of objects of elongated shape for which effective dipole will be much stronger along the major axis. Here we show that GFP-expressing E.Coli in PBS can be used to map electric field lines. **Figure III-19A** shows the random distribution of E. Coli in the absence of electric field. When applying $3V_{pp-}$ at1MHz, the bacteria get aligned with the field lines (**Figure III-19B**).

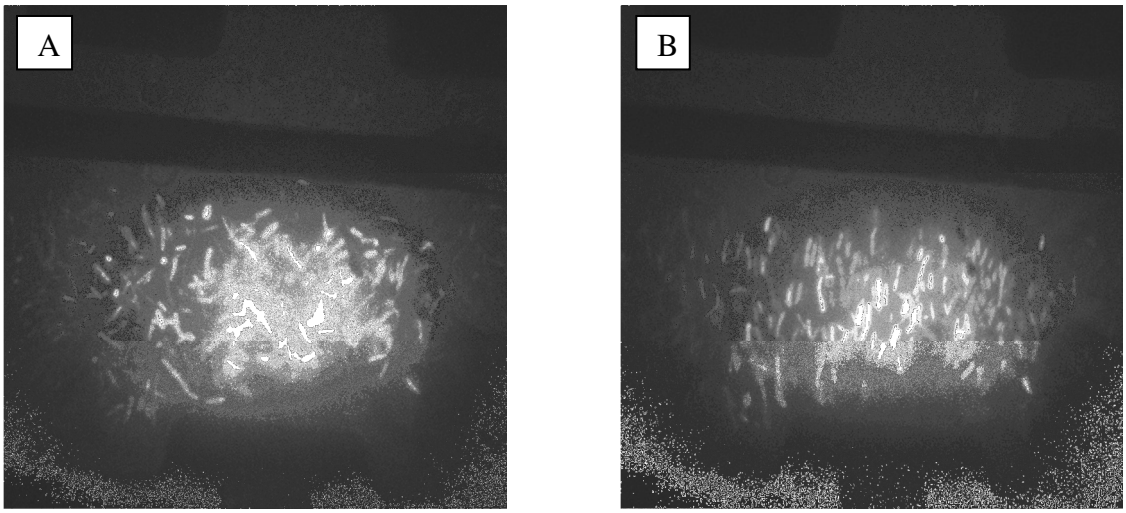


***Figure III-19**. A. E.Coli randomly distributed on top of electrodes. B. E.Coli. repelled and aligned with the electric field lines*

Close to the electrodes, the bacteria experience a torque as long as DEP force and induced dipole moment are misaligned. Further away from the electrodes, bacteria reach steady-state positions and get aligned with the electric field lines. More complicated field distributions can also be looked at as illustrated in **Figure III-20**.

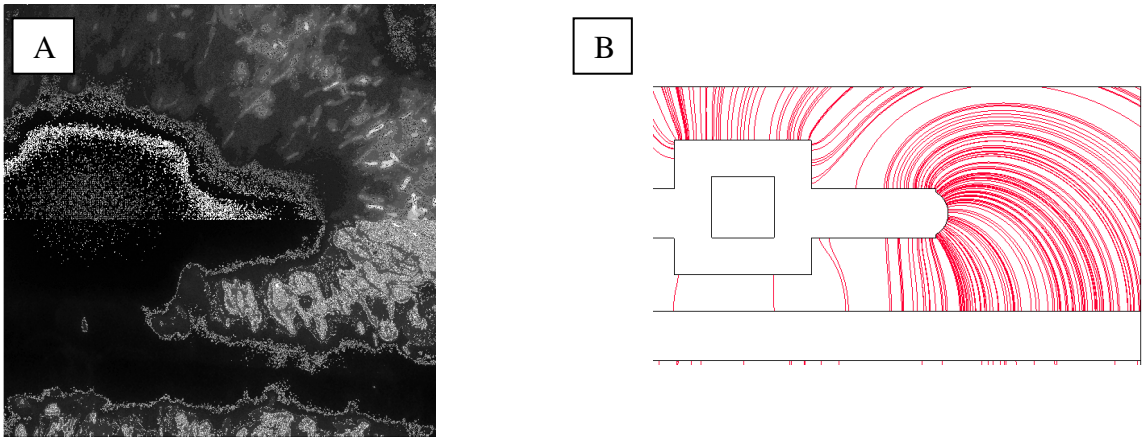


***Figure III-20**. A. Dipole-electric field alignment in E.Coli for complex electrode geometries. B. COMSOL simulated electric field lines for the same geometry.*

Visualization of electric field lines can be used to detect local defects, confirm the function of a DEP trap.

III.4.2. Mapping Z confinement force in nDEP traps

Vertical confinement has been studied theoretically in **III.3.1**. In order to experimentally demonstrate this effect, we used a laser beam expander focused at the glass-solution interface. As molecules get closer to the surface, the overall intensity increases which indicates stronger confinement forces.

III.4.2.1. Example: confinement of 1µm particles

The forces in the absence of flows acting on small particles are mainly DEP and Brownian motion. According to the Einstein-Stokes equation, the diffusion coefficient of a spherical object in a fluid of low Reynolds number is given by:

$$D = \frac{k_B T}{6\pi\eta R} \qquad \textit{Eq. III-12}$$

Here k_B is the Boltzman's constant, T is the absolute temperature, η is the dynamic viscosity and R the radius of the particle. The mean square displacement of such an object for two degrees of freedom is:

$$< x^2 >= 4Dt \qquad \textit{Eq. III-13}$$

Eq III-14 holds for isotropic and unrestricted translational motion. Therefore, any changes in measured mean square displacement indicate the presence of hurdles to diffusion.The average displacement of fluorescent spheres of diameter 1µm suspended in de-ionized water can be tracked with an Electron-Multiplying Charge Coupled Device (emCCD, Cascade II, Photometrics) camera recording movies at 10 frames per second. Using an in-house written code, the trajectories can be easily tracked as shown in **Figure III-21**.

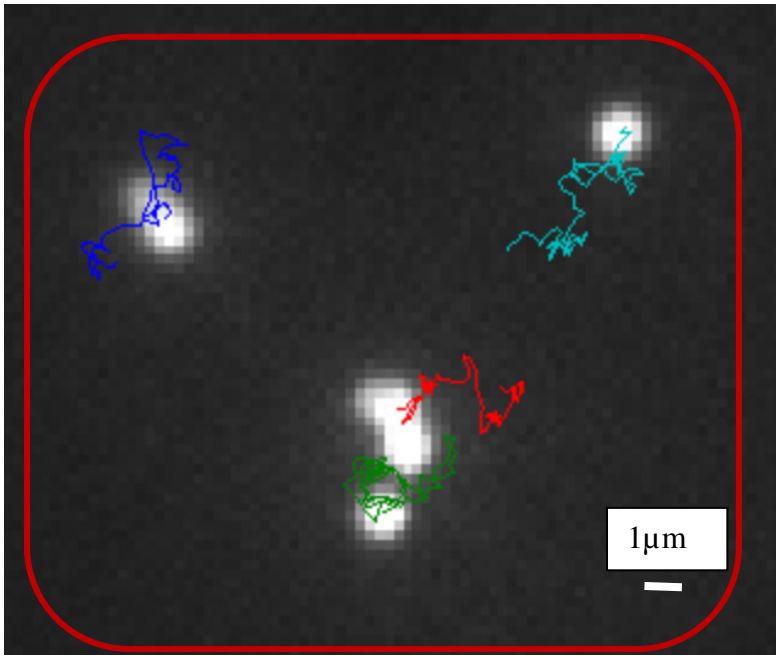


***Figure III-21**. Fluorescence picture of trapped 1µm beads imaged with a 60x water immersion objective with their trajectory overlaid for a 10 seconds recording. The trap edges are shown as a red full line.*

The analysis of these trajectories give insight into their degree of confinement: strongly confined particles will have their motion restricted to low electric potential energy regions and have a lower mean square displacement. The averaged mean square displacement can then be extracted from the trajectories shown in **Figure III-21** and compared to freely diffusing beads as shown in **Figure III-22**.

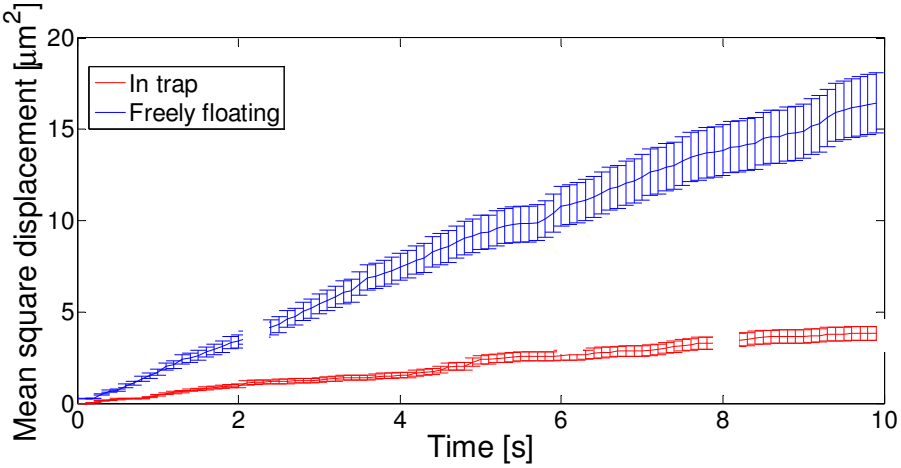


***Figure III-22**. Comparison between DEP restricted displacement under 3Vpp-20MHz (red curve) and freely floating bead (blue curve). The curves represent the average for 4 beads as shown in **Figure III.21**.*

It is seen that diffusion within an nDEP trap is much slower than in solution with a mean square displacement of 3.79µm^2 after 10 seconds compared to 16.44µm^2 in solution. The diffusion coefficients extracted from ***Eq. III-13*** are 4.1.10^{-9}cm^2/s and 0.9.10^{-9}cm^2/s for feely diffusing and trapped beads respectively. The theoretical diffusion value for these spheres from ***Eq. III-12*** is 4.4.10^{-9}cm^2/s which is consistent with the observed experimental value.

The overall recorded intensity of these spheres depends on their remoteness to the excitation volume. Therefore intensity gives information on vertical confinement. **Figure III-23** shows a snapshot of bead intensities as a function of voltage for the same set of beads in the same trap.

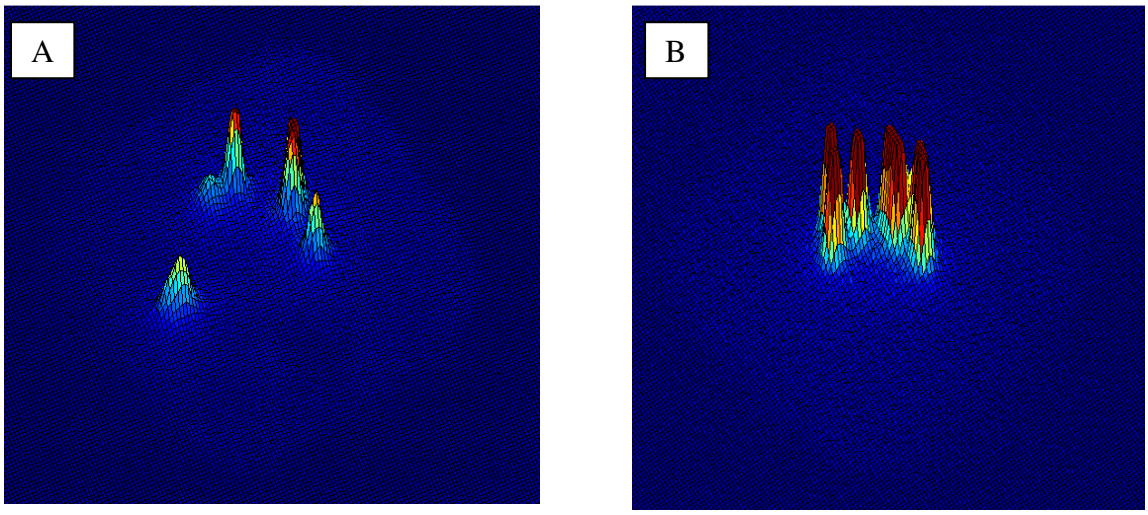


Figure III-23*. Snapshot of trapped bead fluorescence intensity seen as 3D Gaussian peaks as a function of applied voltage at a constant frequency of 20MHz.* ***A*** *for 3Vpp and* ***B****. for 6Vpp*

The fluorescence signal is gradually increasing with the voltage applied. Qualitatively, beads get closer to the surface and they cover a smaller surface due to lateral DEP forces. The bead tracking process becomes difficult due to overlap of the fluorescent signals from a confined area.

The ability to keep particles in close distance with the substrate is important in imaging applications using objectives of high numerical apertures and therefore short working distances. It is a crucial parameter for high-resolution acquisitions.

III.5. Single cell trapping

The ability to trap single cells is important for subsequent analyses. Here we evaluated the influence of voltage and cell density on cell trapping.

III.5.1. Influence of trapping voltage

To assess the trapping capability of square traps, open reservoirs made of PDMS arranged in an array format were fabricated to easily inject large quantities of cells. The schematic of the 'DEP titerplate' chip is shown in **Figure III-24**. Here the trapping array had 7 x 18 traps.

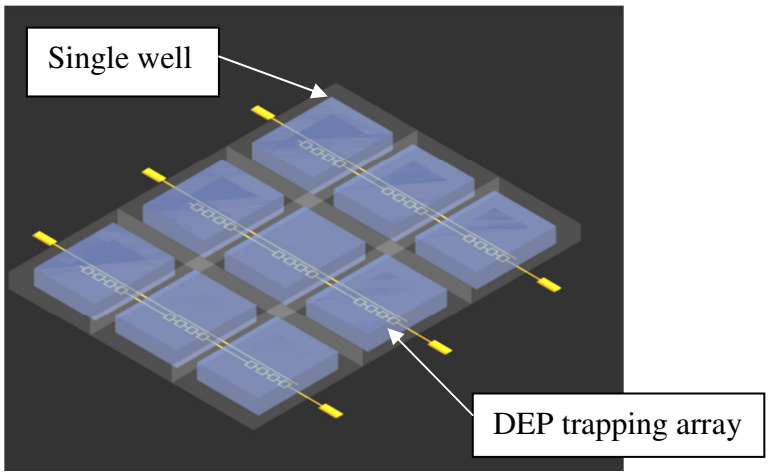


***Figure III-24**. DEP titerplate for assessing single cell trapping capabilities for a given electrode geometry.*

Next, a 100µL solution of Jurkat cells at a density of 500000 cells/mL was pipetted on top of a trapping array. The electrical signal was subsequently applied keeping a fixed frequency of 1MHz. **Figure III-25** represents the frequencies for which traps contain 0, 1 or 2 or more cells after 15 minutes incubation.

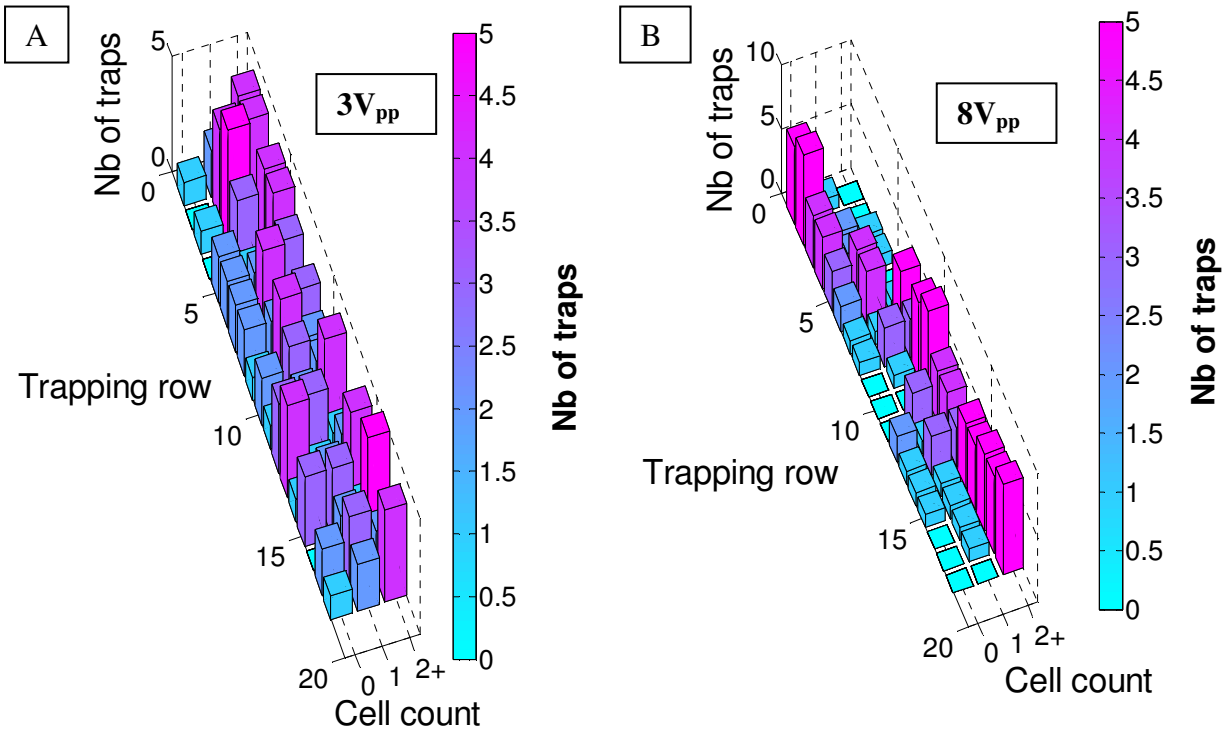


***Figure III-25**. Number of traps having 0, 1 or more than 2 cells trapped depending on trapping voltage. **A**. at 3Vpp **B**. at 8Vpp.*

It was found that voltage merely affects the number of cells trapped unless it is too low to trap cells; this is because cells are not excluded from falling into the potential wells defined by each trap. Being vertically repelled by nDEP, cells are moving above the trapping array until they fall in a potential well. In turn, the probability of a trap having a single cell was not found dependent on voltage in the range 3-6Vpp. In **Figure III-25**, at 3Vpp, the distribution of cells is seen quite homogeneous over the trapping area. However, at 8Vpp, the pattern is less symmetric with many cells trapped at the bottom of the array. This is due to a bulk convective flow driving more cells towards the bottom and therefore increasing the chances of cells reaching a local potential minimum.

III.5.2. Influence of cell density

Cell density was varied between 4.10^4 cells/mL and 5.10^5 cells/mL. Density was measured by using a cell counting haemocytometer. The same experiment was performed as described in

the previous paragraph. **Figure III-26** shows snapshots of the trapping array using various densities of Jurkat cells.

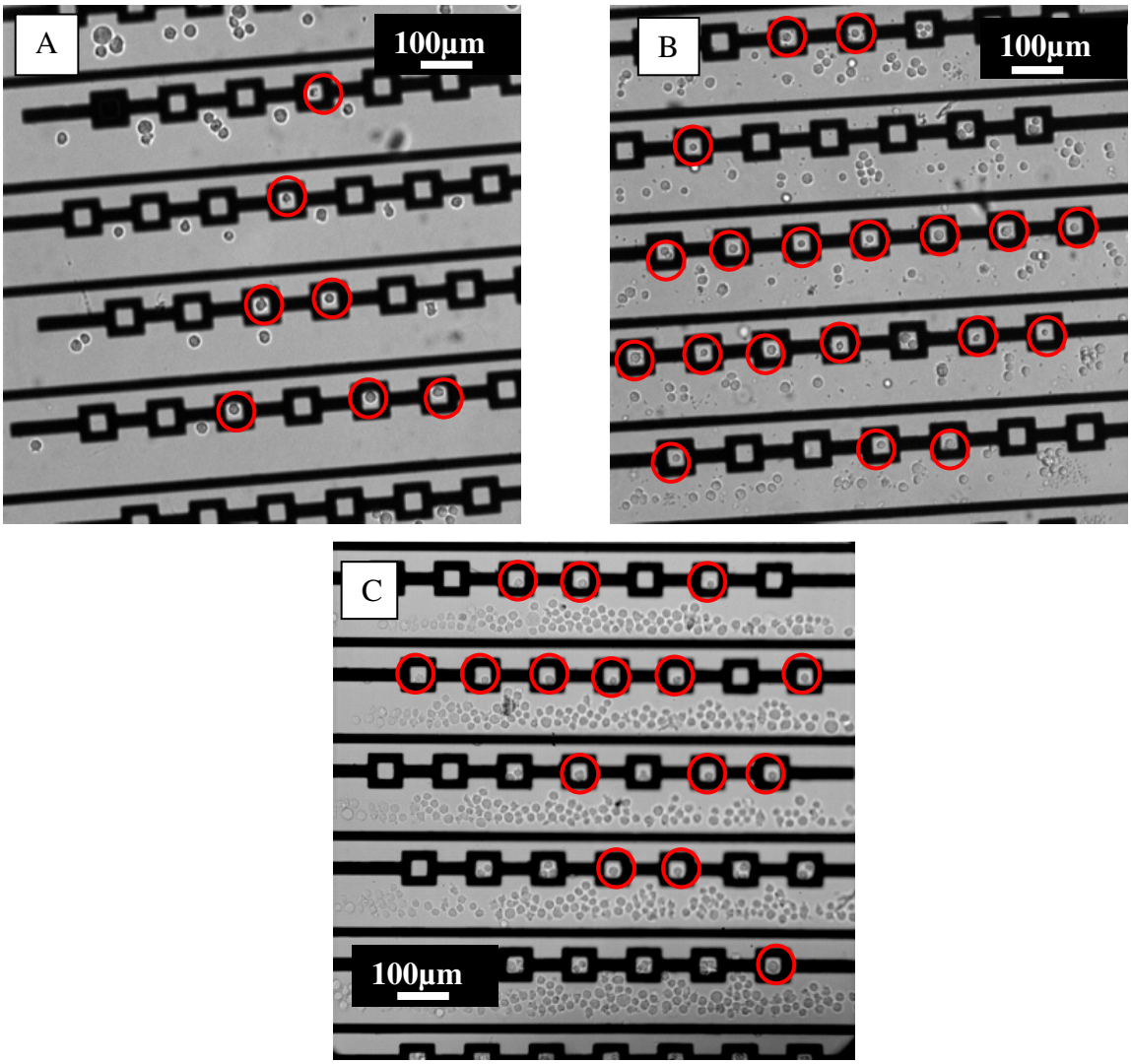


***Figure III-26**. Snapshots showing trapped cells at different cell density. A. 4.10^4 cells/mL, B. 8.10^4 cells/mL and C. 5.10^5 cells/mL. Red circles indicate single cells.*

At a concentration of 4.10^4 cells/mL, traps are mostly empty due to the random dispersion of cells over the substrate. At 8.10^4 cells/mL and above, the trapping area is statistically covered by cells and most traps have 1 or more cells. By counting the number of traps with single cells, the density dependent capture of single cells can be plotted as in **Figure III-27**.

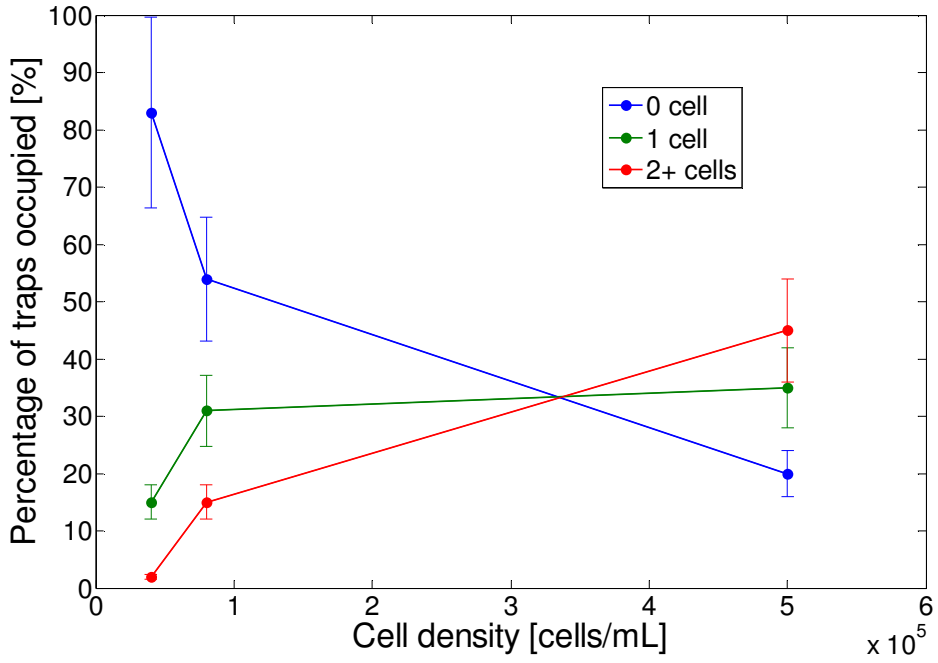


***Figure III-27**. Cell trapping capability as a function of cell density.*

The probabilistic trapping behaviour shows that high cell densities are not required to achieve high single-cell trapping efficiency (> 30 %) above a certain density threshold (here around 8.10^4 cells/mL). However, this is true only for a density of square traps comparable to **Figure III-26**.

When working in microchannels, the small volume over the capture zone implies cell density has to be scaled up. A typical volume for a microchannel of 100µm height x 1mm width x 10mm length is 1µL. Consequently, at a density of 8.10^4cells/mL, only 80 cells will be available for capture. The equivalent density of cells for maximizing single cell trapping based on **Figure III-27** is therefore 8.10^7cells/mL. This is clearly a limiting factor for cells in limited availability and these with slow division cycles. The delivery of single cells towards DEP traps can be improved via the introduction of microstructures to direct flows towards traps or the use of other tools such as micropipetting.[31, 32]

III.6. Resistance to flows for trapped particles

The ability to assay single cells relies on their stability inside DEP traps. Here we studied the holding strength of PS beads as a function of voltage as shown in **Figure III-28**. Beads were trapped by incubating the surface at a high concentration of particles. Subsequently, the electric field at constant frequency 10MHz and high amplitude (10Vpp) was turned on. The flow rate was set at a constant value. After waiting for the flow to be steady, the voltage was decreased by steps of $1V_{pp}$. The threshold voltage for which particles escaped was recorded as the holding force. The $1V_{pp}$ step is sufficiently big that most beads trapped in different square traps would escape for that same threshold. Flow velocities close to the trapped particles were calculated from the velocity of freely floating particles from recorded movies.

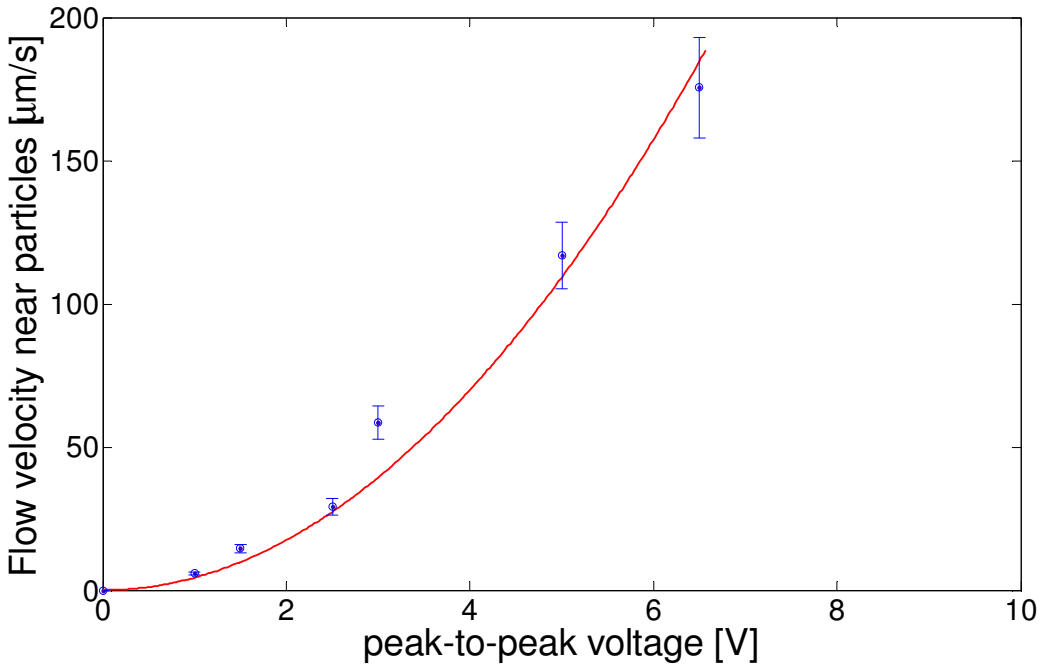


***Figure III-28**. Holding force as a function of flow velocity near a trapped PS bead. The red line shows the quadratic fit associated.*

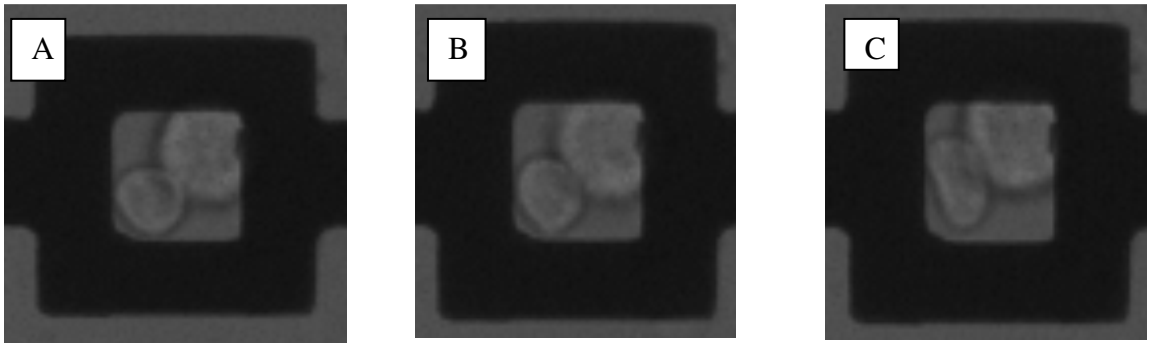
While the drag force increases linearly with the flow velocity, the DEP force increases in a quadratic manner with the applied voltage which therefore dominates the overall response. The function form of the fit in **Figure III-28** was $y=A.v^2$, with A close to 4.37 ($R^2=0.98$). This quadratic relationship confirms that particles are held by DEP forces. The values of flow rates they can sustain are in the order of 100µm/s; this translates into an average linear

velocity of 350µm/s in a 100µm deep channel. In practice, the flows were initiated thanks to a micro-pump operating around 1µL/min with a corresponding linear average velocity of 166µm/s.

This calibration test is difficult to transpose to cells which tend to experience contacting forces with the glass substrate and therefore do not escape traps easily. However, this gives a good indication of the strength needed to sustain typical micro-flows.

III.7. Cell viability in permanent electric fields

The artificial environment created by the use of electric fields constitutes a threat to cell viability. For instance, the orientation of cell division has been found dependent on small direct-current electric fields.[33] Additionally, low-intensity electric fields have the ability to disrupt the division of cancer cells and slow the growth of tumors.[34] By contrast, the growth and division of yeast cells above micro-electrodes has been demonstrated higher than in bulk cultures.[35] Here we examined the effect of a permanent AC electric field on Jurkat cell division. A constant AC field of 6Vpp-1MHz was applied to a solution containing Jurkat cell in culture medium. Continuous bright-field recording of a trapping array was done throughout 2 days. The interval between two snapshots was 2 minutes. The division of a cell could be observed in one of the DEP trap as shown in **Figure III-29.**



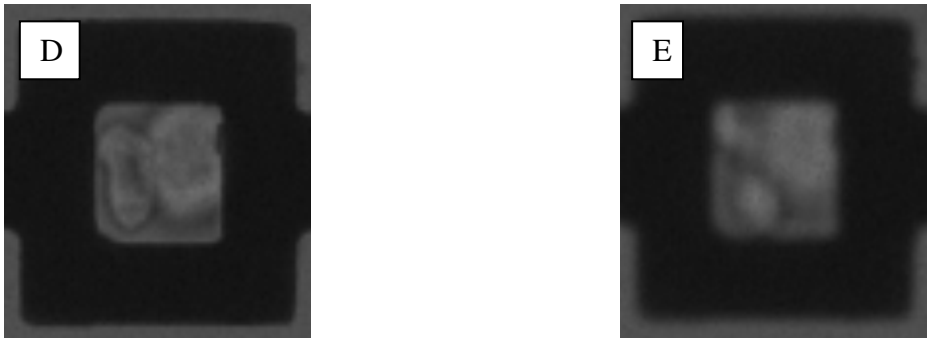


***Figure III-29**. Snapshots of 2 trapped Jurkat cells, one of them undergoing division. The five snapshots correspond to different times: **A**. initially, **B**. after 14min, **C**. after 24min, **D**. after 30min and **E**. after 36min.*

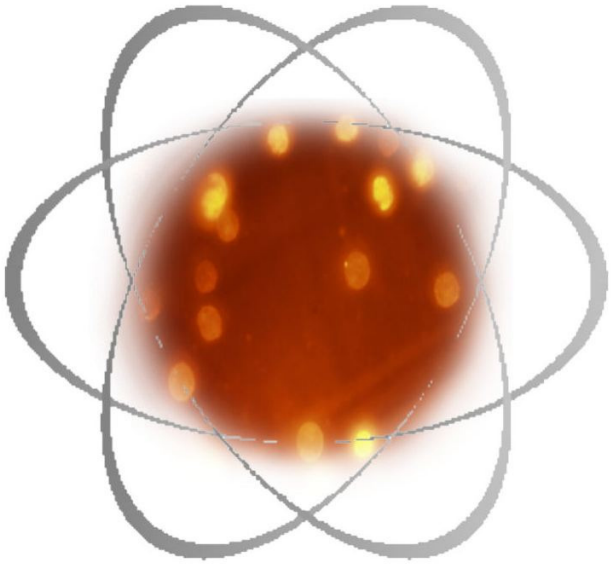
The cell shown in **Figure III-29** had been exposed to the electric fields for 120 minutes prior to division showing long-term survival. This highlights Jurkat cells can survive and divide when cultured under a permanent 1MHz AC field in nDEP traps. To confirm full integrity, a more thorough investigation of other cell functions such as protein expression should be performed.

III.8. References

(1) Pohl, H. A.; Crane, J. S. *Biophysical Journal* **1971**, *11*, 711-&.
(2) Kang, Y. J.; Li, D. Q.; Kalams, S. A.; Eid, J. E. *Biomedical Microdevices* **2008**, *10*, 243-249.
(3) Tabeling, P., Introduction to Microfluidics, *Oxford University Press* **2005**.
(4) Albrecht, D. R.; Sah, R. L.; Bhatia, S. N. *Biophysical Journal* **2004**, *87*, 2131-2147.
(5) Thomas, R. S.; Morgan, H.; Green, N. G. *Lab on a Chip* **2009**, *9*, 1534-1540.
(6) Chuang, C. H.; Lee, Y. C.; Huang, H. S.; Hsiao, F. B.; Hsu, Y. M.; Wang, K. H.; Dinj, L.; Hsu, H. J., Zhuhai, People's Rep. of China, Jan 18-21 2006; Ieee; 1207-1210.
(7) Suehiro, J.; Pethig, R. *Journal of Physics D-Applied Physics* **1998**, *31*, 3298-3305.
(8) Chiou, P. Y.; Ohta, A. T.; Wu, M. C. *Nature* **2005**, *436*, 370-372.
(9) Heida, T.; Rutten, W. L. C.; Marani, E. *Journal of Physics D-Applied Physics* **2002**, *35*, 1592-1602.
(10) Cui, L.; Morgan, H. *Journal of Micromechanics and Microengineering* **2000**, *10*, 72-79.
(11) Ying, H.; Holzel, R.; Pethig, R.; Wang, X. B. *Physics in Medicine and Biology* **1992**, *37*, 1499-1517.
(12) Jones, T. B., Electromechanics of Particles, *Cambridge University Press* **1995**.
(13) Asami, K.; Takahashi, Y.; Takashima, S. *Biochimica Et Biophysica Acta* **1989**, *1010*, 49-55.
(14) Huang, Y.; Holzel, R.; Pethig, R.; Wang, X. B. *Physics in Medicine and Biology* **1992**, *37*, 1499-1517.
(15) Ermolina, I.; Morgan, H. *Journal of Colloid and Interface Science* **2005**, *285*, 419-428.
(16) Pethig, R. *Biomicrofluidics* **2010**, *4*, 35.
(17) Lin, R.-Z.; Ho, C.-T.; Liu, C.-H.; Chang, H.-Y. *Biotechnology Journal* **2006**, *1*, 949-957.
(18) Yang, J.; Huang, Y.; Wang, X. J.; Wang, X. B.; Becker, F. F.; Gascoyne, P. R. C. *Biophysical Journal* **1999**, *76*, 3307-3314.
(19) Li, H. B.; Bashir, R. *Sensors and Actuators B-Chemical* **2002**, *86*, 215-221.
(20) Sabuncu, A. C.; Liu, J. A.; Beebe, S. J.; Beskok, A. *Biomicrofluidics*, *4*, 7.
(21) Huang, Y.; Wang, X. B.; Becker, F. F.; Gascoyne, P. R. C. *Biophysical Journal* **1997**, *73*, 1118-1129.
(22) Li, H. B.; Zheng, Y. N.; Akin, D.; Bashir, R. *Journal of Microelectromechanical Systems* **2005**, *14*, 103-112.
(23) Jaggi, R. D.; Sandoz, R.; Effenhauser, C. S. *Microfluidics and Nanofluidics* **2007**, *3*, 47-53.
(24) Williams, P. S.; Koch, T.; Giddings, J. C. *Chemical Engineering Communications* **1992**, *111*, 121-147.
(25) Ramos, A.; Morgan, H.; Green, N. G.; Castellanos, A. *Journal of Physics D-Applied Physics* **1998**, *31*, 2338-2353.
(26) Green, N. G.; Ramos, A.; Gonzalez, A.; Morgan, H.; Castellanos, A. *Physical Review E* **2000**, *61*, 4011-4018.
(27) Stubbe, M.; Holtappels, M.; Gimsa, J. *Journal of Physics D-Applied Physics* **2007**, *40*, 6850-6856.
(28) Gielen, F.; deMello, A. J.; Cass, T.; Edel, J. B. *Journal of Physical Chemistry B* **2009**, *113*, 1493-1500.

(29) Rosenthal, A.; Voldman, J. *Biophysical Journal* **2005**, *88*, 2193-2205.
(30) Mittal, N.; Rosenthal, A.; Voldman, J. *Lab on a Chip* **2007**, *7*, 1146-1153.
(31) Skelley, A. M.; Kirak, O.; Suh, H.; Jaenisch, R.; Voldman, J. *Nature Methods* **2009**, *6*, 147-152.
(32) Di Carlo, D.; Wu, L. Y.; Lee, L. P. *Lab on a Chip* **2006**, *6*, 1445-1449.
(33) Zhao, M.; Forrester, J. V.; McCaig, C. D. *Proceedings of the National Academy of Sciences of the United States of America* **1999**, *96*, 4942-4946.
(34) Kirson, E. D.; Dbaly, V.; Tovarys, F.; Vymazal, J.; Soustiel, J. F.; Itzhaki, A.; Mordechovich, D.; Steinberg-Shapira, S.; Gurvich, Z.; Schneiderman, R.; Wasserman, Y.; Salzberg, M.; Ryffel, B.; Goldsher, D.; Dekel, E.; Palti, Y. *Proceedings of the National Academy of Sciences of the United States of America* **2007**, *104*, 10152-10157.
(35) Arnold, W. M.; Franich, N. R. *Current Applied Physics* **2006**, *6*, 371-374.

Chapter IV. Temperature mapping in nDEP traps



In this chapter, we examine the local modifications of temperature created by the electric fields needed to generate dielectrophoretic forces. The heat generation, due to current flows in conductive buffers, is first examined theoretically. Temperature mapping with submicron resolution using time-resolved spectroscopy is subsequently shown. The knowledge of temperature rise within traps is valuable to interpret experiments involving thermodynamics processes such as membrane dynamics.

IV.1. Introduction

Spatial and temporal temperature variations are a primary concern in many applications making use of electric fields such as electrophoresis[1, 2], electro-osmosis[3], electrochemotherapy[4] and dielectrophoresis[5] (DEP). For DEP, this is because planar microelectrodes create a temperature gradient within which the particle of interest is manipulated. For commonly used buffers such as Phosphate Buffered Saline (PBS) of conductivity 1.6S/m or Dulbecco's Modified Eagle Medium (DMEM) of conductivity 1.4S/m, Joule heating sets constraints on the operational range of the analytical device.

DEP trapping experiments for biological applications normally involves keeping particles or cells within electric fields for extended periods of time and knowledge of the temperature at or around the cell within a micro-fabricated DEP trap significantly impacts interpretation of experimental results. The consequences of temperature rise on DEP experiments relying on proteins, DNA, cellular functions or membrane dynamics have to be considered. In certain cases, temperatures above 40-45ºC will lead to a reduction in biological activity or denaturation and cell death.[6] The temperature at which membrane proteins unfold can be extracted via differential scanning calorimetry. As described in **Chapter I**, a lipid melting transition will be seen as a peak of heat capacity needed to keep the temperature of the membrane at the same temperature as the reference cell. **Figure IV-1** gives a typical heat capacity plot for the membrane of E.Coli. The high peaks above 60ºC indicate protein unfolding events have occurred.

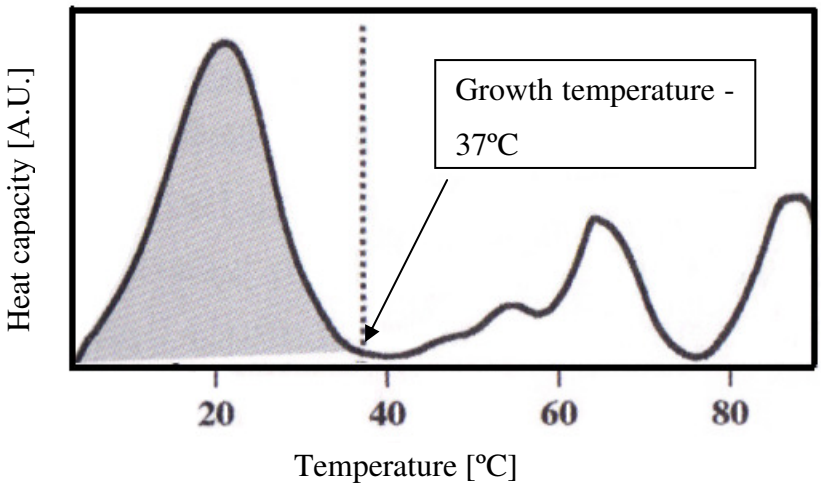


***Figure IV-1**. Heat capacity profile as a function of temperature for the membrane of E.Coli. The grey area corresponds to lipid melting and the peaks at 60ºC and above to protein denaturation events (adapted from [7]).*

As seen in **Figure IV-1**, the membrane is mostly fluid at temperatures lower than the growth temperature. Importantly, cells will try to keep membrane fluidity by adapting membrane composition to growth environment. Other peaks seen above 60ºC correspond to protein denaturation events. At these temperatures, cells lose most of their functions.

Joule heating may be circumvented by using low-conductivity media such as isotonic sucrose buffers.[8, 9] However, in this case, DEP forces turn positive for mammalian cells making them migrate towards high electric field regions where they experience risks of charging and other electrochemical damage unless insulated from electrodes (e.g. by a permeation layer). Furthermore, the practicality of using high-conductivity physiological buffer should not be neglected.

The essential question for microfabricated DEP traps is whether temperature rises can be accurately quantified.

IV.2. Theory

IV.2.1. Heating with planar micro-electrodes

The temperature in a DEP trap can be described by the balance between power generation and dissipation and can be written as follows:[10]

$$\rho_m c_p v \nabla T + \rho_m c_p \frac{\partial T}{\partial t} = k \nabla^2 T + \sigma E^2 \qquad \textit{Eq. IV-1}$$

Here, T is the absolute temperature, E the norm of the electric field, c_p is the specific heat at constant pressure, k the fluid thermal conductivity, v the velocity, ρ_m the density, σ is the electrical conductivity of the medium. As the electrical conductivity of the buffer increases with temperature, additional coupling of *Eq. IV-1* and ***Eq. IV-2*** must be taken into account. This can be expressed as:

$$\sigma = \sigma_0 [1 + \alpha (T - T_0)] \qquad \textit{Eq. IV-2}$$

Here α is the temperature compensation factor of the buffer. For water, this value is 1.8%/ºC.[11] As has been shown by Ramos *et al.*, in a typical interdigitated electrode geometry, with a 20µm electrode gap, the order of magnitude of the temperature rise can be estimated using dimensional analysis of**Eq. IV.1**.[12]

$$\Delta T \approx \frac{\sigma V_{rms}^{\ 2}}{k} \qquad \textit{Eq. IV-3}$$

Here V_{rms} is the root-mean-square potential difference across the electrodes. There are several limitations to validating this estimate, especially the omission of geometry-related parameters. Indeed, the complexity of geometries inherent to DEP traps implies actual electric fields differ from the analytical voltage-to-distance ratio. Poor control over boundary conditions has also been recognized.[13]

Factors that contribute to misestimating temperature include variations in electrical resistance (also varying through the temperature coefficient of resistance) and roughness of the metal electrodes. Heat diffusion in the electrodes is also neglected in ***Eq. IV-3***.[4]

In general, ***Eq. IV-3*** typically gives an upper limit estimate of the temperature rise within the microfluidic chip. The analytical solving of temperature rise in a parallel plate geometry indicates a temperature rise 8 times smaller than ***Eq. IV-3***.[12] There are many parameters contributing to heat sinking that can be modeled but are hard to theoretically estimate. Williams *et al.* introduced a correction factor for the voltage in order to simulate field losses.[14] Furthermore, this correction factor increases with buffer conductivity. In practice, V_{rms} has to be replaced by an effective voltage making up the physical treatment of the system.

IV.3. Calibration

The dye rhodamine B has been found to have a fluorescence lifetime strongly dependent on temperature.[15] In order to use this dye as a temperature probe, a calibration step must be performed. Although local temperature values can be accurately determined in certain temperature ranges with lifetime spectroscopy using polymers[16], the wide dynamic range exhibited by rhodamine B makes it especially useful for detecting large temperature changes.

Calibration was done using a Peltier element having an active cooling fan. Briefly, a microfluidic chamber made up of two fused silica glass slides separated approximately by a 3mm spacer was built and fixed on top of the Peltier effect heat pump (RS, UK). A first K type thermocouple probe was linked to the surface of the Peltier while a second one was placed within the built chamber and recorded the actual fluid temperature. A few tens of micro-liters of a solution of 100µM rhodamine B in PBS 1x was pipetted from one side of the chamber, immersing the inner thermocouple. A photograph of the actual calibration setup is shown in **Figure IV-2**.

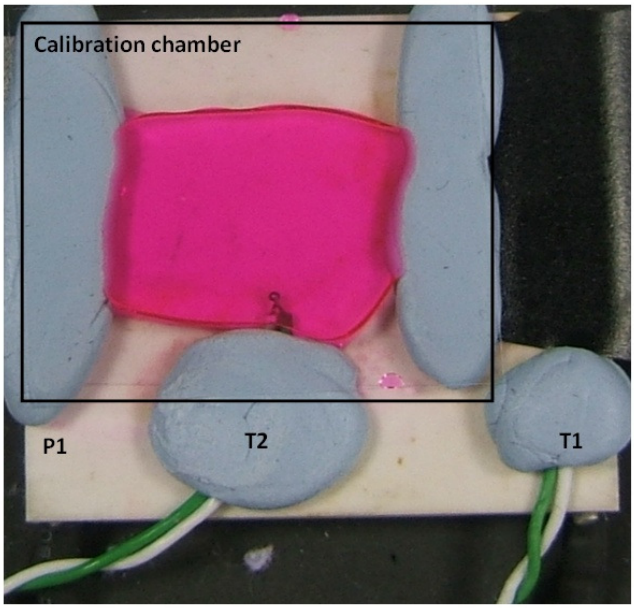


***Figure IV-2**. Schematic of the calibration chamber with a rhodamine B solution. P1.Peltier element, T1 and T2 are thermocouples linked to Peltier and calibration solution respectively.*

The chamber was placed on top of a 20x air objective to avoid heat transfer to the objective. A schematic of the experimental setup is drawn in **Figure IV-3**.

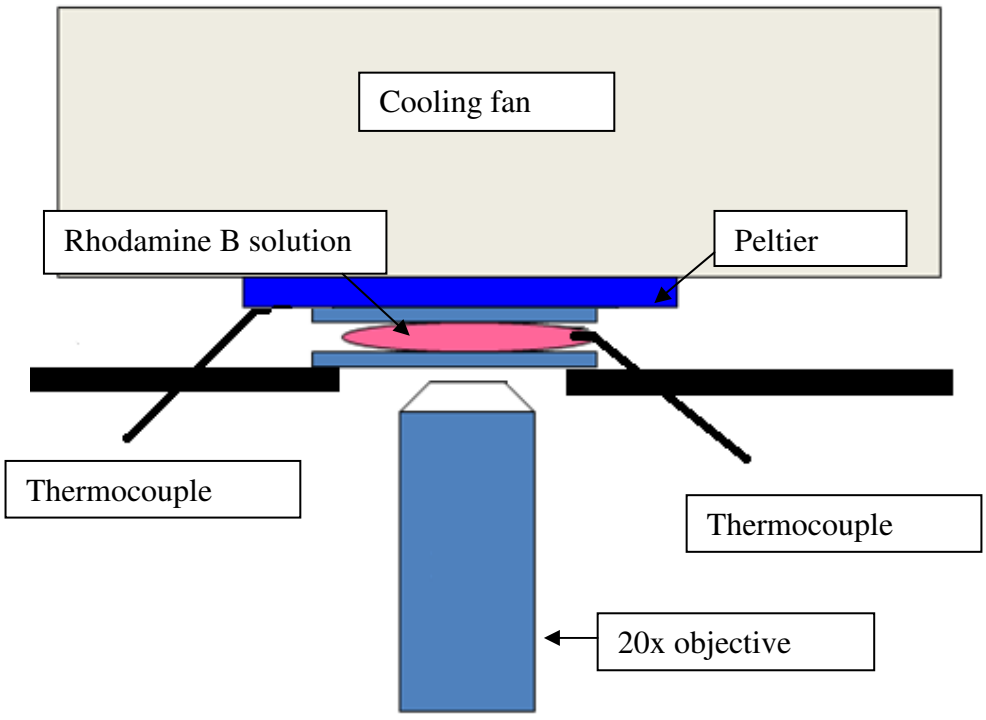


***Figure IV-3**. Schematic of the calibration setup.*

The Peltier was subsequently ramped from room temperature up to 90 degrees and the intensity and fluorescence lifetime of a 100µM rhodamine B solution in PBS monitored in real-time.

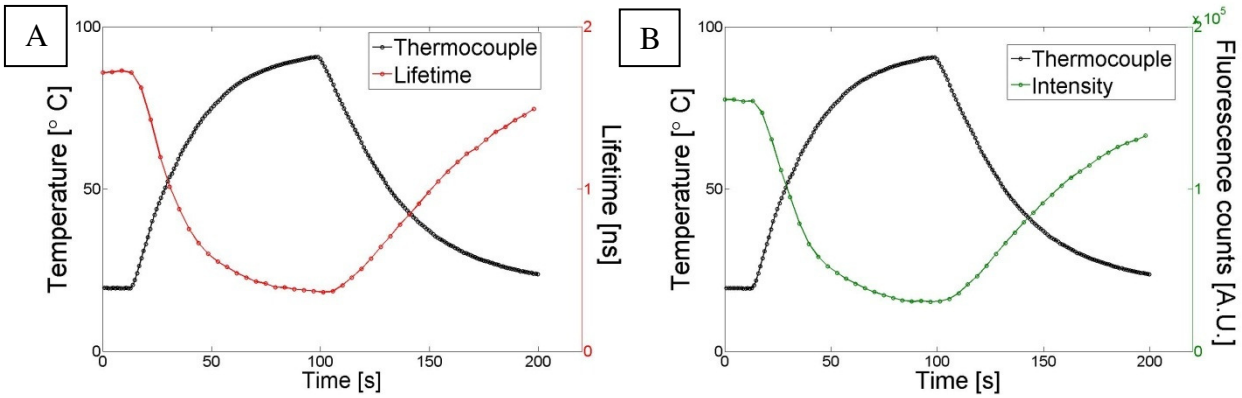


***Figure IV-4**. Recorded lifetime (A) and temperature (B) as a function of time for a temperature ramp from RT to 90 degrees C.*

As seen in **Figure IV-4**, the fluorescence lifetime of rhodamine B responds to a temperature step with lifetime falling from 1.6ns at room temperature (19.9 ºC) down to 0.3ns at 90 ºC. We fitted both temperature data from the thermocouple and lifetime data with exponential fits. The functional form was $y=Ae^{-Bx}+C$. The fitting parameters are shown in **Table IV.1**.

Fitting parameter	Temperature from thermocouple	Average fluorescence lifetime
A	-127.2ºC	2.34ns
B	$0.037s^{-1}$	$0.025s^{-1}$
C	94.4ºC	0.43ns

***Table IV.1**. Fitting parameters for temperature and lifetime calibration measurements.*

This allowed extracting lifetime as a function of temperature. **Figure IV-5** is a calibration plot for rhodamine B in terms of its fluorescence lifetime and normalized intensity.

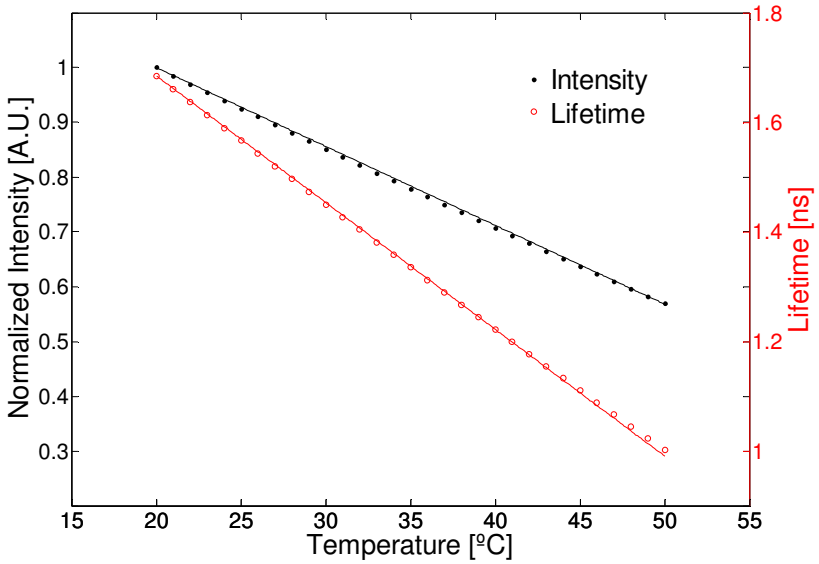


***Figure IV-5**. Calibration plot for measuring temperature with rhodamine B: intensity and fluorescence lifetime decay with temperature at a rate 1.12%/°C and 1.07 %/°C respectively.*

Linear fits of the intensity and lifetime calibration data yield a decrease of 1.12 %/ºC and 1.07 %/ºC respectively. The fast temperature ramp applied to the rhodamine B solution is believed to minimize photo-physical damage to the dye and may explain the difference from exponential decay data published previously.[17] Furthermore, these decay rates correspond well to previously published values. [5]

The extraction of the values for absolute temperature from intensity measurements remain limited by photo-physical effects induced by heating. In particular, the fluorescence intensity might not fully recover after a thermal cycle.[18] That is why relative measurements, recording either intensity changes are more accurate. Although lifetime measurements require more data for statistical treatment, they can be used without standard using absolute values.

The concentration of rhodamine B in PBS used in the calibration and for further temperature mapping measurements was fairly high (100µM). Temperature mapping using a similar high concentration has already been published several times.[15, 19] The practically of using high concentrations is that laser powers can be reduced significantly and pile-up effects avoided. The fluctuation of dyes in the confocal volume can be minimized using high concentrations but unwanted photo-physical effects can lead to a high degree of fluctuation for quantification purposes. On the other hand, lifetime imaging is insensitive to these artefacts.

We found that 100µM gives a good linear dynamic range for lifetime-temperature calibration, which is essential for accurate temperature imaging.

IV.4. High-resolution temperature mapping

Mapping temperature with high spatial resolution cannot be achieved using integrated thermocouple probes[20] whose size and fabrication restrict their use to indirect measurement of average temperature. Seger *et al*[5] have described the heat dissipation of a negative DEP barrier and the temperature gradient at the vicinity of electrodes using fluorescence detection but with limited spatial resolution. Non-invasive fluorescent techniques, such as intensity-based measurements have been found to give good estimates of average temperature within a microchannel but are very sensitive to well-known artefacts including a dependency on dye concentration and detection efficiency.[21] On the other hand, the use of fluorescence lifetime imaging allows artefact-free measurements of excited state decay times which conveys information on the local fluorophore environment.[15, 19] This latter technique is the one we applied to map heat distribution in a high conductivity buffer.

IV.4.1. Setup

A schematic of the fluidic chamber and 1 x 4 trap array used in this study is shown in **Figure IV-6A**. The PDMS chamber had a width of 1mm and a depth of 30µm. **Figure IV-6B** is a bright field image of a single electrode trap using an Olympus BX51 upright microscope equipped with a 20x objective.

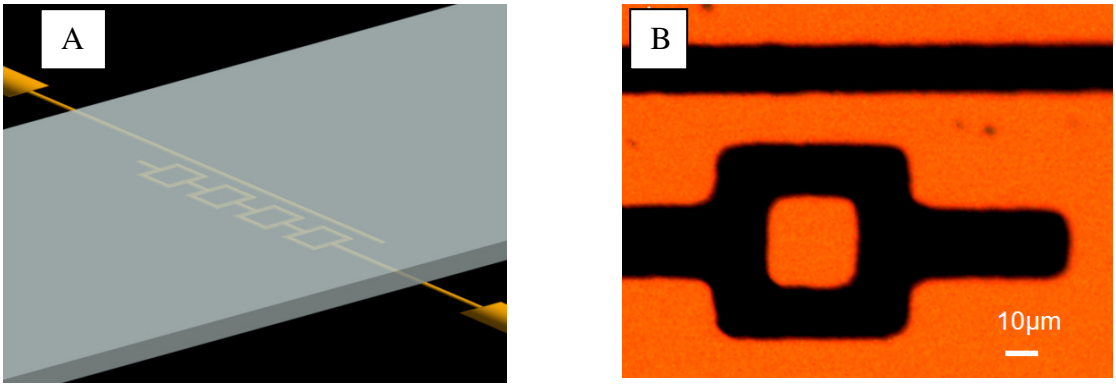


***Figure IV-6**. **A**. Schematic of the microfluidic device including gold electrodes patterned on glass and the fluidic chamber; **B**. bright field picture of a single nDEP trap.*

IV.4.2. Spatial distribution of heat

The temperature distribution is not uniform within the encapsulated solution because of the localized application of current. To grasp the physical extension of the temperature rise, we acquired fluorescence lifetime maps over an area of 1200µm x 1200µm with a 10x objective. **Figure IV-7**shows a lifetime map over electrodes energized at $5V_{pp}$-1MHz. The heat is seen as a yellow region diffusing from the centre until it gets more uniform away from the high electric field region.

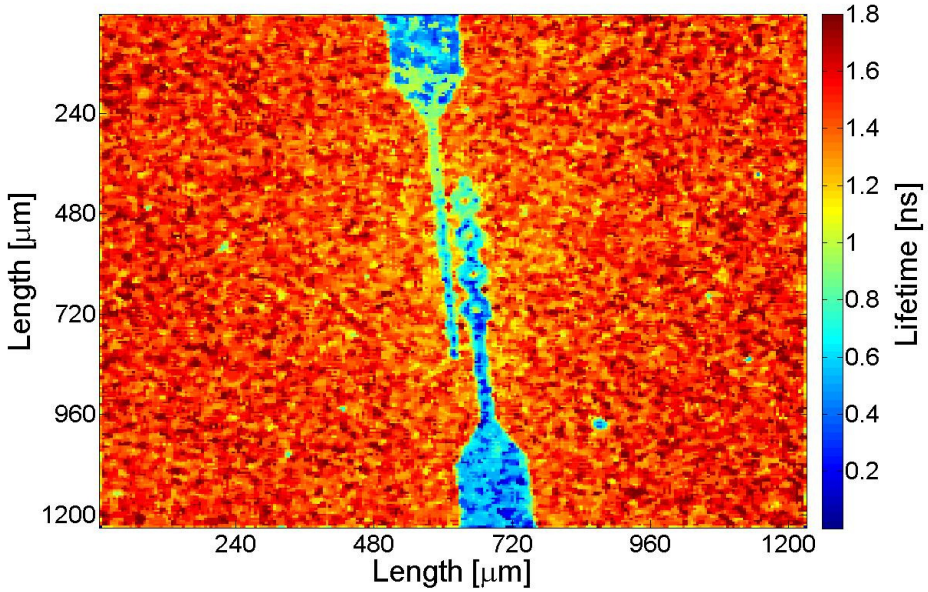


***Figure IV-7**. Lifetime map over electrodes energized at $5V_{pp}$-1MHz.*

Scattering and low photon collection over the electrodes make them appear with a very low lifetime around 0.4ns; however, this does not correspond to a real temperature change. The average temperature profile over the electrodes can be reconstructed by taking the average lifetime per column in **Figure IV-7**. This can be subsequently compared to the temperature profile in the absence of electric field as shown in **Figure IV-8**.

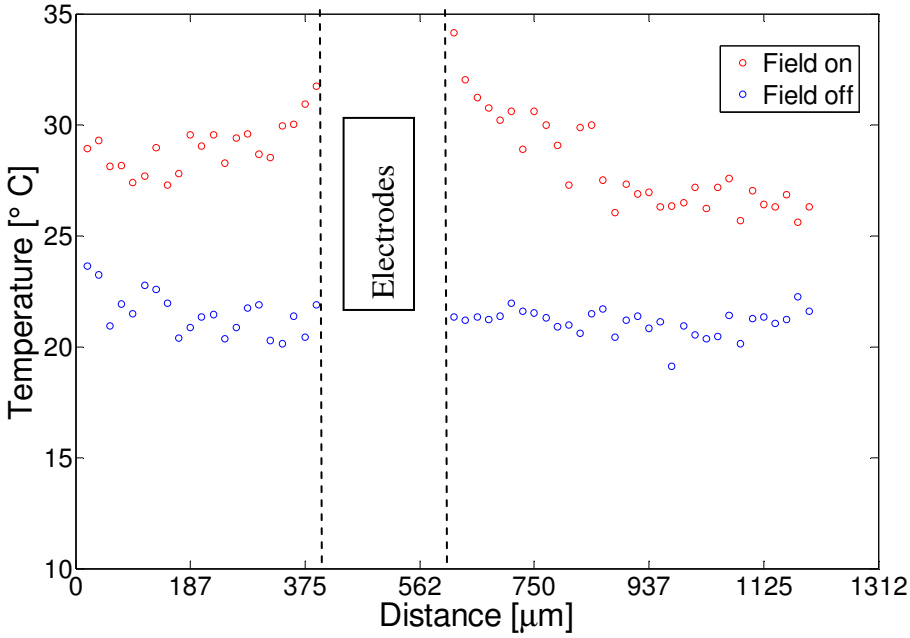


***Figure IV-8**. Reconstituted heat profiles at the vicinity of the microelectrodes in the presence and absence of field.*

The temperature is seen sharply increasing over the trapping area making extrapolation of the actual temperature difficult. This high gradient in temperature has been reported using Intensity-based measurements in an nDEP sorter.[5] The temperature change extends up to millimeters inside the microchannel, which means it will affect most of the microchip. The types of measurements shown in **Figure IV-7** justifies the need for a high resolution mapping of temperature within a DEP trap as it cannot be extrapolated from low resolution maps.

IV.4.3. Transient temperature rise and cooling of the microsystem

We studied the transient temperature change after the application of a voltage step and on switching off the electric field. Specifically, fluorescence intensity pictures of the DEP trap were acquired continuously at a focal plane of 5 microns above the glass surface before the

application of electric fields and well after it had been turned off. The variations in average intensity were recorded on a frame-by frame basis and can be plotted as a temperature variation over time (**Figure IV-9**). The electric fields were switched off 28 seconds after application of the fields. Exponential fits in **Figure IV-9** are displayed simply as visual aids.

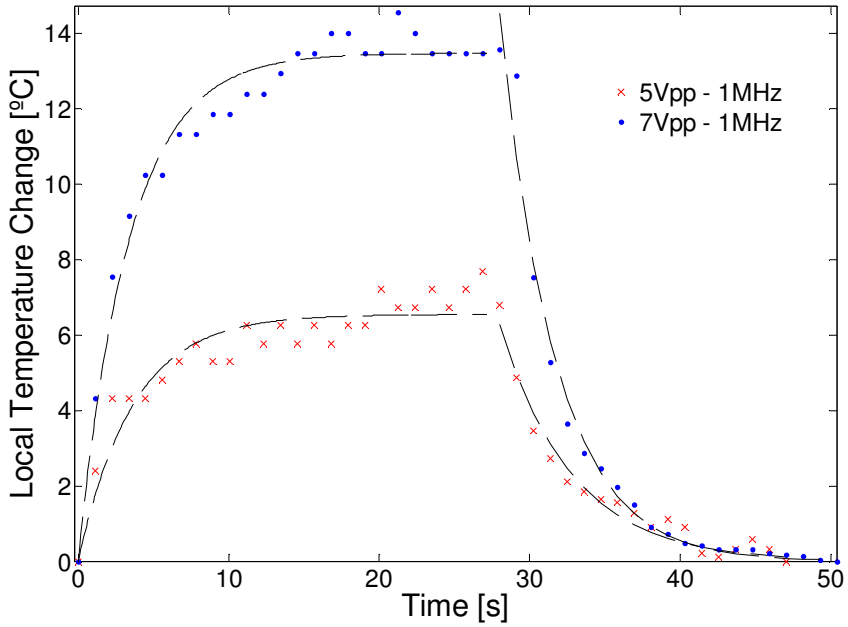


***Figure IV-9**. Transient increase in temperature upon a voltage step. The focal plane was adjusted at 5 µm above the surface of the device.*

The steady-state temperature rises within the system were found to be 6.5ºC and 13.5ºC and the characteristic heating time based on single exponential fits constant τ_h was 3.5 seconds and 3.3 seconds for applied voltages of $5V_{pp}$ and $7V_{pp}$ respectively at a fixed frequency of 1MHz. It can be seen that steady-state was reached within approximately 10 seconds. Interestingly, the steady-state temperature is reached long after the thermal equilibrium resulting from the diffusion of the temperature front which has a theoretical value of 1ms.[12] Cooling of the trapping area surrounding the electrodes has been studied the same way. The characteristic cooling time constant τ_c of the system was 4.8 seconds and 3.7 seconds for applied voltages of $5V_{pp}$ and $7V_{pp}$ respectively. The dissipation is mainly happening via conduction to the substrate and that is why heat dissipation can be improved by using a substrate of higher thermal conductivity. As shown by Ramos *et al*[12], these types of microelectrode structures cannot be easily cooled down by fluid injection: even at high flow rates, the temperature profile is preserved. This has been tested experimentally at average in-

channel velocities of up to 0.5mm/s although this exceeds typical holding strength of DEP traps. Flow cooling is ultimately limited by the Poiseuille flow profile within a microchannel where surface flow velocities are very low.

IV.4.4. Temperature map from intensity

For microfluidic devices that incorporate electrodes, the presence of metal complicates fluorescence-based experiments. For instance, the fluorescence of gold under UV-Vis wavelengths limits its use with competitive fluorescence studies although it has many direct applications.[22] In particular, although the fluorescence decay can be composed of several independent components, it is preferable to have a single route to decay (i.e. a mono-exponential decay law). Scattering effects as well as the adsorption of molecules on a surface at high-concentrations also restrict the use of non-confocal fluorescence setups.[23] To circumvent these drawbacks, specific imaging of the area of interest has to be performed with maximum resolution.

Here, temperature mapping of a DEP trap with a captured polystyrene sphere was performed at steady-state. Here we used $7V_{pp}$ and a frequency of 1MHz. Focusing was performed by finding the maximum auto-fluorescence level of the gold electrodes and moving the objective 5µm above that level. The polystyrene beads absorb the excitation radiation and therefore appear as low count regions in the intensity map. The data processing was done as follows.

The raw photon counts collected with electric field turned off was acquired from the Avalanche PhotoDiode (**Figure IV-10A**). It was then thresholded to remove parts of the pictures with low counts or where the bead had moved (here 40 counts/pixel is chosen from the intensity distribution histogram) (**Figure IV-10B**). Eventually, a median filter of size 5x5 was applied to reduce statistical noise (**Figure IV-10C**). The same data treatment was done for the field 'on' case and the latter one was divided by the former map to obtain the relative pixel by pixel variation in intensity (**Figure IV-10D**).

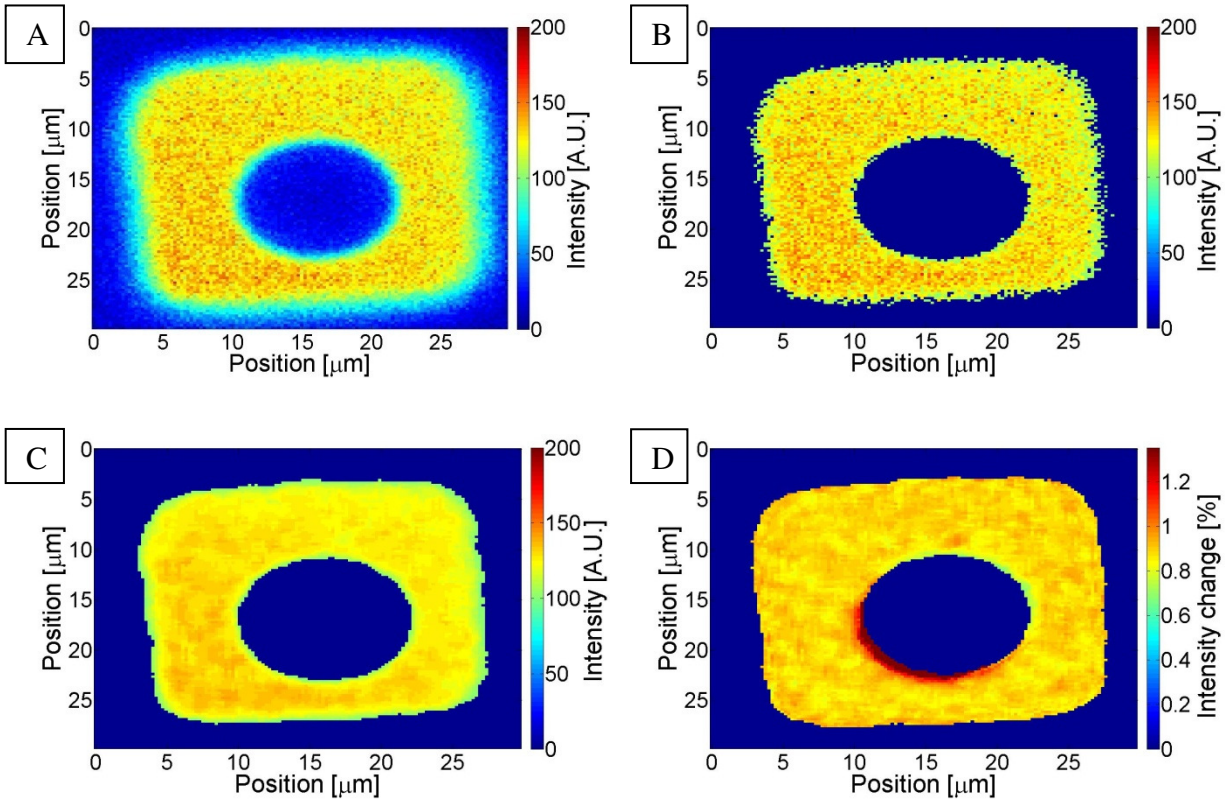


***Figure IV-10**. Data treatment to obtain temperature variation from intensity measurements. **A**. raw data **B.** after thresholding **C.** after applying the median filter **D.** after division of intensity maps 'on'/'off'.*

In **Figure IV-10**, the second line electrode was located at the bottom of the trap. **Figure IV-11** shows the temperature map derived from intensity change for the same DEP trap. Because of the repulsion of the bead from high-electric fields regions, the analysis of fluorescence intensity is limited to areas where the bead is not present.

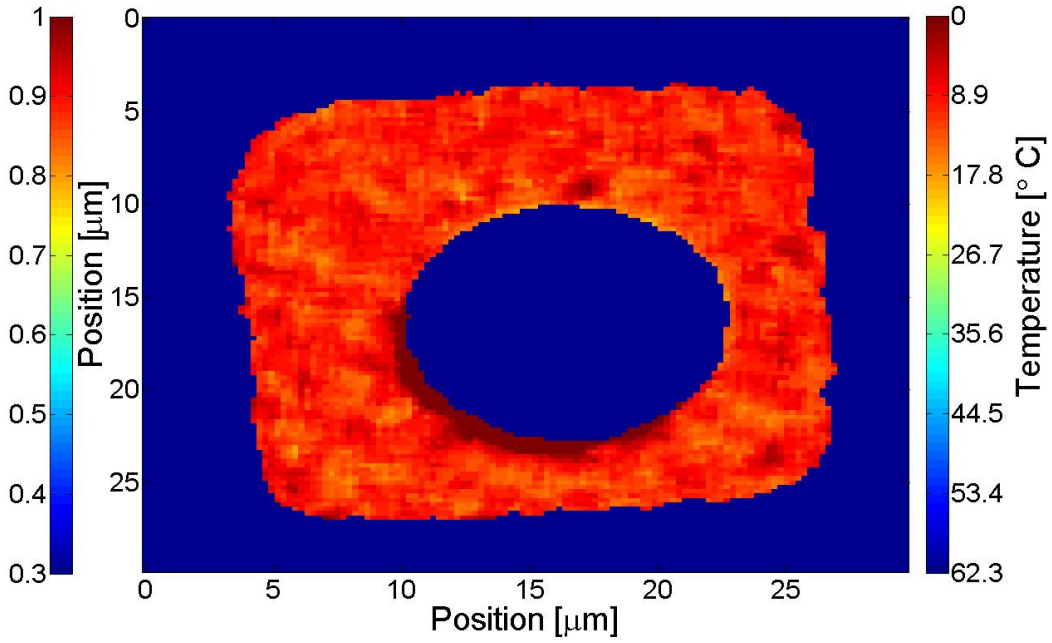
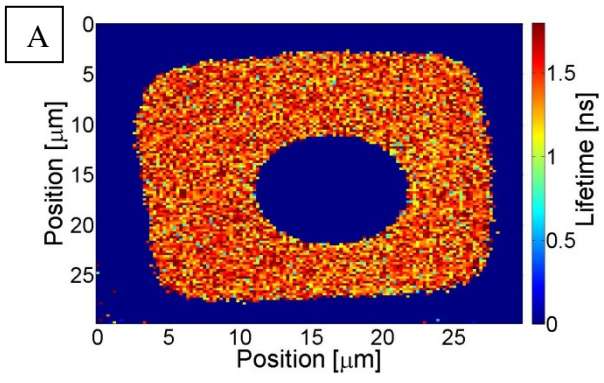


***Figure IV-11**. Temperature map from intensity measurements.*

The temperature is seen fairly homogeneous with regions at the bead interface with poor estimate. Edge effects are clearly limiting the spatial extent of such plots.

IV.4.5. Temperature map from FLIM

For the FLIM mapping, pixels having at least 40 counts were analyzed to get accurate lifetime decay fits. The fitted lifetime was plotted directly after applying the same 5x5 median filter. The FLIM map when the field is on is plotted as relative temperature variation based on absolute lifetime measurement data. **Figure IV-12** illustrates the raw lifetime map and corresponding temperature map obtained from FLIM measurements.



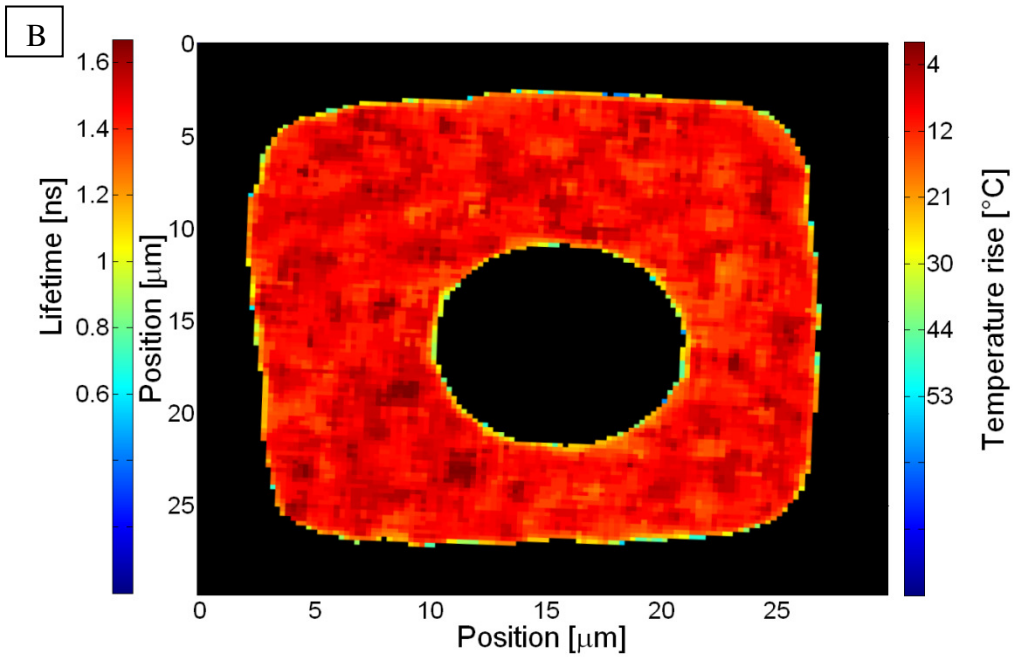


***Figure IV-12**. FLIM pictures before (**A**) and after (**B**) applying the median filter of size 5x5 and converting lifetime to temperature rise.*

Because of rejection of light from the surface via the confocal pinhole, the contribution of the electrodes was also negligible and, after excluding the gold and polystyrene contribution from the lifetime calculation analysis, the data could be well fitted with a single-exponential decay law.

IV.4.6. Discussion

As previously discussed, the temperature map from intensity measurements is plotted as a relative decrease in intensity while the FLIM picture when the electric field is turned on is plotted as absolute values. Lifetime measurements can therefore give straightforward information on the state of a given system. Moreover, comparing **Figure IV-11** with **Figure IV-12**, the number of workable pixels is 25 % more from the lifetime map than from the intensity map. For the analysis of 2 or more particles within a single trap, and as the number of workable pixels decreases, lifetime imaging can provide much more accurate data than intensity measurements. In particular, the bead appears bigger in the intensity map due to the fact the bead moves as soon as the electric field is turned on and because of a refractive index mismatch between polystyrene (1.55) and water (1.3). Accordingly, temperature can be

accurately described at the interface between the fluid and particle using fluorescence lifetime imaging.

The lifetime histogram for each analyzed pixel shows the shift towards lower lifetimes after switching on the electric field. The lifetime distribution was fitted by a Gaussian curve and shown in **Figure IV-13**.

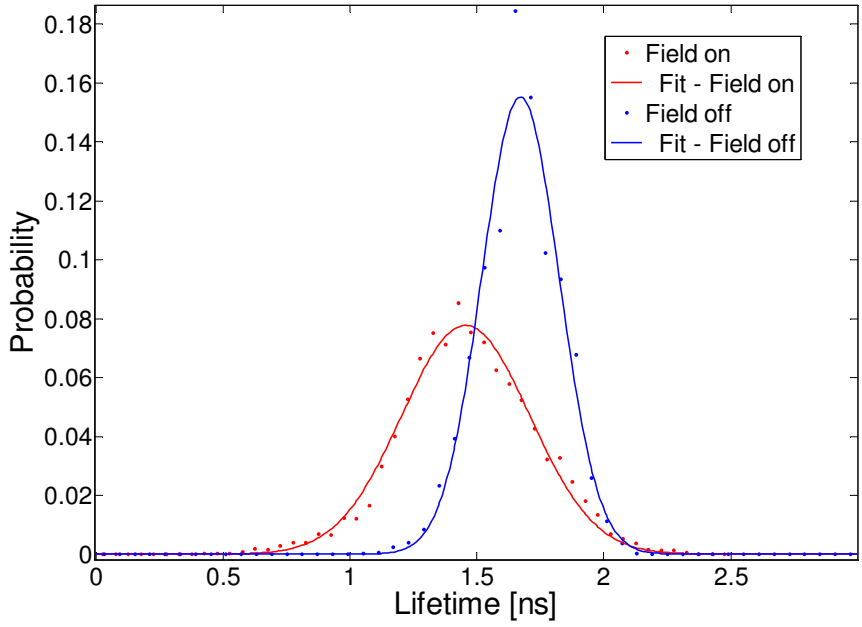


***Figure IV-13**. Fluorescence lifetime distributions before (in blue) and after (in red) switching on the electric field.*

The equation for the fits takes the form:

$$y = Ae^{-\frac{(t-\mu)^2}{2v^2}}$$ ***Eq. IV-4***

The coefficients were found using Matlab fitting tool and are summarized in **Table IV.2** below.

	Electric field off	Electric field on ($7V_{pp}$-1MHz)
A	0.156	0.077
μ [ns]	1.67	1.46
v [ns]	0.15	0.25

Table IV.2. *Fitting parameters for the Gaussian curves obtained from lifetime probability distribution.*

In this equation, μ is the mean of the Gaussian distribution and is used for temperature quantification. In this case, the lifetime decay fit shows a reduction of the mean value from 1.67ns (field off) down to 1.46ns (field on). This corresponds to a 13.5ºC temperature rise. The Full Width Half Maximum (FWHM) of the distributions is respectively 0.36ns and 0.6ns when the electric field is turned off and on. The broadening of the FWHM implies the creation of a temperature gradient in the imaging plane which is directly reflected by the FLIM map.

The temperature change within each of the traps in the array was found to be fairly similar in the voltage range tested (within 10%) while inter-device testing showed higher discrepancy levels (up to 30%). This is thought to be due to the electrode deposition process and non-reproducible thicknesses of the electrodes. Furthermore, no significant frequency dependence was observed in the range 100kHz to 20MHz.

IV.5. Comparison with theory

By measuring the decrease in average lifetime over the imaged trap for different voltages after steady-state is established, the variation of temperature rise as a function of applied voltage can be plotted (**Figure IV-14**). The comparison with ***Eq. IV-3*** shows a good agreement with the analytical approximation. Effective voltages were found to be approximately 90% of the applied values which translate into a difference of only few degrees centigrade at high voltages.

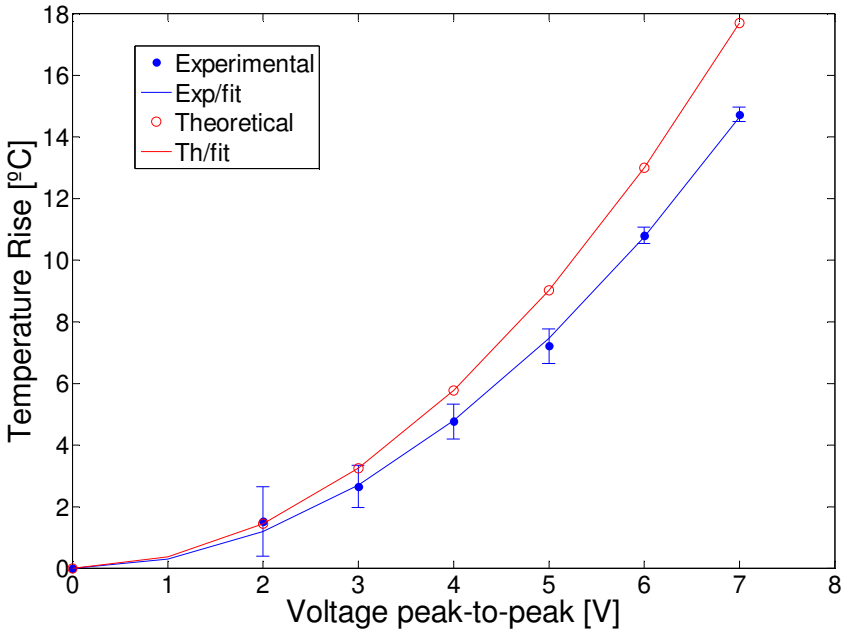


***Figure IV-14**. Relationship between temperature rise and applied voltage: the blue curve corresponds to experimental data while the red one is based on **Eq.** **IV-3**.*

IV.6. Summary

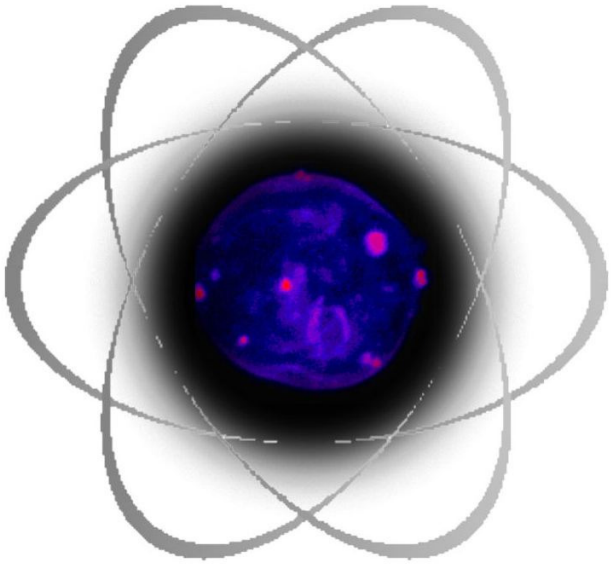
Temperature imaging within nDEP traps can be performed using both fluorescence intensity and lifetime data. However, FLIM allows for more efficient, artefact-free measurements. Results demonstrate that the local temperature in the vicinity of a trapped particle can be accurately determined experimentally and match analytical approximation well. However, for relatively high voltages (>5V_{pp}), this difference could wrongly estimate local temperatures as over a given threshold (e.g. 37ºC for cells). These types of measurements can be made prior to other studies by patterning 'experimental' and calibration micro-electrodes on a single substrate.

The modest temperature rise seen for typical electric field conditions (<10ºC) in the DEP traps tested ensures the micro-environment of single cells is kept below their culturing temperature and the fluidity of their membrane is preserved and close to their physiological conditions.

IV.7. References

(1) Muyzer, G.; Smalla, K. *Antonie Van Leeuwenhoek International Journal of General and Molecular Microbiology* **1998**, *73*, 127-141.
(2) Serwer, P. *Electrophoresis* **1983**, *4*, 227-231.
(3) Zhao, T. S.; Liao, Q. *Journal of Micromechanics and Microengineering* **2002**, *12*, 962-970.
(4) Lackovic, I.; Magjarevic, R.; Miklavcic, D. *Ieee Transactions on Dielectrics and Electrical Insulation* **2009**, *16*, 1338-1347.
(5) Seger, U.; Panayiotou, M.; Schnydrig, S.; Jordan, M.; Renaud, P. *Electrophoresis* **2005**, *26*, 2239-2246.
(6) Douple, M. U. a. E. B. *Utrecht, The Netherlands: VSP* **1988**.
(7) Heimburg, T., Thermal biophysics of Membranes, *Wiley*, **2007**.
(8) Sankaran, B.; Racic, M.; Tona, A.; Rao, M. V.; Gaitan, M.; Forry, S. P. *Electrophoresis* **2008**, *29*, 5047-5054.
(9) Suehiro, J.; Pethig, R. *Journal of Physics D-Applied Physics* **1998**, *31*, 3298-3305.
(10) Landau, L. D. a. L. E. M. *Oxford:Pergamon* **1959**.
(11) Hayashi, M. *Environmental Monitoring and Assessment* **2004**, *96*, 119-128.
(12) Ramos, A.; Morgan, H.; Green, N. G.; Castellanos, A. *Journal of Physics D-Applied Physics* **1998**, *31*, 2338-2353.
(13) Mittal, N.; Rosenthal, A.; Voldman, J. *Lab on a Chip* **2007**, *7*, 1146-1153.
(14) Williams, S. J.; Chamarthy, P.; Wereley, S. T. *Journal of Fluids Engineering-Transactions of the Asme* **2010**, *132*, 7.
(15) Benninger, R. K. P.; Koc, Y.; Hofmann, O.; Requejo-Isidro, J.; Neil, M. A. A.; French, P. M. W.; deMello, A. J. *Analytical Chemistry* **2006**, *78*, 2272-2278.
(16) Chee, C. K.; Rimmer, S.; Soutar, I.; Swanson, L. *Polymer* **2001**, *42*, 5079-5087.
(17) Shah, J. J.; Gaitan, M.; Geist, J. *Analytical Chemistry* **2009**, *81*, 8260-8263.
(18) Low, P.; Kim, B.; Takama, N.; Bergaud, C. *Small* **2008**, *4*, 908-914.
(19) Robinson, T.; Valluri, P.; Manning, H. B.; Owen, D. M.; Munro, I.; Talbot, C. B.; Dunsby, C.; Eccleston, J. F.; Baldwin, G. S.; Neil, M. A. A.; de Mello, A. J.; French, P. M. W. *Optics Letters* **2008**, *33*, 1887-1889.
(20) Nishikawa, T.; Kambara, H. *Electrophoresis* **1996**, *17*, 1115-1120.
(21) Markham, J.; Conchello, J. A. *Journal of Microscopy-Oxford* **2001**, *204*, 93-98.
(22) He, H.; Xie, C.; Ren, J. *Analytical Chemistry* **2008**, *80*, 5951-5957.
(23) Glawdel, T.; Almutairi, Z.; Wang, S.; Ren, C. *Lab on a Chip* **2009**, *9*, 171-174.

Chapter V. Dielectric cell response in highly conductive buffers



In this chapter, we study the cell response to a non-uniform electric field when placed in a highly conductive medium such as the physiological situation. The knowledge of this response can be used to optimize dielectrophoretic trapping conditions or exploited for impedance based label-free cell identification and separation methods. Analytical solutions are first extracted from the single-shell model for cell dielectric modelling and a simple microfluidic device has been built and used to probe live/dead Jurkat cell responses at different frequencies.

V.1. Introduction

Historically, the most sensitive and practical dielectric identification schemes are those relying on cells immersed in an isotonic low conductivity medium.[1-3] This is due to the DEP response of cells or bacteria switching between a negative DEP regime (where cells are less polarizable than the buffer) and a positive DEP regime (where cells are more polarizable than the buffer) in low conductivity media. Such an effect introduces an observable change in behaviour which can quantified in terms of the cross-over frequency (where the cell's response to the electric field is zero). However, this transition is highly frequency dependent and dictates a complex analysis of the response. In contrast, cells suspended in high conductivity buffers always undergo negative DEP (cells always remain less polarizable than the buffer regardless of operating frequency).

One key challenge when using a low conductivity medium is to reduce its impact on cell long-term viability.[4] By keeping cells in physiological buffers (of high conductivity), the cell environment is left unmodified throughout the analysis process. This ensures cell viability and increases the potential throughput of the overall identification procedure. The key disadvantage of using a high conductivity medium lies in the possibility of sample heating and electrochemical damage. However, these effects can be minimized by using low actuation voltages and applying high frequencies.[5]

Cell response under DEP has been addressed theoretically and its impedance quantified as a function of membrane conductivity, capacitance, thickness, cell cytoplasm conductivity and permittivity and cell radius.[6] These parameters have been integrated into the effective single-shell model which can be used to accurately predict mammalian cell behaviour in applications such as cellular trapping, discrimination and separation.[7] The model has been introduced analytically in **Chapter III**. Here we examined the case where cells are immersed in highly conductive buffers (>1S/m),and found approximations for different frequency regimes. Understanding the dielectric response in buffers of high conductivity and the relevant dielectric parameters associated is essential before designing identification or separation strategies.

Next, a practical identification tool, able to monitor changes in cellular response under nDEP in a high conductivity medium is presented. Using this system, cells can be continuously floated over the detection zone with analytical throughput being limited by the flow rate of the cells which is limited by the global polarization response time and the cell density. Specifically, it is shown that high-frequency responses of live and dead cells cause differences in the flow pattern over the identification zone. The temporal and spatial interaction between cells and electrodes is maximized by leveraging geometrical and electrical confinement effects within a shallow polydimethysiloxane (PDMS) microchannel (30 μm deep). and examined the slowing down pattern of cells flowing over line electrodes in a shallow microchannel.

V.2. Theoretical frequency response in high conductive buffers

V.2.1. High frequencies

As cell response varies significantly over the typical DEP frequency range [100kHz-100MHz], an understanding of the different frequency regimes allows for interrogation of distinct dielectric properties. Assuming Maxwell-Wagner-Sillars interfacial polarization, the transition between conductivity dominated behaviour and the dielectric permittivity regime is given by:

$$\tau_{MW} = \frac{\varepsilon_c + 2\varepsilon_m}{\sigma_c + 2\sigma_m} \qquad \textit{Eq. V-1}$$

Here τ_{MW} is the Maxwell-Wagner charge relaxation time, ε_c is the absolute permittivity of the cell cytoplasm, σ_c is the electrical conductivity of the cytoplasm and σ_m is the electrical conductivity of the medium. The corresponding frequency is in excess of 250MHz for cells in high conductivity buffers. Above this value, the cell response is given by:

$$\mathrm{Re}(CM) \approx \frac{\varepsilon_c - \varepsilon_m}{\varepsilon_c + 2\varepsilon_m} \qquad \textit{Eq. V-2}$$

Because the cell cytoplasm has a dielectric permittivity very close to that of water, the response is close to zero above this transition frequency.

V.2.2. Intermediate frequencies

In the effective single shell model, the frequency spectrum of cells contains an intermediate region where the voltage drops almost entirely across the cell membrane. In high conductivity buffers (>1S/m), this region is located between 1 and 100MHz, with a characteristic plateau being strongly dependent of cytoplasm conductivity. An analytical expression can be derived from theory described in reference 8 and applied to the case of high conductivity buffers, i.e.[8]

$$\mathrm{Re}(CM) \approx \frac{\sigma_c - \sigma_m}{\sigma_c + 2\sigma_m} \qquad \textit{Eq. V-3}$$

Figure V-1 models the frequency response of a cell based on the full single-shell model explicited in **Eq. III.4**. The dependence in conductivity of the cytoplasm for the intermediate frequency range is illustrated in **Figure V-1A** for the dielectric parameters given in the caption.

V.2.3. Low frequencies

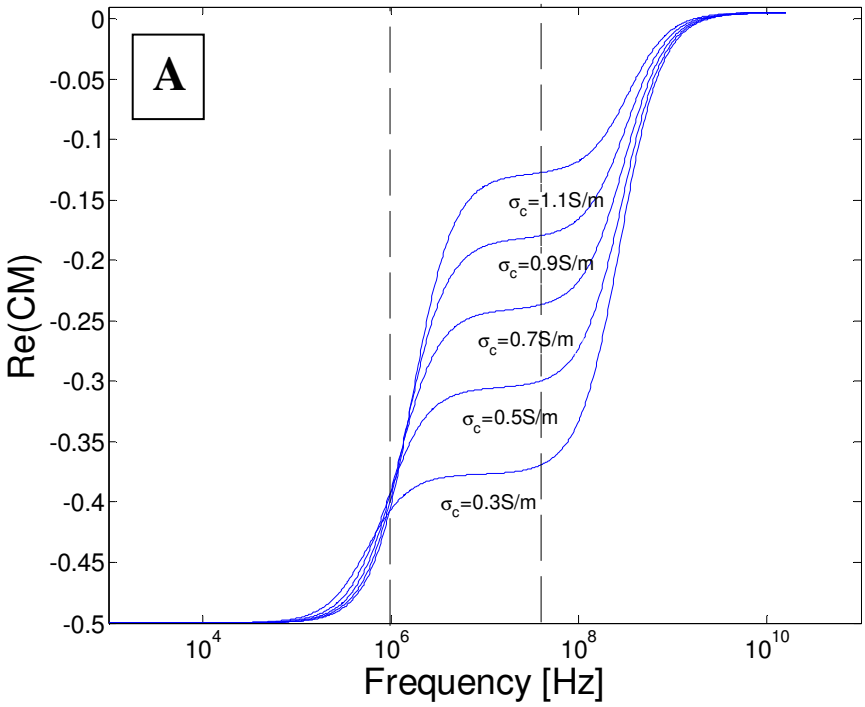
At low frequencies (<<1MHz), the membrane conductivity plays an important role in the overall cell response. Live cells with preserved membrane integrity typically have a very low conductivity (10^{-7}S/m) and a CM factor close to the maximum value of -0.5. Conversely, heat-treated cells exhibit a membrane conductivity increase by several orders of magnitude due to the formation of irreversible pores.[9] A change in membrane capacitance is also expected due to morphological changes that occur above the denaturation temperature of proteins. As mentioned in prior studies, the induced change in membrane capacitance strongly depends on the method used to kill cells and is therefore difficult to predict.[10] If one

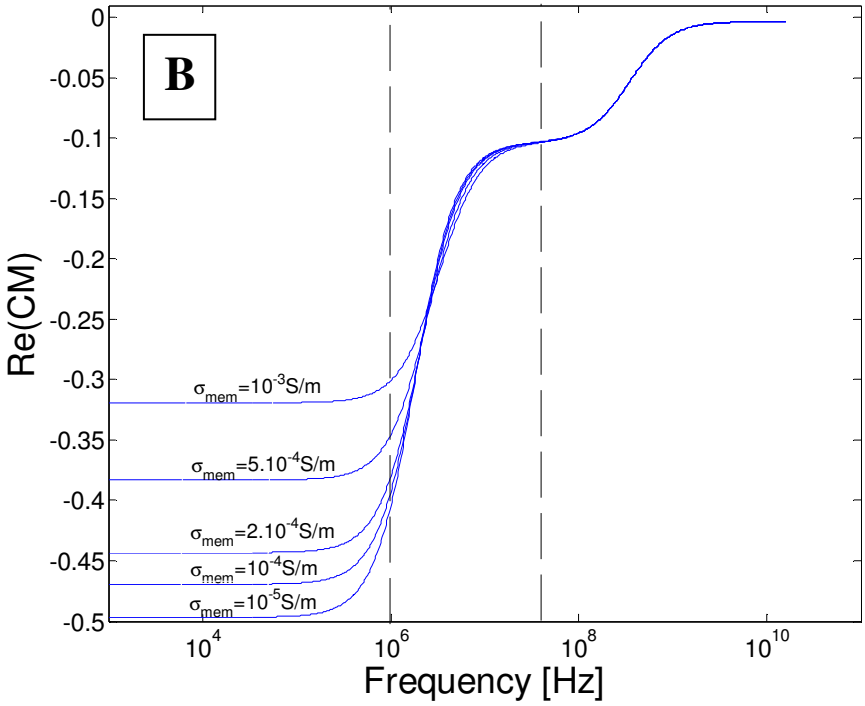
assumes that the conductivity of the cell cytoplasm is less than or of the same order of magnitude as that of the medium, the low frequency response can be approximatedby:

$$\mathrm{Re}(CM) \approx -\frac{{\sigma_m}^2}{2{\sigma_m}^2 + c\sigma_m\sigma_{mem}}, c = \frac{9R^3}{t(3R^2 - 3Rt + t^2)} - 4 \qquad \textit{Eq. V-4}$$

Here σ_{mem} is the conductivity of the membrane and *t is* the thickness of the lipid bilayer (7nm in average). The significance of membrane conductivity variations in dead cells is illustrated in **Figure V-1B**.

Membrane capacitance influences the transition frequency between low and intermediate responses. The membrane capacitance was simulated between 5-20mF/m^2 (the literature value for Jurkat cell being 13mF/m^2).[10] Other parameters were kept constant. A simulated change from 10mF/m^2 to 15mF/m^2 will trigger a change in the cell response lower than 10 % for all frequencies. Simulation plots for membrane capacitance change are given in **Figure V-1C**. This theoretical analysis shows that significant differences in DEP response for live and heat-treated mammalian cells can be seen through independent levels within distinct frequency bands.[2]


A
Re(CM)
Frequency [Hz]
σc=1.1S/m
σc=0.9S/m
σc=0.7S/m
σc=0.5S/m
σc=0.3S/m


B
Re(CM)
Frequency [Hz]
σmem=10-3S/m
σmem=5.10-4S/m
σmem=2.10-4S/m
σmem=10-4S/m
σmem=10-5S/m

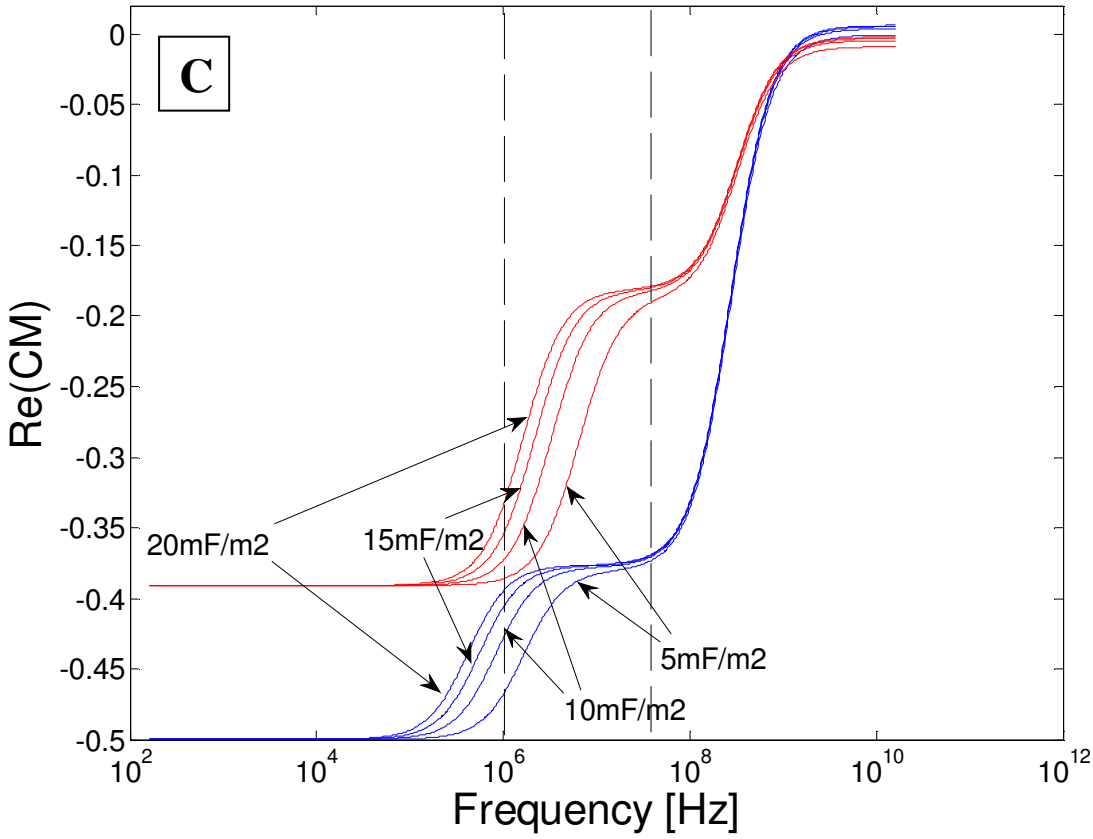


Figure V-1*. Theoretical frequency response of cells based on the effective single-shell model. Vertical dashed lines indicate 1MHz and 40MHz.* ***A****. The cell cytoplasm conductivity changes from 0.3S/m to 1.1S/m for a set membrane conductivity of 10^{-7}S/m and membrane capacitance 13mF/m^2.* ***B****. The cell membrane conductivity changes from 10^{-5}S/m to 10^{-3}S/m for a set cytoplasm conductivity of 1.2S/m and membrane capacitance 13mF/m^2.* ***C****. Theoretical frequency response when varying the cell membrane capacitance from 5 to 20mF/m^2 for live and heat-treated cells (cytoplasmic conductivity of 0.3S/m and 0.9S/m respectively) immersed in a high conductivity buffer (1.65S/m).Cytoplasm dielectric constant was 80, membrane thickness 7nm, cell radius 5.1µm for all plots.*

V.3. In-flow cell identification

V.3.1. Microfluidic design

To interrogate cell response and confirm the predictions of the single-shell model applied to

highly conductive buffers, we designed a 1mm wide, 5mm long and 30µm deep PDMS microchannel with 2 embedded planar electrodes. **Figure V-2A** displays a schematic of the longitudinal cross-section of the microfluidic PDMS channel where two parallel planar gold electrodes are embedded on a glass substrate. Here the goal is to ensure that each cell encounters the same electric gradient perpendicular to the flow path and that the drag force overcomes the dielectrophoretic force. This forces the cells to transit through the DEP barrier. As a consequence, close to the high electric field region, cells will slow down before being lifted up and pass over electrodes. This deceleration pattern is graphically represented in **Figure V-2B**. **Figure V-2C** is a bright field top view of a live cell approaching the patterned electrodes. The voltage is kept constant at $5V_{pp}$.

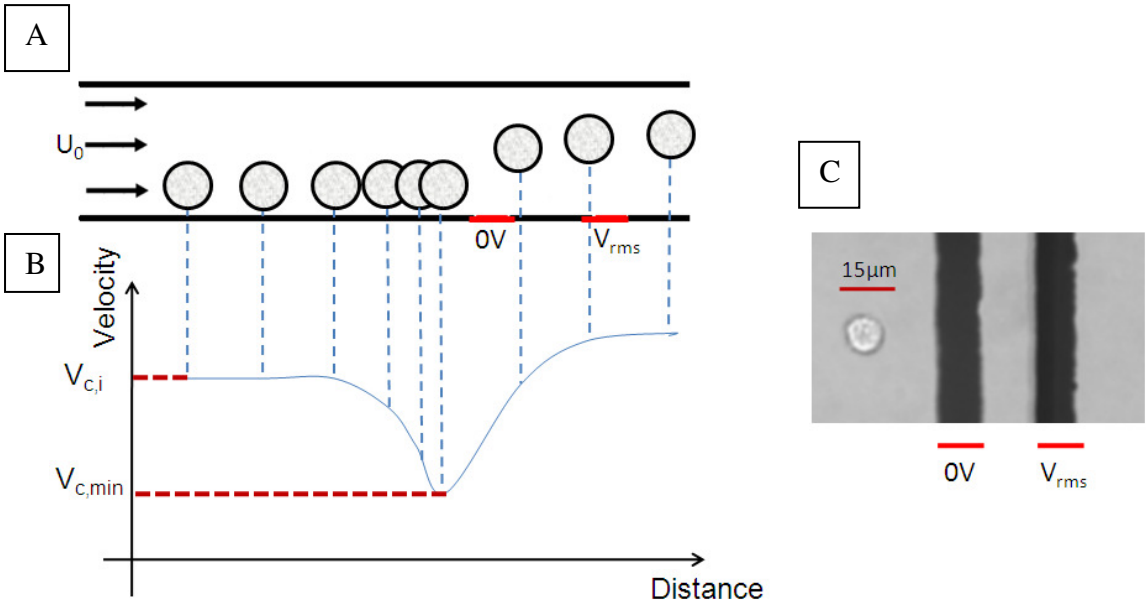


***Figure V-2**. **A**. Schematic of the microfluidic flow cell with embedded planar electrodes. **B**. Corresponding cell velocity as a function of travelling time. **C**. Bright field snapshot of a live T-cell approaching the electrodes.*

V.3.2. Theoretical balance of forces

The balance between the DEP and drag forces strongly depends on the characteristic lengths of the system. Importantly, the mass density of Jurkat cells higher than water[11] combined with the restriction in channel height ensures the vast majority of cells will be immersed in

the high electric field region. Assuming that cells flow at constant velocity (no drag) towards electrodes, the DEP force ($\vec{F}_{DEP}$) will exert a backward component close to the electrode edge that causes a decrease in cell velocity. This is combined with Electro-HydroDynamic (EHD) flows which is assumed to form a constant flow field.[12] At this point, the drag force $\vec{F}_{Drag}$ increases and the cell forced to overcome the DEP/EHD barrier. Assuming a quasi-trapping regime, the DEP, EHD and drag forces are approximately equal near the electrodes where velocity is at a minimum, i.e.

$$\left|\vec{F}_{Drag}\right| \approx \left|\vec{F}_{DEP}\right| + \left|\vec{F}_{EHD}\right| \qquad \textbf{Eq. V-5}$$

EHD flows are created by local temperature rise close to the electrodes giving rise to both conductivity and permittivity gradients. In our system, maximum temperature rise can be estimated to less than 10°C at 3.5Vrms [5, 13]. EHD flows are supposed to be steady and the corresponding force – as a type of drag force - proportional to the radius of the cells. Under the electric conditions applied, EHD forces were found negligible compared to the pressure-driven drag force. Combination of ***Eq. V-5*** with the classical time-averaged DEP force expression yields,

$$k\frac{V_{c,i} - V_{c,\min}}{R^2} \approx \frac{\varepsilon_m \,\mathrm{Re}(CM)}{3\eta}\nabla\left|\vec{E}\right|^2 + C_{EHD} \qquad \textbf{Eq. V-6}$$

Here $V_{c,i}$ and $V_{c,min}$ are the incoming and minimum cell velocity respectively, k is a non-dimensional correction factor for the wall effect [14], C_{EHD} is a constant factoring in EHD contributions and R is the radius of the cell in micrometers. CM is the Clausius-Mossotti factor, ε_m is the absolute permittivity of the medium, η is the dynamic viscosity of the medium, and $\vec{E}$ is the electric field.

From ***Eq. V-6***, a slowing down factor S can be defined, normalizing for incoming cell velocity:

$$S = \frac{V_{c,i} - V_{c,\min}}{V_{c,i}} \frac{1}{R^2}$$ **Eq. V-7**

Using such a definition, the slowing down factor will be 0 for cells with no measurable change in velocity and approximately $1/R^2$ for cells strongly decelerated. This factor has to be finally linearly corrected to compensate for the fact residence time in the high electric field region decreases with increasing flow velocity. If the electric field is kept constant, the slowing down factor reflects the response of the cell. After deceleration, cells are repelled vertically and accelerate towards a faster streamline as found in DEP-FFF. However the exiting velocity in a shallow channel is a complex correlation between incoming the cell height, local electrohydrodynamic flow (driven by the temperature and permittivity gradient over the electrodes), cell rotation and surface-cell interactions.

In the presented system, cells can be continuously floated over the detection zone with analytical throughput being limited by the flowing rate of the cells limited by the global polarization response time and the cell density injected with upper density limit reached when cell motion becomes affected by the presence of other cells. Specifically, high-frequency responses of live and dead cells cause differences in the flow pattern over the identification zone. The temporal and spatial interaction between cells and electrodes is maximized by leveraging geometrical and electrical confinement effects within a shallow polydimethysiloxane (PDMS) microchannel (30µm deep).

V.3.3. Cell viability upon heating

In order to produce control dead cells, an aliquot was heated in an oven for a given time at 65°C and subsequently stained with a 20 % Trypan blue solution (Sigma). Cell membrane integrity is typically looked at through dye-exclusion assays. For example, the dye Trypan blue gives a characteristic blue colour to the cytoplasm if it is able to permeate through the plasma membrane. This dye is widely employed for cell counting and apoptosis applications. The resulting cell viability as a function of heating time is shown in **Figure V-3**.

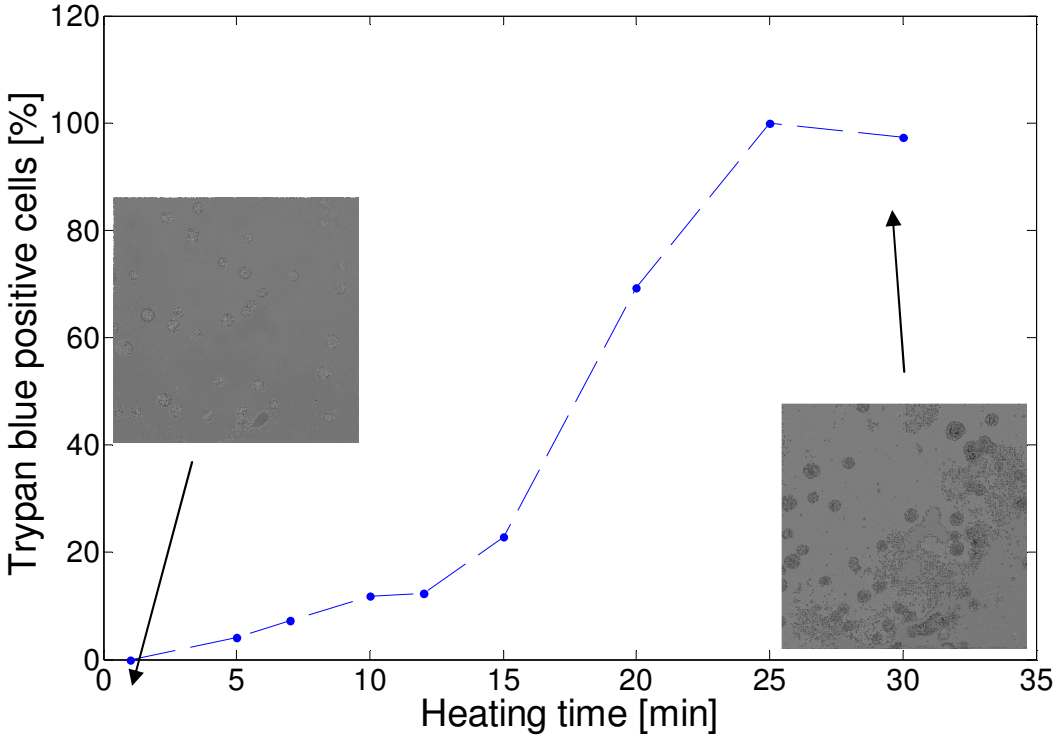


***Figure V-3**. Percentage of dead cells as a function of heating time at 65ºC.*

Here the integrity of the membrane of Jurkat cells is mostly preserved until 15 minutes incubation at 65ºC. After this threshold incubation time, cells become quickly damaged and reach close to 100 % leakage after 25 minutes incubation.

For performing cell identification experiments, live cells taken from the culture flask were equally split in two aliquots. One aliquot was heated for 20 minutes at 65°C, mixed with the other aliquot and 20% Trypan Blue solution (Sigma) was added. The overall mixture conductivity was measured to be 1.35S/m. Jurkat cells were measured by image analysis of miscroscopy pictures as described in **Chapter II**. The live cells had an average diameter of 10.2 ±3.5µm and the dead cells had an average diameter of 10.7 ±3.5µm.

V.3.4. Slowing down factors

The algorithm written in Matlab extracts the frame-by-frame intensity map and tracks cells by using image segmentation methods. The recorded position is taken as being the barycentre of the area occupied by the cell. As the cell cannot be seen when they pass over the gold

electrodes, the minimum velocity is extracted as being the average velocity between 10µm before the first parallel electrode (defined for the front edge of the cell) and the middle of the inter-electrode gap, covering a distance of 32.5µm. Velocities were extracted as the slopes of the position plot. Whenever several cells were present in the detection area, the data was extracted only if they were far apart to neglect modification of the local fluid flow close to one cell.

A typical position versus time plot for a single cell is represented in **Figure V-4** with the slopes taken for evaluating incoming velocity and minimum velocity highlighted as dashed red lines.

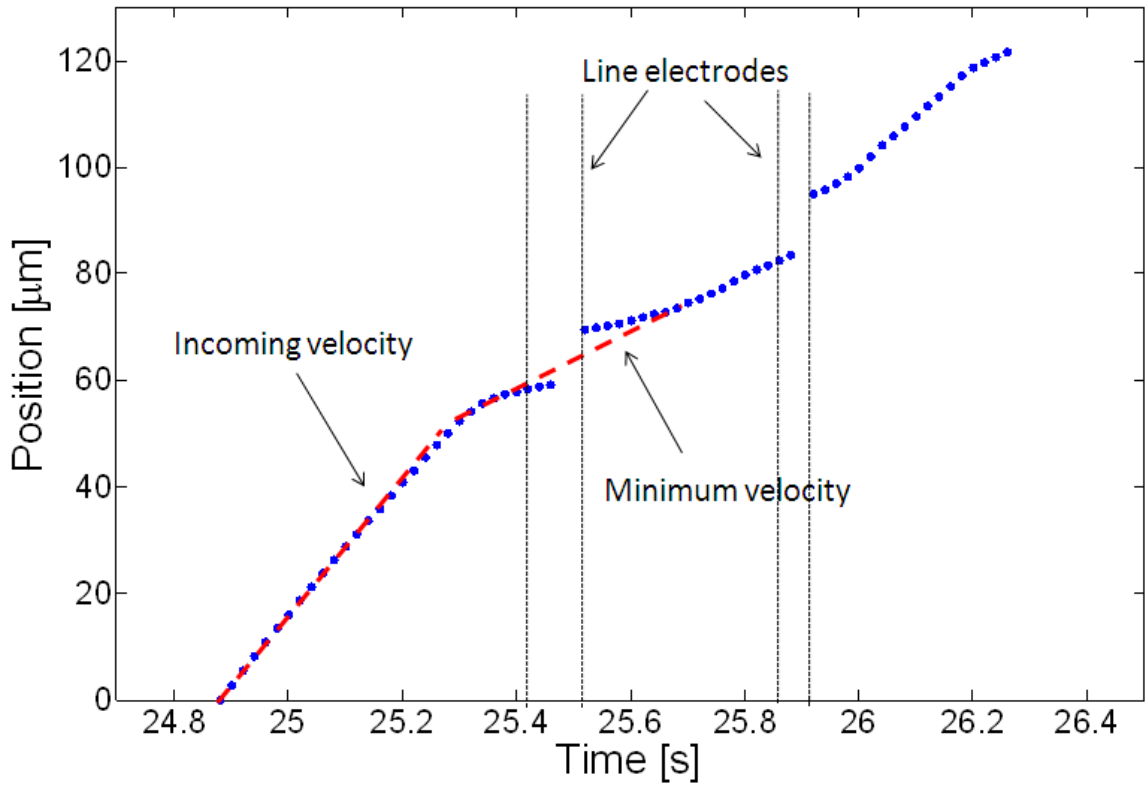


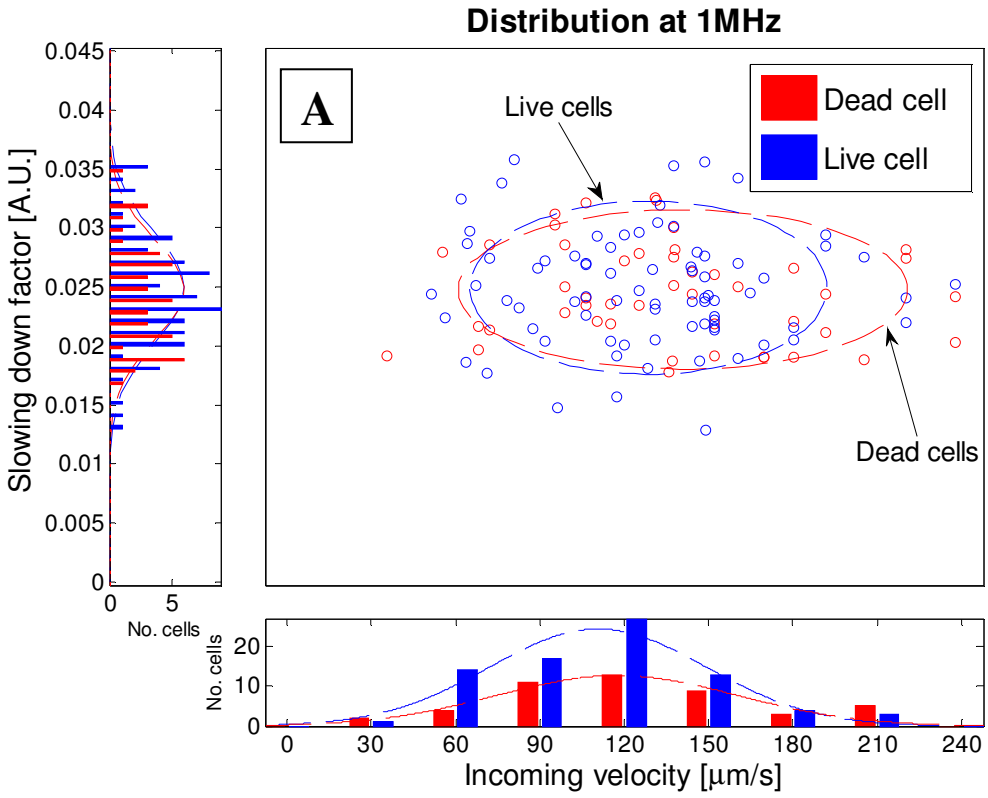
***Figure V-4**. Position versus time for a single cell as extracted from the image analysis software. Incoming velocity and minimum velocity were measured as the slopes of the red dashed lines.*

With cells passing over electrodes, the tracking algorithm only detects parts of the cell not hidden by the metal and the position is therefore underestimated. That is why instantaneous velocity cannot be extracted using the technique. Line electrodes appear with different widths

because of the local cell velocity difference. **Figure V-4** tends to suggest that cells are pushed upwards when passing above the first line electrode towards the ceiling of the shallow microchannel where they experience a reduced drag force. This hypothesis is confirmed by the fact cells do not accelerate quickly after the second electrode. This could contribute to slowing down cells in addition to DEP repulsion forces.

In the particular case of **Figure V-4**, incoming velocity and minimum velocity were found to be 126.7µm/s and 49.5µm/s respectively. The corresponding S factor for a cell of radius 5.1µm was thus 0.023.

By testing a range of incoming velocities, the slowing down factor was calculated and plotted for frequencies of 1 and 40MHz (**Figure V-5**). Given the high electric field gradients (in excess of 10^5V/m), the occurrence of AC electro-osmosis prevents access to frequencies much lower than 1MHz.



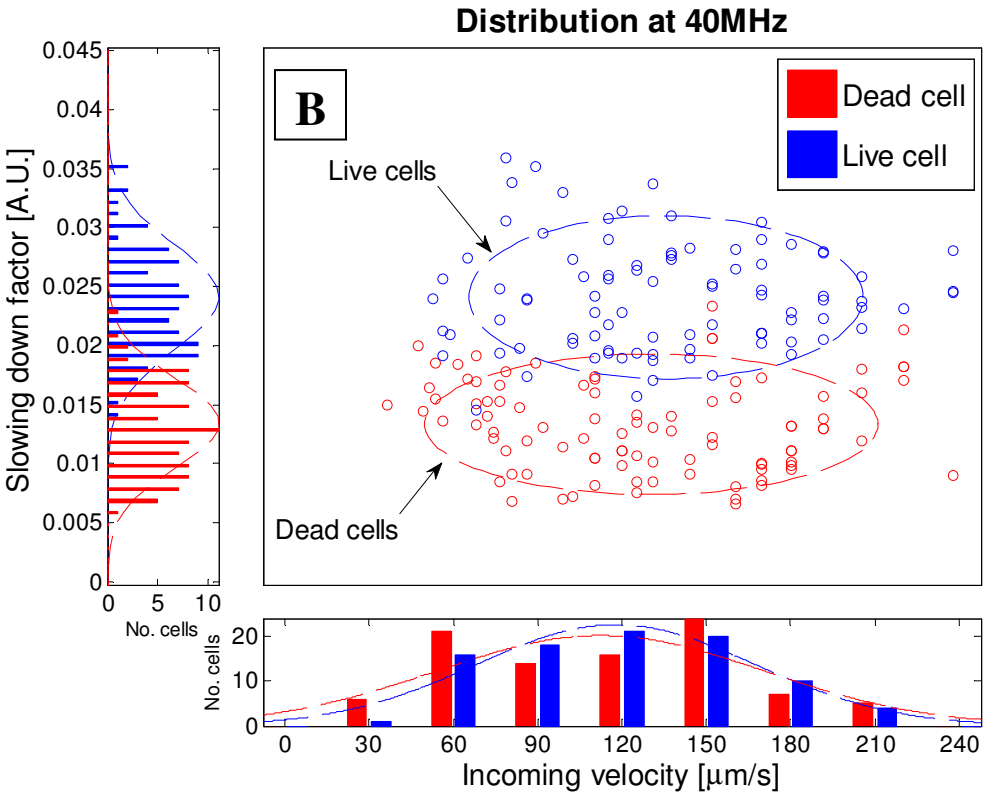


Figure V-5. *Slowing down factor versus incoming velocity at 1MHz (A) and 40MHz (B) exhibit the presence of two distinct populations. The probability ellipses for both distributions correspond to 1σ.*

The observed dispersion of data points can be accounted for by differences in incoming depth, variability in cell morphology and intrinsic biological variability, with each cell having a unique set of dielectric parameters. Strategies to reduce this dispersion include decreasing the channel height or parallelization of the electrode pattern. For velocities greater than 200µm/s, the time resolution needed to monitor slowing down events has to be increased.

The data from the scatter histograms in **Figure V-5** are summarized in **Table V.1**. The distributions were fitted to a Gaussian model having the functional form $Ae^{-\frac{(S-\mu)^2}{2\sigma^2}}$.

	Live cells		Dead cells	
	1MHz	**40MHz**	**1MHz**	**40MHz**
Number of cells tested	79	90	48	95
A	7.14	7.94	4.14	8.93
μ [a.u.]	0.024	0.023	0.024	0.013
σ [a.u.]	6.10^{-3}	6.10^{-3}	7.10^{-3}	6.10^{-3}

Table V.1*. Number of cells screened for each frequency and fitting parameters with mean μ and standard deviation σ for the Gaussian fits of histograms of slowing down factors at 1MHz and 40MHz.*

The ellipses plotted in **Figure V-5** represent a confidence limit of one standard deviation. The area overlap between the two ellipses is 77% at 1MHz and 5% at 40MHz. For two standard deviations, the overlap of the ellipses becomes 79% at 1MHz and 25% at 40MHz.

Using simulation plots, mean slowing down factors were used to set up a qualitative analysis of frequency responses. The consistency between the response of live cells at both 1MHz and 40MHz indicate the cell cytoplasm had a conductivity much lower than that of the buffer. This is in broad agreement with previous studies suggesting the presence of ion flow barriers within live cells.[15, 16]

The large difference in response seen at 40MHz between live and dead cell is primarily accounted for by cytoplasmic conductivity differences. This confirms that the increased permeability during the heat treatment led to an increased cytoplasm conductivity. As the response was found only halved compared to live cells, this also suggest that organelles within the cytoplasm do behave as resistive elements even though the intracellular ionic strength would be of similar value to that of the buffer.

Overall, the analysis of the frequency bands gives insights into how to exploit the dielectric properties of live and heat-treated cells and forms the basis for future separation works.

V.4. Summary

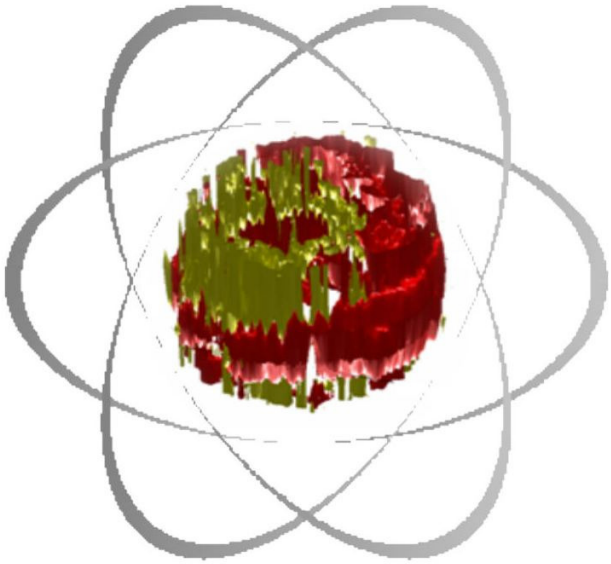
Sensing cell response within a non-uniform field in a highly conductive buffer has been devised and successfully applied to the identification of live and dead Jurkat T-cells. This functional scheme exploits both geometrical and electrical confinement effects. Operation at a frequency of 40MHz was found to achieve efficient cell identification based on dielectric properties that vary due to a change in membrane permeability. This technique can be readily adapted to the screening of apoptotic cells experiencing changes in their DEP response spectrum [17, 18]. Importantly, the architecture is adaptable and is likely to find application in other areas of high-throughput detection and counting of cells in physiological buffers. The complete automation of the proposed architecture to a sorting system could be achieved by coupling the particle image velocimetry method to an active valve system. Parallelization of the electrode pattern along the fluidic microchannel could also provide multiple screening steps that would further reduce the error contributions brought about by hydrodynamics. Selective trapping of live cells can also be achieved when operating at lower flow rates. It will be especially useful to quickly identify mixtures of cells having different dielectric properties without introducing changes to their suspending environment.

Where flow cytometry measures fluorescence responses of single cells at high-throughput, examining the impedance spectra of single cells at high speed is also the subject of numerous studies and remains an active field of research.[19-21] In the framework of lab-on-a-chip platform, it becomes increasingly important to integrate and automate separation steps before the actual analysis is performed. The ability to distinguish live and dead cells without the use of expensive cell separation techniques has great academic and industrial potential.

V.5. References

(1) Lapizco-Encinas, B. H.; Simmons, B. A.; Cummings, E. B.; Fintschenko, Y. *Analytical Chemistry* **2004**, *76*, 1571-1579.
(2) Huang, Y.; Joo, S.; Duhon, M.; Heller, M.; Wallace, B.; Xu, X. *Analytical Chemistry* **2002**, *74*, 3362-3371.
(3) Mernier, G.; Piacentini, N.; Braschler, T.; Demierre, N.; Renaud, P. *Lab on a Chip* **2010**, *10*, 2077-2082.
(4) Puttaswamy, S. V.; Sivashankar, S.; Chen, R. J.; Chin, C. K.; Chang, H. Y.; Liu, C. H. *Biotechnology Journal* **2010**, *5*, 1005-1015.
(5) Gielen, F.; Pereira, F.; deMello, A. J.; Edel, J. B. *Analytical Chemistry* **2010**, *82*, 7509-7514.
(6) Huang, Y.; Holzel, R.; Pethig, R.; Wang, X. B. *Physics in Medicine and Biology* **1992**, *37*, 1499-1517.
(7) Pethig, R. *Biomicrofluidics* **2010**, *4*, 35.
(8) Jones, T. B., Electromechanics of Particles, *Cambridge University Press* **1995**.
(9) Alder, G. M.; Austen, B. M.; Bashford, C. L.; Mehlert, A.; Pasternak, C. A. *Bioscience Reports* **1990**, *10*, 509-518.
(10) Pethig, R.; Talary, M. S. *Iet Nanobiotechnology* **2007**, *1*, 2-9.
(11) Jaggi, R. D.; Sandoz, R.; Effenhauser, C. S. *Microfluidics and Nanofluidics* **2007**, *3*, 47-53.
(12) Morgan, H., Green N *Research Studies Press, Baldock* **2003**.
(13) Grom, F.; Kentsch, J.; Muller, T.; Schnelle, T.; Stelzle, M. *Electrophoresis* **2006**, *27*, 1386-1393.
(14) Li, H. B.; Zheng, Y. N.; Akin, D.; Bashir, R. *Journal of Microelectromechanical Systems* **2005**, *14*, 103-112.
(15) Huang, Y.; Wang, X. B.; Holzel, R.; Becker, F. F.; Gascoyne, P. R. C. *Physics in Medicine and Biology* **1995**, *40*, 1789-1806.
(16) Asami, K.; Takahashi, Y.; Takashima, S. *Biochimica Et Biophysica Acta* **1989**, *1010*, 49-55.
(17) Wlodkowic, D.; Khoshmanesh, K.; Sharpe, J. C.; Darzynkiewicz, Z.; Cooper, J. M. *Analytical Chemistry* **2011**, *83*, 6439-6446.
(18) Khoshmanesh, K.; Akagi, J.; Nahavandi, S.; Skommer, J.; Baratchi, S.; Cooper, J. M.; Kalantar-Zadeh, K.; Williams, D. E.; Wlodkowic, D. *Analytical Chemistry* **2011**, *83*, 2133-2144.
(19) Sun, T.; Morgan, H. In *Microfluidics Based Microsystems: Fundamentals and Applications*; Springer: Dordrecht, 2010, pp 507-527.
(20) Malleo, D.; Nevill, J. T.; Lee, L. P.; Morgan, H. *Microfluidics and Nanofluidics* **2009**, *9*, 191-198.
(21) Asphahani, F.; Wang, K.; Thein, M.; Veiseh, O.; Yung, S.; Xu, J. A.; Zhang, M. Q. *Physical Biology* **2011**, *8*, 11.

Chapter VI. Mapping lateral heterogeneities of cellular membranes using time-resolved fluorescence spectroscopy



This chapter summarizes the fluorescence and fluorescence lifetime measurements performed on the plasma membranes of live Jurkat and U937 cells using fluorescent lipid analogs. The spatial and temporal resolutions are first expounded to highlight the main limitations of FLIM. The fluorescent lifetimes of membrane intercalated dyes have been acquired and lifetime distributions are discussed. The influence of cholesterol on lifetime measurements is also examined. Eventually, double labelling with a FRET pair in a membrane is discussed and analyzed using the FLIM-FRET technique.

VI.1. FLIM of membrane micro-domains

As discussed in **Chapter I**, the imaging of membrane micro-domains has attracted a lot of attention over the last few decades. These domains are essential to the understanding of cellular signaling, trafficking and disease processes. One particular class of micro-domains, lipid rafts, are especially challenging to study. Indeed, in live, resting cells, it is believed that these domains are only a few tens of nanometres in diameter and exist for milli- or even micro-seconds at a time.[1] Therefore, the distribution and partitioning of membrane components have to be studied with the highest spatial and temporal resolution.

VI.1.1. Spatial and temporal resolution

VI.1.1.1. Spatial resolution

With respect to micro-domain imaging, with minimum sizes from 10-200nm, the highest spatial resolution should be sought after. This is done in this work by using a diffraction-limited microscope with a high Numerical Aperture (NA) objective. High resolution techniques such as single molecule detection can give high spatial/temporal resolution but only for a very limited number of probes and therefore are unable to capture the global heterogeneities found on the whole membrane structure. With the optical setup described in **Chapter II**, resolution in the XY and Z planes has been found to be 248nm and 500nm respectively. This is bigger than the size of lipid rafts but can resolve bigger domains as clusters or aggregates. As an example, **Figure VI-1B** displays a close-up map of fluorescence along part of a plasma membrane of a DiI labelled Jurkat cell for a single scan. The whole area was scanned in 1.12seconds.

The intensity and FLIM maps shown in **Chapter VI** and **Chapter VII** are for the 'green' channel unless explicitly mentioned.

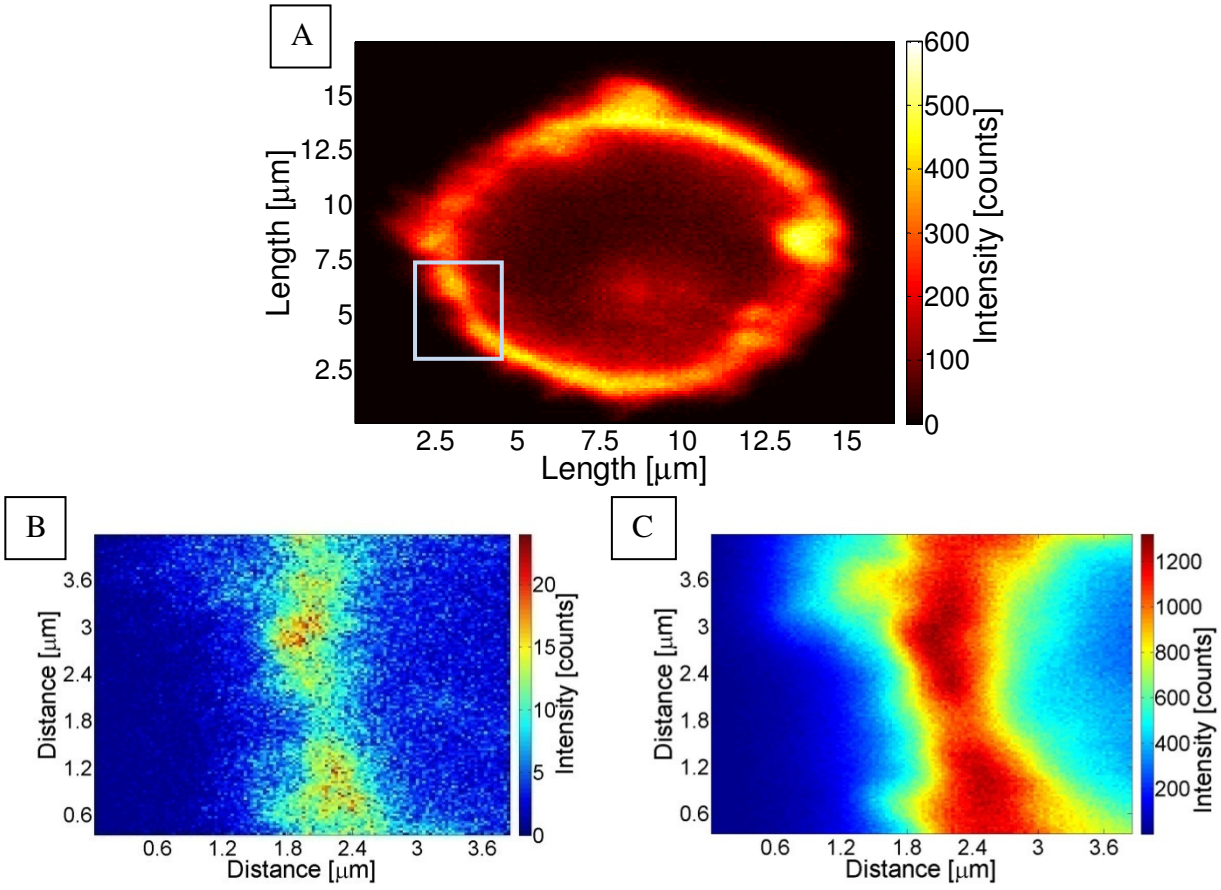


Figure VI-1 A.*Intensity map for a DiI labelled Jurkat cell. The white square indicates the scanning area for figures B and C.* ***B****. Membrane close-up showing the spatial resolution limit for a single frame* ***C****. for an accumulated 50 frames .*

Where the average membrane thickness should be 7nm, it appears as an average 500nm because of the diffraction limit. The accumulated intensity map built from 50 individual scans (**Figure VI-1C**) is further affected by membrane undulation and global cell motion although local high dye concentration areas are still resolved.

VI.1.1.2. Temporal resolution

The challenge that arises in FLIM is the requirement for high photon collection rates in short time periods. Theoretically, FLIM has a very high time resolution and is thus suitable for detecting fast events such as raft formation. To resolve two lipid domains, fluorescent emission has to occur with the dye in the same phase as during excitation, that is, it should not change environment during at least several (>5) times its lifetime. This is approximately 7.5ns in the case of DiI-C18. During this time, assuming a typical diffusion coefficient of

$10^{-7}cm^2/s$, the fluorophore would diffuse 0.5nm, which is smaller than raft size. Incidentally, this highlights the advantage of working with short lifetime dyes such as dicarbocyanine lipid analogues.

To get enough statistical data in order to accurately fit fluorescence decay curves, many photons have to be collected. This is dictated by the residence time of the focussed laser beam for each pixel in a lifetime map. A map of 128 x 128 pixels (after binning) in 1.12 seconds corresponds to 486µs at pixel level. This is still in the order of magnitude of raft existence but limits the technique to long-lived lipid ordered domains. In 486µs, a 20MHz pulsed laser will produce 9720 repetitions. Typically, the number of photons collected for each pixel will be less than 10. For high-rate photon collection, concentrating the laser power on the cell by zooming in is the preferred method. On the other hand too high power might either lead to pile-up effects, dye photo-bleaching and quenching or Avalanche PhotoDiode (APD) saturation. As a result, FLIM maps typically require the averaging of 50-70 frames over a total scanning time of 56 seconds (1.12s/frame). It is worth pointing out that lipids diffusion time is much faster than the overall acquisition time and therefore individual pixels will collect photons from different molecules in different environment. The primary goal of averaging is to increase statistical data for a better fit of the fluorescence lifetime decay. However, on a single frame basis, the lifetime can also be approximate using an improved algorithm making use of a Maximum Likelihood Estimator (MLE).[2] Time resolution can be improved by using other fitting algorithms but their use is limited to dyes in homogeneous environments and with simple photo-physical properties [3, 4].

In **Figure VI-2**, we show a comparison of FLIM maps between a single frame and 50 frames for the same membrane area as in **Figure VI-1**. Single frame lifetime analysis is done by using the MLE algorithm.

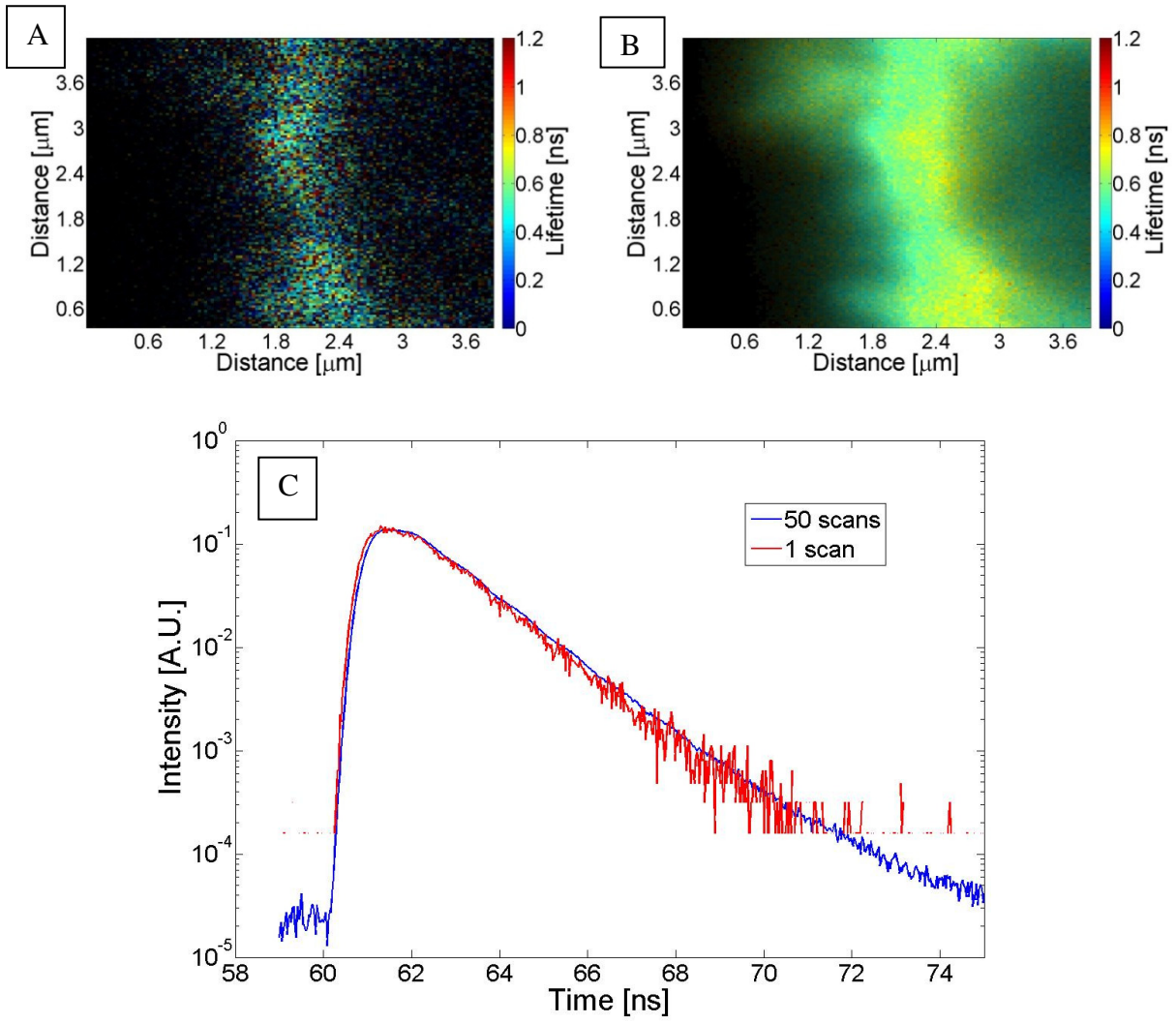


***Figure VI-2**. Membrane close-up showing the FLIM map of a membrane close-up. **A**. for a single frame **B**. for an accumulated 50 frames. **C**. Fluorescence decay curves for a single frame and 50 accumulated frames show a decrease in statistical noise.*

The noise seen in the FLIM map of **Figure VI-2A** come from the error in fitting fluorescence decay with a low count number combined with intrinsic lifetime heterogeneities. Work on the deconvolution of these effects has been the subject of many studies.[2, 5] Only after accumulation of a large number of counts per pixel can the lifetime be accurately fitted and mapped (**Figure VI-2B**). **Figure VI-2C** is a plot of the lifetime histograms for a single frame and a 50-frame scan. It is seen that statistical noise is highly reduced by using repeated scans and that the histogram extracted from a single frame scan correlates well with the accumulated scans case.

VI.1.2. Example of FLIM use

Fluorophores reporters of membrane order have been introduced in **Chapter I**. For instance, carbocyanine dyes with long alkyl chain lengths have been shown to have longer fluorescence lifetimes in more rigid environments[6] Thanks to this property, two lipid domains can be resolved by FLIM as schematically illustrated in **Figure VI-3**. In one of the domain the lifetime of the fluorophore will be much lower (here in region A) than in the second one. The overall histogram will reveal two distinct peaks corresponding to each of the regions that can then be analyzed individually.

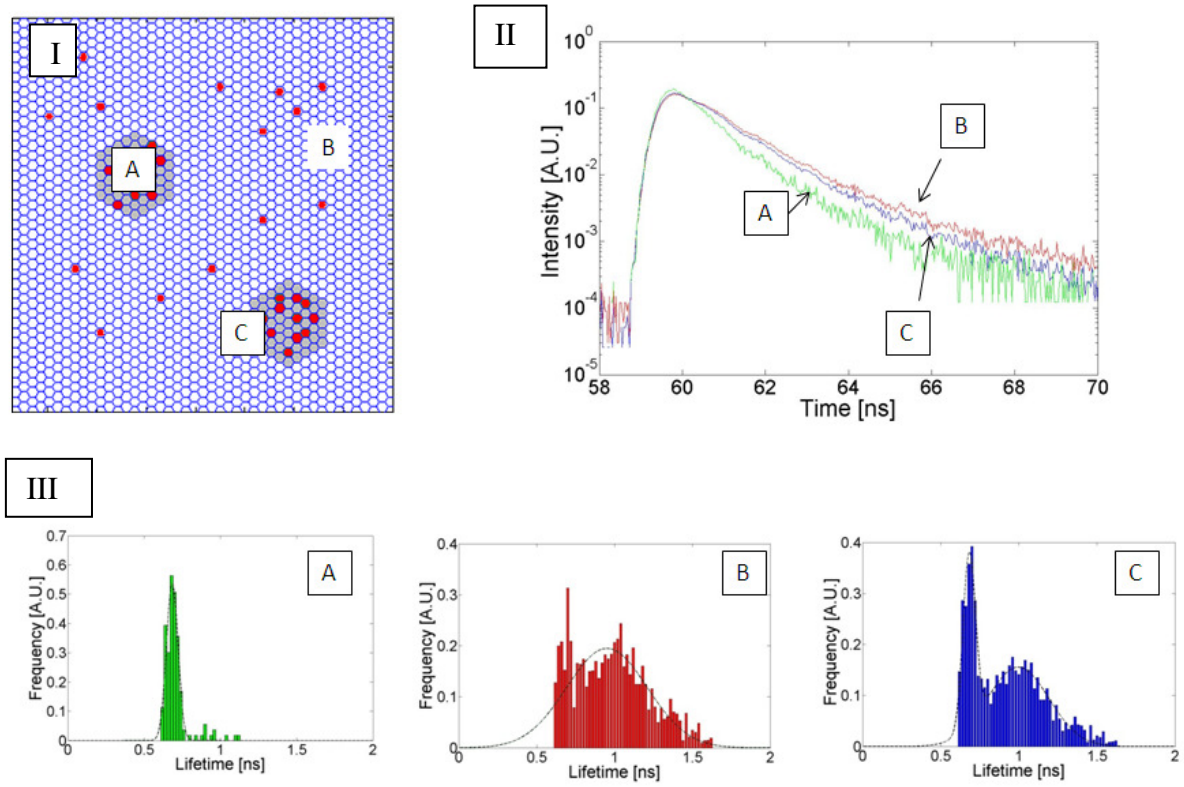


***Figure VI-3**. Schematic analysis of membrane domains using FLIM. **I**. A model membrane with 2 rigid regions represented as grey patches. **II**. Fluorescence decay curves corresponding to regions A, B and C of schematic I. **III**. Corresponding lifetime histograms.*

Often, the presence of more ordered regions cannot be seen on the FLIM map as a result of averaging. However, a multi-component lifetime fit will reveal the presence of longer lifetimes, which can be subsequently mapped using the corresponding pre-exponential factors. An example of such mapping is given in **paragraph VI.4**.

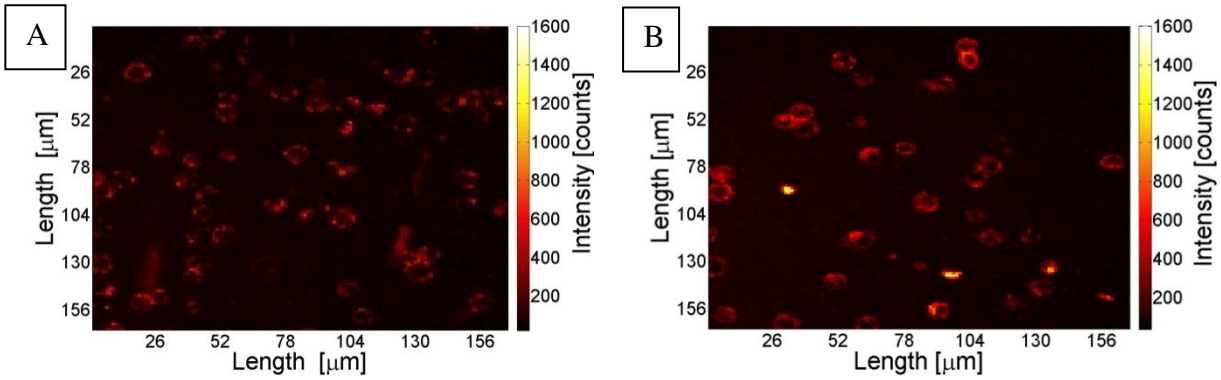
VI.2. Probe distribution

VI.2.1. Importance of labelling conditions

The making of a membrane directly depends on the conditions at which cells were cultured. One important thermodynamic variable for each membrane component is their melting temperature. For lipids or proteins, this temperature differs largely. Melting characteristics, in turn, determine the overall fluidity of a plasma membrane. For a mammalian cell grown at 37ºC, the overall thermodynamic state is fluid from typical Room Temperature (RT) and above.[7]

In addition to preserve fluidity, the incorporation of a fluorescent reporter has to be carefully controlled as too few molecules cannot be easily detected by standard fluorescence detection setups and too many molecules might affect the morphology and membrane dynamics properties. In addition, internalization of dyes will take place at high labelling temperatures.

First, we examined the distribution of DiO labels on Jurkat cell membranes based on both labelling temperature and incubation time in presence of the dye. **Figure VI-4** shows typical fluorescence maps for different labelling conditions. These intensity maps have been normalized for the number of scans.



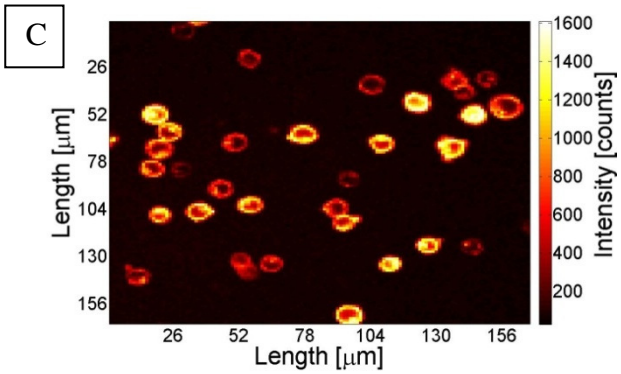


***Figure VI-4**. Quantitative incorporation of DiO depending on labelling conditions. **A**. RT for 15 minutes. **B**. 37ºC for 3 minutes and **C**. 37ºC for 15 minutes.*

Figure VI-4 highlights that probe incorporation strongly depends on labelling conditions. At RT, the fluorescence signal emitted from the membrane is very low compared to the same incubation time at 37ºC (**Figure VI-4A** and **Figure VI-4C**). It is equivalent to labelling only for 3 minutes at 37 ºC (**Figure VI-4B**). The decreased membrane fluidity at RT might explain the poor incorporation rate seen at low temperatures. Furthermore, the limited solubility of carbocyanine dyes in water triggers dye precipitation, which hinders efficient dye incorporation. Osmolarity regulating agents or the absence of salts are sometimes used to tackle this issue.[8]

The second aspect of cell labelling worth pointing out is that there are large cell-to-cell differences in dye incorporation. The average fluorescence at single cell level is plotted in **Figure VI-5**.

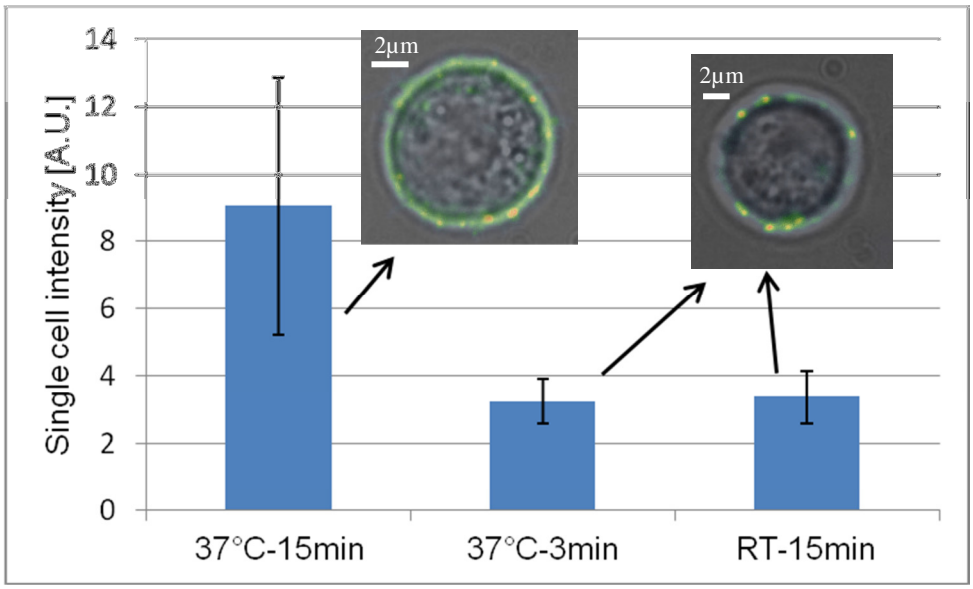


***Figure VI-5**. Average fluorescence from each cell based on different labelling conditions.*

The relative standard deviation is seen to be especially high (above 50 %) for Jurkat cells labelled at 37ºC for 15min for which most of the cells had a uniform dye coverage. This means controlled and reproducible dye delivery to the membranes of single cells cannot be achieved using standard labelling techniques relying purely on diffusion.

As seen in the representative insets of **Figure VI-5**, only little intra-cellular fluorescence is detected indicating efficient confinement of the dye to the plasma membrane. On the other hand, the presence of intra-cellular fluorescence also means the dye can be present on either membrane leaflet (exoplasmic or cytoplasmic).

A typical surface density for the uniform labelling condition is 10^4-10^5 probes/µm^2 which corresponds to approximately one fluorescent molecule for 1000-10000 membrane lipids respectively. This figure is based on similar studies for which fluorescence of the labelling solution was measured before and after the labelling step.[9] This estimation technique, however, only gives access to average dye incorporation for a large number of cells. A more accurate technique to assess single cell dye loading is to convert fluorescence counts into local concentration of dye. However, this assumes the accurate knowledge of dye-cell interactions, the quantum efficiency of the dye in the membrane and other photo-chemical properties such as photo-bleaching, photo-blinking rates.

Similar dye loading patterns were observed for the U937 cell line and the optimum labelling conditions for uniform labelling were found for an incubation of the cell-dye mix at 37°C for 10-15 minutes. DiI and DiO had similar incorporation rates into either Jurkat or U937 cell membranes.

VI.2.2. Minimizing photobleaching

Although photo-bleaching does not affect fluorescence lifetimes, minimizing its effects is necessary to ensure sufficient photon collection during the course of multiple scans. Owing to the fact that carbocyanine dyes typically have low quantum yields (<10% in water), the energy needed to generate enough photons will be high. We studied photo-bleaching of individual DiO labelled Jurkat cells after each scan and drew the normalized intensity decrease as a function of number of scans as show in **Figure VI-6**.

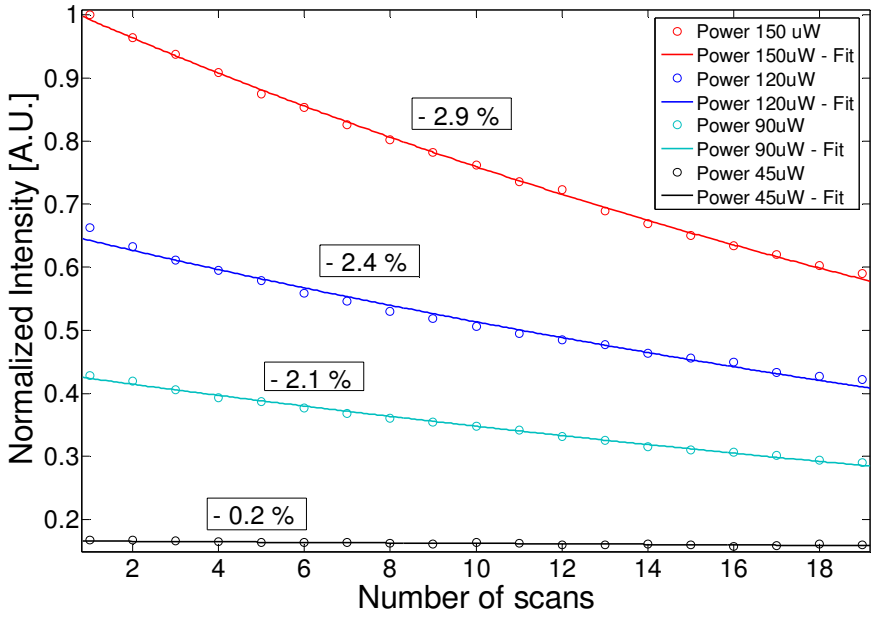


***Figure VI-6**. Photobleaching rate of a single DiO labelled Jurkat cell at different illumination powers.*

It is seen that at a power at sample level of 45µW, photobleaching effects are well minimized with an average fluorescence decrease of 0.2 % per scan. It is worth pointing out that the laser power had to be adjusted with the surface scanned in order to keep exposure dose constant.

VI.3. FLIM mapping of labelled U937 cells

In a live cell membrane, the dye is inserted into a complex matrix where it can diffuse. As a direct consequence of membrane heterogeneities and phase co-existence, the non-radiative decay rate of the dye takes different values depending on the dye's local environment. It has been recently showed that the average lifetime of DiI steadily increases with order of the membrane.[10] A general increase in fluorescence lifetimes with ordering has also been reported using other dyes.[11] **Table VI.1** summarizes the different average lifetimes found when using model unilamellar vesicles containing DiI.

DiI-C18 lipidic environment	Average lifetime [ns]
Fluid phase (DOPC)	0.80
Egg phosphatidylcholine	0.96
Gel phase (DPPC)	1.13
Liquid-ordered composition (DPPC/cholesterol, 0.7:0.3 mol/mol)	1.54

Table VI.1. *DiI lifetime depending on its local lipid environment: average lifetime increases with order (from [10]).*

The presence of multiple phases within a plasma membrane can therefore be detected using DiI. **Figure VI-7** displays an example fluorescence decay curve for a DiI labelled U937 cell together with the Instrument Response Function (IRF).

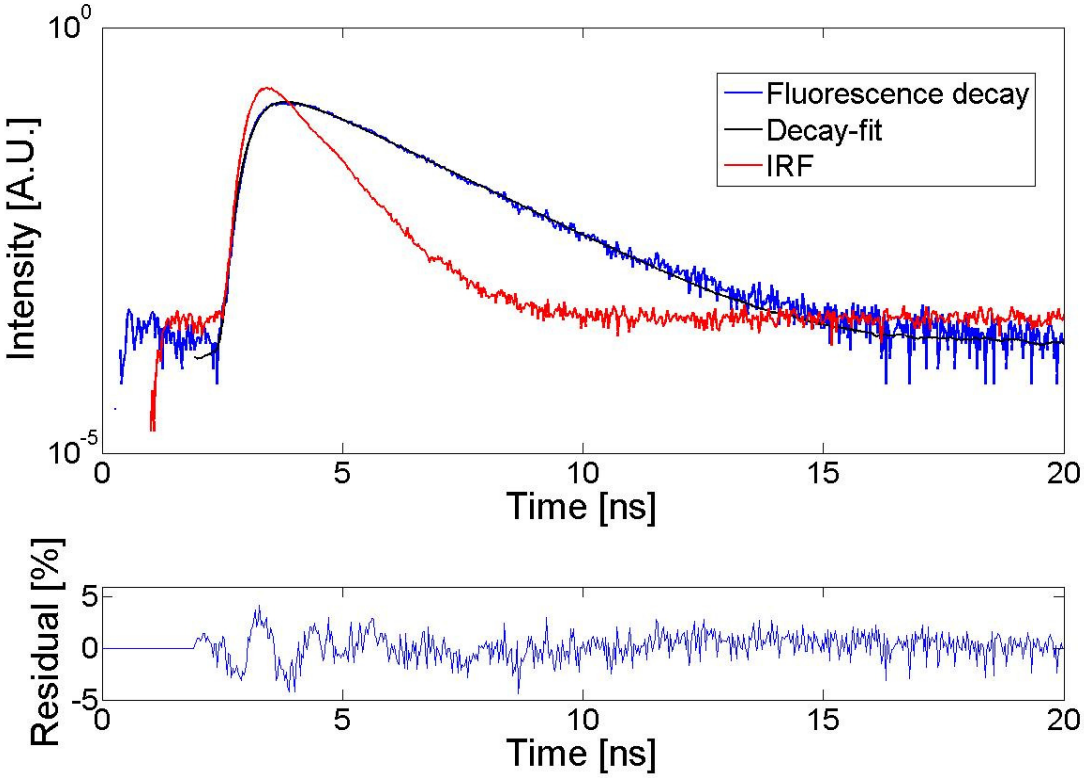


***Figure VI-7**. Normalized lifetime decay histogram (blue curve) obtained from the TCSPC electronics for a DiI labelled U937 cell and corresponding fit (black line). The Instrument Response Function measured from the dye Rose Bengal in water is shown in red. The residuals plot reflects the goodness of the fit.*

The residuals plot reflects the goodness of the fit. Here, the χ^2 parameter was found to be 1.34. The fitting parameters are summarized in **Table VI.2** for a two components lifetime fit. The functional form of the fit was $I = I_1 e^{-\tau_1} + I_2 e^{-\tau_2}, \mu = \frac{I_1\tau_1 + I_2\tau_2}{I_1 + I_2}$

τ_1[ns]	I_1 [A.U.]	τ_2 [ns]	I_2 [A.U.]	μ [ns]
0.41	0.23	1.56	0.77	0.89

***Table VI.2**. Fitting parameters for the lifetime histogram of DiI in the membrane of a U937 cell.*

Figure VI-8 displays intensity and lifetime maps of for the same cell.

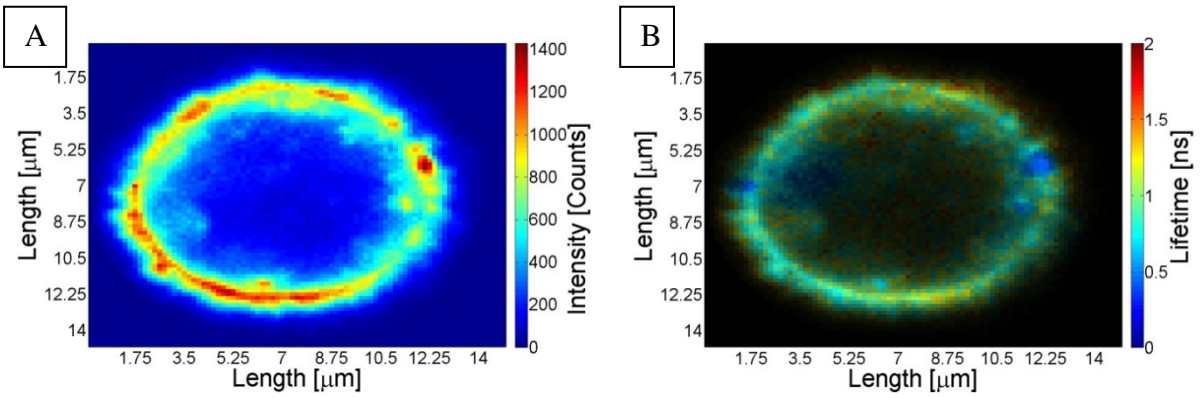


***Figure VI-8**. (**A**) Intensity map for a DiI labelled U937 cells. (**B**) lifetime map of DiI incorporated in the membrane*

The intensity map is a direct visualization of dye concentration in the absence of self-quenching effects. It is seen that while covering the whole membrane, the dye tends to concentrate in specific regions. The lifetime map gives complementary information to the intensity picture, highlighting large heterogeneities that do not fully correlate to intensity fluctuations. This is because the environment of the dye does not depend on its local concentration. The average lifetime histogram extracted from the cell above is presented in **Figure VI-9**. It is close to a broad Gaussian shape plot with lifetime values falling in the range 0.5 and 1.5ns with a variance of 0.23ns.

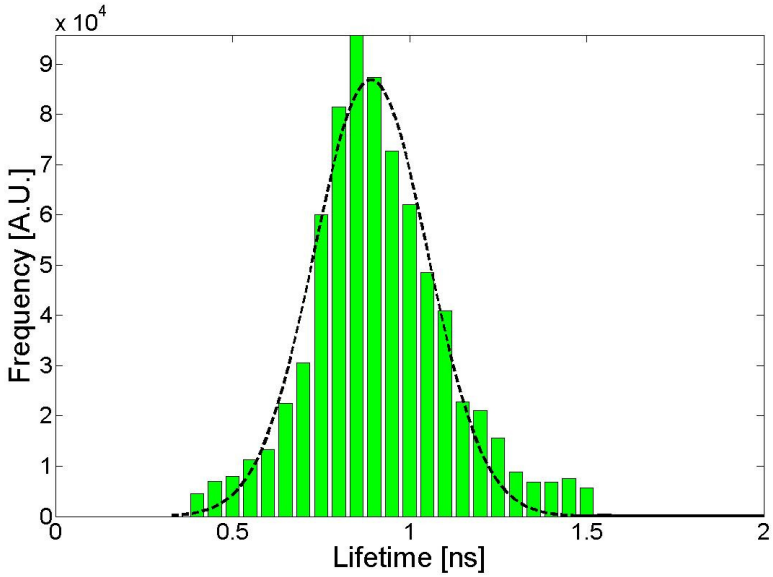


***Figure VI-9**. Example of average lifetime distribution for DiI in a U937 cell membrane.*

The width of the lifetime histogram is an indirect indicator of membrane heterogeneity. As stated above, the overall lifetime distribution is made up of two fixed lifetime components. These are τ_1=0.41ns (A_1=0.23 %), τ_2=1.56ns (A_2=77 %). The presence of these two components can be accounted for phase coexistence with more rigid phases corresponding to longer lifetimes. Longer lifetimes arise from more rigid environment presumably because more steric hindrance can take place, decreasing the number of pathways for energy decay.

It is worth pointing out that average lifetimes can vary significantly on a batch-to-batch level and that comparative measurements have to be taken using the same batch of cells on the same day.

Lifetime distributions in a membrane can be compared to a known environment such as the solvent in which the dye is dissolved. Here we used ethanol as solvent. **Figure VI-10** is a representation of average lifetimes found for individual pixels after IRF correction for 5µM DiI dissolved in ethanol. A window 160 x 160µm of the solution was scanned. The fluorescence decay could be fitted with a single exponential component.

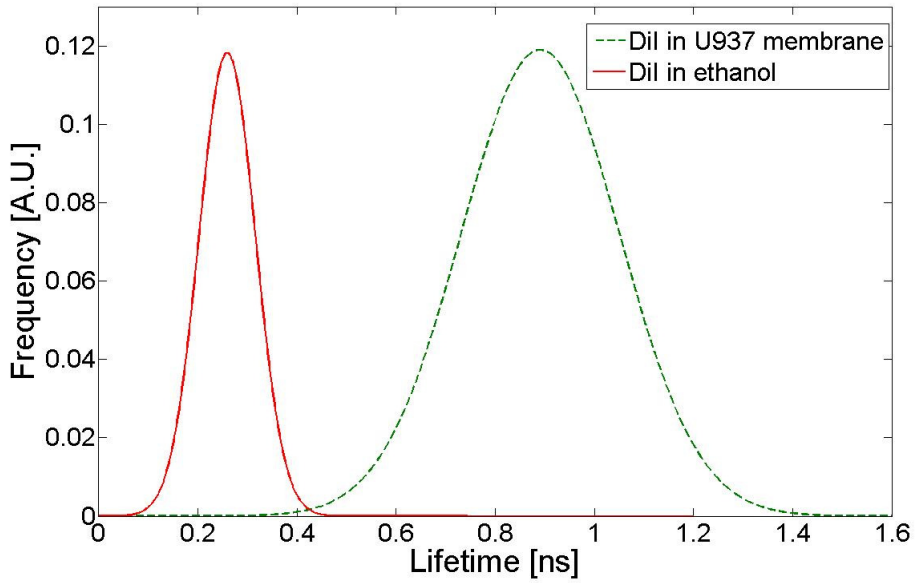


***Figure VI-10**. Fluorescence Lifetime histograms for 5µM DiI in ethanol. The Gaussian fit of the same dye in a U937 membrane is given for comparison.*

The Gaussian fits for the lifetime histograms had the functional form:

$$f(\tau) = Ae^{-\frac{(\tau-\mu)^2}{\nu^2}}$$ ***Eq. VI-1***

The fitting parameters were a mean value of 0.26ns and a variance of 0.08ns. As a comparison, the variance for the cell shown above was 0.23ns.

The dissolved dye in ethanol possesses a very short lifetime sharply centred on its average value. That indicates a homogeneous environment for the dye with easy change of the conformations of the molecules and provides a valuable control for FLIM measurements on live cell membranes.

For each pixel in a lifetime map, pre-exponential factors corresponding to each lifetime component were extracted. As a consequence, the intensity-normalized map of pre-exponential factors can also be drawn, as shown in **Figure VI-11** for the short lifetime component.

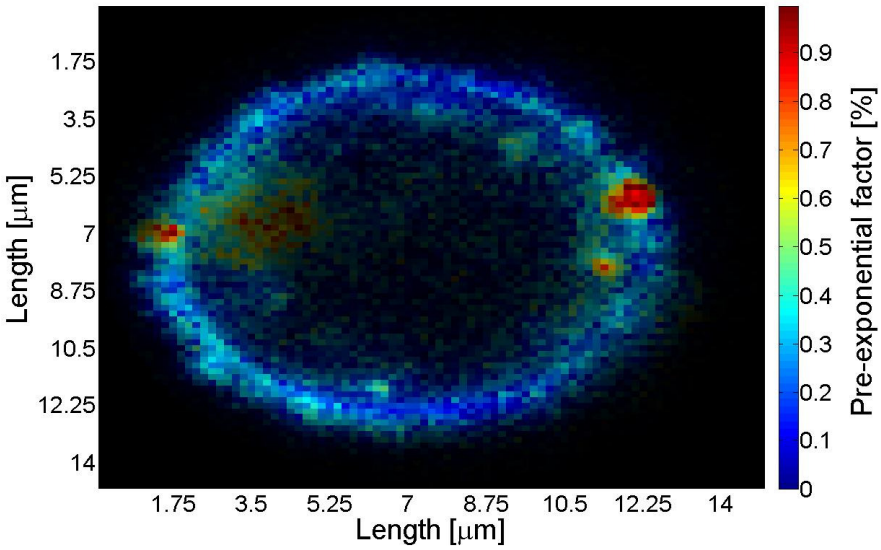


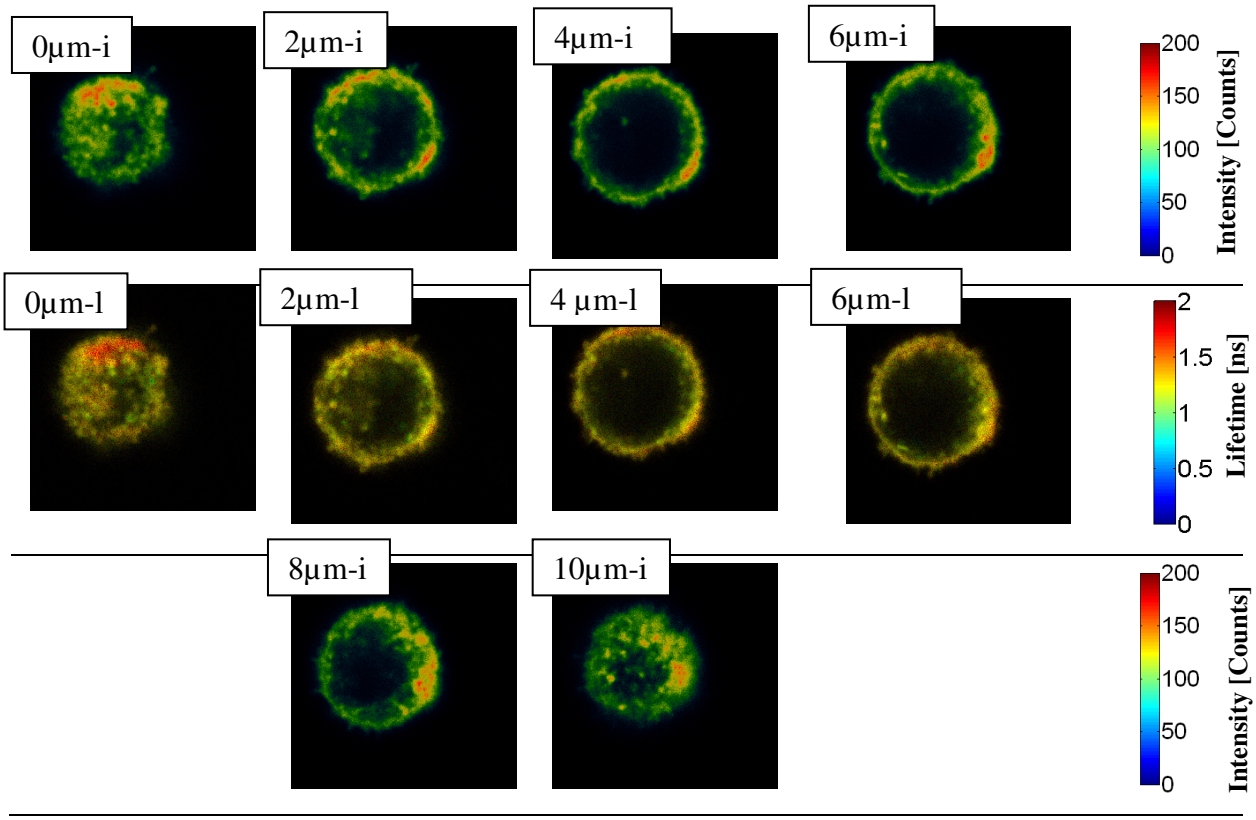
Figure VI-11*. Normalized pre-exponential factor map representing the weight of the short lifetime component. The map was weighted by intensity.*

The plot can be used in order to highlight regions where either low or long lifetimes dominate, as being representative of local long-lived degree of order.

As a summary, **Figure VI-8** demonstrates the ability of FLIM to interrogate dye environment. The intensity picture alone (**Figure VI-8A**) reflects regions with higher or lower dye concentration including exclusion areas. A FLIM picture of the same cell (**Figure VI-8B**) can further detail homogeneities of the dye local environment. A more detailed analysis of lifetime components reveals the pre-dominant distribution of longer/lower lifetimes (**Figure VI-11**) and gives insights into local ordering.

VI.4. 3D mapping

Two-dimensional confocal slices might not be representative of the global state of a membrane. Ideally, the 3D map of a whole cell has to be acquired. This is possible thanks to the high-resolution (piezoelectric) control of the microscope objective in the Z direction. In **Figure VI-12**, we show a succession of slices taken every 2 microns for a DiI labelled U937 cell.



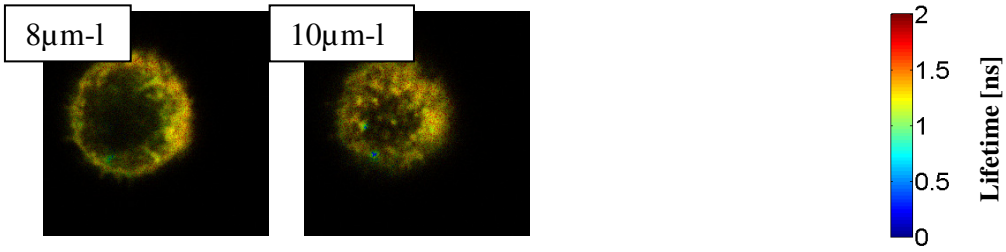


***Figure VI-12**. 2D slices of a DiI labelled U937 cell with focus moved upwards by steps of 2 microns from 0 to 10µm. Series **i** label intensity pictures, series **l** label FLIM maps.*

For each slice, 30 frames were acquired and the total acquisition time therefore reached 4 minutes. Focus dependent variations in the intensity and FLIM maps are seen but lifetime histograms extracted from a single slice are consistent with one another except for the first slice close to the substrate for which cell-surface interactions shift the histogram towards longer lifetimes. This is shown in **Figure VI-13**.

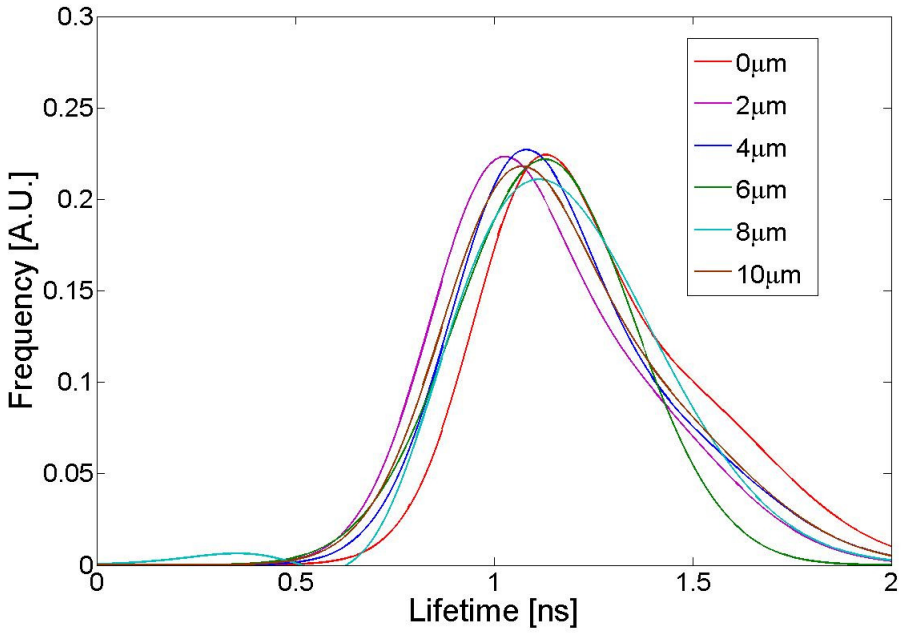


***Figure VI-13**. Lifetime histograms corresponding to each slice.0µm represents picture 1 in* Figure VI-12.

The long acquisitions times required for 3D mapping limit their current use but are bound to becoming routine for High-Content Screening (HCS) applications.[12]

VI.5. Fluorescence lifetime and fluidity

In order to confirm that longer lifetimes are seen in more rigid regions of the membrane, cholesterol has to be depleted from the cell. Cholesterol is abundant in mammalian cells with quantities in the region 30–50 mol % and is a direct modulator of membrane bilayer viscosity[13, 14]. The cholesterol extraction agent Methyl-Beta CycloDextrin (MBCD) is a 7 sugar ring molecules as shown in **Figure VI-14** and is routinely used to remove cholesterol from membranes.[13, 15, 16]

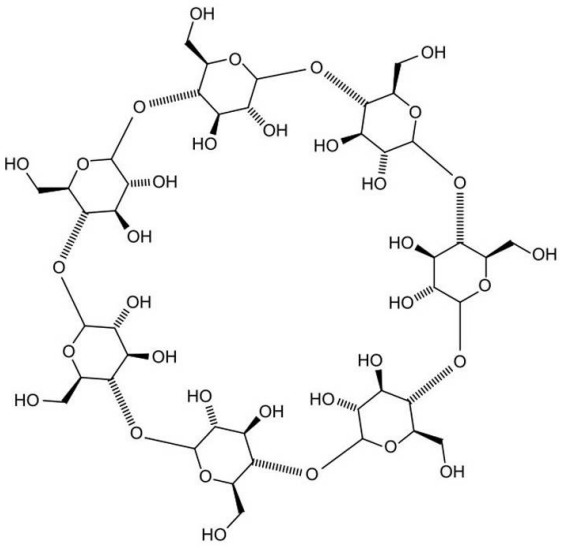


Figure VI-14*. Chemical structure of beta-cyclodextrin.*

Functionally, MBCD binds and extract cholesterol molecules but does not bind or inserts into the cell membrane.[17] There are also indications it may disrupt the cell cytoskeleton.[18] Cholesterol disruption defines the basic assay for characterizing fluidity and markers for fluidity in live cell membranes. Over a large number of cells (>50), statistical data can be collected to characterize the average lifetime of a dye as a function of cholesterol content, i.e. of membrane fluidity. Here, in **Figure VI-15**, the lifetime of DiI on U937 membrane was analyzed before and after 15 minutes treatment with 3mM MBCD dissolved in PBS. Concentration of MBCD has to be carefully chosen as too high levels (>5mM) result in significant membrane protein release which therefore affects membrane dynamics.[17] At the concentration level of MBCD used, most cholesterol was be extracted within 15 minutes.[13] The same batch of cells was analyzed to ensure reproducibility in the average lifetime found.

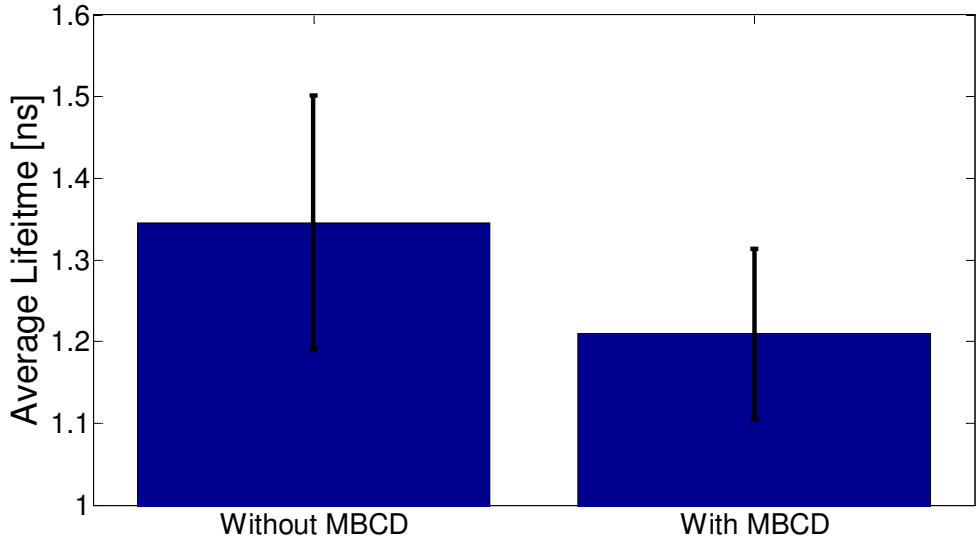


***Figure VI-15**. Exposure to MBCD reduces the average fluorescence lifetime of DiI in U937 plasma membranes.*

The average lifetime is seen decreasing by 0.15ns after MBCD treatment; this confirms lifetime of the dye decreases with increasing fluidity of the membrane it is inserted in.

VI.6. Colocalization of identical dyes in the membrane

As already mentioned, the incorporation of the dye in Jurkat cell membranes at RT is very unfavorable. The resulting dye localization is very inhomogeneous with hot spots of high concentrations appearing frequently. These high concentration spots do not represent evidence for molecular proximity because of the optical resolution limit. However, the lifetime of these hot spots is seen as much lower than other regions of the membrane. This is unexpected as fluorescence lifetime is independent of concentration. Here, this is believed to be due to a crowding effect leading to a homo-FRET process.

Homo-FRET occurs between identical fluorophores depending on the spectral overlap between the tail of the emission spectrum and the front of the absorption spectrum. In homo-FRET, the steady-state intensity as well as fluorescence lifetime of the dye remains unchanged. The usual technique to observe it is fluorescence anisotropy.[19]

For the DiO dye, the absorption and emission spectra were measured in ethanol. The superposition of these two plots is shown in **Figure VI-16** with a significant spectral overlap. This small Stokes shift means DiO is prone to undergoing homo-FRET.

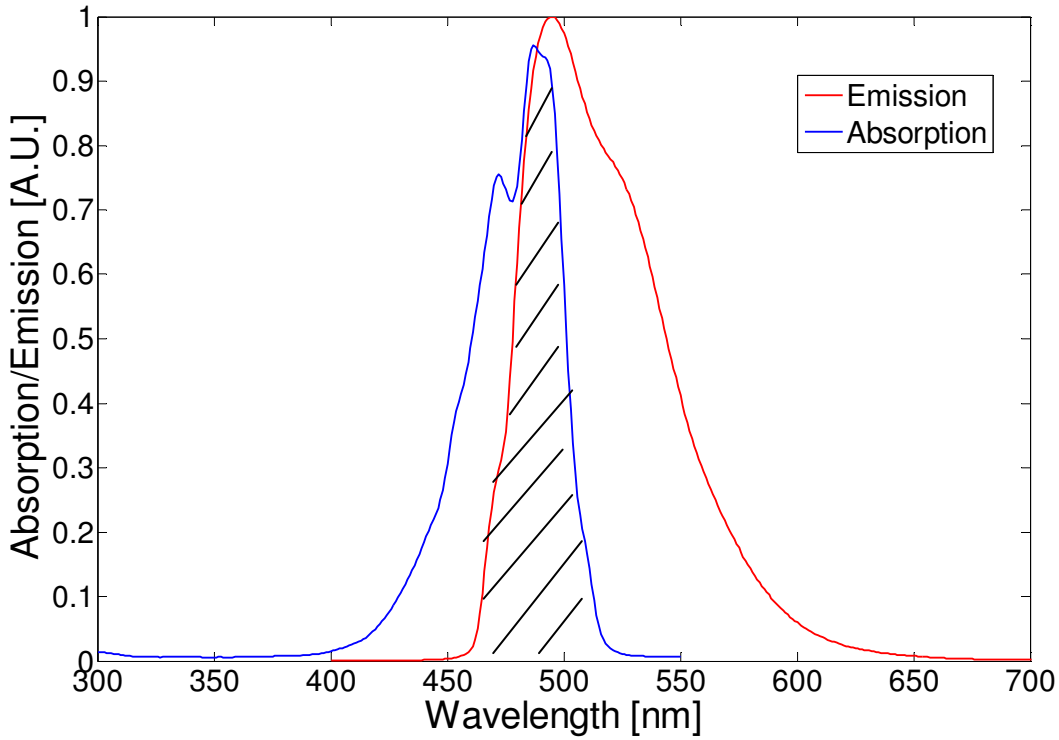


***Figure VI-16**. Absorption and emission spectra of DiO in ethanol. The spectral overlap is hatched.*

In cellular membranes, the environment provides many platforms for lipids to aggregate based on their differential interactions and it is therefore expected to result in homo-FRET events. **Figure VI-17** is an example of Jurkat cell labelled with DiO in typical conditions for uniform dye coverage and displaying intensity hot spots.

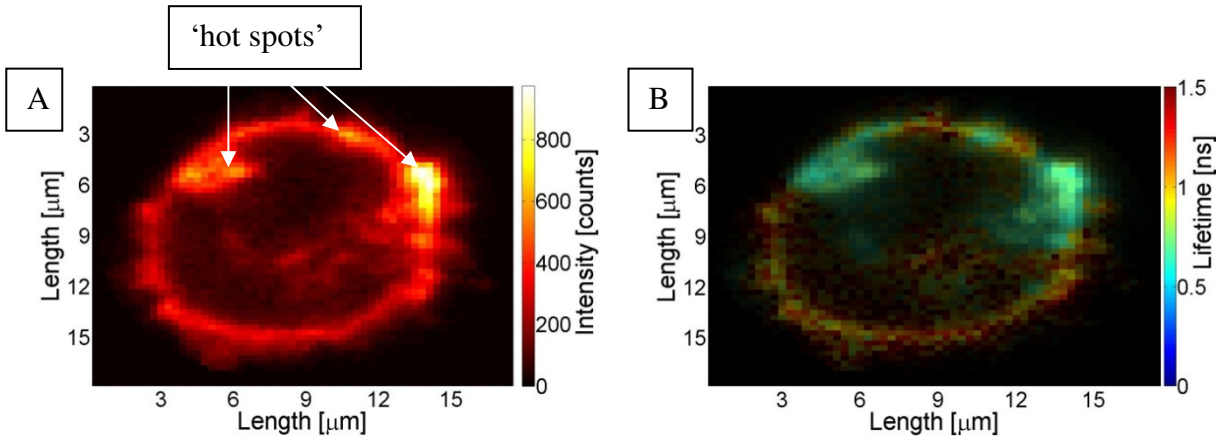


***Figure VI-17**. Example of a DiO labelled Jurkat cell with hot spots. **A**. Intensity map. **B**. Average lifetime map for the green channel.*

The high intensity regions of **Figure VI-17** had a corresponding lifetime in the green channel 30 % lower than the average seen on the rest of the membrane. The presence of these low lifetimes, here centred on 0.7ns is confirmed by the lifetime histogram plotted in **Figure VI-18** representing a bimodal distribution. The rest of the membrane had a Gaussian distribution centred on 1ns. These low lifetimes cannot originate from pile-up effects as data analysis shows that individual pixels within these spots had a number of photon counts lower than 4 per scan. Knowing that each pixel receives an average 85 pulses in typical scanning conditions (with a 20MHz laser repetition rate and a 512 x 512 scanning area), the acceptable number of photons is 5 % the repetition rate which translates into 4.25 photons.

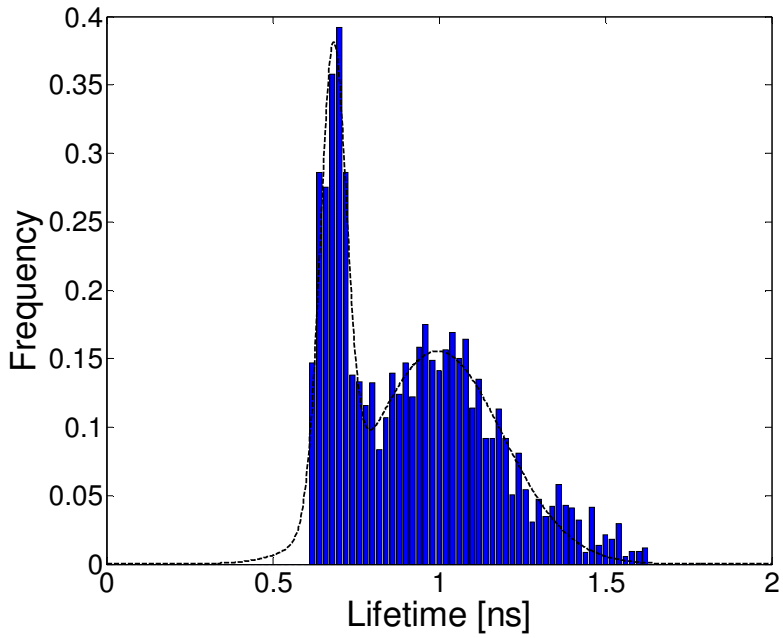


***Figure VI-18**. Lifetime histogram for the green channel highlighting the bimodal distribution*

In a reported intracellular experiment, the FRET pair CFP-YFP was found to undergo a concentration-dependent self-quenching which was attributed to the homo-FRET between spectrally shifted forms of the proteins.[20] Donors with proper location and orientation will therefore decay faster than others, a phenomenon which might be seen if dyes tend to dimerize or are in very close proximity in high numbers. In our setup, the spectral separation of photons between green and red channels allows readily monitoring of this particular form of homoFRET and might explain these low lifetimes values found in the green channel. Correspondingly, lifetimes higher than average were recorded in the red channel. This suggests the average lifetime over both channels would be close to the average lifetimes found elsewhere on the membrane.

The scatter plot shown in **Figure VI-19** is a measure of how lifetime is related to dye concentration. Each dot corresponds to one pixel belonging to the membrane of the Jurkat cell.

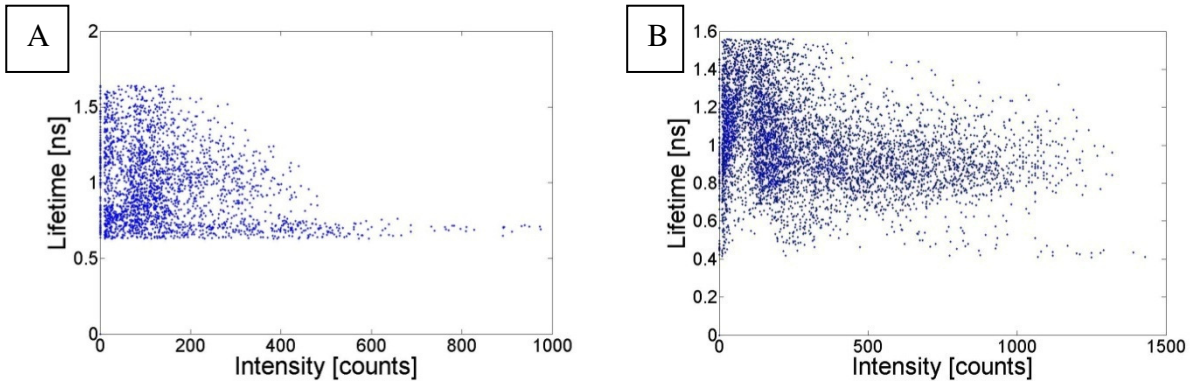


***Figure VI-19**. Scatter plot of intensity versus lifetime for each pixel analyzed in a FLIM map.*
***A**. for a cell having hot spots. **B**. for a cell without hot spots.*

For cells with hot spots (**Figure VI-19A**), the lifetime is seen gradually decreasing with increasing photon counts whereas a cell without hot spots has no obvious bias (**Figure VI-19B**).

These observations are likely due to a crowding effect of dyes and consistent with a model of concentration-dependent energy transfer previously reported.[20] Crowding effects were often seen when labelling with DiI or DiO, presumably because of their reported preference for rigid phases, where they either incorporate as aggregates or form spontaneously through

diffusion. Although colocalization of identical dyes can be an interesting tool in the study of dye organization dynamics, it should be minimized for applications targeting individual reporters in a cell membrane.

VI.6.1. Colocalization after cholesterol extraction

The correlation between dye colocalization and presence of cholesterol was examined. Jurkat cells were labelled with DiO for 15 minutes at RT which is a labelling format, as seen in **VI.2.1**, unfavorable for uniform incorporation of dye molecules. A cell aliquot was labelled with 3mM MBCD in PBS together with 5μM DiO while control cells were incubated with the same concentration of dye in PBS. The removal of cholesterol using MBCD produces a much more uniform labelling as shown in **Figure VI-20**.

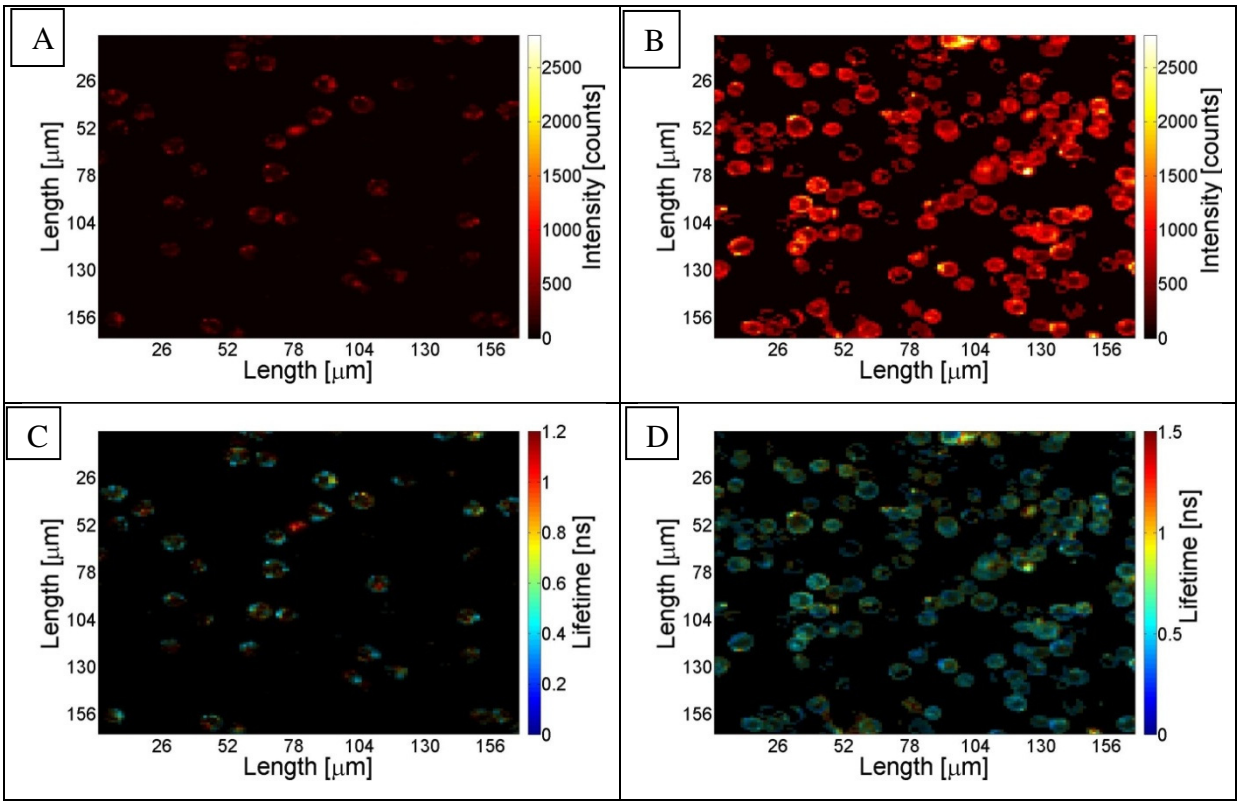


***Figure VI-20**. Intensity (**A** and **B**) and lifetime maps (**C** and **D**) when labelling at RT native cells and cells without cholesterol respectively. The same number of scans has been taken for comparison purposes.*

The lifetime histograms show the disappearance of the low lifetime peak when in the presence of a high number of aggregates.

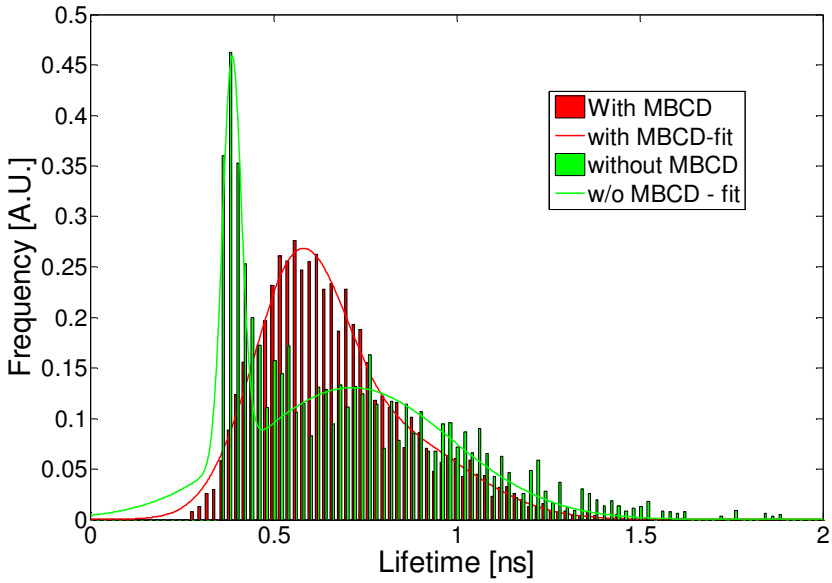


Figure VI-21**. Lifetime histogram with and without cholesterol extraction corresponding to the cells in **Figure VI-20

The fitting parameters for the histograms of **Figure VI-21** show a change of the Gaussian fit from 2 to 1 component indicating the removal of the high-concentration peak (**Table VI.3**).

	Before	**After**
μ [ns]	0.39-0.71	0.56
v [ns]	0.036-0.38	0.17

Table VI.3**. Fitting parameters for the lifetime histograms of **Figure VI-21

This study highlights the importance of cholesterol in the limited incorporation of DiO in Jurkat cells and the formation of dye-concentrated platforms.

VI.7. FLIM-FRET

VI.7.1. 2D unlinked FRET in a cell membrane

Chapter I stressed the importance of performing nearest-neighbour experiments and the suitability of FRET to that goal. It is worth pointing out that they make use of two unlinked dyes with suitable photo-physical properties, which are put into close proximity by thermodynamics effects. For instance, the presence or absence of FRET determines the tendency of 2 lipids to colocalize in the same type of domains. **Figure VI-22** shows a schematic of how this type of experiment is typically interpreted.

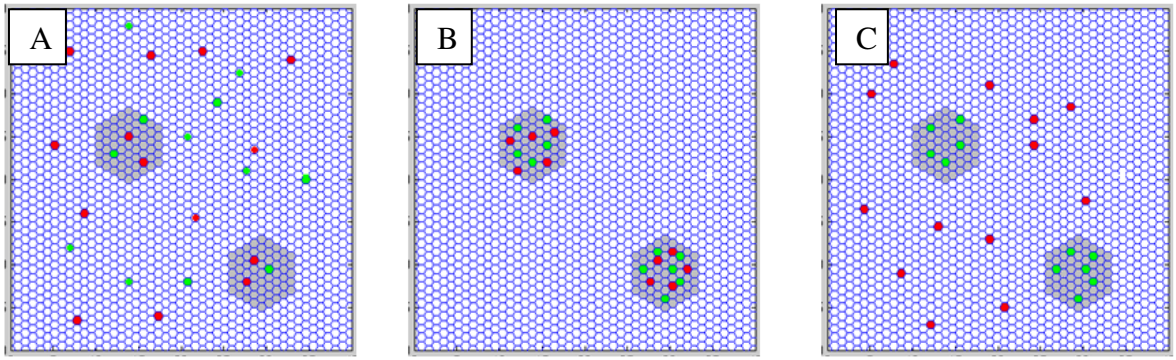


***Figure VI-22**. **A**. Random mix of donors and acceptors. **B**. Donors and acceptors in the same phase. **C**. donors and acceptors in different phases.*

In **Figure VI-22A**, donor and acceptor lipid analogues adopt a random distribution and the FRET signal is low. In contrast, donor and acceptor can strongly colocalize in one domain and result in a strong FRET signal (**Figure VI-22B**) or segregate into different phases with little or no FRET (**Figure VI-22C**).

The odds of seeing FRET events strongly depend on the relative concentrations of donors and acceptors. Typically, the concentration of acceptors should be much higher than that of donor to minimize homo-FRET while maximizing hetero-FRET. The direct consequence is that each donor will be in the presence of multiple acceptors, increasing the probability of energy transfer.

We simulated the random diffusion path of lipids over a schematic membrane to investigate the effect of diffusion on FRET. A FRET event is detected whenever one donor and one acceptor are located in adjacent locations. At each step of the simulation, every lipid is able to move to an adjacent cell in a 50 x 50 matrix, representing a 25nm x 25nm region of a

membrane. The equivalent dye density for the schematic membrane of **Figure VI-23A** would be 24:1000, a concentration much higher than practical dye loading.

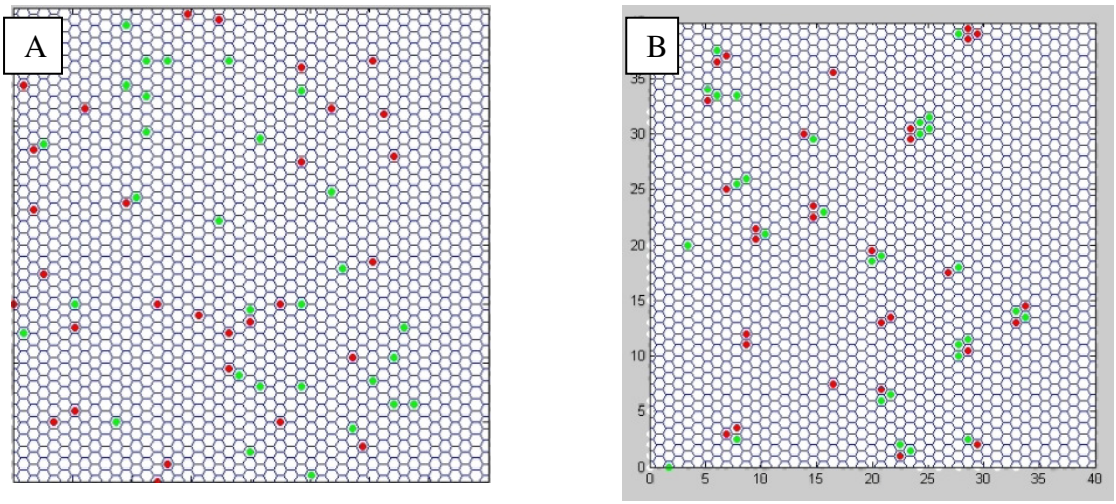


***Figure VI-23**. **A**. Schematic snapshot of lipid diffusion with no colocalization resulting in a random distribution of donors (green) and acceptors (red). **B**. Schematic snapshot in the presence of lipid colocalization.*

In the first instance, lipids do not tend to colocalize often and very a low number of door-acceptor pairs is seen (**Figure VI-23A**). This highlights the fact that FRET does not arise from random 2D motion of lipids. In contrast, lipids that strongly colocalize with no possibility of dissociation will generate many FRET platforms (**Figure VI-23B**).

Figure VI-24 shows the FRET signal after 50 steps of simulation as a function of donor/acceptor densities (supposed to be equal for simplicity).

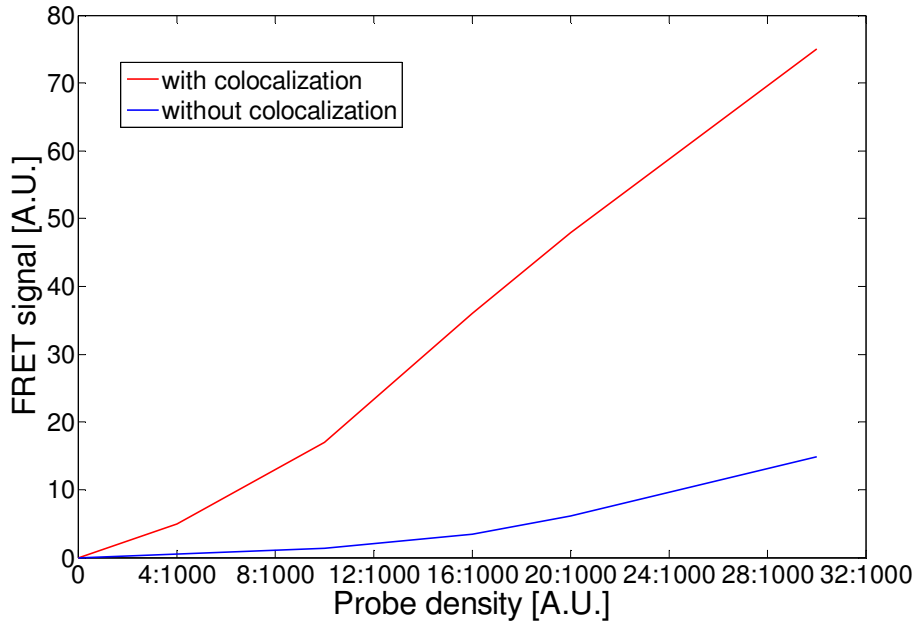


***Figure VI-24**. Simulated FRET intensity as a function of donor/acceptor initial density and colocalization events.*

A FRET signal 10 times higher is expected in presence of colocalization events. In practice, FRET occurs through long-range dipole-dipole interactions and lipids should be located inside a circle of Förster radius (5-6nm for DiO-DiD) to be able to generate FRET. This means there can be up to 10 lipid molecules separating them.

VI.7.2. Membrane FRET in U937 cells using DiO/DiD

DiO and DiD dyes are able to undergo FRET through their spectral overlap as seen in **Figure VI-25** showing the emission spectrum of 5µM DiO and absorption spectrum of 5µM DiD, both dissolved in ethanol.

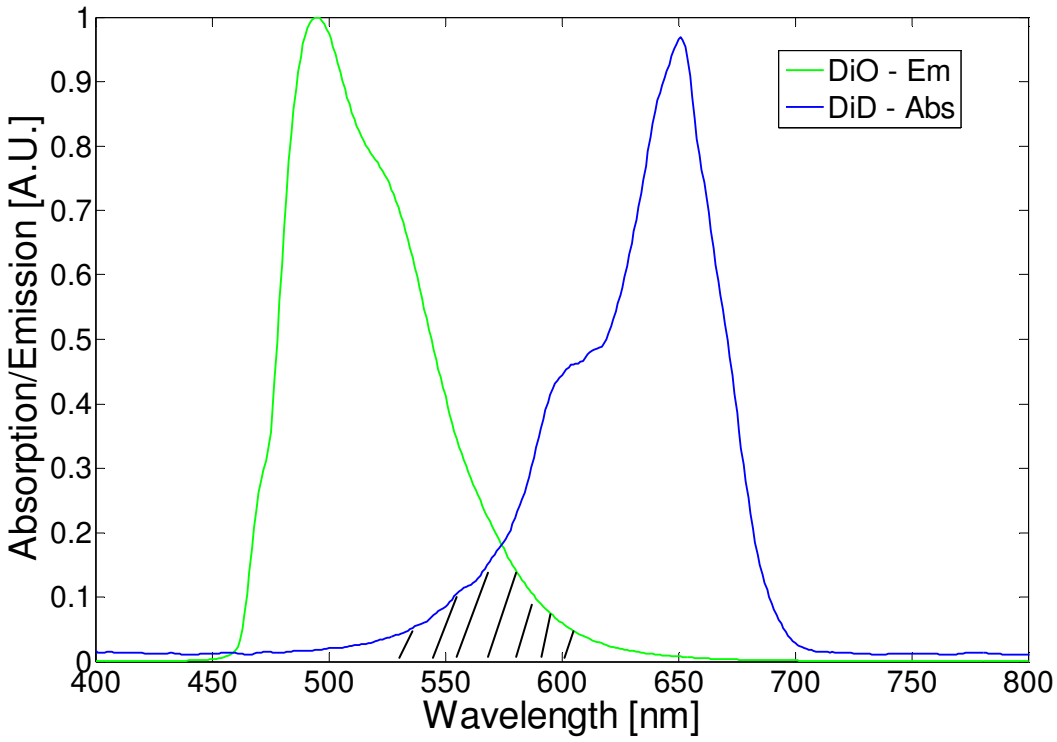


***Figure VI-25**. Emission spectrum of DiO and absorption spectrum of DiD shows the hatched spectral overlap needed for FRET.*

The Forster radius has already been reported to be around 5-6nm for this FRET pair.[9]

In order to qualitatively observe FRET, DiO and DiO + DiD labelled U937 cells were pipetted onto a microscope glass coverslip and left for 5 minutes to allow settling down. Part of the doubly labelled cells was incubated for 15 minutes in 3mM MBCD in PBS before being resuspended in plain PBS. Average lifetimes of individual cells in the green channel were subsequently extracted and plotted in **Figure VI-26**.

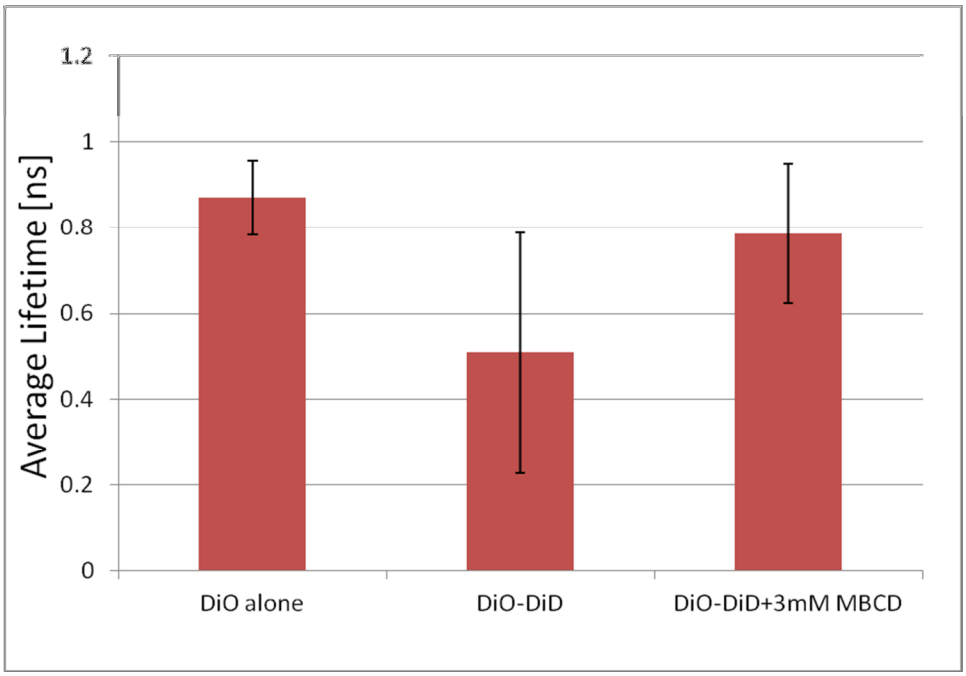


***Figure VI-26**. Average lifetime of DiO as a function of labelling conditions.*

Although intensity maps showed an increased red contribution, it is difficult to assign true FRET events and leakage emission of the acceptor dye as local concentration of acceptor dyes cannot be easily quantified. In contrast, FRET was readily detected as a decrease in average lifetime from 0.9ns to 0.5ns, which is a 44 % decrease. The efficient quenching of the donor dye confirms DiO and DiD strongly colocalize. The level of FRET did vary greatly on a cell by cell basis which has to be related to dye loading reproducibility already discussed in **paragraph VI.2.1**.

Finally we studied the influence of cholesterol for the formation of FRET platforms. After 15 minutes incubation in 3mM MBCD, the lifetime of FRET cells is seen as recovering to higher values. This indicates a disruption of FRET domains. However, the exact amount of disruption is hard to assess as DiO will see its lifetime simultaneously decrease with the reduction in cholesterol content as discussed in **paragraph VI.5**.

VI.8. Summary

FLIM has the potential to resolve long-lived domains with sizes close to the diffraction limit of the detection instrument. Although this is clearly a limitation for fast dynamic events, it

provides a clear global overview of the state of a membrane while keeping high spatial resolution.

Fluorescence measurements of carbocyanine lipid analogs showed large non-uniformities in their lateral distribution, even using optimum labelling conditions. This is accounted because of their preference for more rigid phases present in the membrane. Local heterogeneities are seen as a widening of the FWHM in the lifetime histograms of such dyes.

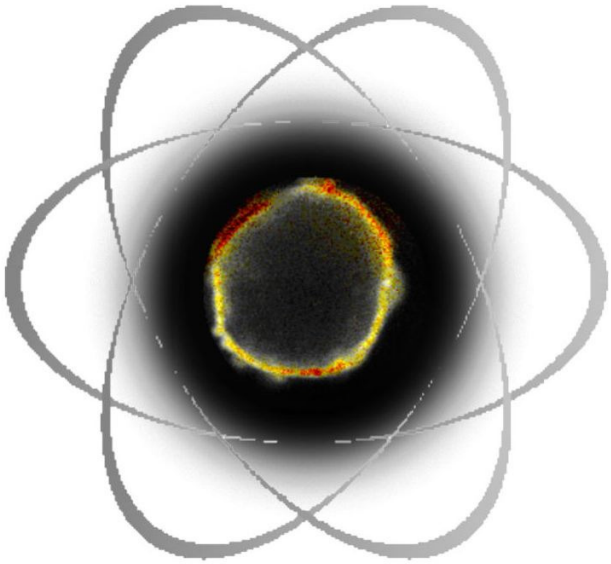
The colocalization of single probes within a membrane was most likely producing homo-FRET signals that were seen as an effective lifetime decrease in the green channel of the FRET detection path. These homo-FRET effects were greatly attenuated in the absence of cholesterol suggesting the dyes aggregate in cholesterol-rich domains.

Studies involving doubly labelled cells demonstrate the existence of FRET and its sensitivity to cholesterol depletion. They form the basis of the assays performed in dielectrophoretic cages and presented in **Chapter VII**.

VI.9. References

(1) Owen, D. M.; Neil, M. A. A.; French, P. M. W.; Magee, A. I. *Seminars in Cell & Developmental Biology* **2007**, *18*, 591-598.
(2) Edel, J. B.; Eid, J. S.; Meller, A. *Journal of Physical Chemistry B* **2007**, *111*, 2986-2990.
(3) Robinson, T.; Schaerli, Y.; Wootton, R.; Hollfelder, F.; Dunsby, C.; Baldwin, G.; Neil, M.; French, P.; Demello, A. *Lab Chip* **2009**, *9*, 3437-3441.
(4) Benninger, R. K. P.; Koc, Y.; Hofmann, O.; Requejo-Isidro, J.; Neil, M. A. A.; French, P. M. W.; deMello, A. J. *Analytical Chemistry* **2006**, *78*, 2272-2278.
(5) Verveer, P. J.; Squire, A.; Bastiaens, P. I. H. *Biophysical Journal* **2000**, *78*, 2127-2137.
(6) Bacia, K.; Scherfeld, D.; Kahya, N.; Schwille, P. *Biophysical Journal* **2004**, *87*, 1034-1043.
(7) Schwille, P.; Korlach, J.; Webb, W. W. *Cytometry* **1999**, *36*, 176-182.
(8) Gullapalli, R. R.; Demirel, M. C.; Butler, P. J. *Physical Chemistry Chemical Physics* **2008**, *10*, 3548-3560.
(9) Sengupta, P.; Holowka, D.; Baird, B. *Biophysical Journal* **2007**, *92*, 3564-3574.
(10) Davey, A. M.; Walvick, R. P.; Liu, Y. X.; Heikal, A. A.; Sheets, E. D. *Biophysical Journal* **2007**, *92*, 343-355.
(11) Stockl, M.; Plazzo, A. P.; Korte, T.; Herrmann, A. *Journal of Biological Chemistry* **2008**, *283*, 30828-30837.
(12) Heise, B.; Sonnleitner, A.; Klement, E. P. *Microscopy Research and Technique* **2005**, *66*, 312-320.
(13) Hao, M. M.; Mukherjee, S.; Maxfield, F. R. *Proceedings of the National Academy of Sciences of the United States of America* **2001**, *98*, 13072-13077.
(14) Goodwin, J. S.; Drake, K. R.; Remmert, C. L.; Kenworthy, A. K. *Biophysical Journal* **2005**, *89*, 1398-1410.
(15) Orr, G.; Hu, D. H.; Ozcelik, S.; Opresko, L. K.; Wiley, H. S.; Colson, S. D. *Biophysical Journal* **2005**, *89*, 1362-1373.
(16) Christian, A. E.; Haynes, M. P.; Phillips, M. C.; Rothblat, G. H. *Journal of Lipid Research* **1997**, *38*, 2264-2272.
(17) Ilangumaran, S.; Hoessli, D. C. *Biochemical Journal* **1998**, *335*, 433-440.
(18) Chichili, G. R.; Rodgers, W. *Cellular and Molecular Life Sciences* **2009**, *66*, 2319-2328.
(19) Gautier, I.; Tramier, M.; Durieux, C.; Coppey, J.; Pansu, R. B.; Nicolas, J. C.; Kemnitz, K.; Coppey-Moisan, M. *Biophysical Journal* **2001**, *80*, 3000-3008.
(20) Grailhe, R.; Merola, F.; Ridard, J.; Couvignou, S.; Le Poupon, C.; Changeux, J. P.; Laguitton-Pasquier, H. *Chemphyschem* **2006**, *7*, 1442-1454.

Chapter VII. Membrane FRET assays for membrane dynamics



This chapter presents the use of high-resolution time-resolved imaging for membrane assays performed within dielectrophoretic traps. A proof-of-concept assay for real-time FRET monitoring on live cell membrane is described. The simultaneous measurement of FRET disruption upon cholesterol extraction for multiple cells shows the potential of such tool for single cell high-content screening applications.

VII.1. Methodology for membrane assays

Membrane assays were performed following 6 main steps that are schematically represented in **Figure VII-1**. The first step consists in the flooding of the fluidic microchannel with cells by injecting them at high density (>10^5cells/mL) over the patterned electrodes array, which typically had 7 x 18 traps (c.f. **Chapter III.5.2**). This was done by filling a 1mL plastic syringe with the cell solution and manually pushing them through a connected Teflon tubing of internal diameter 200µm towards the microfluidic channel of width 1mm and height 120µm. Next, an electric field was applied to allow for DEP trapping of single cells. Typically, initial wide scans of the fluorescence map were acquired and cells with sufficient fluorescence counts were selected for preliminary imaging at high resolution (50nm pixel size). This served as a preliminary control and defined the original response of the assay. Flow was subsequently initiated by connecting the syringe to a syringe pump, sucking in reagents such as fluorescent dyes loaded in an Eppendorf towards the capture zone. This step also served as a washing step for untrapped cells. Flow velocity was kept low by the help of the visual feedback of untrapped cells being washed away. After a sufficient incubation time, imaging was finally done to extract single cell responses.

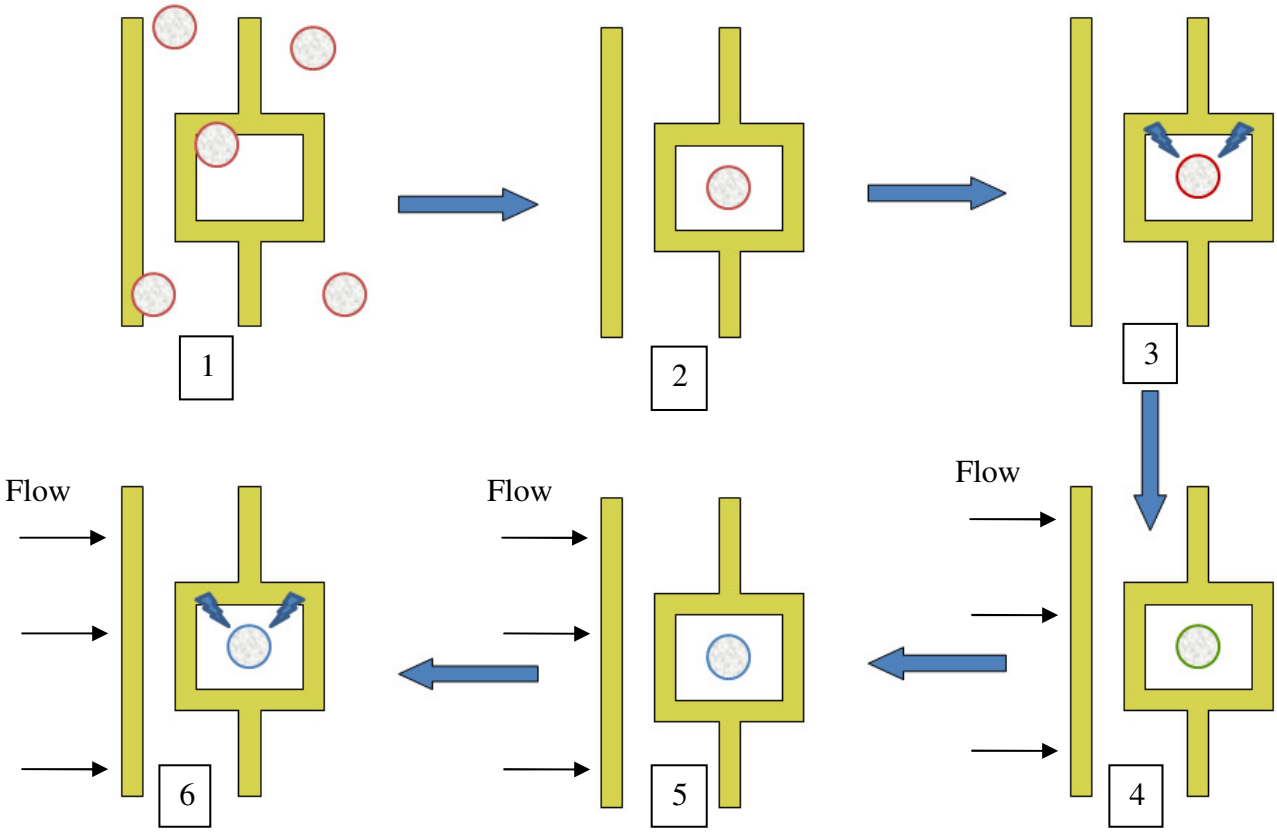


***Figure VII-1**.Single cell membrane assays in DEP traps were performed by following 6 steps. **1**. Incubation of cells at high density. **2**. DEP trapping. **3**. Imaging of selected cells. **4**. Addition of reagent. **5**. Incubation **6**. End-point imaging of selected cells.*

VII.2. Effect of electric field on fluorescence lifetime measurements

VII.2.1. Excluding electrode contributions

Often, non-specific binding or auto-fluorescence of gold meant a fluorescent signal was detected on the electrodes. For efficient fitting of fluorescent decays, these regions were cropped out as shown in **Figure VII-2A** and only photons emitted from the trapped cell were analyzed. The FLIM map obtained by including all photon counts in the fluorescence decay gives an inconsistent map (**Figure VII-2B**) whereas the analysis of only relevant pixels produces a better lifetime map (**Figure VII-2C**).

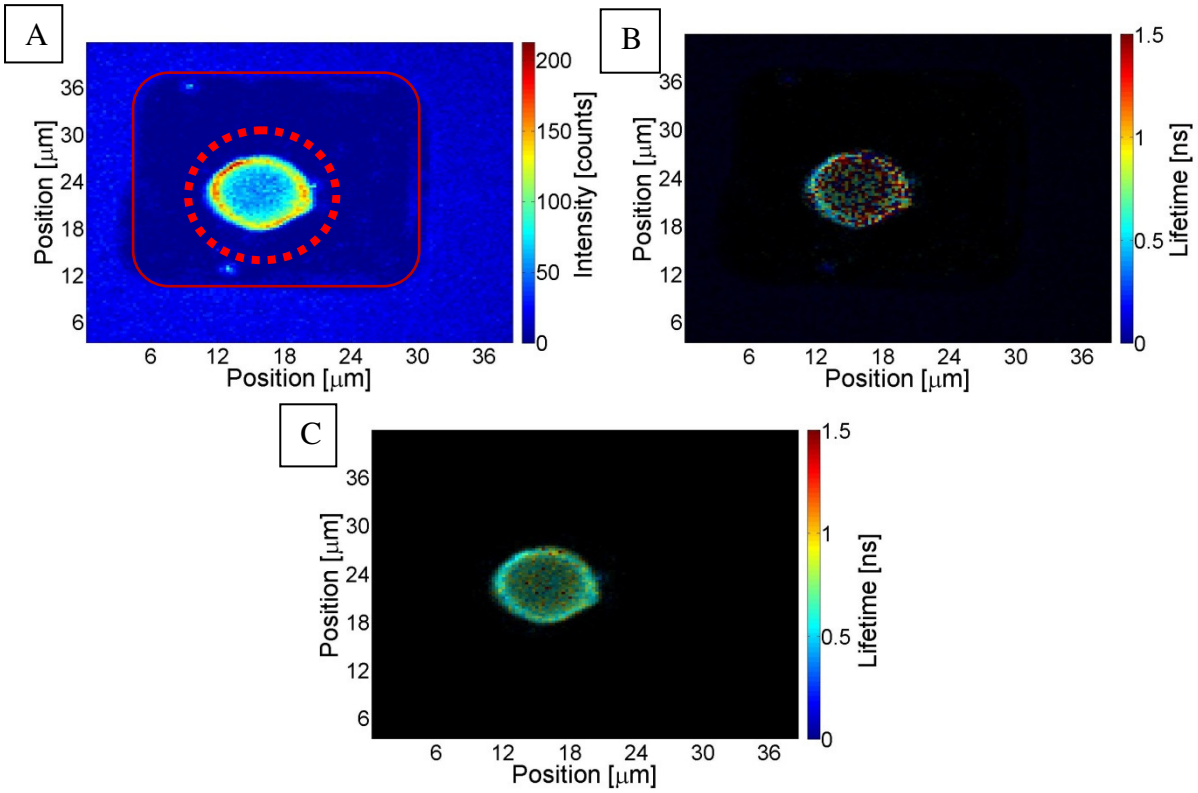


***Figure VII-2**. **A**. Intensity picture of a Jurkat cell in a square nDEP trap. Electrode contribution is apparent. The rounded square highlights the electrode edges while the dashed circle shows the pixels used to produce figure C. **B**. FLIM map including the contribution of the electrodes in the overall fluorescence decay fit. **C**. FLIM map excluding electrode contributions.*

VII.2.2. Fluorescence lifetime and electric fields

One requirement for performing fluorescence lifetime assays in DEP traps is that the electric field does not significantly alters the photo-chemical properties of the dyes under investigation. Examples of voltage-sensitive dyes include di-4-ANEPPS or di-4-ANEPPDHQ. Literature studies indicate that carbocyanine dyes with short alkyl-chain lengths do exhibit voltage dependent photo-physics (for example for $DiOC_6(3)$) whereas long alkyl chain lengths dyes do not.[1]

Here we analyzed fluorescence lifetime change of DiO labelled Jurkat cells when applying an external electric field. We first imaged a cell floating over the trapping area to record the original FLIM map before turning on the electrodes at $5V_{pp}$-100kHz and scanning the cell

after it was kept trapped for 5 minutes (**Figure VII-3**). The qualitative motion of the cell is shown in **Figure VII-3** with superimposed fluorescent scans before and after trapping.

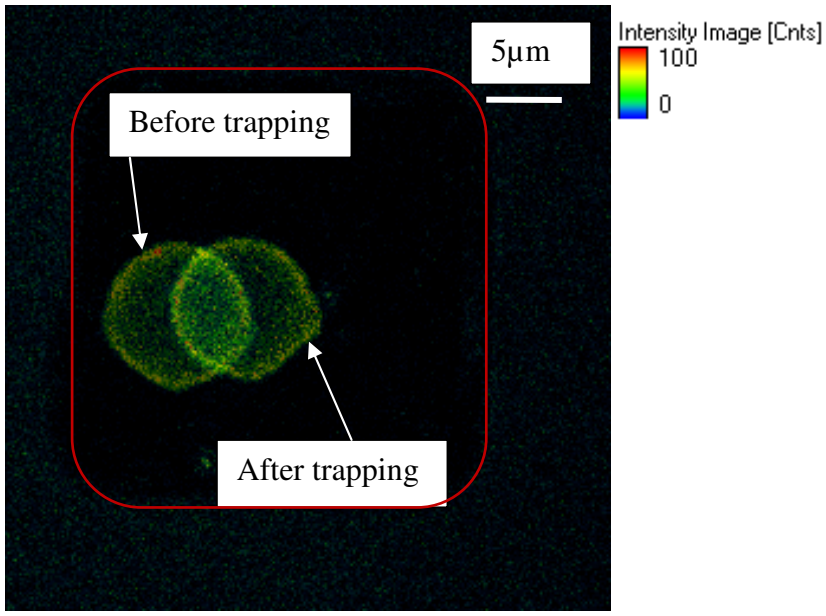


***Figure VII-3**. Qualitative motion of a cell showing superimposed fluorescence snapshots before and after trapping. The edge of the trap is highlight by a red square.*

The lifetime histograms corresponding to the pre- and post-trapping situations is displayed in **Figure VII-4** with the Gaussian fitting parameters summarized in **Table VII.1**.

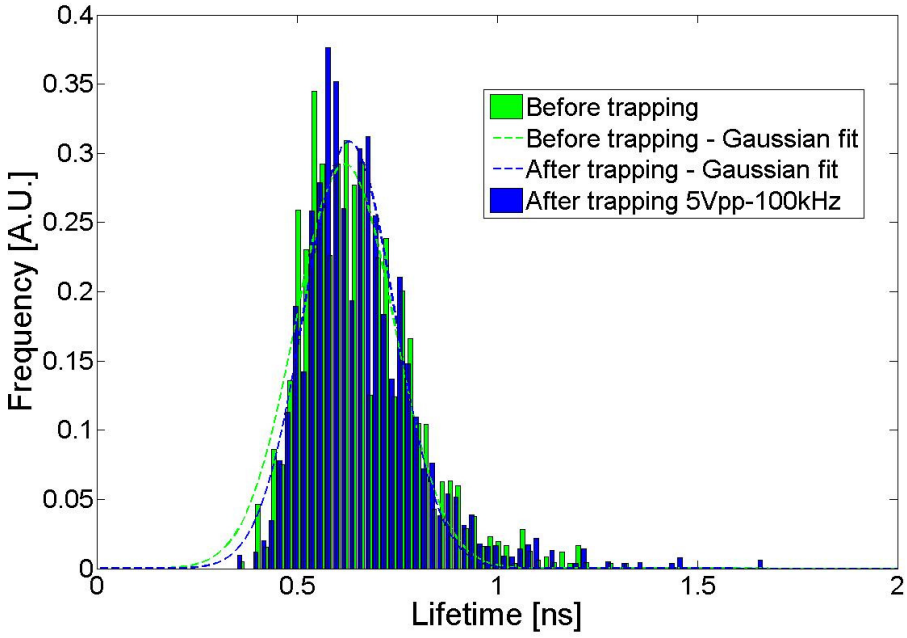


***Figure VII-4**. Lifetime histograms for DiO in absence and presence of an electric field.*

	Before trapping	After trapping
τ [ns]	0.63	0.62
v [ns]	0.16	0.17

Table VII.1**. Gaussian fitting parameters for the lifetime histograms of **Figure VII-4.

As the membrane behaves like a high-pass filter, higher AC frequencies will not significantly increase the transmembrane potential and as such not change the lifetime of the dye. The lifetime histograms plotted in **Figure VII-4** show that average lifetime as well as Gaussian fit. Importantly, this indicates that no voltage dependence on lifetime was observed and that DiO can be used for subsequent assay studies in a DEP trap.

VII.3. DiO/DiD FRET colocalization assay on Jurkat cell membranes

As stated in **Chapter VI**, colocalization of molecules in membranes has to be studied using increasing high concentrations of FRET acceptors. For this reason, membrane FRET is typically studied with acceptor dyes in large excess compared to donor dyes in order to minimize homo-FRET events between donor dyes and maximize hetero-FRET. The resulting FRET efficiency versus FRET acceptor concentration dose response curve is a direct measure of the tendency for two probes to share the same domain. Typically, each point of the dose response curve is obtained by averaging FRET efficiencies for a large number of cells having a known acceptor concentration deduced from incorporation rate of the dye into the membrane (linked to dye incubation time, incubation temperature and concentration).[2] This methodology, however, cannot be transferred to single cell measurements without means to trap and track single cell response over time. Following this principle, we studied the response of FRET acceptor incorporation (DiD) into the membrane of a U937 cell pre-labelled with FRET donor DiO.

VII.3.1. Initial state

A Jurkat cell was trapped at $5V_{pp}$-1MHz and imaged before bringing in the labelling agent DiD. The corresponding intensity maps for the green and red channels as well as the lifetime map for the green channel are displayed in **Figure VII-5**.

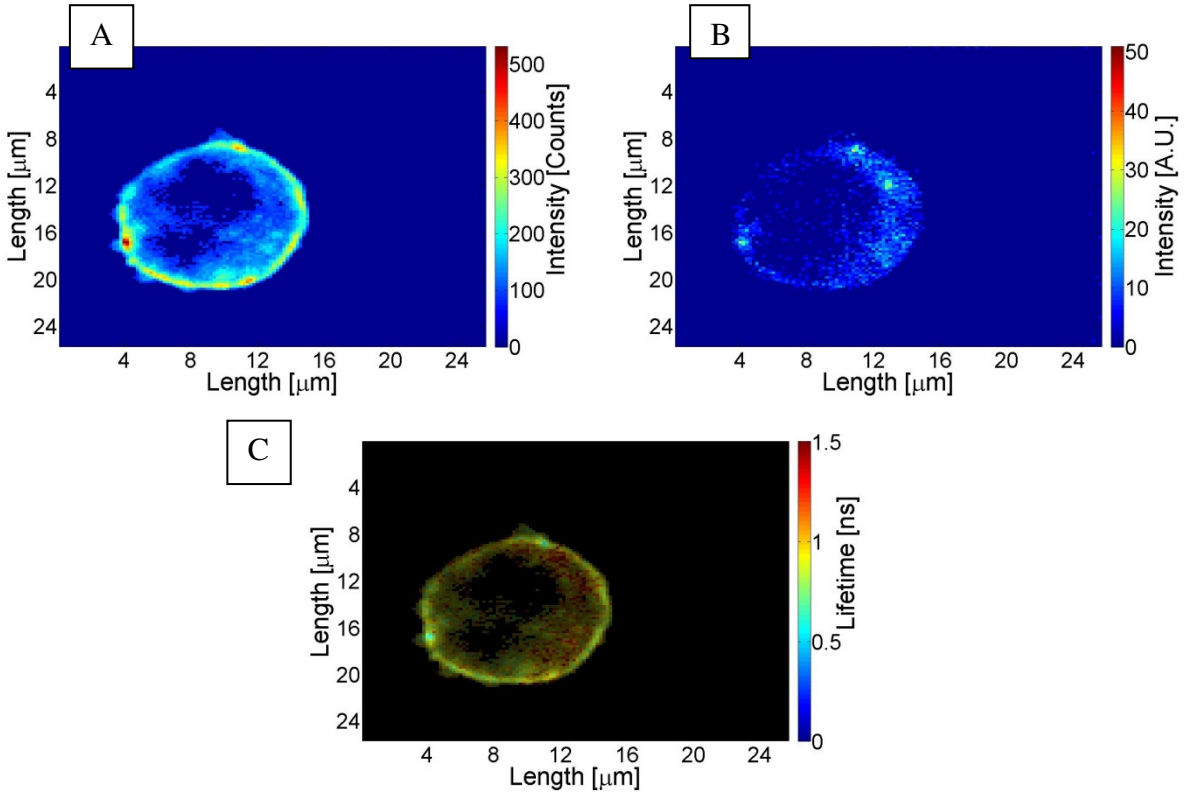


***Figure VII-5**. Intensity map for a DiO-labelled Jurkat cell in the green (**A**) and red (**B**) channel. **C**. FLIM map for the green channel.*

Fluorescence leakage of DiO in the red channel was seen less than 5% which is consistent with the emission spectrum of DiO (c.f. **Chapter VI.6**). The lifetime map shows very little crowding effects and thus little homo-FRET at the start of the analysis.

VII.3.2. Acceptor dye incorporation

A solution of 5µM DiD in a Phosphate-Buffered Saline (PBS) solution was subsequently injected in the flow channel at 0.2µL/min. The starting of the labelling time was approximated by taking flow rate and length of the tubing into account. After around 1 minute incubation in the highly concentrated DiD solution, the cell was scanned at the same focal plane as the initial state. The resulting intensity and lifetime maps are shown in **Figure VII-6**. The solution was flown from the bottom of the pictures shown.

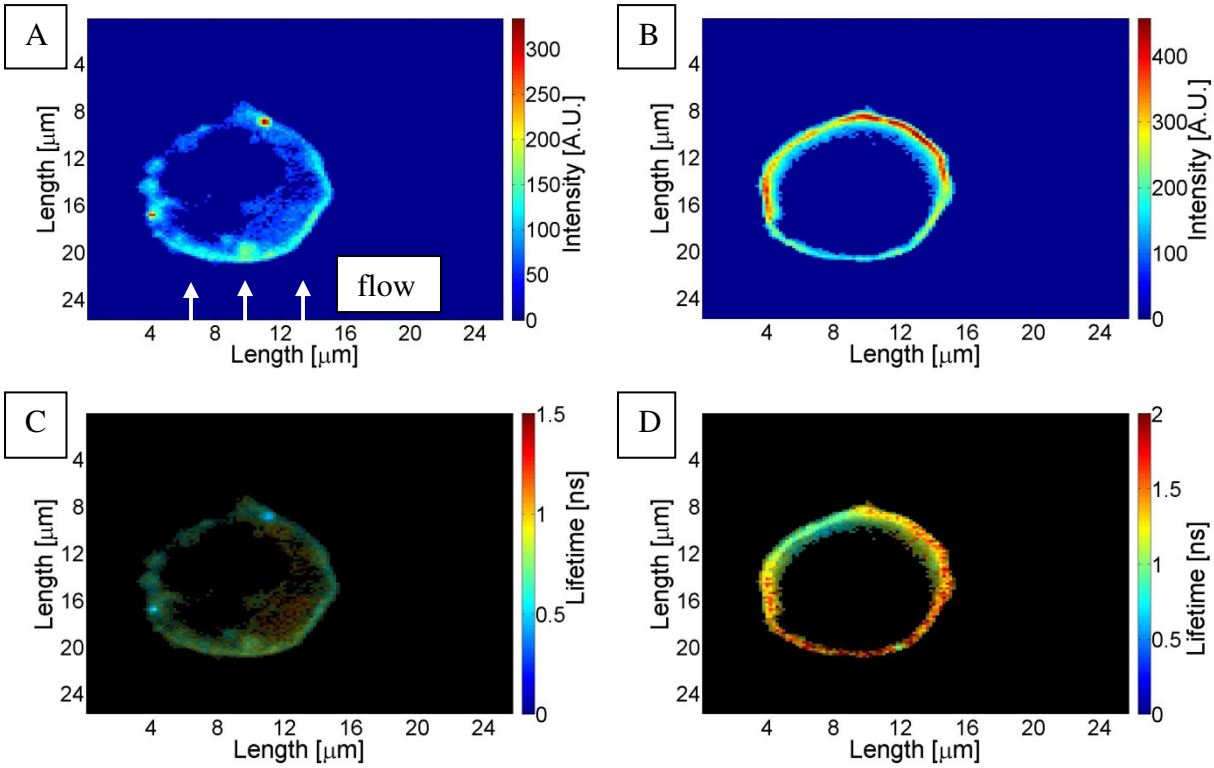


***Figure VII-6**. Intensity map after 1 minute incubation in a 5µM DiD solution for the green (**A**) and red (**B**) channels. **C**-**D**. FLIM maps for the green and red channel respectively.*

The maps shown in **Figure VII-5** and **Figure VII-6** are taken from the same number of scanning frames for comparison purposes. The intensity in the green channel is seen decreasing to an average 120 counts per pixel down from 200 while the red channel has counts up to 400. For the green channel, the actual photon count results from a combination of photobleaching and the quenching of the dye DiO due to FRET. For the red channel, photons detected at the acceptor photo-detector come either from FRET contribution or non-FRET DiD dyes alone. The intensity mapping alone allows detection of regions with high count values but cannot single out FRET/non-FRET events. Indeed, the constant incorporation and resulting high concentration of DiD molecules may be sufficient to be detected even though the dye has only a 1% absorption of laser excitation at 488nm. However, control cells labelled with DiD alone at the same concentration had a maximum number of counts per pixel lower than 100 under the same experimental conditions.

The lifetime map of the green channel shows a shift in average lifetime from 0.88ns down to 0.72ns (based on the thresholded pixels displayed in **Figure VII-6**) which can be explained by the presence of FRET events. The rather uniform low lifetimes seen is an indication that

most DiO are in the presence of DiD molecules even after very short labelling times. This is probably because the incorporation of the acceptor dye is not diffusion-limited when it is kept flowing over the cell.

Simultaneously, the red lifetime shows large lateral heterogeneities in lifetimes which are due to the presence of two dye populations: the dye diffusing alone on the membrane and FRET complexes. Acceptor lifetime is expected to increase in the presence of FRET with the presence of a rise component although there is currently no simple analytical model for quantifying acceptor lifetimes in a 2D unlinked FRET format.[3]

Next, scans were acquired at different labelling times, namely 1 minute, 3 minutes and 5 minutes. The normalized lifetime histograms for the green channel for the initial state and these different labelling times are displayed in **Figure VII-7**.

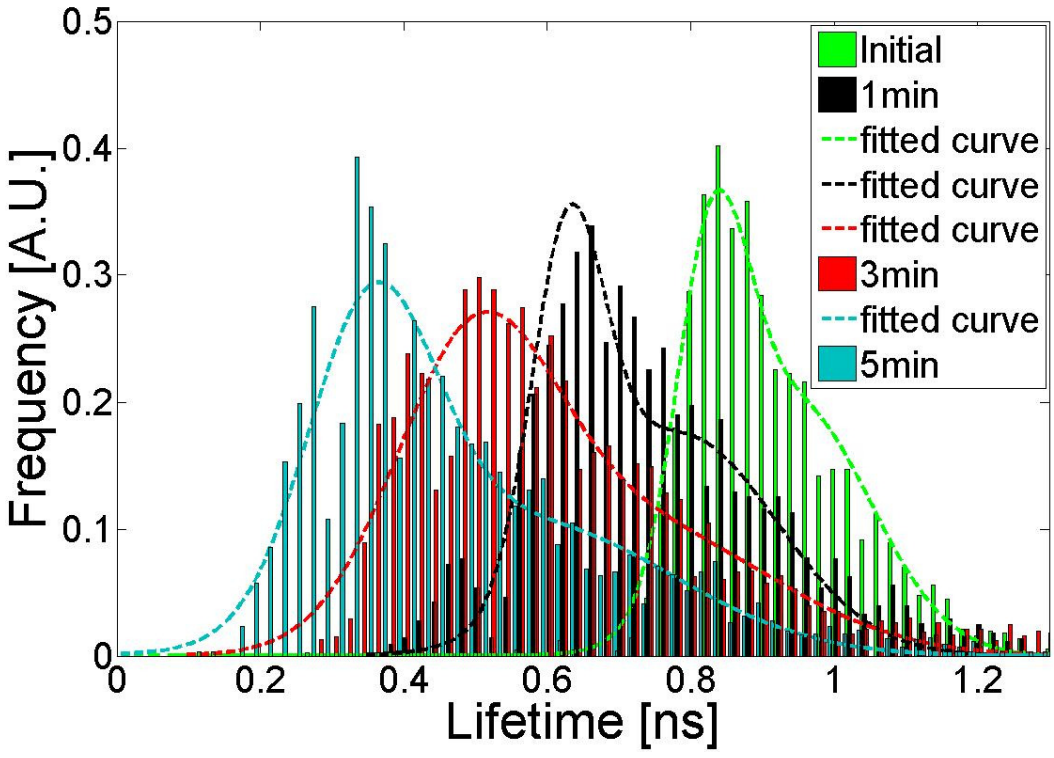


***Figure VII-7**. Normalized lifetime histograms for the green channel at different times during DiD incorporation.*

The average lifetimes are seen gradually decreasing and this is confirmed by the lower component of the 2 components Gaussian fits summarized in **Table VII.2**.

	Initial	**1 minute**	**3 minutes**	**5 minutes**
τ_1 [ns]	0.83	0.62	0.47	0.36
v_1 [ns]	0.07	0.07	0.05	0.12
τ_2 [ns]	0.94	0.79	0.63	0.58
v_2 [ns]	0.15	0.19	0.18	0.28

***Table VII.2**. Two components Gaussian fitting parameters: average lifetimes and variances for the green channel at different times of labelling.*

The variance of the fits is seen increasing after DiD incubation which also suggests that DiO undergoes FRET with a broad range of efficiencies as well as no FRET. However, this is also due to statistical fitting errors made as the number of detected photons in the green channel goes from 250 in average over the membrane pixels for the initial picture down to 50 after 5 minutes incubation. Both Gaussian components are seen decreasing monotonically which correlates the idea of increased FRET efficiency over time.

The normalized lifetime histograms in the red channel show a quick decrease in average lifetimes and thinning of the Gaussian distributions (**Figure VII-8** and **Table VII.3**). Upon long incubation times, the variance of the lifetime histograms went back to values found for single dyes in a membrane indicating a more homogeneous dye environment. This all points to a dominant contribution of non-FRET DiD molecules for long incubation times.

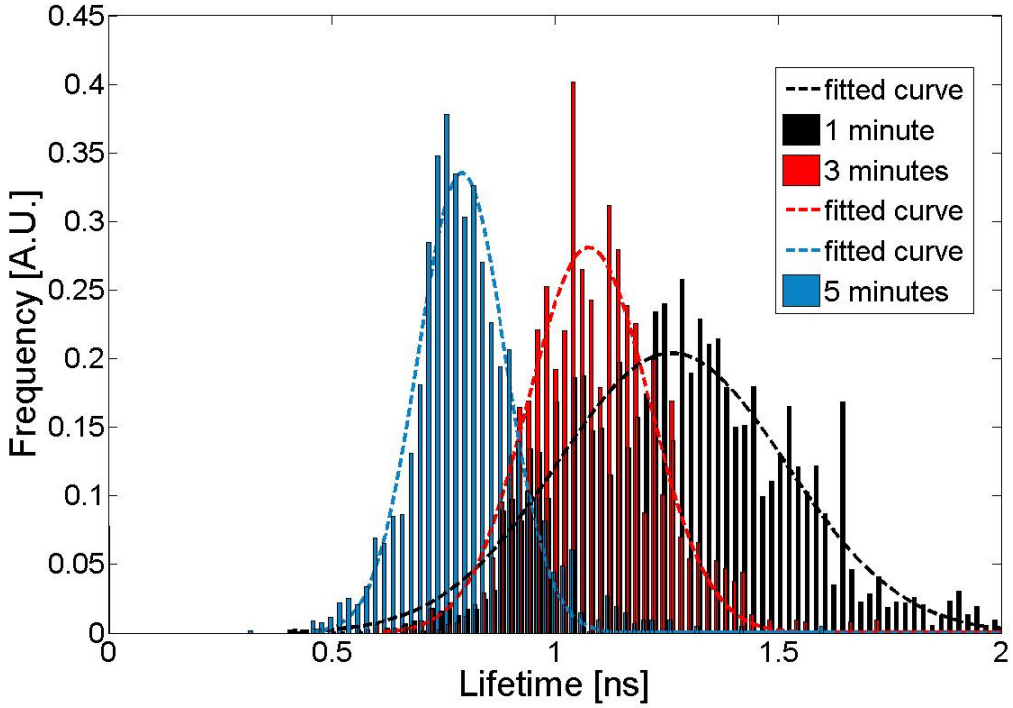


***Figure VII-8**. Lifetime histograms for the red channel at different times of DiD labelling*

1 minute		**3 minutes**		**5 minutes**	
τ [ns]	**v [ns]**	**τ [ns]**	**v [ns]**	**τ [ns]**	**v [ns]**
1.17	0.40	0.99	0.20	0.76	0.15

***Table VII.3**. Mean and variance of Gaussian fits for the lifetime histogram at different FRET acceptor labelling times*

The FRET efficiency can be found by integrating the donor fluorescence decay curves for the recorded TCSPC files as described in **Chapter II**. The resulting plot is depicted in **Figure VII-9**.

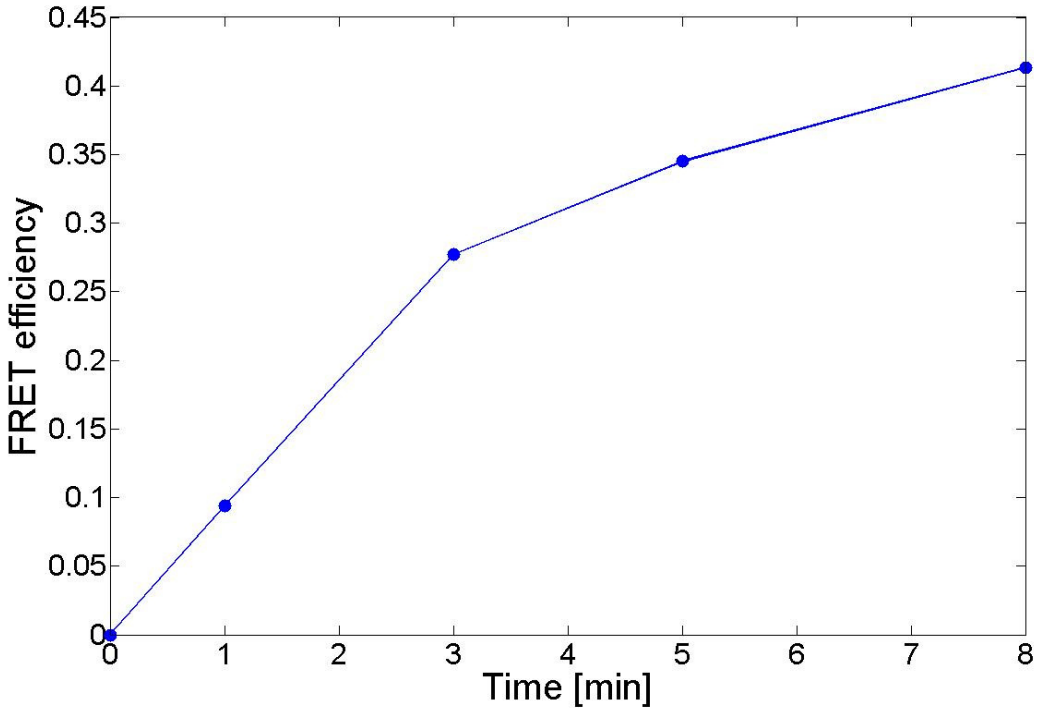


***Figure VII-9**. FRET efficiency as a function of labelling time.*

FRET events in this assay format rely on the random incorporation of DiD in the membrane combined with the diffusion of both donor and acceptor dyes. As studied in **Chapter VI**, random distribution of dyes would not result in significant FRET signals, even at high labelling ratios. Therefore, FRET comes mostly from preferred incorporation in domains with high donor content and diffusion towards these domains.

As reflected in **Figure VII-9**, the closest distance between donor and acceptor dyes keeps decreasing with labelling time meaning the dyes tend to diffuse towards the same domains. Assuming constant incorporation rate of the FRET acceptor, the curve of **Figure VII-9** can also be plotted as FRET efficiency versus relative acceptor concentration.

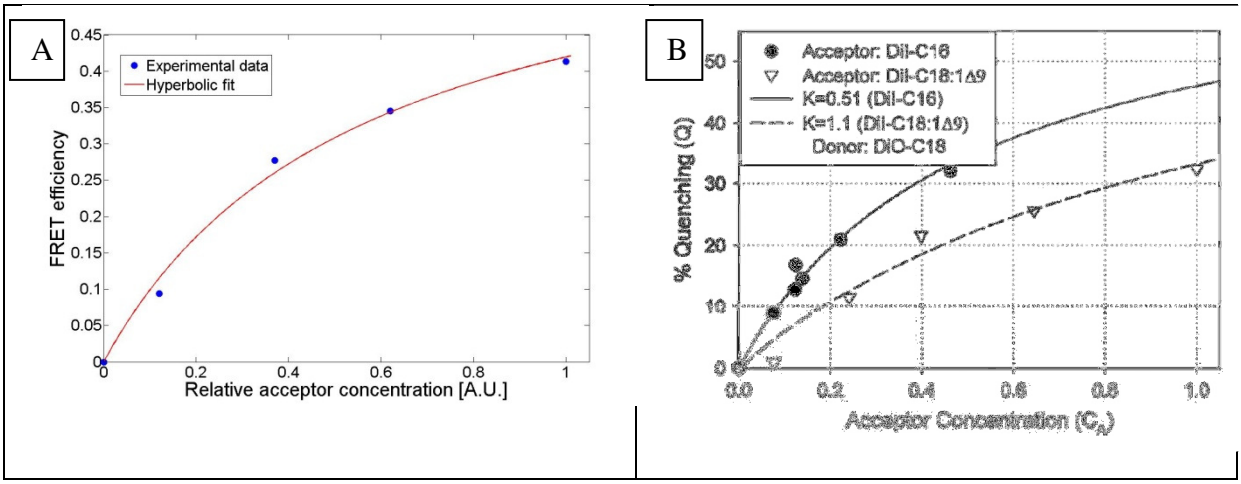


***Figure VII-10**. **A**. FRET efficiency versus relative acceptor concentration fitted with a hyperbolic function. **B**. Quenching of FRET donor DiO-C18 as a function of acceptor DiI-C16 concentration in RBL cells as published in [2] for a similar FRET pair.*

This curve bears strong resemblance to a similar reported experiment where the FRET pair DiO-C18/DiI-C16 were incubated in a membrane of RBL cells at different acceptor concentrations with FRET signal averaged over many cells placed in a spectrophotometer cuvette (**Figure VII-10B**).[2] The curve of **Figure VII-10A** was fitted using a hyperbolic function:

$$F = \frac{F_{\max} C_A}{C_A + K} \qquad \textit{Eq. VII-1}$$

In this equation, F is the FRET efficiency, F_{max} the maximum FRET efficiency, C_A the relative acceptor concentration and K a constant. K represents the acceptor concentration for which there is half-maximum of FRET efficiency. Therefore, K reflects the proximity between donor and acceptor probes. The fit gave a value of F_{max} at 65% efficiency, translating into an average minimum distance between the two dyes at 6.3 nm. The parameter K was evaluated at $0.56C_A$.

VII.3.3. Discussion

The decrease in number of photons emitted by donors combined with photo-bleaching directly limits the acquisition of FLIM maps for the green channel. This might be overcome in the future by imaging the cell a single time after a long DiD labelling time. One of the pending question is the incorporation rate of DiD which quickly shadows the actual FRET contribution and makes red FLIM maps difficult to interpret. Using lower dye concentrations should reduce this effect.

Although the local concentrations of the two dyes are not directly accessible, the FRET efficiency plot demonstrates the chip ability to monitor coupling of the two carbocyanine dyes. FLIM-FRET based on lifetime analysis circumvents many issues linked with intensity measurements and artefacts. It allows calibration-free quantification of FRET at single cell level which is a powerful advantage compared to intensity measurements requiring multiple control steps.[4] However, in the framework of membrane analysis, lifetime measurements also rise the challenge of de-correlation between different populations (FRET/non-FRET) having distinct lifetimes. This is challenging because modest decreases in donor lifetime cannot be easily tracked as a separate lifetime component fit in the fitting algorithm.

In order to grasp quantitative information on the tendency of two dyes to colocalize, the same experiment could be carried out using the same FRET donor and various acceptors. The K value described in ***Eq. VII-1*** can then be directly expressed as a ratio to distinguish tendencies between weak and strong colocalization.

VII.4. FRET exclusion assay in U937 cell membrane

VII.4.1. Experiment

To investigate the influence of cholesterol on the colocalization of the FRET pair DiO/DiD, we performed a cholesterol-depletion assay using Methyl-Beta-CycloDextrin (MBCD) as described in **Chapter VI**. First, U937 cells labelled with both DiO and DiD (c.f. **Chapter II** for methodology) were trapped in a PBS buffer under the same conditions as explained in paragraph **VII.1.** The initial imaging phase is shown in **Figure VII-11** with 5 imaged traps

labelled from 1 to 5. Trap numbered 2 contained 2 cells while the others had single cells. The scanning area was 250 x 250µm**.**

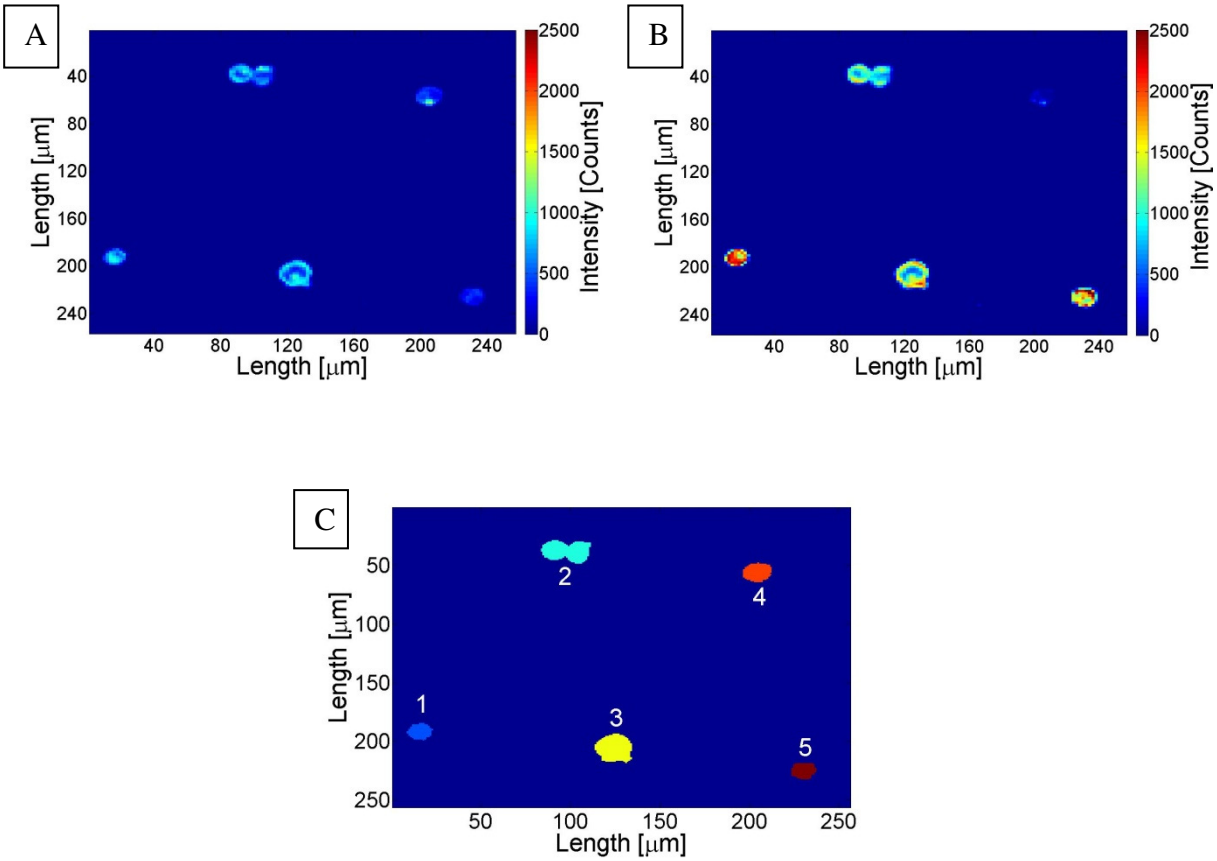


Figure VII-11*. A. Fluorescence intensity map of trapped U937 cells in 5 individual traps B. cells labelled from 1 to 5.*

The fluorescence level in the red channel is higher than the green channel suggesting the presence of FRET with weaker signals from the cell labelled 4.

Next, these cells were incubated in 3mM MBCD dissolved in a PBS solution. The solution was flown from the bottom of the pictures shown and stopped for subsequent incubation. The same area was scanned after 15 minutes of reaction and the lifetime maps and FRET intensity maps of initial state and post-reaction are shown in **Figure VII-12**.

.

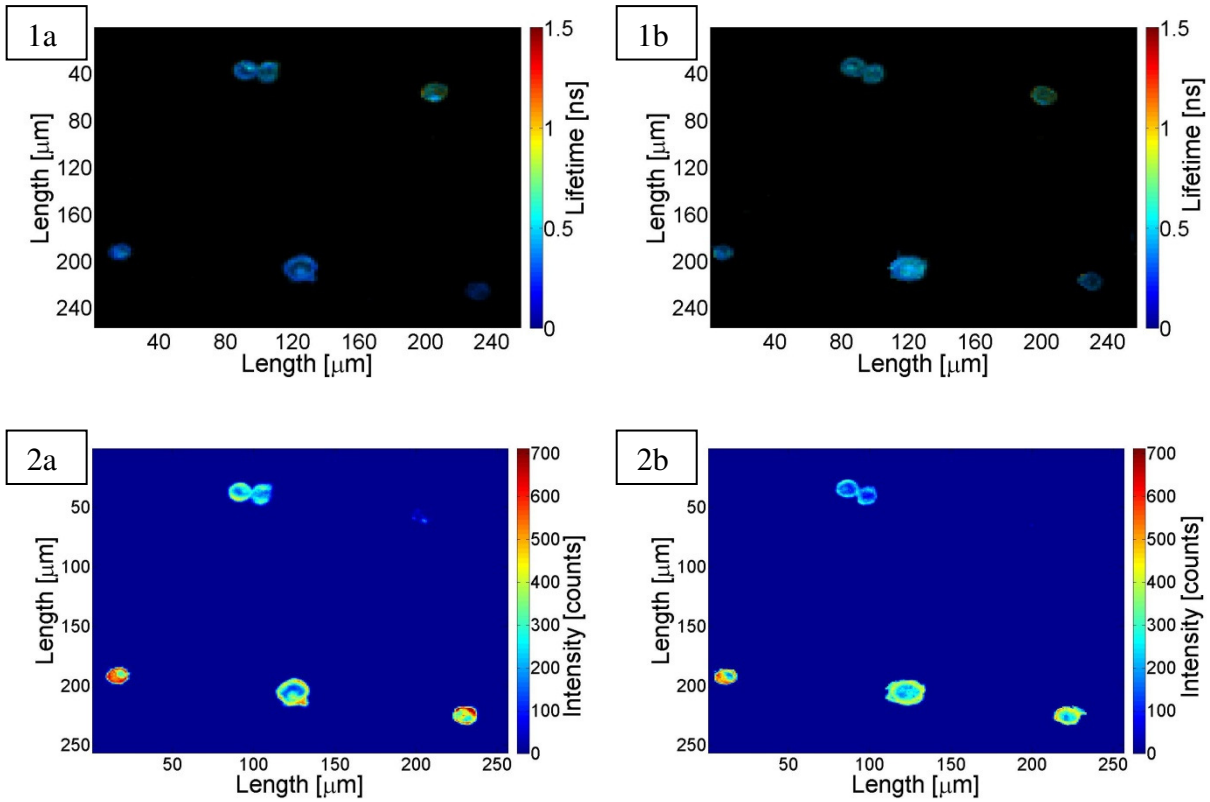


***Figure VII-12**. Lifetime maps (1a,1b)and FRET intensity maps (2a,2b) before (series a) and after 15 minutes incubation in 3mM MBCD (series b).*

Qualitatively, an increase in average fluorescence lifetimes was seen as a colour change in the lifetime map. At the same time, the number of FRET photons decreased for most cells, although this was in part due to a contribution of photo-bleaching of the donor dye combined with a change in plane of focus due to cell rotations within the traps. Lifetime maps, however, can be used for quantitative analyses by plotting the lifetime histograms for each cell. The trap containing 2 cells was analyzed as being a single cell.

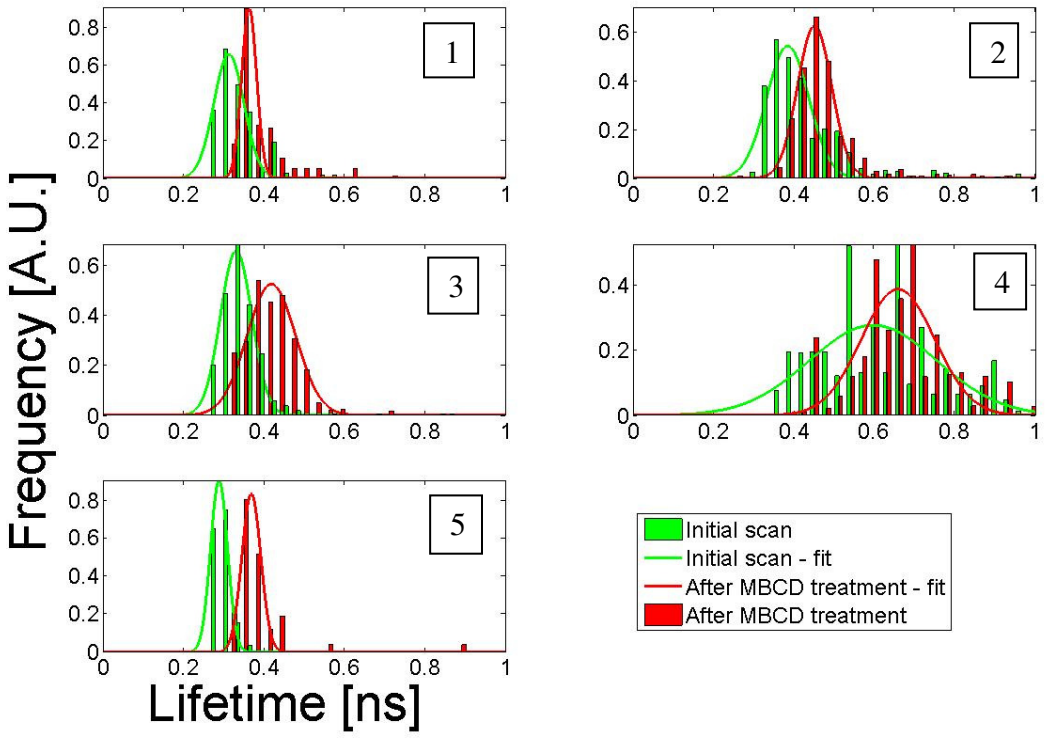


***Figure VII-13**. Lifetime histograms in the green channel for individual cells show a shift towards higher lifetimes.*

As summarized in **Table VII.4**, the shift in average lifetime $\Delta\tau$ can be quantified from the fits of the histograms of **Figure VII-13**.

	Cell nb.1	**Cell nb.2**	**Cell nb.3**	**Cell nb.4**	**Cell nb.5**
$\Delta\tau$ [ns]	0.05	0.07	0.1	0.08	0.09

***Table VII.4**. Difference in average lifetime extracted from single component Gaussian fits before and after treatment with MBCD.*

The modest change in average lifetime seems consistent for all cells and is in the order of 0.07ns ±0.02. As described in **Chapter VI.5**, the effect seen for MBCD treatment of singly labelled cells is a decrease in the average lifetime as DiO fluorescent properties depend on membrane fluidity. Here, the increase in average lifetime of the donors seen for doubly labelled cells can therefore be attributed to a decreased quenching level of the green dyes which is linked to lowered FRET efficiencies.

VII.4.2. Results & discussion

The decreased FRET efficiency confirms at least partial colocalization of the FRET pair in domains of high cholesterol content. However, the actual dye-dye distance cannot be inferred from these measurements which have to be deconvoluted from the case where the singly labelled cell is depleted of its cholesterol content. This type of assay can be generalized to all FRET pairs where association takes place in rigid or rafts domains and test their tendency to share the same domains.

The simultaneous detection of 5 cells automatically limits resolution for each of them. Here, the signal-to-noise for each of them was found high enough to extract fluorescence decay curves but lifetime histograms have a poor resolution. This could be tackled in the future by programming the laser scanning path over the 5 individual traps and acquire individual files for each of them.

VII.5. Summary

The membrane assays presented in this chapter highlights the wealth of information which can be extracted from single cells in little time. Spatially-resolved fluorescent maps represent local reporter concentration and can be used to assess labelling uniformity. Fluorescent maps further give information of local dye environment, such as local membrane order. They can also be used to detect crowding effects. The comparison of fluorescent and lifetime maps for both the donor and acceptor channels before and after introduction of a given reagent helps quantifying the interaction between two dyes as well as its evolution. The fast acquisitions of these maps do not limit analyses to steady-state studies but give information over the first few minutes of labelling and therefore monitor the fast diffusion effects of the dye. Further improvements to data acquisitions times would help resolving the transient response to the presence of acceptors.

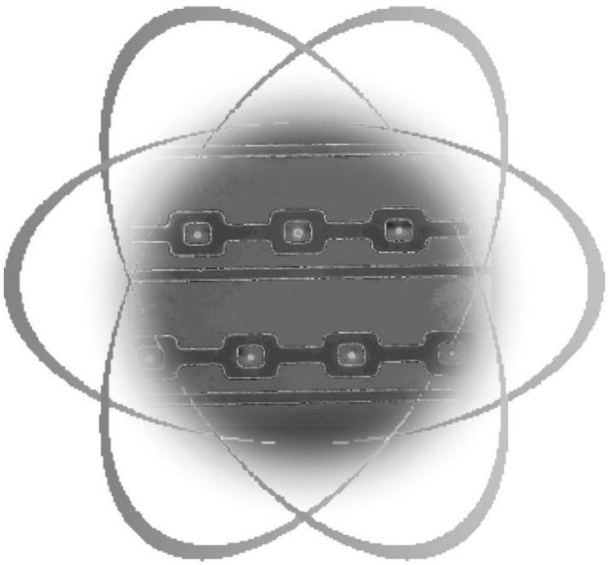
Combinations of assays in DEP traps could also be performed. For example, the acceptor incorporation assay followed by the cholesterol depletion assay could assess whether two

given fluorescent reporters colocalize in cholesterol-rich regions. The combination of single cell trapping, microfluidic control and high-resolution imaging has yet to be fully exploited in a more systematic manner.

VII.6. References

(1) Rottenberg, H.; Wu, S. L. *Biochimica Et Biophysica Acta-Molecular Cell Research* **1998**, *1404*, 393-404.
(2) Sengupta, P.; Holowka, D.; Baird, B. *Biophysical Journal* **2007**, *92*, 3564-3574.
(3) Loura, L. M. S.; de Almeida, R. F. M.; Silva, L. C.; Prieto, M. *Biochimica Et Biophysica Acta-Biomembranes* **2009**, *1788*, 209-224.
(4) Jares-Erijman, E. A.; Jovin, T. M. *Nature Biotechnology* **2003**, *21*, 1387-1395.

Chapter VIII. Conclusions and outlook



This chapter summarises the key achievements presented and discussed throughout this thesis. Possible improvements to the different aspects of this multidisciplinary project as well as future trends are subsequently outlined.

VIII.1. Summary of achievements

DEP has been recognized as a powerful method to capture single cells in vitro with fine control over their positioning.[1] However, although the technological hurdles encountered in the fabrication of the DEP traps have lowered with the development of tools and processes used in the semiconductor industry, their use for biological applications have remained modest and focus more on the sole use of the electric field such as electroporation, electrofusion or for the inhibition of cell growth.[2, 3]

In this thesis, we showed the applicability of DEP as a tool to perform membrane dynamics assays at the single cell level. The thesis focuses on the use of negative DEP traps as these can be used for trapping cells in physiological high conductivity buffers.

As a starting point, DEP traps were designed, fabricated and experimentally characterized. The use of multi-physics simulations provides useful insights into trapping operation such as confinement force mapping. For instance, the DEP vertical force was found strongly dependent on the depth of the microchannel below a certain threshold. The trapping strength was characterized experimentally by measuring the maximum flow velocity a particle can sustain before escaping the trap. This study demonstrates that stable trapping can be achieved for flow velocities up to hundreds of microns per second paving the way for the quick replacement of the trapping buffer by other reagents and therefore to the performing of sequential assays. Cell viability within these traps was also confirmed.

Next, the temperature rise created by the application of electric fields onto microelectrodes was investigated. Temperature is an important thermodynamics variable which influences the phase status of individual lipids and proteins making up the cellular membrane. In turn, this defines the overall fluidity of the membrane. The application of typical electric fields ($<10^5$V/m) raised the temperature to a maximum of 10 degrees C which was found in good agreement to values derived from analytical approximation studies. This study also highlighted the need of experimental data to access local temperature, especially when it is an integral part of the final data interpretation.

The identification of live and dead cells is typical done by assaying cellular membrane integrity using exclusion dyes such as Trypan blue staining cells with damaged membranes. In the context of lab-on-a-chip technologies where pre-assaying steps can be integrated in a single chip format, it was worthwhile to assess whether this identification step could be done solely using DEP. The physiological high conductivity buffer was assumed as the one used throughout the whole analysis. Exploiting differences in polarization, it was shown that live and dead cells differ in their flow pattern over parallel microelectrodes at high frequencies (around 40MHz). This was consistent with the single-shell model for predicting cell response to non-uniform fields with the main factor influencing the difference being an increase in plasma membrane conductivity and cytoplasm conductivity for dead cells. Although the method presented has limitations in terms of sensitivity and throughput, it constitutes a first step towards DEP separation of live/heat-treated cells using solely nDEP forces.

Fluorescence lifetime assays were set-up in order to perform subsequent DEP trapping assays. Jurkat cells or U937 cells were labelled with carbocyanine dyes having long fatty acid chains mimicking the structure of membrane phospholipids. The use of FLIM for membrane imaging was expounded insisting on the need for higher spatial and temporal resolutions. Typical lifetime histograms obtained from live cells showed a broad distribution of lifetimes, indicator of the heterogeneities of the environment in which the dyes sit. Of primary importance for membrane rigidity, cholesterol was removed by extraction using Methyl Beta CycloDextrin (MBCD) and the average lifetime of the dye for a cell population was found to decrease. This showed DiI can be used as a fluidity marker. In the same manner, the change of average fluorescence lifetimes between cell populations labeled with a FRET pair and only labelled with donor dye highlighted that FRET did occur within the membrane. The disruption of cholesterol was found to decrease the amount of FRET indicating part of the dye colocalization happened in rigid regions of the membrane. For all these assays, the variability was found to be very high. This was accounted for both biological heterogeneities and non-uniform labelling of cells. This stresses the importance of performing assays in a single cell format with acquisition of initial and final states.

After the introduction and trapping of single cells, the combination with a custom-built scanning confocal microscope was examined. The influence of electric fields on the lifetime of the fluorescent dyes used was found negligible. Next, assays were performed by sucking in reagents over trapped cells. The time response for the incorporation of acceptor dyes in a

donor labelled cell was acquired. This showed time-dependent FRET increase which was accounted for a concentration-dependent process. This study confirmed dyes quickly interact and colocalize in native cell membranes.

As a second example, multiple FRET cells were simultaneously imaged and their cholesterol content was extracted. Each cell was subsequently individually analyzed showing the applicability and potential for performing single cell assays in relatively high throughput.

VIII.2. Suggested improvements

For the cellular assays presented, a standard trapping density was used. However, the density can be largely increased by simple variations of the presented design. On the other hand, a minimum exclusion distance has to be kept to ensure careful isolation of single cells. The parallelization of these assays can also be achieved by patterning parallel microchannels with independent inlets/outlets. This way, at least one of the parallel tracks could be used for control, standardization and validation purposes.[4]

One of the parameter limiting the applicability of such DEP traps is the instabilities of micro--flows within microchannels, especially when using very shallow channels (<50µm). To minimize these effects, fluidic connections must be tight with no air trapped when initially filling the PDMS channel. The use of an air-tight glass syringe instead of plastic ones was also found valuable.

Finally, single cell delivery is also a challenge when it comes to using DEP traps embedded in microchannels. One solution is to design and fabricate hybrid devices combing passive and active trapping. The use of micropipettes to deliver single cells over traps can also be envisaged.[5]

VIII.3. Outlook

The ability to interrogate single cells becomes extremely valuable when working with rare cells such as cells extracted from tumor biopsies. The matching between the detection techniques used, the characteristic time of an assay and the cell trapping technique will be essential. DEP is especially suited for projects requiring high-resolution imaging as it can be readily adapted for use by commercial microscopes.[6] The ability to perform fast 3D scans will improve the relevance of data sets obtained from single cells as opposed to those relying on confocal slices. This should occur through improvements of the speed and programming of the scanning mirrors of laser scanning microscopes.[7]

With the maturity of the microfluidic field, the fabrication and performing of miniaturized single cell assays will be facilitated. Fully automated systems will pave the way towards high-throughput information rich detection tools. This will allow the systematic investigation of lipid and protein dynamics as a means to assess their functional role. FLIM-FRET can be employed to screen lipid-lipid, lipid-protein or protein-protein interactions. The development of more specific and more sensitive fluorescent probes for lateral segregation will be crucial. Other ultra-high resolution microscopy techniques such as Scanning Near-field Optical Microscopy (SNOM) or Atomic Force Microscopy (AFM) already constitute valuable complementary tools.[8, 9]

In a more applied development, the possibility of performing membrane assays with FLIM and fluidity markers in-vitro or in-vivo is envisioned as a powerful diagnostic tool when comparing lifetime histograms between healthy cells and cancer cells.[10, 11]

VIII.4. References

(1) Pethig, R. *Biomicrofluidics* **2010**, *4*, 1.

(2) Kirson, E. D.; Dbaly, V.; Tovarys, F.; Vymazal, J.; Soustiel, J. F.; Itzhaki, A.; Mordechovich, D.; Steinberg-Shapira, S.; Gurvich, Z.; Schneiderman, R.; Wasserman, Y.; Salzberg, M.; Ryffel, B.; Goldsher, D.; Dekel, E.; Palti, Y. *Proceedings of the National Academy of Sciences of the United States of America* **2007**, *104*, 10152-10157.

(3) Beebe, S. J.; Fox, P. M.; Rec, L. J.; Willis, L. K.; Schoenbach, K. H. *Faseb Journal* **2003**, *17*, 1493-+.

(4) Buffi, N.; Merulla, D.; Beutier, J.; Barbaud, F.; Beggah, S.; van Lintel, H.; Renaud, P.; van der Meer, J. R. *Lab on a Chip* **2011**, *11*, 2369-2377.

(5) Rodowicz, K. A.; Francisco, H.; Layton, B. *Chemistry and Physics of Lipids* **2010**, *163*, 787-793.

(6) Khoshmanesh, K.; Akagi, J.; Nahavandi, S.; Skommer, J.; Baratchi, S.; Cooper, J. M.; Kalantar-Zadeh, K.; Williams, D. E.; Wlodkowic, D. *Analytical Chemistry* **2011**, *83*, 2133-2144.

(7) Piltti, K. M.; Haus, D. L.; Do, E.; Perez, H.; Anderson, A. J.; Cummings, B. J. *Stem cell research* **2011**, *7*, 256-263.

(8) Hess, S. T.; Girirajan, T. P. K.; Mason, M. D. *Biophysical Journal* **2006**, *91*, 4258-4272.

(9) Subramaniam, V.; Kirsch, A. K.; Jovin, T. M. *Cellular and Molecular Biology* **1998**, *44*, 689-700.

(10) Sok, M.; Sentjurc, M.; Schara, M.; Stare, J.; Rott, T. *Annals of Thoracic Surgery* **2002**, *73*, 1567-1571.

(11) Yatvin, M. B. *International Journal of Radiation Biology* **1977**, *32*, 513-521.

Increasing the Trapping Efficiency of Particles in Microfluidic Planar Platforms by Means of Negative Dielectrophoresis

Fabrice Gielen,[†,‡,§] Andrew J. deMello,[‡] Tony Cass,[†] and Joshua B. Edel[*,†,‡]

Department of Chemistry, Institute of Biomedical Engineering, and Chemical Biology Centre, Imperial College London, South Kensington, London, SW7 2AZ, United Kingdom

Received: October 08, 2008; Revised Manuscript Received: November 12, 2008

We present a novel planar electrode geometry in which particles (typically 10 μm in diameter) are focused near a defined surface before being trapped using negative dielectrophoresis. The focusing element can deflect particles having speeds up to hundreds of micrometers per second. This trapping configuration results in improved trapping yields and a decrease in overall reagent consumption. Particles are trapped dynamically while flowing in a microfluidic channel.

Introduction

The handling of individual particles in a microfluidic environment includes several manipulation techniques including filtering, focusing, trapping, and sorting.[1] Focusing refers to the deviation of particles toward a chosen convergence location. This is the key principle used in flow cytometry but it also finds applications in the separation of dielectric particles.[2,3] Importantly, this focusing step is extremely valuable when working with biological samples having low analyte concentration or when a subsequent detection technique assumes a particle flow over a small detection volume.

Focusing particles in contact or close to a defined surface can find applications in diagnostics (e.g., heterogeneous immunoassays),[4,5] combinatorial chemistry based on particle manipulation,[6,7] or cell biology, especially cellular membrane studies.[8,9] Generally speaking, the motion of particles in contact or in the vicinity of a surface can be used for particle−surface interaction studies. For example, the amount of contact a cellular membrane can have with a defined surface could be controlled and subsequently used to examine change in the local mechanical properties of a lipid bilayer. Furthermore focusing of particles at a single plane level is especially useful when followed by trapping due to planar electrodes rarely reach 100% focusing yields (number of particles actually focused/total number of flowing particles) due to the limited electric field extension away from electrodes.

The particle manipulation techniques aforementioned can be performed using dielectrophoresis (DEP) and integrated on a single laboratory-on-a-chip platform.[1−3,10−12] Dielectrophoresis typically uses nonuniform AC electric fields (10 kHz to 100 MHz) to position particles guided by an electric field gradient.[13] DEP exerts dipolar forces on dielectric particles such as microbeads or cells. If the medium is more polarizable than the particle, the force brings the particle away from high field regions; this is referred to as negative dielectrophoresis (repulsion forces). In the case of nonconductive dielectric particles or cells in physiological high conductivity medium, negative DEP (nDEP) is always obtained. In addition to beads, DEP is extremely well suited for cellular manipulation due to the specific polarization responses to a high frequency electric field.[14−17] Furthermore it has been shown that cells can be cultured even under permanently applied fields.[17]

Focusing near a Surface with DEP. Focusing can be achieved using both positive and negative DEP.[18,19] In many articles utilizing DEP focusing, particles are moved to the geometric center of a microchannel.[1,3,10−12] This is usually achieved using two aligned planar electrodes on both the bottom and ceiling of a fluidic channel. Hydrodynamic focusing has been investigated but cannot easily confine particles down to a surface.[3] Few studies rely on three-dimensional (3D) fabrication techniques to build 3D electrodes[12] as the fabrication of these geometries is difficult due to multilayer alignment and packaging.

Combining Planar nDEP Focusing and nDEP Trap. Two dimensional traps based on negative dielectrophoresis have been repeatedly reported;[20−22] however, within a microfluidic chip, high reagent consumptions are typically experienced due to particles being repelled out of high electric field gradients. Electrohydrodynamic forces can then be utilized as a tool to increase trapping yields.[23] Planar focusing allows for fast in-flow routing of particles toward a given DEP trap. In this article, the focus-and-trap function of a novel electrode geometry is characterized. Simulations are also used to determine the effect of channel height and velocity on the trapping forces.

Theory

The time-averaged DEP force can be written as[13]

$$\vec{F}_{DEP} = 2\pi\varepsilon_m R^3 \mathrm{Re}[\mathrm{CM}(\omega)]\nabla\vec{E}^2(r,\omega) \qquad (1)$$

Here $\vec{F}_{DEP}$ refers to the dipolar approximation of the DEP force, ε_m is the dielectric permittivity of the surrounding medium, R is the radius of the particle, and $\vec{E}(r, \omega)$ is the complex applied electric field, where r is the spatial coordinate of the particle and ω is the angular frequency of the applied field. CM is the Clausius−Mossotti (CM) factor, whose definition depends on the kind of particle considered. A positive CM factor indicates that the DEP force pushes particles toward the electrodes to the electric-field maximum (pDEP) whereas a negative CM factor indicates that the DEP force pushes particles away from the electrodes to the electric field minimum (nDEP).

* To whom correspondence should be addressed. E-mail: joshua.edel@imperial.ac.uk.
† Institute of Biomedical Engineering.
‡ Department of Chemistry.
§ Chemical Biology Centre.

10.1021/jp808897g CCC: $40.75 © 2009 American Chemical Society
Published on Web 01/14/2009

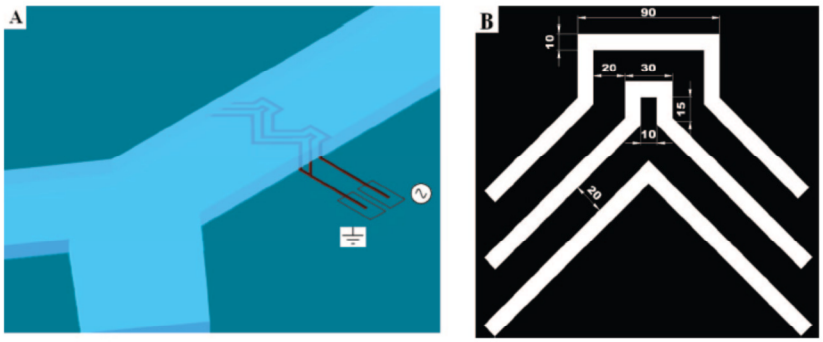


Figure 1. (A) Focused square electrode geometry proposed for cell patterning near a defined surface. (B) Electrode pattern as designed (dimensions are given in microns).

The expression of the time-averaged DEP force (1) is based on the dipolar approximation. Higher order moments may also contribute to the global DEP force. Importantly, in the case of a complex geometry, when nonuniformities in the electrode pattern are commensurate with the size of the particle, higher order moments are likely to be induced.[24] However, in the case of nDEP, particles are pushed out of high gradient regions; the influence of the high order moments is therefore greatly diminished. In addition, high order moments can be neglected in known geometry configurations.[25]

One of the most significant implications of the expression of the DEP force is that it is extremely dependent on geometry through the gradient term$\nabla\vec{E}^2$. Careful design of complex geometries can thus lead to new functions and increased control over particles or cells.[25]

The frequency response of a particle to an externally applied electric field is determined through its CM factor. If we consider a simple dielectric particle with Ohmic conductivity but no dielectric losses immersed in a dielectric medium, the CM factor can be written:

$$\mathrm{CM} = \frac{\varepsilon_p - \varepsilon_m}{\varepsilon_p + 2\varepsilon_m} \tag{2}$$

Here ε_m and ε_p are the complex permittivities of the medium and particle, respectively, and can be each written as

$$\mathrm{Re}(\varepsilon) = \varepsilon + \frac{\sigma}{j\omega} \tag{3}$$

Here Re(ε) is the real part of the complex permittivity, ε is the permittivity of the medium or particle, σ is the conductivity of the medium or particle, and j is $\sqrt{-1}$.

At typical buffer permittivity and conductivity conditions, the medium is more polarizable, which results in the DEP force always being directed toward the electric field minima resulting in negative DEP.

Fabrication and Geometry

Indium Tin Oxide (ITO) Patterning. A microfluidic chip was built using a combination of ITO-coated glass (SPI supplies) and PDMS. The microelectrode design was patterned on an ITO glass substrate using standard photolithography and wet chemical etching. The thickness of the glass substrate was 500 μm and that of the ITO coating was 100 nm. ITO is a metal transparent to visible light and thus optically transparent at the wavelengths of interest.

For ITO etching, AZ 1512HS (MicroChemicals) photoresist was used as a protective layer and exposed to UV light through a lithographic mask (designed by AutoCAD and subsequently printed on a film (JD Phototools)). The exposure dose was adapted to the resist thickness. Nonexposed parts of the resists were then developed with a developer solution AZ 400K (Clariant). An aqueous solution of 4:2:1 HCl/H_2O/HNO_3 was prepared for etching ITO. The ITO glass was dipped in the solution for approximately 30 s. After completing the etching process, the substrate was thoroughly rinsed in deionized (DI) water. Finally, the photoresist was removed with acetone. The devices were further cleaned in isopropyl alcohol (IPA) and DI water before being stored in a Petri dish.

PDMS Microchannel. A master mold was fabricated by photolithography on a 4 in. silicon wafer (100) and used as the substrate. The silicon wafer was uniformly coated with SU-8 50 (or SU-8 100) photoresist (coated at 500 rpm for 15 s followed by 3000 rpm for 30 s), soft baked for 15 min at 65 °C and 30 min at 95 °C, exposed with UV light, and developed. The thickness of the microchannel was either 30 or 120 μm. A mixture of PDMS prepolymer (SYLGARD 184 Silicone Elastomer Kit, Dow Corning, Midland, MI) and the curing agent was degassed in a vacuum chamber for 30 min to remove any air bubbles and to ensure complete mixing of the two parts. The mixture was then poured onto the master mold in a Petri dish. It was cured for 12 h at 65 °C on a hotplate. After curing, the PDMS replica was peeled off from the master mold. Fluidic inlets and outlets were punched through the PDMS channel using a syringe needle.

Before PDMS bonding on the ITO patterned glass, the latter was rinsed in 0.5 M KOH solution followed by DI water and nitrogen blowing. The PDMS channel was cleaned using a N_2 gun. Both were plasma oxidized, aligned using a standard microscope and bonded manually. Finally the chips were cured on a hotplate at 95 °C for 5 min.

Packaging. The ITO contact pads were covered with silver glue (RS) and pin connectors (RS) were pressed on it. After curing for a minimum of four hours at room temperature, epoxy (ITW Devcon) was deposited to strengthen the bond between the connectors and microfluidic chip. After curing of the epoxy at 65 °C overnight, electric wires (RS, 0.25 mm^2) were soldered to the pins.

Geometry. A 3D illustration of the design is given in Figure 1A. The geometry itself is inspired by the square electrode design previously reported by Rosenthal et al.[20] The fundamental

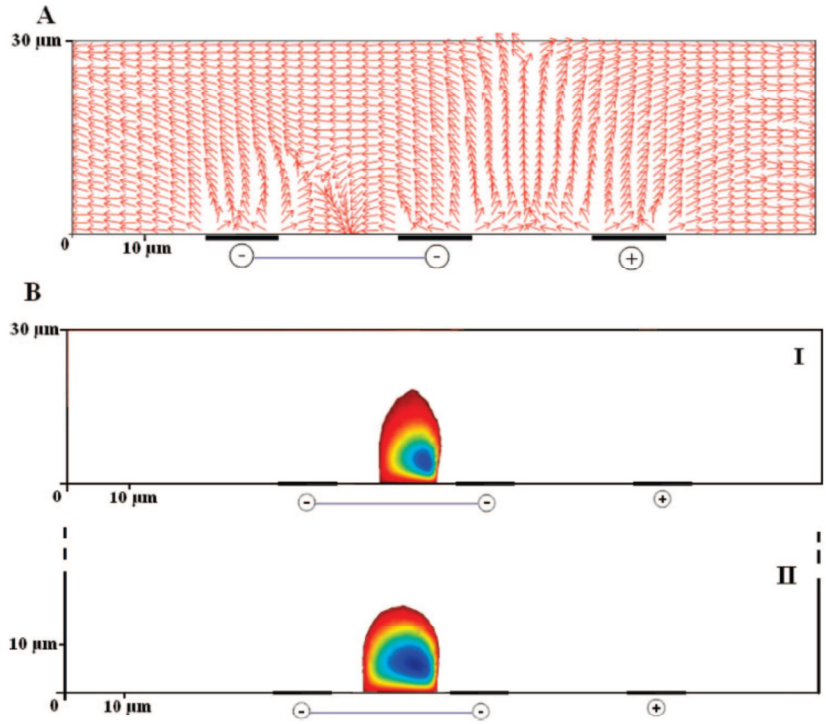


Figure 2. (A) Normalized DEP force direction associated with three line electrodes geometry. (B) Negative component of $|\nabla_z^{\rightarrow} E^2|$ in **I**, a shallow channel (30 μm high) geometry, and **II**, a nonshallow (120 μm high) geometry. Blue regions correspond to higher gradients.

difference lies in a focusing element being introduced that is made up of three parallel line electrodes. Importantly, two metal lines are connected to form the cathode. The basic dimensions are given in Figure 1B. Using this geometry, several cages can be aligned or arrayed.

Design Rules. The design rules adopted here are based on the idea that the spacing between cathodes should be at least bigger than the diameter of particles of interest in order to trap them (size selectivity) and to avoid higher-order moments which would make the trapping behavior hard to predict. Nonetheless, a big gap between cathodes translates into decreased electric gradients. For mammalian cell experiments, given the heterogeneities of a cell population, a spacing of 20 μm is a good compromise. The spacing between the anode and inner cathode should be as close as possible to generate high gradients. Here again, 20 μm seems realistic. The width of the electrodes should ensure that fields are not too strongly localized which could lead to cell damage but also not too low to ensure efficient trapping. Ten micrometers is a reasonable value comparable to existing geometries. The angle of the three parallel lines with respect to the flow was chosen as 45°. In real devices, arrays of 5 rows × 4 columns elements were interconnected.

Materials

Flow was initiated via a precision syringe pump (PHD 2000, Harvard Apparatus) using a 1 mL Becton−Dickinson syringe. Bead stock solutions were made with appropriate conductivity by combining appropriate volumes of 18 MΩ cm deionized water containing 0.1% Triton X-100 (to ensure the beads will not stick to the channel surfaces and keep them monodisperse) and phosphate-buffered saline (Sigma Aldrich). Conductivities were measured using a Dist 5 conductivity meter (VWR). Polystyrene (PS) beads (PolySciences) had a density of 1.062 g/cm^3, packaged at 2.5% solids in water. Fluorescent beads (FluoSpheres, Molecular Probe) were 2% solid solutions of polystyrene beads with encapsulated fluorescent dyes (yellow-green fluorescent). Their peak absorption wavelength was 505 nm and their peak emission wavelength was 515 nm.

A function generator (TG2000, Thurlby Thandar Instruments) was connected to the electrodes by BNC cables with adapted wire grip leads gripping the conducting wires of the contact pads to the microelectrodes. A sinusoidal signal with voltage varying between 1 to 20 V_{pp} and a fixed frequency of 10 MHz was applied to the microelectrodes. Imaging and observation was performed using an Olympus IX71 microscope.

Simulations

Principle of the Focusing Element: Leveraging the Downward DEP Force. A DEP cage exists when a particle is forced to go back to its original location (to a potential well) when slightly moved away from its equilibrium. Simulations of such traps require electric field distribution study. They have been performed using the Comsol package based on the finite element method (FEM).

In the 2D model of Figure 2A, the channel height is chosen to be 30 μm. Three line electrodes of width 10 μm have a spacing of 20 μm. The two left electrodes represent the cathode (potential −5 V) while the right electrode is the anode (potential +5 V). The boundary conditions for the fluidics are no-slip on the walls and a null outlet pressure, respectively. The fluid parameters are those of deionized water. The arrows in Figure 2A represent the normalized DEP force direction. Depending

on the location of the particle, the direction of the force varies as follows: (1) Between the anode and cathode, the force is upward toward the center of the electrodes; the particle will be lifted up. This phenomenon is known as DEP levitation. (2) Between the two cathodes the force is downward and pushes particles toward the center of the cathodes; this region defines the DEP trap. If we were to transform the geometry of Figure 2A into a 3D model, we would be in a situation where particles can move between the two cathodes. This forms an open trap which can be used as a focusing element. (3) Outside the outer cathode (the left in Figure 2A), particles are weakly pushed backward (due to the low gradient far from the anode−cathode gap). (4) Outside the anode (the right in Figure 2A), particles are strongly pushed forward.

The device is based on electric field distribution inside a microfluidic channel. It is therefore not surprising that the height of the channel has a tremendous influence on its ability to trap particles. In this section, we analyze the differences between a shallow channel (chosen 30 μm high) in which the electric field is strongly confined and a nonshallow channel (chosen 120 μm high) in which the electric field is weakly confined.

Representation of an nDEP Cage. One representation of a DEP cage in the case of a planar geometry is its downward electric gradient. If z defines the vertical axis of the system, the region for which $|\nabla_z \tilde{E}^2|$ is negative will confine particles near a surface. Figures 2B compares qualitatively the surface intensity of this quantity according to the shallowness of the channel. In this figure, particles are coming from the left-hand side. The important parameter is the incoming height of the particle. Indeed, in a device with integrated planar electrodes, the DEP force scales as

$$F_{\mathrm{DEP}} \propto \frac{V^2}{h^3} \tag{4}$$

Here V is the applied potential and h the height of the center of the particle above the substrate. This expression indicates that the strength of the DEP force vanishes quickly with height above the electrodes. In the case where the cage occupies half of the channel height as in the 30 μm high channel (case **I**), there is therefore increased probability of a trapping event with respect to the case of a deep channel.

The distribution of the downward force also varies. While it is strongly located on the edge of the inner cathode (the blue region corresponds to higher gradients) for a shallow channel (case **I**), it is more evenly distributed for a deeper channel (case **II**).

Influence of the Height of the Channel. As predicted in Figure 2A, the outer electrode will lift particles up, creating a DEP barrier. If a particle is uplifted too much, it will not enter the focusing region and will be able to escape. Simulations show the relative magnitude of this barrier $\nabla_z \tilde{E}^2$ at 5 μm above the substrate as a function of channel height (Figure 3). For a shallow 30 μm high channel, the barrier is about 2.5 times weaker than for a 120 μm high channel.

This can be explained by the restriction of the field due to the small vertical extension. In other words, there is confinement of the electric field nonuniformities near the adjacent anode and cathode.[25] This difference in barrier height is sufficient to change trapping methodologies according to channel height as detailed in the results section. Figure 4 shows the maximum barrier height as a function of channel height. The potential was kept constant at 10 V_{pp}. The figure reflects the degree of confinement of the electric field: the shallower the channel, the lower the DEP barrier. For channel heights of 200 μm and above, there is no more confinement and the barrier height is maximum.

Results and Discussion

In shallow channels, the methodology for trapping particles is to sequentially activate the flow of beads (at a desired concentration) with the syringe pump at a flow rate suitable for trapping (in μL/min) and turn on the electric field. Beads flowing close enough to the electrodes will be automatically trapped. The trapped beads can accumulate in the DEP cage until the focusing region is completely filled (beads accumulate and form lines). After turning off the field, beads are carried away by the flow.

In nonshallow channels, particles cannot enter the trap due to the aforementioned "barrier". The field has to be switched on manually when beads are located in-between the two cathode line electrodes. Importantly, in this case trapped beads cannot interact with untrapped ones while the electric field is present. The manual trapping requires a feedback that can be simply visual using a microscope eyepiece or a camera. Figure 5 displays a series of pictures showing a focus-and-trap event of a single polystyrene bead in a nonshallow channel.

Velocity Analysis. Whether particles actually contact the surface in the presented focusing element can be studied via velocity analyses of single particle. This also gives more insight into the principle of operation. A Cascade II camera (Photometrics, Roper Scientific, Inc.) was used to record fluorescence movies of flowing fluorescent beads. A maximum of 29 frames per second was used to record 512 × 512 pixel movies. The image postprocessing of the individual frames of the recorded movies was performed using Matlab.

Figure 6 represents a typical velocity curve for a fluorescent bead flowing sufficiently close to the patterned surface to get focused and subsequently trapped.

Four regions can be highlighted on this graph:

1. When the particle is incoming, its velocity is constant and there is no polarization effect from the electric field.

2. The particle reaches the edge of the outer ITO line, its velocity increases quickly to nearly twice its previous speed.

3. Approaching the inner ITO cathode, the particle is quickly slowed down and gets focused.

4. The particle is finally trapped and stops.

Interestingly, the velocity profile is rather flat in the focusing region and amounts to around 60% of the incoming speed. This decrease in speed before the trapping region increases the probability of a trapping event and hence trapping efficiency. The velocity profile also clearly rules out contact with a surface in which case the speed would be either very low (permanent contact) or fluctuating (particles bouncing). In fact, contact is prevented by the hydrodynamic uplift and the focusing speed mainly depends on the angle of the focusing line electrodes as well as the radius of the particles (although no experiments have been performed to prove this point). This focusing velocity could thus be used for size determination of a population of cells/particles.

Trapping and Holding Force. Trapping and holding force of an nDEP trap represent a figure of merit. For the shallow devices, the trapping force is the threshold voltage at a given flow rate under which flowing spheres cannot be focused and trapped anymore. For the nonshallow devices, the electric field is turned on manually when spheres are passing within the two cathodes and the same definition applies.

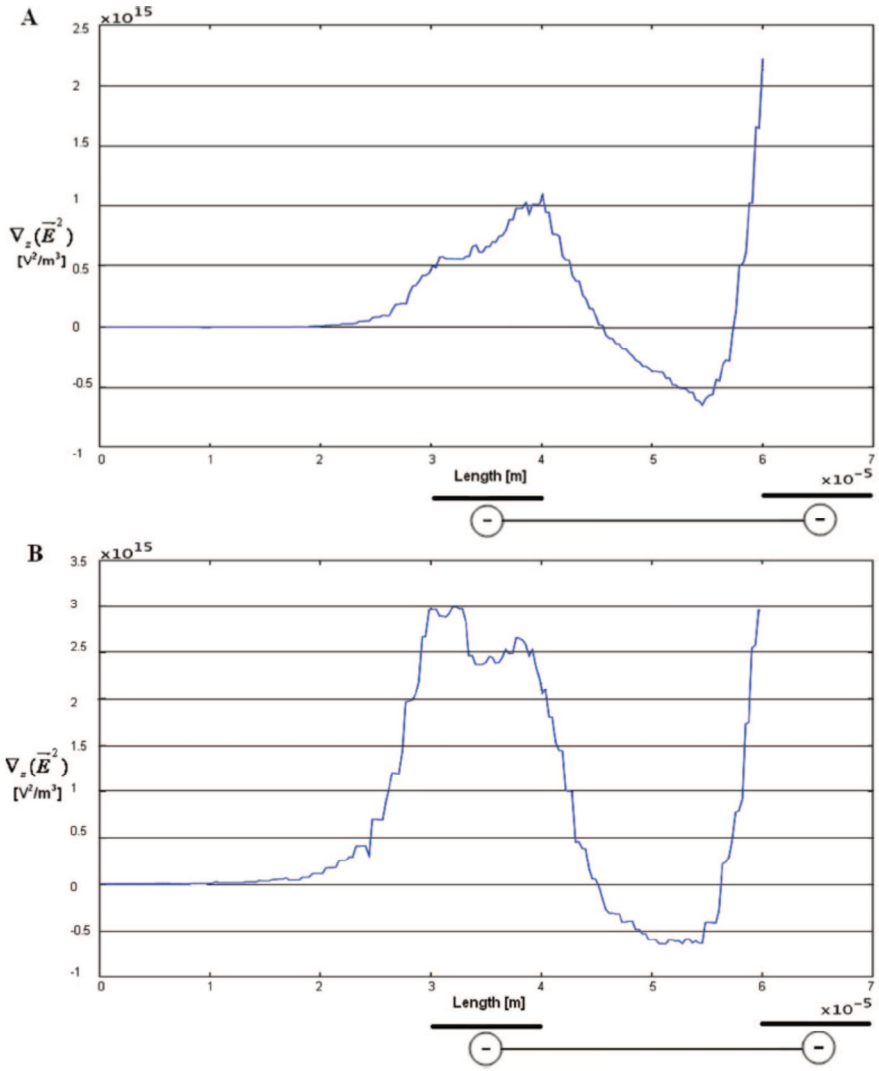


Figure 3. Cross-section of $\nabla_z(\vec{E}^2)$ 5 μm over the cathode line electrodes in (A) a shallow 30 μm high channel and (B) a 120 μm high channel.

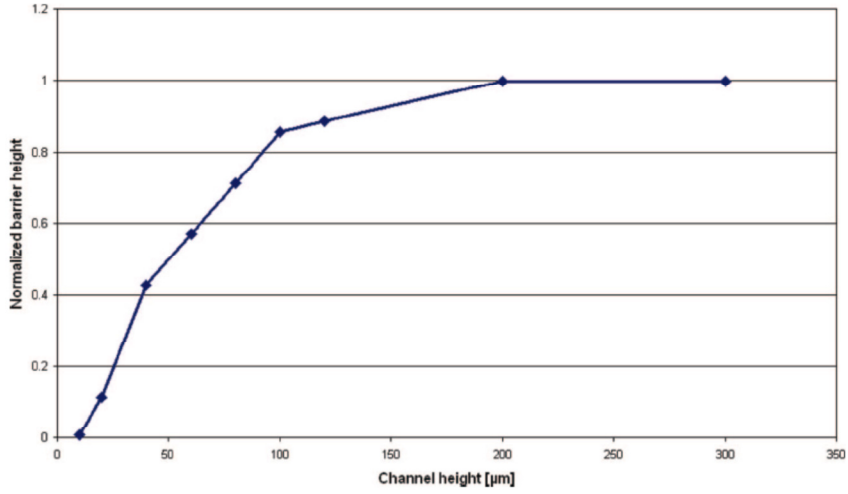


Figure 4. Normalized DEP barrier height (upward DEP force) over the first line electrode as a function of channel height at constant voltage.

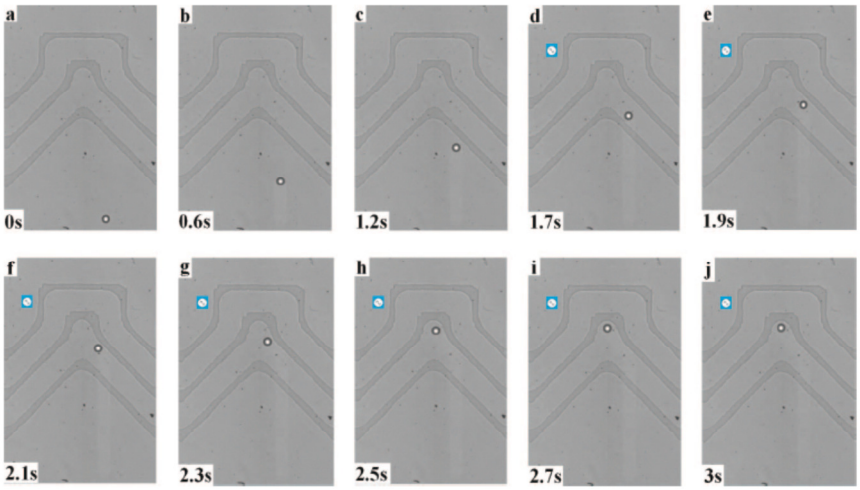


Figure 5. Planar focusing and trapping in a nonshallow channel. (a−c) Incoming PS bead of 10 μm in diameter. (d) The electric field is manually turned on when the bead enters the gap between the two cathodes. (e−h) The bead is focused. (i,j) The bead finally becomes trapped.

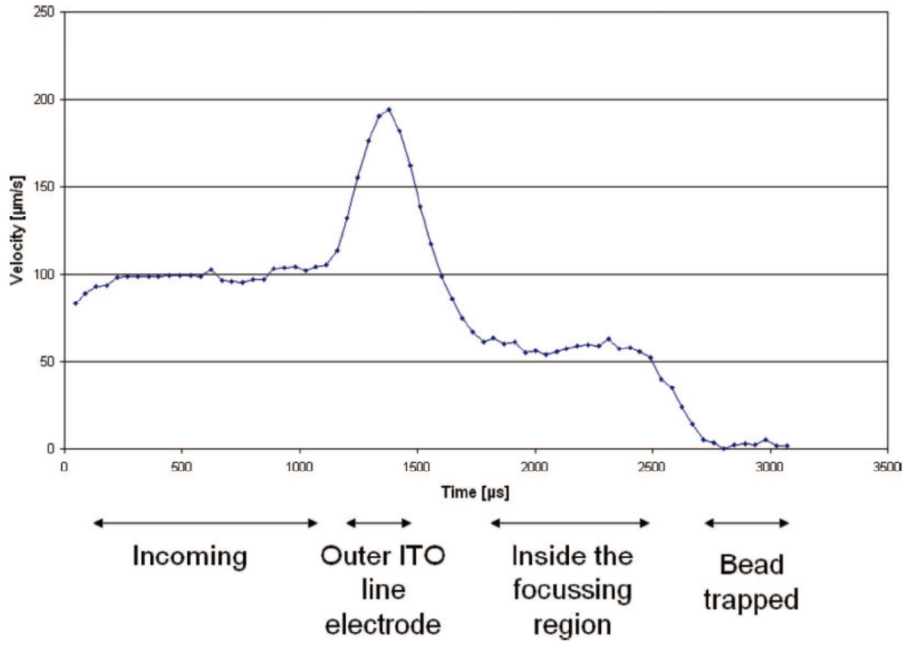


Figure 6. Velocity of a single particle being focused and subsequently trapped in the DEP cage.

The holding force is the threshold voltage at a given flow rate under which trapped spheres get carried away by the flow.

Quantifying the Trapping Force. Chips were cleaned by injecting ethanol for roughly 5 min. After this step, a high density of beads (around 100 beads/μL) was injected inside the microchannel and the flow rate was set at a constant value. The electric field was a sinusoidal wave of frequency 10 MHz and low amplitude. After waiting for the flow to be steady, the voltage was increased by steps of 1 V_{pp}. The threshold voltage for which particles get focused and trapped corresponds to the trapping force. This was visualized using a high speed camera (Phantom v5.1, Vision Research).

Quantifying the Holding Force. Particles are now assumed to be already trapped. The electric field was a sine wave of frequency 10 MHz and the amplitude was set much higher than the trapping threshold. The flow rate was set at a constant value. After waiting for the flow to be steady, the voltage was decreased by steps of 1 V_{pp}. The threshold voltage for which particles escape corresponds to the holding force. The 1 V_{pp} step is sufficiently big that most beads trapped in different cages (in the case of a trap array) would escape at that same threshold.

The curves in Figure 7 showing the trapping and holding force were obtained with 30 μm spacing between electrodes in a 120 μm high channel geometry. The conductivity of the nonfluorescent bead buffer was adjusted to 0.18 S/m. The curves show a quadratic trend as expected from eq 1: while the drag force increases linearly with the flow velocity, the DEP force increases in a quadratic manner with the applied voltage. The functional

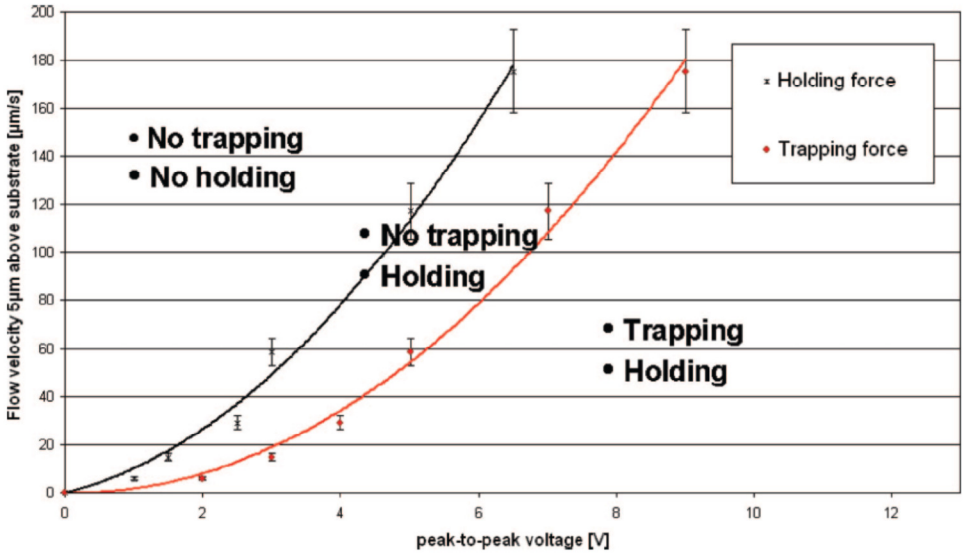


Figure 7. Trapping and holding regions according to flow velocity 5 μm above the substrate and peak-to-peak voltage.

form of the fit in Figure 7 is $y = Ax^2 + Bx$. The three regions it delimitates are as follows. For low flow velocities and high voltage, beads can be trapped and held. At a certain velocity threshold, spheres can be held but not trapped. For high flow velocities and low voltage, spheres can neither be trapped nor held.

The direct observation made in Figure 7 is that the trapping force is weaker than the holding force. These two distinct curves can be accounted for by the balance between drag flow and the counteracting DEP force. For the trapping force, a bead is in motion and has to be deviated until it reaches a potential well. After reaching its stable position in a trap, the bead experiences a stronger DEP force and can therefore withstand stronger flow rates (i.e., the holding force is higher). In order to compare the holding force with the square electrode design, extrapolations from the data provided in (20) are performed. At a peak voltage of 5 V and for corrected electrode spacing and channel geometry, the presented design is found only 20% weaker.

Single-particle trapping can be achieved using this design by working near the holding force threshold. The device can also be used in high-throughput format by increasing the flow rate and adjusting the field to just above the trapping threshold voltage. For cellular work, the use of a low electric field strength is a requirement. Many studies suggest the maximum field strength leading to acceptable transmembrane loading is in the order of 10^6 V/m.[16,25,26] Other interesting applications of the developed system include line patterning of particles, focusing particles in stream lines or creating arrays.

The trapping yield for previously reported devices is typically very low (<1%) because the surface has to be initially fully covered by particles. While this is a rather quick step, the untrapped particles will for the most part not be used and therefore constitute waste. Using the focusing element would allow to dramatically improve the trapping yield which was found as high as 50% in favorable conditions (shallow channel, low flow rate and high voltage).

Conclusions

A novel geometry for focusing particles or cells in-flow near a defined surface has been presented. The speed of operation is substantially higher than previously reported designs for trapping as practical flow velocities are high (up to hundreds of micrometers per second). Simulations have shown the principle of a semiopen trap and highlighted the influence of channel height over the trap strength and operation. The trapping and holding force of polystyrene microbeads have been quantified in terms of balance between field strength and flow velocity. The holding force was found only slightly weaker than previously reported planar geometries. Using this novel focus-and-trap element for cell experiments would ensure cells do not get into direct contact with metal electrodes which avoids charging and improves cell viability.

References and Notes

(1) Cheng, I. F.; Chang, H. C.; Hou, D.; Chang, H. C. *Biomicrofluidics* **2007**, *1*, 15.
(2) Choi, S.; Park, J. K. *Lab Chip* **2005**, *5*, 1161.
(3) Holmes, D.; Morgan, H.; Green, N. G. *Biosens. Bioelectron.* **2006**, *21*, 1621.
(4) Wild, D. *The immunoassay handbook*, 3rd ed.; Elsevier: New York, 2005
(5) Wiklund, M.; Toivonen, J.; Tirri, M.; Hänninen, P.; Hertz, H. M. *J. Appl. Phys.* **2004**, *96*, 1242.
(6) Gordon, E. M.; Barrett, R. W.; Dower, W. J.; Fodor, S. P.; Gallop, M. A. *J. Med. Chem.* **1994**, *37*, 1385.
(7) Pregibon, D. C.; Toner, M.; Doyle, P. S. *Science.* **2007**, *315*, 1393.
(8) Tourovskaia, A.; Figueroa-Masot, X.; Folch, A. *Lab Chip* **2005**, *5*, 14.
(9) Khine, M.; Lau, A.; Ionescu-Zanetti, C.; Seo, J.; Lee, L. P. *Lab Chip* **2005**, *5*, 38.
(10) Holmes, D.; Sandison, M. E.; Green, N. G.; Morgan, H. *IEE Proc.: Nanobiotechnol.* **2005**, *152*, 129.
(11) Muller, T.; Gradl, G.; Howitz, S.; Shirley, S.; Schnelle, T.; Fuhr, G. *Biosens. Bioelectron.* **1999**, *14*, 247.
(12) Wang, L. S.; Flanagan, L.; Lee, A. P. *J. Microelectromech. Syst.* **2007**, *16*, 454.
(13) Pohl, H. A. *Dielectrophoresis*; Cambridge University Press: New York, 1978
(14) Fuchs, A. B.; Romani, A.; Freida, D.; Medoro, G.; Abonnenc, M.; Altomare, L.; Chartier, I.; Guergour, D.; Villiers, C.; Marche, P. N.; Tartagni, M.; Guerrieri, R.; Chatelain, F.; Manaresi, N. *Lab Chip* **2006**, *6*, 121.
(15) Docoslis, A.; Kalogerakis, N.; Behie, L. A. *Cytotechnology.* **1999**, *30*, 133.
(16) Fuhr, G.; Glasser, H.; Muller, T.; Schnelle, T. *Biochim. Biophys. Acta* **1994**, *1201*, 353.
(17) Archer, S.; Li, T. T.; Evans, A. T.; Britland, S. T.; Morgan, H. *Biochem. Biophys.* **1999**, *257*, 687.

(18) Chu, H.; Doh, I.; Cho, Y. H. *21st IEEE International Conference on Micro Electro Mechanical Systems, Technical Digest*; IEEE: New York, 2008; p 622.
(19) Yu, C. H.; Vykoukal, J.; Vykoukal, D. M.; Schwartz, J. A.; Shi, L.; Gascoyne, P. R. C. *J. Microelectromech. Syst.* **2005**, *14*, 480.
(20) Rosenthal, A.; Voldman, J. *Biophys. J.* **2005**, *88*, 2193.
(21) Ozkan, M.; Pisanic, T.; Scheel, J.; Barlow, C.; Esener, S.; Bhatia, S. N. *Langmuir*. **2003**, *19*, 1532.
(22) Hughes, M. P. *Biophys. J.* **1999**, *77*, 516.
(23) Heida, T.; Rutten, W. L. C.; Marani, E. *J. Phys. D: Appl. Phys.* **2002**, *35*, 1592.
(24) Voldman, J.; Braff, R. A.; Toner, M.; Gray, M. L.; Schmidt, M. A. *Biophys. J.* **2001**, *80*, 531.
(25) Albrecht, D. R.; Sah, R. L.; Bhatia, S. N. *Biophys. J.* **2004**, *87*, 2131.
(26) Arnold, W. M.; Franich, N. R. *Curr. Appl. Phys.* **2006**, *6*, 371.

JP808897G

Anal. Chem. **2009,** *81,* 7321–7325

Electro-Coalescence of Digitally Controlled Droplets

Xize Niu,[†,‡] Fabrice Gielen,[‡] Andrew J. deMello,[*,†] and Joshua B. Edel[*,†,‡]

Department of Chemistry, and Institute of Biomedical Engineering, Imperial College London, Exhibition Road, South Kensington, London SW7 2AZ, United Kingdom

In this paper we describe a universal mechanism for merging multiple aqueous microdroplets within a flowing stream consisting of an oil carrier phase. Our approach involves the use of both a pillar array acting as a passive merging element, as well as built-in electrodes acting as an active merging element. The pillar array enables slowing down and trapping of the droplets via the drainage of the oil phase. This brings adjacent droplets into close proximity. At this point, an electric field applied to the electrodes breaks up the thin oil film surrounding the droplets resulting in merging.

In the past decade, droplet based microfluidic systems have drawn much attention in the scientific community.[1−8] For example, it has recently been shown that reactions and biological assays within these small nano- to pico- liter sized droplets can be performed and detected on a microsecond time scale.[9] Such applications often require fusion or mixing of droplets to study reactions or assays to completion. With this in mind, reproducible and selective merging of droplets is needed to ensure precise and accurate delivery of a particular analyte or solvent. This is especially true for large scale applications where multiple reagents are involved[10] and for systems where hydrodynamic instabilities in droplet delivery induce irregularities in the merging of droplets.

Different approaches have been demonstrated to successfully merge droplets. These include, the use of electric fields,[11−14] magnetic nanoparticles[15] electrorheological conditions,[16] optical components,[17] or by the use of either patterned surfaces or microfluidic structures.[18−20] All these merging techniques utilize either passive or active merging approaches. Importantly, passive approaches have the ability to adjust the spatial distribution of the droplets by controlling the aqueous and oil regional flow fields. On the other hand, active approaches rely on initiating a sufficiently strong disturbance between neighboring droplets to achieve merging. For example, electrocoalescence can be used where the disturbance is initiated by applying an electric field. Interestingly this mechanism has yet to be fully understood, and there are still debates as to the underlying merging mechanism.[12,13,21] What is clear is that active components are especially useful in applications where surfactants are used to stabilize droplets over long time periods.[22] In the presence of surfactant, droplets tend not to merge even if they are tightly compressed unless an electric field is applied.

In this paper, we combined the advantages of both passive and active merging approaches, to create a novel merging element which can merge droplets regardless of droplet content. It should be noted, that Frenz et al. amongst others have already shown electrical field induced droplet fusion within an expansion channel;[23] however, our approach offers significant advantages which include the ability to adjust the interdroplet distance in a facile manner, precisely control of the number and sequence of droplets being merged, and finally achieve efficient merging under high surfactant concentrations.

* To whom correspondence should be addressed. E-mail: a.demello@imperial.ac.uk (A.J.deM.), joshua.edel@imperial.ac.uk (J.B.E.).
† Department of Chemistry.
‡ Institute of Biomedical Engineering.

(1) Huebner, A.; Sharma, S.; Srisa-Art, M.; Hollfelder, F.; Edel, J. B.; Demello, A. J. *Lab Chip* **2008**, *8*, 1244–1254.
(2) Engl, W.; Roche, M.; Colin, A.; Panizza, P.; Ajdari, A. *Phys. Rev. Lett.* **2005**, *95*, 208304.
(3) Thorsen, T.; Roberts, R. W.; Arnold, F. H.; Quake, S. R. *Phys. Rev. Lett.* **2001**, *86*, 4163–4166.
(4) Song, H.; Chen, D. L.; Ismagilov, R. F. *Angew. Chem., Int. Ed.* **2006**, *45*, 7336–7356.
(5) Anna, S. L.; Bontoux, N.; Stone, H. A. *Appl. Phys. Lett.* **2003**, *82*, 364–366.
(6) Cristobal, G.; Benoit, J. P.; Joanicot, M.; Ajdari, A. *Appl. Phys. Lett.* **2006**, 89.
(7) Dollet, B.; van Hoeve, W.; Raven, J. P.; Marmottant, P.; Versluis, M. *Phys. Rev. Lett.* **2008**, 1.
(8) Hsiung, S. K.; Chen, C. T.; Lee, G. B. *Journal of Micromechanics and Microengineering* **2006**, *16*, 2403–2410.
(9) Song, H.; Ismagilov, R. F. *J. Am. Chem. Soc.* **2003**, *125*, 14613–14619.
(10) Jeffries, G. D. M.; Kuo, J. S.; Chiu, D. T. *Angew. Chem., Int. Ed.* **2007**, *46*, 1326–1328.
(11) Ahn, K.; Agresti, J.; Chong, H.; Marquez, M.; Weitz, D. A. *Appl. Phys. Lett.* **2006**, 88.
(12) Herminghaus, S. *Physical review letters* **1999**, *83*, 2359–2361.
(13) Priest, C.; Herminghaus, S.; Seemann, R. *Appl. Phys. Lett.* **2006**, 89.
(14) Sgro, A. E.; Allen, P. B.; Chiu, D. T. *Anal. Chem.* **2007**, *79*, 4845–4851.
(15) Nguyen, N. T.; Ng, K. M.; Huang, X. Y. *Appl. Phys. Lett.* **2006**, 89.
(16) Niu, X. Z.; Zhang, M. Y.; Wu, J. B.; Wen, W. J.; Sheng, P. *Soft Matter* **2009**, *5*, 576–581.
(17) Baroud, C. N.; de Saint Vincent, M. R.; Delville, J. P. *Lab Chip* **2007**, *7*, 1029–1033.
(18) Tan, Y. C.; Fisher, J. S.; Lee, A. I.; Cristini, V.; Lee, A. P. *Lab Chip* **2004**, *4*, 292–298.
(19) Bremond, N.; Thiam, A. R.; Bibette, J. *Phys. Rev. Lett.* **2008**, 1.
(20) Niu, X. Z.; Gulati, S.; Edel, J. B.; deMello, A. J. *Lab Chip* **2008**, *8*, 1837–1841.
(21) Mostowfi, F.; Khristov, K.; Czarnecki, J.; Masliyah, J.; Bhattacharjee, S. *Appl. Phys. Lett.* **2007**, *90*, 3.
(22) Holtze, C.; Rowat, A. C.; Agresti, J. J.; Hutchison, J. B.; Angile, F. E.; Schmitz, C. H. J.; Koster, S.; Duan, H.; Humphry, K. J.; Scanga, R. A.; Johnson, J. S.; Pisignano, D.; Weitz, D. A. *Lab Chip* **2008**, *8*, 1632–1639.
(23) Frenz, L.; El Harrak, A.; Pauly, M.; Begin-Colin, S.; Griffiths, A. D.; Baret, J. C. *Angew. Chem., Int. Ed.* **2008**, *47*, 6817–6820.

10.1021/ac901188n CCC: $40.75 © 2009 American Chemical Society
Published on Web 07/21/2009

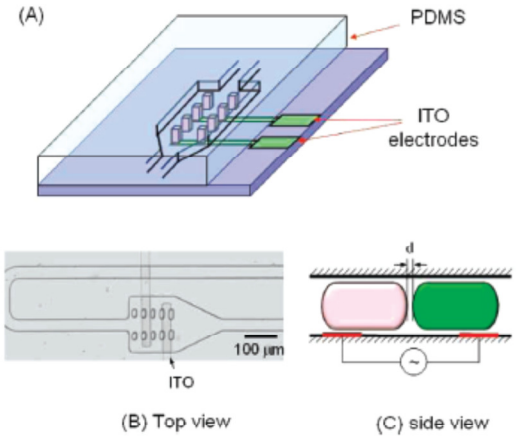


Figure 1. (A) Schematic of the merging chamber. (B) Bright field optical image of the merging chamber. (C) Cross sectional schematic of two droplets being merged.

EXPERIMENTAL SECTION

A schematic of the fluidic chip design and operating mechanism is shown in Figure 1. The fluidic channels have a 50 × 50 μm rectangular cross section and dilate to a width of 250 μm. This wider chamber is effectively the heart of the "merging element". This chamber consists of two parallel pillar arrays. The size and location of the pillars were designed to ensure that droplets of similar size can be slowed down and trapped between the two sets of pillars. The pillars have a 20 μm square cross section and a pitch of 36 μm. Also embedded within the merging chamber are two parallel indium tin oxide (ITO) electrodes, which were integrated onto the lower substrate. These electrodes were designed to run perpendicular to the pillars. The distance between electrodes was designed to be either 100 or 200 μm (Figure 1b). By applying an alternating current (AC) electric field to the ITO electrodes, the interface between the trapped droplets within the chamber element is ruptured resulting in complete merging.

The fluidic channel and pillars were fabricated from polydimethylsiloxane (PDMS) using standard soft lithographic techniques. More specifically, to fabricate the microfluidic chip, PDMS base and curing agent (Sylgard 184; Dow Corning, Wiesbaden, Germany) was mixed in a ratio of 10:1 w/w, degassed and decanted onto an SU-8 master. The resulting structure was cured overnight in an oven at 65 °C. After thermal curing, the polymer layer was peeled off the master. This was followed by inlet and outlet holes being punched through the reservoirs. The device was sealed with ITO coated glass. Prior to sealing, the ITO layer (100 nm thick) was patterned using standard lithographic techniques to fabricate the electrodes (Figures 1b and 1c). Importantly, ITO has the added advantage of being optically transparent; therefore droplets could easily be observed directly above the electrodes. The substrates were cleaned and plasma treated, and finally, the two layers were manually aligned and bonded under an optical microscope.

In initial experiments, hexadecane oil (Sigma-Aldrich) was used as the continuous phase with Span 80 added at various concentrations to act as a surfactant. All experiments were performed at room temperature. Deionized water or deionized water containing a small amount of food dye was used as the discrete aqueous

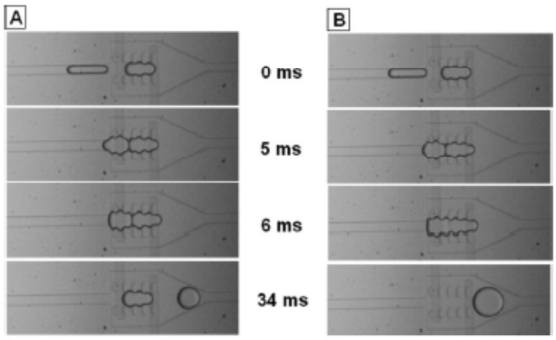


Figure 2. Merging device during operation. (A) In the absence of electric field, the droplets, containing surfactant, entering the merging chamber do not merge. (B) With an applied electric field, the droplets entering the chamber coalesce.

phase. Syringe pumps (PHD 2000, Harvard Apparatus) were used to pump fluids into the microfluidic channels at total flow rates ranging from 1−10 μL/min. Droplet generation frequencies up to 300 Hz could be achieved with our current platform. A high speed camera (Phantom, v5.1, Vision Research) was used for data acquisition, and Matlab was used to analyze and process recorded images.

Figure 2 shows an optical image of the microfluidic device during operation. On the left-hand column of Figure 2, no electric field was applied to the electrodes. At time 0 ms, a static droplet is trapped within the pillar array. A flowing droplet generated upstream arrives at the entrance of the merging chamber after 5 ms. As the second droplet gets pushed further into the array, the first droplet is expelled without any merging taking place due to the presence of surfactant. On the other hand, Figure 2b depicts a similar scenario; however, this time with an electric field applied to the electrodes. As in the previous case after 5 ms the second droplet approaches the first trapped droplet within the array and after 6 ms, the two droplets fuse together. This is followed by the newly formed droplet departing the merging chamber after 34 ms. The next part of the manuscript describes the differences between the mechanisms leading to merging and non-merging, respectively.

Merging Mechanism and Calibration. It has previously been shown by Mostowfi et al. that the rupture potential inducing coalescence of droplets is linearly dependent on the separation distance between the droplets.[24] In our design where the pillar array ensures drainage of the oil phase between the droplets, the voltage needed to rupture the interface can be as low as 50 V/mm, instead of 500 V/mm as has been previously reported.[11] To precisely determine the exact conditions in terms of voltage, amplitude, and frequency at which point coalescence occurs, the device was calibrated using different concentrations of surfactant (Span-80), ranging from 0 to 0.5 w/w %. Here hexadecane was used as carrier phase and deionized water as the discrete phase. The size of the droplets created by our T-junction was adjusted by varying the flow rates so that the droplets would be approximately 200 μm in length and 50 μm wide. These dimensions

(24) Ruckenst., E.; Jain, R. K. *Journal of the Chemical Society-Faraday Transactions II* **1974**, *70*, 132–147.

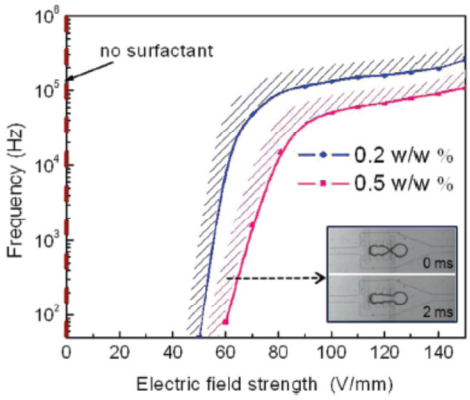


Figure 3. Calibration diagram of the merging threshold as a function of voltage and frequency.

were chosen so that the passive merging chamber could contain anywhere from 2−4 droplets at any given time.

The curves shown in Figure 3 delimitate transition regions between coalescence and non-coalescence of all droplets in the presence of 0, 0.2, and 0.5 w/w% surfactant. The threshold voltage required to cause coalescence scales up with the surfactant concentrations which is consistent with the fact that surfactants generally improve droplet stability. Without any surfactant present, all droplets within the pillar array merge under no applied electric field. A purely passive merger such as this has been studied in depth and published by the authors in 2008.[20] However, when a surfactant concentration of 0.2 and 0.5 w/w% was used, a clear trend in the applied electric field can be seen as a function of operating frequency. Any conditions to the right of these curves will result in droplets being merged. Within the hatched transition areas in Figure 3, merging is either not reproducible or merges via decompression.[19] An image demonstrating this process is shown in the inset within Figure 3. At voltages well above threshold with frequencies lower than 10−100 kHz, electrocoalescence events always occur between the patterned electrodes. Importantly, no failure in merging was observed under continuous operation of the device for several hours. Interestingly, at frequencies above 100−500 kHz, no coalescence was seen.

Thickness of the Oil Interface at Merging. The oil membrane thickness between droplets is not only crucial to further understand droplet merging, but also important for reagent exchange and diffusion between droplets. It is generally a difficult task to optically observe and measure this thickness (typically less than 1 μm) prior to merging. Our merging chamber provides a platform to slow down the droplets sufficiently to study the oil membrane thickness between two microdroplets. More specifically, the oil drainage rate between the droplets can be deduced theoretically and verified with a high speed camera. The average membrane thickness at the time of merging can then calculated from the drainage rate.

A detailed observation of the merging process in Figure 2 shows that the first droplet in the merging chamber will reach a Newtonian force balance, and is trapped and stopped before merging with the succeeding droplet. The succeeding droplet, sustains a hydraulic pressure from the oil pushing it forward (compared with the flow direction) and an inner pressure from

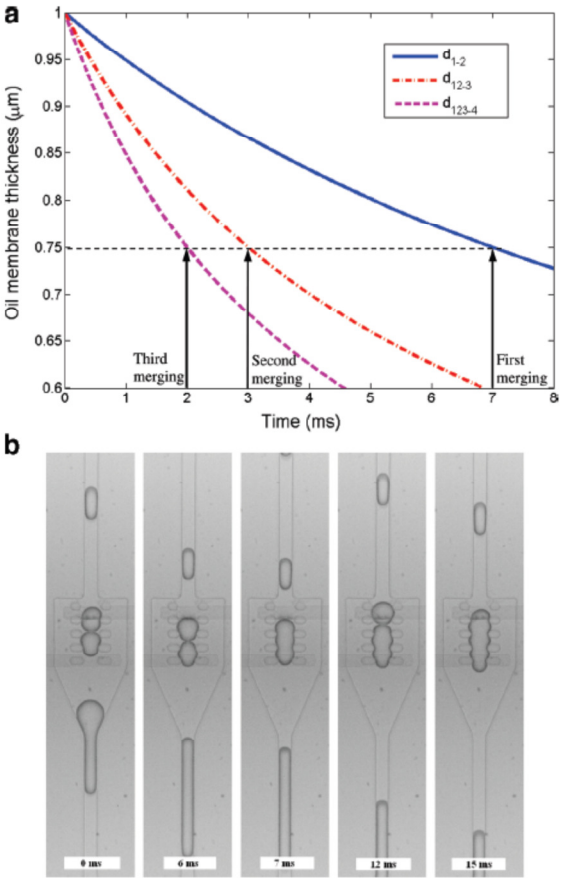


Figure 4. (A) Calculated oil film membrane thickness as a function of time for three successive droplet merging events. d_{1-2} indicates thickness of the oil interface between the first and second droplet. d_{12-3} indicates the thickness of the oil interface between the third droplet entering the chamber and the merged d_{1-2} droplet. Finally, d_{123-4} indicates the thickness of the oil interface between the third droplet entering the chamber and the merged d_{12-3} droplet. The arrows indicate the experimental merging time for the three successive merging events. The intersections between the experimental and theoretical results indicate a film thickness of 750 nm. (B) Time sequence of 3 droplets being merged.

the surface tension pushing it backward. The pressure balance can be described as follows[20]

$$\Delta P = \Delta P_h - \Delta P_d \quad (1)$$

where ΔP_h is the hydraulic pressure and ΔP_d the inner pressure. To infer a realistic value for ΔP, we simulated droplet accumulation in the merging chamber using the Comsol simulation package. The results suggest that the pressure at the inlet of the chamber is around 600 Pa. The oil film drainage rate between the two droplets can therefore be derived from the Reynold's equation and can be written as follows:

$$d(1/D^2)/dt = a\Delta P, \quad a = 4/(3\eta r^2) \quad (2)$$

Here D is the interface thickness, t the time, η the dynamic viscosity, and r the radius of the droplet. The merging chamber

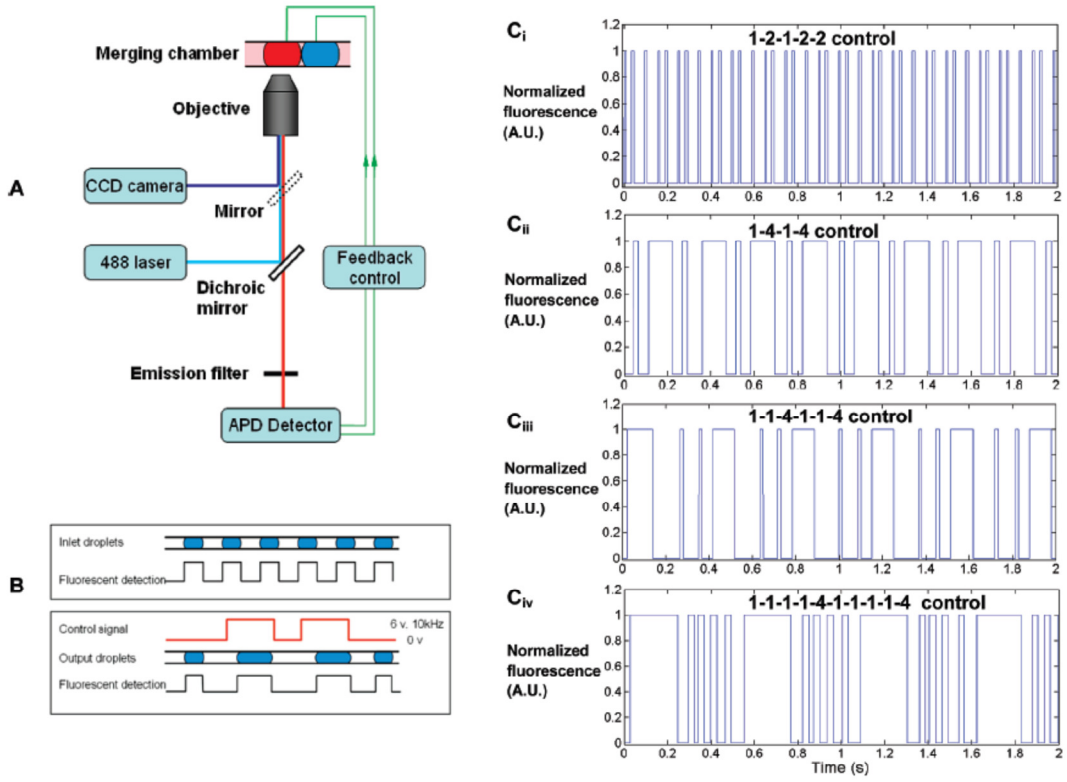


Figure 5. (A) Schematic of the optical setup used for selective merging of droplets. (B) Schematic of the detected fluorescence signal with and without the use of feedback control. (C) Normalized fluorescence signal obtained by merging droplets in the following sequence: (i) 1−2−1−2−2, (ii) 1−4−1−4, (iii) 1−1−4−1−1−4, (iv) 1−1−1−1−4−1−1−1−1−4.

was designed to merge up to four consecutive droplets (via three separate merging events). As a result, differences in the oil drainage rate can be monitored. As the droplet increases in size as does the differential pressure ΔP resulting in a faster oil drainage rate. This can be seen in Figure 4a where a plot is shown correlating the oil membrane thickness as a function of time using eq 2 for three successive merging events. The interface thickness for these three merging events is defined as d_{1-2}, d_{12-3}, and d_{123-4} respectively. Movies with 100 ns frame times were used to verify that no abrupt acceleration or deceleration takes place during the merging process. This effectively confirms that eq 2 remains valid prior to merging taking place.

Moreover, experimental snapshots of the merging events enabled characterizing the merging time based on the number of droplets present in the pillar chamber (Figure 4b). The merging time was defined as the time elapsed between droplets 1 μm apart and their merging. For example, the merging time decreases from 7 ms (between 0 and 7 ms, in Figure 4b) for the first pair of droplets to 3 ms for the second pair (between 12 and 15 ms). Average merging times are denoted by arrows as is shown in Figure 4a. This intercept also highlights the oil film thickness prior to merging. Interestingly, we found that from Figure 4a, that all merging events take place when droplets are approximately 750 nanometers away from each other. Such a distance is much larger than the commonly assumed several nanometers[25] derived from the distance of two monolayers of surfactant molecules.

Selective Merging for Digital Reactions. The electric field applied to the ITO electrodes can be easily computer controlled or programmed by a function generator to selectively merge droplets, in a systematic manner flowing through the merging chamber. Importantly, this can find applications in controlled sequential reactions[4,10] or droplet logic.[26] We experimentally verify the feasibility of this by doping the aqueous droplets with a 1 mM fluorescein solution. The fluorescence signal detected at a single point in the middle of the merging chamber was recorded, and the intensity was used as a feedback mechanism to precisely control the number of droplets being merged. The schematic of the optical setup is shown in Figure 5a. Briefly, a 488 nm laser beam excitation source is focused into the microfluidic channel with a 20× objective. The emitted photons are collected using the same microscope objective, and the fluorescence light is focused onto an avalanche photodiode detector. Figure 5b shows a schematic of the process. Initially a train of uniformly spaced droplets are introduced into the merging chamber (Figure 5b, top). Once in the chamber, the fluorescence signal can be read out, and merging can be subsequently achieved by triggering the function generator to apply an electric field to the ITO electrodes. Patterns such as those shown in the bottom of Figure 5b can be generated to perform alternate merging or merging with a well-defined number of droplets.

(25) Leneveu, D. M.; Rand, R. P.; Parsegian, V. A.; Gingell, D. *Biophys. J.* **1977**, *18*, 209–230.
(26) Cheow, L. F.; Yobas, L.; Kwong, D. L. *Appl. Phys. Lett.* **2007**, 90.

Figure 5c$_i$ shows experimental results of the optical signal when the laser beam was focused at the outlet point of the merging chamber. In this case, the control signal was delivered using a sinusoidal waveform at a frequency of 10 kHz, over a 2 s acquisition time. After merging, the detected width of the fluorescence peak increases by a factor of 2, which implies successful merging (the fluorescence signal was normalized for visualization purposes). In the second example (Figure 5c$_{ii}$−c$_{iv}$), a series of four droplets are merged in varying sequences in a reproducible manner. In both examples, no perturbation in droplet size and spacing was found. Such selective merging can be nicely coupled to a passive sorting approach to collect fused droplets based on droplet size.[18,26] These merging examples demonstrate the capabilities of the platform to selectively merge up to four droplets in a reproducible manner.

CONCLUSION

We have engineered a system capable of selective merging one or more aqueous microdroplets in a reproducible manner. The hybrid platform exploits the advantage of both passive and active merging mechanisms. The chip was designed to permit low voltage coalescence events. Although the merging of droplets, in this paper, was predominantly performed using hexadecane, Span 80, and DI water, other combinations were also tested. For example, FC-40 with 1.8% (w/w) E2K0660 surfactant[22] was used as the oil phase and 20 nM streptaviden labeled with alexa 488 (Invitrogen, Paisley, U.K.) was used as the aqueous phase. Importantly, changing of the droplet and oil conditions did not affect droplet merging. The platform described in this paper will prove to be especially useful in applications where merging a well defined number of droplets in required. Importantly, this platform also offers significant advantages where surfactants are added to the oil phase in order to stabilize the system. Potential applications include sequential chemical/biological reactions and assays (e.g., cascade reactions), manipulation of elastic lipid vesicles, droplet logics, and droplet sorting.

ACKNOWLEDGMENT

This work was supported by the RCUK Basic Technology Programme. We would like to thank Miss Mengying Zhang from HKUST for helpful discussions on oil/water emulsions.

SUPPORTING INFORMATION AVAILABLE

Additional information in the form of AVI files. This material is available free of charge via the Internet at http://pubs.acs.org.

Received for review June 1, 2009. Accepted July 6, 2009.

AC901188N

Anal. Chem. **2010**, *82*, 7509–7514

High-Resolution Local Imaging of Temperature in Dielectrophoretic Platforms

Fabrice Gielen,[‡,†,§] Fiona Pereira,[†] Andrew J. deMello,[*,†] and Joshua B. Edel[*,‡,†]

Department of Chemistry, Institute of Biomedical Engineering, and Chemical Biology Centre, Imperial College London, South Kensington, London, SW7 2AZ, United Kingdom

The use of dielectrophoretic forces is crucially tied to the knowledge of Joule heating within a fluid, since the use of planar microelectrodes creates a temperature gradient within which the particle of interest is manipulated. Mapping temperature with sufficient spatial resolution within a dielectrophoretic trap is recognized to be of high importance. Herein, we demonstrate local temperature measurements in the vicinity of a trapped micrometer-size particle using confocal fluorescence spectroscopy. Such measurements are shown to provide a novel calibration tool for screening temperature-mediated processes with high resolution.

Spatial and temporal temperature variations are a primary concern in many applications making use of electric fields such as electrophoresis,[1,2] electro-osmosis,[3] electrochemotherapy,[4] and dielectrophoresis[5] (DEP). Indeed, even small currents flowing through buffers of high conductivity generate significant Joule heating. For commonly used buffers such as phosphate buffered saline (PBS) of conductivity 1.6S/m or Dulbecco's Modified Eagle medium (DMEM) of conductivity 1.4S/m, Joule heating sets constraints on the operational range of the analytical device.

Dielectrophoresis (DEP) relies on the manipulation of micro- or nano-objects using high-frequency nonuniform electric fields. DEP trapping for biological applications normally involves keeping particles or cells within electric fields for extended periods of time, and knowledge of the temperature at or around the cell within a microfabricated DEP trap significantly impacts interpretation of experimental results. For instance, cell growth has been demonstrated within RF fields,[6,7] but the consequences of temperature rise on DEP experiments relying on proteins, DNA, and cells must also be considered. In certain cases, temperatures above 40−45 °C will lead to a reduction in biological activity or denaturation and cell death.

Joule heating may be circumvented using low-conductivity media such as isotonic sucrose buffers.[8,9] However, in this case, DEP forces turn positive for mammalian cells making them migrate toward high electric field regions where they experience risks of charging and other electrochemical damage unless insulated from electrodes (e.g., by a permeation layer). Quantifying theoretical temperature rises is limited by uncontrollable changes to experimental conditions such as material properties, buffers, etc.

Mapping temperature with high spatial resolution cannot be achieved using integrated thermocouple probes[10] whose size and fabrication restrict their use to indirect measurement of average temperature. Seger et al.[5] have described the heat dissipation of a negative DEP barrier and the temperature gradient at the vicinity of electrodes using fluorescence detection but with limited spatial resolution. Noninvasive fluorescent techniques, such as intensity-based measurements, have been found to give good estimates of average temperature within a microchannel but are very sensitive to well-known artifacts including a dependency on the dye concentration and detection efficiency.[11] On the other hand, the use of fluorescence lifetime imaging allows artifact-free measurements of excited state decay times which conveys information on the local fluorophore environment.[12,13]

Herein, we apply confocal fluorescence spectroscopy to the accurate probing of temperature close to a defined surface where DEP traps are patterned. We achieve local mapping of temperature around a particle of interest using both lifetime and intensity imaging, with submicrometer spatial resolution.

EXPERIMENTAL SECTION

Microfluidic Design and Fabrication. A schematic of the fluidic chamber and trap array used is shown in Figure 1a. The PDMS chamber with a 1 mm wide and 30 μm deep channel was

* To whom correspondence should be addressed. E-mail: joshua.edel@imperial.ac.uk (J.B.E.); a.demello@imperial.ac.uk (A.J.dM.).
† Department of Chemistry.
‡ Institute of Biomedical Engineering.
§ Chemical Biology Centre.

(1) Muyzer, G.; Smalla, K. *Antonie Van Leeuwenhoek* **1998**, *73*, 127–141.
(2) Serwer, P. *Electrophoresis* **1983**, *4*, 227–231.
(3) Zhao, T. S.; Liao, Q. *J. Micromech. Microeng.* **2002**, *12*, 962–970.
(4) Lackovic, I.; Magjarevic, R.; Miklavcic, D. *IEEE Trans. Dielectr. Electr. Insul.* **2009**, *16*, 1338–1347.
(5) Seger, U.; Panayiotou, M.; Schnydrig, S.; Jordan, M.; Renaud, P. *Electrophoresis* **2005**, *26*, 2239–2246.
(6) Fuhr, G.; Glasser, H.; Muller, T.; Schnelle, T. *Biochim. Biophys. Acta, Gen. Subj.* **1994**, *1201*, 353–360.
(7) Arnold, W. M.; Franich, N. R. *Current Applied Physics* **2006**, *6*, 371–374.
(8) Sankaran, B.; Racic, M.; Tona, A.; Rao, M. V.; Gaitan, M.; Forry, S. P. *Electrophoresis* **2008**, *29*, 5047–5054.
(9) Suehiro, J.; Pethig, R. *J. Phys. D: Appl. Phys.* **1998**, *31*, 3298–3305.
(10) Nishikawa, T.; Kambara, H. *Electrophoresis* **1996**, *17*, 1115–1120.
(11) Markham, J.; Conchello, J. A. *J. Microsc. (Oxford, U.K.)* **2001**, *204*, 93–98.
(12) Benninger, R. K. P.; Koc, Y.; Hofmann, O.; Requejo-Isidro, J.; Neil, M. A. A.; French, P. M. W.; deMello, A. J. *Anal. Chem.* **2006**, *78*, 2272–2278.
(13) Robinson, T.; Valluri, P.; Manning, H. B.; Owen, D. M.; Munro, I.; Talbot, C. B.; Dunsby, C.; Eccleston, J. F.; Baldwin, G. S.; Neil, M. A. A.; de Mello, A. J.; French, P. M. W. *Opt. Lett.* **2008**, *33*, 1887–1889.

10.1021/ac101557g © 2010 American Chemical Society
Published on Web 08/04/2010

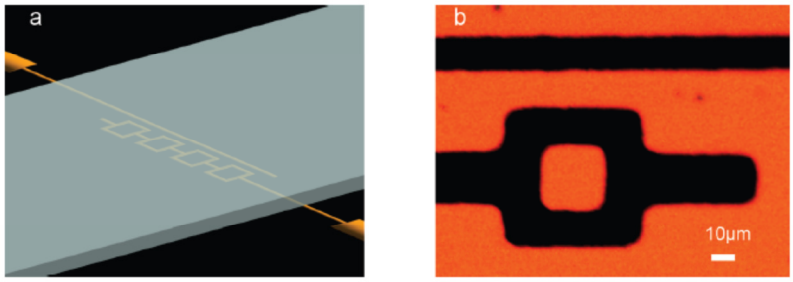


Figure 1. (a) Schematic of the microfluidic device including gold electrodes patterned on glass and the fluidic chamber; (b) bright field picture of a single nDEP trap.

fabricated using standard lithographic techniques.[14] The square electrode geometry used has been previously published,[15] the only difference being a 15 μm gap between electrodes and larger line electrodes. Figure 1b is a bright field image of a single electrode trap using an Olympus BX51 upright microscope equipped with a 20× objective.

Gold electrodes were patterned following a lift-off process. AZ 1512HS (MicroChemicals) photoresist was first patterned on thin glass (borosilicate glass, thickness #1) and used as a sacrificial layer. Exposure to UV light through a lithographic mask and development revealed the electrode pattern. An estimated 60 nm gold layer was deposited using a sputter coater (Emitech, K550). The photoresist was then stripped off with acetone. The devices were further cleaned in isopropanol and deionized water, dried with nitrogen gas, and stored at room temperature. Finally, the PDMS chamber was plasma bonded, and the electrodes were connected as described previously.[16]

Materials. Rhodamine B was obtained from Sigma-Aldrich and dissolved in a phosphate buffer solution to a final concentration of 100 μM. The 1× PBS buffer was made of 2.6 mM KCl, 1.4 mM KH_2PO_4, 136 mM NaCl, and 8.1 mM Na_2HPO_4 (Sigma Aldrich). A polystyrene bead stock solution with a mean diameter of 10 μm, 2.5% solids (w/v) in water (Polybead Microspheres, PolySciences), was pelleted down and resuspended in the same phosphate buffer. This was added to the rhodamine B-loaded PBS solution with a final dilution factor of 1000. Conductivities were measured using a Dist 5 conductivity meter (VWR). The conductivity of the PBS buffer was found to be 1.67 S/m. The thermal conductivity was 0.58W/mK.

Time Correlated Single Photon Counting Setup. The excitation source for all measurements was a spectrally filtered supercontinuum laser (SC450, Fianum) producing 5 ps pulses at a rate of 20 MHz. The 488 nm laser line was selected via an Acousto-Optic Tunable Filter (AOTF) system directly coupled to the laser output. The bandpass was approximately 3 nm. The beam was directed toward the laser-scanning unit of an inverted laser scanning confocal microscope (FV300, Olympus) using a second optical fiber, deflected by a 488 nm dichroic filter (FV3 DM470-2, FV3 DM488-2, Olympus) to the back aperture of a 20× objective and finally into the device. Fluorescence emission was collected with a custom-built detection path. Briefly, the emitted photons were collected through the same objective and same dichroic mirror. A high quality long pass filter (LP02-488RU-25, RazorEdge, Semrock, Laser 2000) was used to further separate excitation from emission light where the former was focused by a lens onto a 100 μm confocal pinhole (P100S, Thorlabs). The Gaussian confocal volume was estimated to be 470 nm in width and 3 μm in depth. This was calculated by measuring the diffusion time of fluorescein using fluorescence correlation spectroscopy. Fluorescence was subsequently directed toward an avalanche photodiode (SPCM-AQRH-13, PerkinElmer Optoelectronics) operating in single photon counting mode. Upon photon arrival, the TCSPC electronics (TimeHarp 200, Picoquant GmbH) were activated, and the time delay between laser pulse and photon arrival were collected in data files. The scanning window allowed 512 × 512 pixels to be scanned in 1.12 s with 4 × 4 binning. The instrument response function (IRF) was recorded using a Rose Bengal solution in water having a fluorescence lifetime lower than 100 ps.[17] Lifetime data was analyzed using SymphoTime software (PicoQuant). A built-in least-squares fitting algorithm was applied in order to extract fluorescence lifetimes and construct two-dimensional fluorescence lifetime maps. Specifically, the program uses a least-squares algorithm to fit a model decay to the data and works to iteratively reduce the measure of the difference between them. The χ^2 value in eq 1 is used to minimize this difference

$$\chi^2 = \sum_n \frac{(I(t_n) - I_{fit}(t_n))^2}{I(t_n)} \quad (1)$$

where $I(t_n)$ is the measured intensity and $I_{fit}(t_n)$ is the fitted decay. The decay which has the minimum χ^2 is then chosen.

Heating with Planar Microelectrodes. Negative dielectrophoretic traps rely on repulsion of cells, particles, or molecules away from high electric field regions and make use of nonuniform AC electric fields in the range of 100 kHz to several MHz. The temperature balance describing power generation and dissipation can be written as follows:[18]

$$\rho_m c_p \nabla T + \rho_m c_p v \frac{\partial T}{\partial t} = k\nabla^2 T + \sigma E^2 \quad (2)$$

(14) Duffy, D. C.; McDonald, J. C.; Schueller, O. J. A.; Whitesides, G. M. *Anal. Chem.* **1998**, *70*, 4974–4984.
(15) Rosenthal, A.; Voldman, J. *Biophys. J.* **2005**, *88*, 2193–2205.
(16) Gielen, F.; deMello, A. J.; Cass, T.; Edel, J. B. *J. Phys. Chem. B* **2009**, *113*, 1493–1500.
(17) Khajehpour, M.; Troxler, T.; Vanderkool, J. M. *Photochem. Photobiol.* **2004**, *80*, 359–365.
(18) Landau, L. D. a. L. E. M. *Fluid Mechanics*; Pergamon: Oxford, 1959.

Here, c_p is the specific heat at constant pressure, k the thermal conductivity, v the velocity, ρ_m is the density. σ and σ_0 is the electrical conductivity of the medium at temperatures T and T_0, respectively. As the electrical conductivity of the buffer increases with temperature, additional coupling of eqs 2 and 3 must be taken into account. This can be expressed as

$$\sigma = \sigma_0[1 + \alpha(T - T_0)] \quad (3)$$

Here, α is the temperature compensation factor of the buffer. For water, this value is 1.8%/°C.[19]

As has been shown by Ramos et al., the temperature rise can be estimated using dimensional analysis of eq 2:

$$\Delta T \approx \frac{\sigma V_{rms}^2}{k} \quad (4)$$

Here, V_{rms} is the potential difference across the electrodes. There are several limitations to validating this estimate, especially the omission of geometry-related parameters. Indeed, the complexity of geometries inherent to DEP traps implies actual electric fields differ from the analytical voltage-to-distance ratio. Poor control over boundary conditions has also been recognized.[20]

Factors that contribute to misestimating temperature include variations in electrical resistance (also varying through the temperature coefficient of resistance) and roughness of the metal electrodes. Heat diffusion in the electrodes is also neglected in eq 4.[4] All these factors add up to conductivity and permittivity gradients due to temperature rise as well as edge effects where heating is much higher than average temperature rises.

In general, eq 4 typically gives an upper limit estimate of the temperature rise within the microfluidic chip. There are many parameters contributing to heat sinking that can be modeled but are hard to theoretically estimate. Stuart et al. introduced a correction factor for the voltage in order to simulate field losses.[21] Furthermore, this correction factor increases with buffer conductivity. In practice, V_{rms} has to be replaced by an effective voltage making up the physical treatment of the system.

RESULTS AND DISCUSSION

In order to use rhodamine B as a temperature probe, the variation of its fluorescence properties with temperature must be calibrated. The use of this dye has been reported in numerous studies due to its large fluorescence quantum yield variation.[12] Although local temperature values can be accurately determined in certain temperature ranges using polymers,[22] the wide dynamic range exhibited by rhodamine B makes it especially useful for detecting large temperature changes.

Furthermore, the extraction of the values of absolute temperature from intensity measurements remains limited by photophysical effects induced by heating. In particular, the fluorescence intensity might not fully recover after a thermal cycle.[23] That is why relative measurements, recording either intensity changes, are more accurate. Although lifetime measurements require more data for statistical treatment, they produce more accurate data sets allowing for measurements close to interfaces.

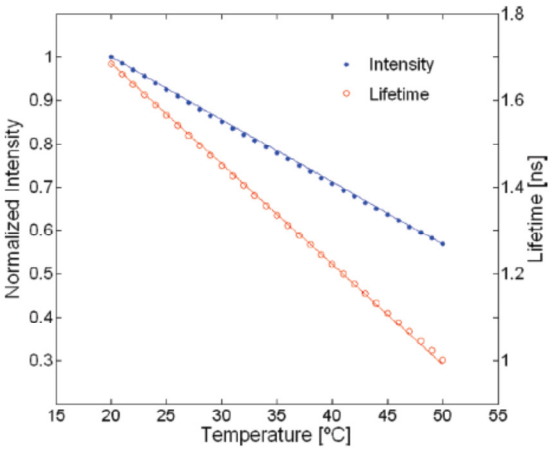


Figure 2. Calibration plot for measuring temperature with rhodamine B: intensity and fluorescence lifetime decay with temperature at a rate of 1.12%/°C and 1.07%/°C, respectively.

Calibration was done using a Peltier element having an active cooling fan. A microfluidic chamber made up of two thin glass slides separated by a spacer was built and fixed on top of the Peltier. A first thermocouple probe was linked to the surface of the Peltier while a second one was placed within the built chamber and recorded the actual fluid temperature. A few tens of microliters of a solution of 100 μM rhodamine B in PBS 1× was pipetted from one side of the chamber, immersing the inner thermocouple. A photograph of the actual calibration setup is shown in the Supporting Information. The chamber was placed on top of a 20× air objective to avoid heat transfer to the objective. The Peltier was subsequently ramped from room temperature up to 50 degrees, and the intensity and fluorescence lifetime of a 100 μM rhodamine B solution was monitored in real time. Figure 2 is a calibration plot for rhodamine B in terms of its fluorescence lifetime and normalized intensity.

Linear fits of the intensity and lifetime calibration data yield a decrease of 1.12%/°C and 1.07%/°C, respectively. The fast temperature ramp applied to the rhodamine B solution is believed to minimize photophysical damage to the dye and may explain the difference from exponential decay data published previously.[24] Furthermore, these decay rates correspond well to previously published values.[5]

The concentration of rhodamine B in PBS used throughout this study was high (100 μM). Temperature mapping using a similar concentration has already been published.[12,13] The practicality of the use of high concentrations is that laser powers can be reduced significantly and pile-up effects avoided. The fluctuation of dyes in the confocal volume can also be minimized using high concentrations. However, under such concentrations, un-

(19) Hayashi, M. *Environ. Monit. Assess.* **2004**, *96*, 119–128.
(20) Mittal, N.; Rosenthal, A.; Voldman, J. *Lab Chip* **2007**, *7*, 1146–1153.
(21) Williams, S. J.; Chamarthy, P.; Wereley, S. T. *J. Fluids Eng.-Trans. ASME* **2010**, *132*, 7.
(22) Chee, C. K.; Rimmer, S.; Soutar, I.; Swanson, L. *Polymer* **2001**, *42*, 5079–5087.
(23) Low, P.; Kim, B.; Takama, N.; Bergaud, C. *Small* **2008**, *4*, 908–914.
(24) Shah, J. J.; Gaitan, M.; Geist, J. *Anal. Chem.* **2009**, *81*, 8260–8263.

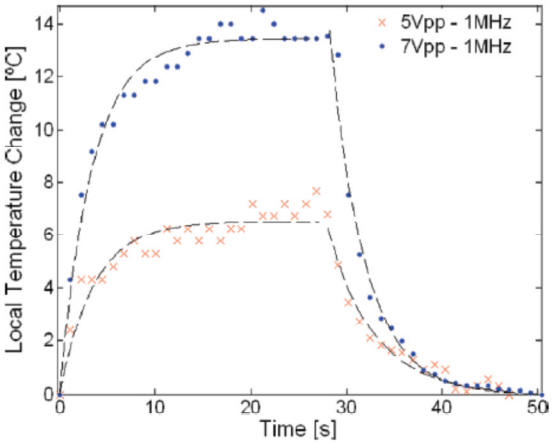


Figure 3. Transient increase in temperature upon a voltage step. The focal plane is adjusted to be 5 μm above the surface of the device.

wanted photophysical effects can at times lead to nonlinear behavior of intensity versus temperature or concentration. On the other hand, lifetime imaging is insensitive to these artifacts. We found that 100 μM gives a good linear dynamic range for lifetime−temperature calibration which is essential for accurate temperature imaging.

Transient Temperature Rise and Cooling of the Microsystem. Here, we study the transient temperature change after the application of a voltage step and on switching off the electric field. Specifically, fluorescence intensity pictures of the DEP trap were acquired at a focal plane of 5 μm above the glass surface before the application of electric fields and well after it had been turned off. The variations in average intensity were recorded on a frame-by-frame basis and can be plotted as a temperature variation over time. The electric fields were switched off 28 s after application of the fields. Exponential fits in Figure 3 are displayed simply as visual aids.

The steady-state temperature rises within the system were found to be 6.5 and 13.5 °C, and the characteristic heating time constant τ_h was 3.5 and 3.3 s for applied voltages of 5 V_{pp} and 7 V_{pp}, respectively, at a fixed frequency of 1 MHz. It can be seen that steady state was reached within approximately 10 s. This is much larger than the theoretical value of 1 ms[25] and is due to capacitive effects possibly arising from the gold nonuniform thickness.

Cooling of the area surrounding the electrodes has been studied in the same way. The characteristic cooling time constant τ_c of the system was 4.8 and 3.7 s for applied voltages of 5 V_{pp} and 7 V_{pp}, respectively. Dissipation mainly happens via conduction to the substrate and that is why heat dissipation can be improved using a substrate of higher thermal conductivity. As shown by Ramos et al.,[25] these types of microelectrode structures cannot be easily cooled down by fluid injection: even at high flow rates, the temperature profile is preserved. This has been tested experimentally at average in-channel velocities of up to 0.5 mm/s. Flow cooling is ultimately limited by the Poiseuille flow profile within a microchannel where surface flow velocities are very low.

Temperature Mapping within an nDEP Trap. For microfluidic devices that incorporate electrodes, the presence of metal complicates fluorescence-based experiments. For instance, the fluorescence of gold under UV−vis wavelengths limits its use with competitive fluorescence studies although it has many direct applications.[26] In particular, although the fluorescence decay can be composed of several independent components, it is preferable to have a single radiative route to decay (i.e., a monoexponential decay law). Scattering effects as well as the adsorption of molecules on a surface at high concentrations also restrict the use of nonconfocal fluorescence setups.[27]

Here, temperature mapping of a DEP trap with a captured polystyrene sphere was performed at steady state. Focusing was performed by finding the maximum autofluorescence level of the gold electrodes and moving the objective 5 μm above that level. The polystyrene beads absorb the excitation radiation and, therefore, appear as low count regions in the intensity map. Because of rejection of light from the surface via the confocal pinhole, the contribution of the electrodes was also negligible, and after excluding the gold and polystyrene contribution from the lifetime calculation analysis, the data could be well fitted with a single-exponential decay law.

Figure 4a shows intensity and lifetime maps for the same DEP trap. Because of the repulsion of the bead from high-electric fields regions, the analysis of fluorescence intensity is limited to areas where the bead does not interact. The temperature map from intensity measurements is plotted as a relative decrease in intensity but does not reflect real temperature variation in the vicinity of the bead. On the other hand, the FLIM picture can be used as absolute values for extracting temperature rise when the electric field is turned on. The second line electrode was located at the bottom of the trap. Here, we used 7 V_{pp} and a frequency of 1 MHz. Ten frames were accumulated to collect sufficient photons and reduce statistical noise. A median filter of size 5 × 5 was further applied to the raw data in order to reduce the remaining noise. The full data processing approach is given in the Supporting Information. In the case of Figure 4a, the number of workable pixels is 25% more in the lifetime map than in the intensity map. For the analysis of 2 or more particles within a single trap, and as the number of workable pixels decreases, lifetime imaging can provide much more accurate data than intensity measurements. In particular, the bead appears bigger in the intensity map because of a refractive index mismatch between polystyrene (1.55) and water (1.3). Accordingly, temperature can be accurately described at the interface between the fluid and particle using fluorescence lifetime imaging alone.

The lifetime histogram for each analyzed pixel (after applying the intensity threshold as described in the Supporting Information) shows the shift toward lower lifetimes after switching on the electric field. The lifetime distribution was fitted to a Gaussian

(25) Ramos, A.; Morgan, H.; Green, N. G.; Castellanos, A. *J. Phys. D: Appl. Phys.* **1998**, *31*, 2338–2353.

(26) He, H.; Xie, C.; Ren, J. *Anal. Chem.* **2008**, *80*, 5951–5957.

(27) Glawdel, T.; Almutairi, Z.; Wang, S.; Ren, C. *Lab Chip* **2009**, *9*, 171–174.

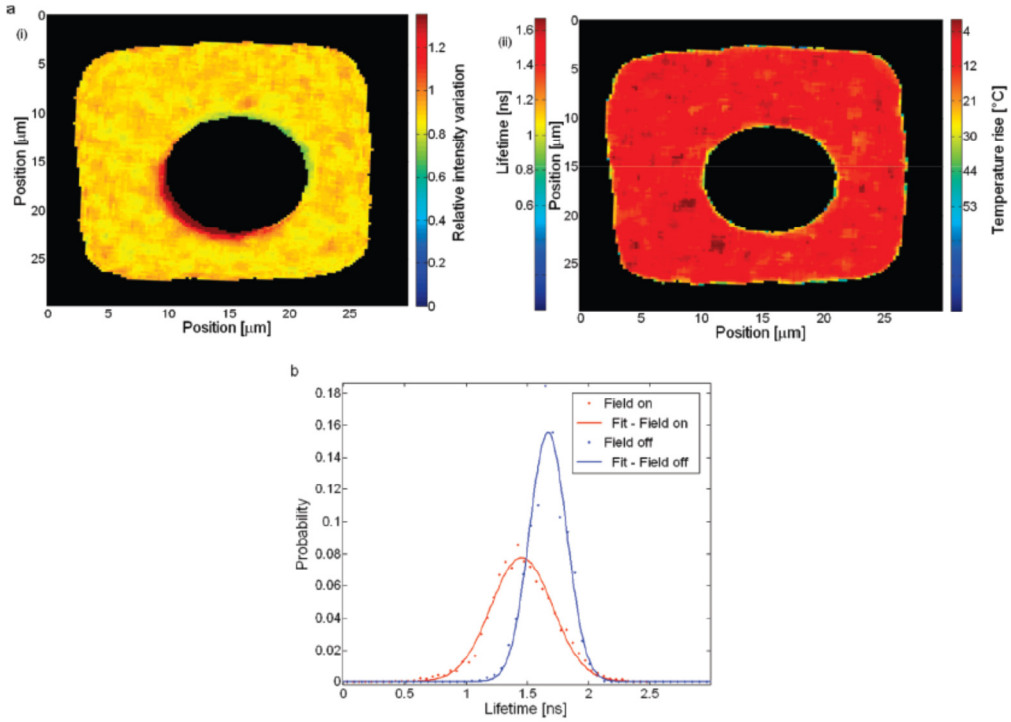


Figure 4. (a) Fluorescence intensity (i) and fluorescence lifetime image after switching on the AC electric field (ii). (b) Fluorescence lifetime distributions before (in blue) and after (in red) switching on the electric field.

Table 1. Fitting Parameters for the Gaussian Curves Obtained from the Lifetime Probability Distribution

	electric field off	electric field on
A	0.156	0.077
μ [ns]	1.67	1.46
v [ns]	0.15	0.25

model $f(t) = A \times \exp(-((t-\mu)^2/2v^2))$. In this equation, μ is the mean of the Gaussian distribution and v is the variance. The coefficients are summarized in Table 1.

In this case, the lifetime shows a reduction of the mean value from 1.67 ns (field off) down to 1.46 ns (field on). This corresponds to a 13.5 °C temperature rise. The fwhm of the distributions are 0.36 and 0.6 ns when the electric field is turned off and on, respectively. The broadening of the fwhm implies the creation of a temperature gradient in the imaging plane which is directly reflected by the FLIM map.

The temperature change within each of the traps in the array was found to be fairly similar in the voltage range tested (within 10%) while interdevice testing showed higher discrepancy levels (up to 30%). This is thought to be due to the electrode deposition process and nonreproducible thicknesses of the electrodes. Furthermore, no significant frequency dependence was observed in the range of 100 kHz to 20 MHz.

By measuring the decrease in average lifetime over the image trap for different voltages, after steady state is established, the variation of temperature rise as a function of applied voltage can be plotted (Figure 5). The comparison with eq 4 shows a clear discrepancy indicating that the effective voltage

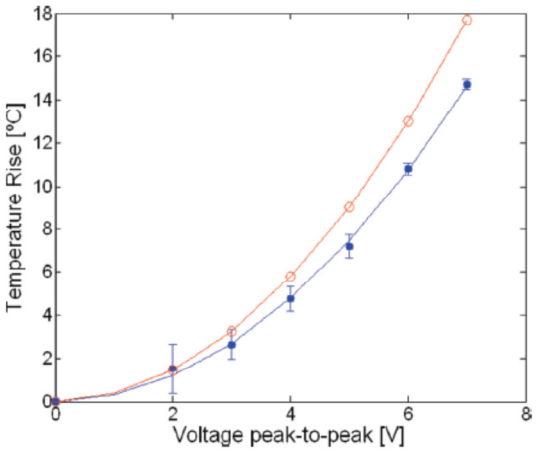


Figure 5. Relationship between temperature rise and applied voltage: the blue curve corresponds to experimental data while the red one is based on eq 4.

is lower than the applied one as discussed previously. Effective voltages were found to be approximately 90% of the applied values which translates into a difference of several degrees centigrade at high voltages.

CONCLUSIONS

Temperature imaging of DEP traps has been performed using both intensity and lifetime data. Results demonstrate that the local temperature in the vicinity of a trapped particle can differ

significantly from mathematical approximations. In particular, for large temperature changes (over 10 °C), this difference raises local temperature over a given threshold (e.g., 37 °C for cells). These types of measurements can be made prior to other studies by patterning "experimental" and calibration electrodes on a single substrate. Further applications, using such traps, can include temperature-dependent cell viability and expression studies, assaying membrane leakage, and controlled particle synthesis.

SUPPORTING INFORMATION AVAILABLE

Additional information as noted in text. This material is available free of charge via the Internet at http://pubs.acs.org.

Received for review June 11, 2010. Accepted July 21, 2010.

AC101557G

nature chemistry

ARTICLES

PUBLISHED ONLINE: 23 MAY 2011 | DOI: 10.1038/NCHEM.1046

A microdroplet dilutor for high-throughput screening

Xize Niu, Fabrice Gielen, Joshua B. Edel* and Andrew J. deMello*†

Pipetting and dilution are universal processes used in chemical and biological laboratories to assay and experiment. In microfluidics such operations are equally in demand, but difficult to implement. Recently, droplet-based microfluidics has emerged as an exciting new platform for high-throughput experimentation. However, it is challenging to vary the concentration of droplets rapidly and controllably. To this end, we developed a dilution module for high-throughput screening using droplet-based microfluidics. Briefly, a nanolitre-sized sample droplet of defined concentration is trapped within a microfluidic chamber. Through a process of droplet merging, mixing and re-splitting, this droplet is combined with a series of smaller buffer droplets to generate a sequence of output droplets that define a digital concentration gradient. Importantly, the formed droplets can be merged with other reagent droplets to enable rapid chemical and biological screens. As a proof of concept, we used the dilutor to perform a high-throughput homogeneous DNA-binding assay using only nanolitres of sample.

High-throughput screening can provide an enormous amount of information on the utility of the components of molecular libraries and is now guiding research directions in diverse areas, ranging from directed evolution to small-molecule synthesis[1,2]. The key parameters that determine the efficiency of such exploration processes are the sample volumes required per screen and the number of reagent combinations that can be examined per unit time. Currently, exploration of molecular diversity is only possible with substantial investment in liquid-handling robots (and their associated infrastructure) that perform screens in microwell plates. Microwell plates are typically open plastic substrates with between 96 and 3,456 sample wells arranged in a 2:3 rectangular matrix. Based on a standard footprint, each well can hold a volume that ranges from tens of nanolitres to several millilitres of liquid. This general automated approach affords screening capacities of $<10^4$ samples per day, utilizes sample and reagent volumes in the order of tens of microlitres and requires a capital investment of tens of millions US dollars.

An attractive alternative to conventional laboratory-based screening technologies involves the adoption of microfluidic or lab-on-a-chip technologies. Recent years have seen considerable progress in the development of such microfabricated systems for use in the chemical and biological sciences[3,4]. Much of this development was driven by a need to perform rapid analytical or synthetic operations on small volumes of sample[5]. However, at a more basic level, the appeal of miniaturized analytical systems is motivated by the fact that physical and chemical processes can be controlled and harnessed more easily when instrumental dimensions are reduced to the micron (or submicron) scale. In the current context, such systems define new operational paradigms and have the potential to transform high-throughput synthesis and compound-library screening. For example, Quake and co-workers pioneered the development of microfluidic large-scale integration and described the use of microfluidic devices that contain thousands of micromechanical valves and hundreds of individually addressable reaction chambers[6–8].

A fundamental and non-trivial challenge associated with the application of microfluidic technology to high-throughput screening is the ability to control and vary the concentration of the analytical sample under investigation. Although this is a standard and simple pipetting operation on the macroscale, the formation of discrete samples of varying concentrations within a microfluidic system is surprisingly challenging. Whitesides and co-workers addressed the problem of concentration-gradient generation in continuous-flow microfluidic systems by exploiting laminar flows[9]. Specifically, the authors utilized controlled diffusive mixing of species flowing in parallel fluid streams. This approach was refined to allow the production of complex spatial and temporal concentration gradients and has been applied to a diversity of chemical and biological systems[10,11].

Unfortunately, the use of such gradient generators is not ideal in situations where multiple, discrete assays need to be performed with high throughput and in a quantitative fashion, because the formed gradients exist in a continuous phase. Indeed, the screening of multiple reactions (or compounds) remains a critical challenge in single-phase microfluidic systems, where sample volumes are restricted (nanolitres to microlitres), and analyte diffusion and Taylor dispersion tend to expand the formed concentration distributions[12]. Moreover, the problems associated with the non-specific binding of reagents to channel surfaces pose serious issues for cross-contamination in any high-throughput approach[13].

In recent years, droplet-based (or segmented flow) microfluidics has emerged as a potential new platform for high-throughput and high-efficiency experimentation in biology and chemistry[14,15]. In simple terms, droplets or plugs can be made to develop spontaneously when multiple lamina streams of aqueous reagents are injected into an immiscible carrier fluid. Importantly, droplets formed in this way have nano- to picolitre volumes, are isolated from channel surfaces and other droplets, and can be manufactured at kilohertz frequencies[16]. Unlike continuous-flow microfluidic systems, processed reagents can be encapsulated or digitized within the carrier phase, allowing for independent control of each

Department of Chemistry, Imperial College London, Exhibition Road, South Kensington, London SW7 2AZ, UK.; †Present address: Department of Chemistry and Applied Biosciences, Institute for Chemical and Bioengineering, ETH Zürich, HCI E125, Wolfgang Pauli Strasse 10, CH-8093 Zürich, Switzerland.
*e-mail: Joshua.edel@imperial.ac.uk; andrew.demello@chem.ethz.ch

© 2011 Macmillan Publishers Limited. All rights reserved.

droplet. Accordingly, there exists an opportunity to generate, order, maintain and utilize sequences of droplets that contain a given analyte at varying concentrations. In the mass production of droplets using microfluidic T-junctions or flow-focusing geometries, the variation of volumetric flow-rate ratios (of the aqueous inputs) during the droplet-formation process provides a direct way of changing the relative concentration of encapsulated reagents[17]. Unfortunately, in practice this approach suffers because flow stabilization occurs over a timescale of many seconds to minutes when using precision syringe pumps and, moreover, flow-rate variations can access only concentration ranges of approximately two orders of magnitude[17] (by Supplementary Fig. S1). Consequently, current approaches to high-throughput screening of reaction conditions using droplet-based microfluidics rely on extracting data from hundreds or thousands of droplets[18].

A distinct property for droplets travelling along microfluidic conduits is that they experience various hydrodynamic interactions[14], because capillary effects dominate viscous forces (capillary numbers range between 10^{-1} and 10^{-5} in most microfluidic systems). Accordingly, such spatial and temporal uncertainties require feedback schemes to realize reliable integrated valving or the implementation of other optical and electrical control tools[19], which significantly increases the level of system complexity. To overcome such difficulties, recent studies utilized the simultaneous transportation of materials with the use of logical control operations by leveraging the capillary effect. For example, bubble logic schemes[20], pillar structures for droplet merging[21,22], droplet selection according to size[23] and the manipulation of ultra-small sample volumes for analytical separations[24] are reported. To address the problems of controlling concentration in droplet-based microfluidics, we proposed an alternative strategy that is able to access concentration ranges in excess of four orders of magnitude, by utilizing water–oil hydrodynamic interactions and manipulating single-droplet interactions.

Results and discussion

Herein, we propose a passive platform that can achieve the controllable dilution of nanolitre samples dispersed within an immiscible phase. The approach is based on liquid–liquid and liquid–channel structure hydrodynamic interactions; a typical device structure is shown in Fig. 1a. The sequence of droplets used in the dilution studies presented can be generated using standard flow-focusing or T-junction approaches[16,25]. However, to screen multiple samples and explore the functionality and potential of the dilution chamber, it is favourable to pregenerate the droplet sequence from different reservoirs into the tubing with the desired volumes, sequences and intervals (in our experiments droplet volumes ranged from 500 pl to 5 nl). Then these droplets can be injected directly into the microdevice for screening. Once inside, the first 'high-concentration' sample droplet can be diluted through interaction with a sequence of subsequent droplets of lower (or zero) analyte concentration. The output of this generic process is a sequence of droplets that have different concentrations of the desired analyte. More specifically, the concentration diminishes in a logarithmic fashion as a function of droplet number, but maintains both droplet size and droplet spacing. The results of this procedure are shown in Fig. 1c. Unlike concentration gradients generated under continuous-flow conditions, the output units of the process described here are dissociated and therefore reagents are kept within individual droplets and can undergo further processing and analysis.

The detailed process of droplet dilution can be partitioned into four steps: droplet trapping, droplet merging, droplet resplitting and droplet mixing (within the trapped 'mother' droplet). Each component of this process is visualized in Fig. 1b. This dilution process is highly analogous to routine pipetting operations

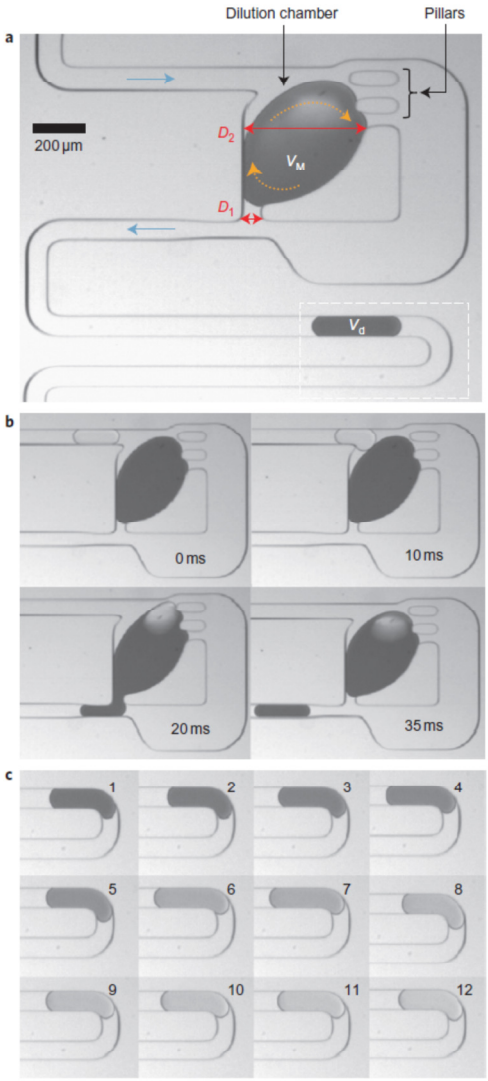


Figure 1 | Design and operation of the droplet dilutor. a, Schematic of the dilution module showing the input channel, the dilution chamber, pillar structures, the side channel and an extended output channel. The flow direction is indicated by blue arrows. A droplet that contains food dye is trapped inside the dilution chamber and forms the 'mother droplet'. The volume of the mother droplet is given by V_M and that of the output droplet by V_d. The dashed orange arrows indicate the recirculatory mixing within the mother droplet caused by the flow of the continuous phase. **b**, Process of sequential dilution. A buffer droplet approaches (0 ms), contacts the mother droplet (10 ms), coalesces and activates the soft valve (20 ms), and finally generates an output droplet (35 ms). Mixing within the mother droplet takes place during and after output-droplet generation. The high-speed Supplementary Movie S1 shows the entire process. **c**, Images of a sequence of droplets flowing through the output channel taken from the dashed rectangular box in (**a**). The concentration of dye in the output droplets decreases exponentially according to the droplet number n following $(1-V_d/V_M)^n$.

© 2011 Macmillan Publishers Limited. All rights reserved.

performed on the bench top, in which samples are aspirated into a certain volume, transported and dispensed into a container, where mixing with the container's contents affords dilution. Such a pipetting process can be repeated to perform a screen of various concentrations. In the experiments, our droplet dilutor operated with volumes between three and six orders of magnitude smaller than typically used in conventional pipetting and robotic screening. In the initial experiments the mother droplet and dilution droplets had volumes of 6 nl and 1 nl, respectively.

To locate and trap droplets, a dilution chamber was designed to have a smaller output channel width ($D_1 = 80$ μm) than the inlet part ($D_2 = 520$ μm), as shown in Fig. 1a. A liquid plug held inside the chamber was thus deformed and subjected to a back pressure (because of surface tension, Supplementary Fig. S3):

$$\Delta p_{\text{surf}} \propto \gamma(2\cos(\theta+\alpha)/D_2 - 2\cos(\theta-\alpha)/D_1) \quad (1)$$

Here γ is the interfacial tension (between 10 and 50 mN m^{-1} for a typical oil–aqueous system), θ is the contact angle of the droplet on the channel wall and α is the angle that defines the non-parallel channel walls between D_2 and D_1 (Supplementary Fig. S3). This yields a back pressure of between 10^1 and 10^2 Pa for the current liquid and channel dimensions. Such back pressures are normally insufficient to stop flows in simple channels that contain a pure expansion in width[26], because of the high hydraulic pressure required to drive the flow along the whole length of the microchannel[20]. However, by implementing a side channel in close proximity to the dilution chamber (Fig. 1a) that conducts the oil flow around the chamber, the hydraulic pressure that the droplet sustains can be decreased dramatically to:

$$\Delta p'_{\text{hydraulic}} \propto \mu' L' Q/(h' w^3) \quad (2)$$

Here μ' is the viscosity of the oil, L' the length of the droplet, Q the total flow rate and h' and w are the height and width of the side channel, respectively. Under typical conditions, the hydraulic pressure is between 1 and 100 Pa, which is equivalent to the back pressure induced by surface tension. Such local droplet manipulation is effective in droplet trapping, flip-flop memory or adjusting the distance between adjacent droplets in a flow[20,27]. Moreover, as both Δp_{surf} and $\Delta p'_{\text{hydraulic}}$ are proportional to $1/L'$, such a local manipulation approach is valid for regimes of low capillary number and further reductions in feature size are feasible for droplet trapping.

With the depletion of oil through the side channels (that is, between the pillars), the subsequent droplet can merge readily with the mother droplet trapped inside the dilution chamber. Crucially, if the accumulated droplet (mother droplet + dilution droplet) becomes larger than the chamber volume, it will block the oil flow in the side channels and a portion of the combined droplet will be pushed out from the outlet, until the now-resumed oil flow cuts the extruded aqueous phase into a secondary droplet at the 'T' junction (Fig. 1b and Supplementary Movie S1). This means that the generation of an output droplet is triggered only by the merging of an input droplet with the mother droplet, which forms a 'soft valve' during the blockage and reopening of the oil flow. By sweeping the size of the input droplets from five times the volume of the mother droplet to one-tenth that of the mother droplet, we constructed a size comparison of the input droplets and the output drops. Supplementary Fig. S4 shows this relationship graphically, and demonstrates that the soft valve maintains the equality in input and output droplet volumes, and thus conserves the mother droplet volume. However, for the current design, when the input droplet volume is less than one-tenth that of the mother droplet volume, the soft valve does not function in a linear manner because the increased droplet volume cannot completely block the side-channel flow.

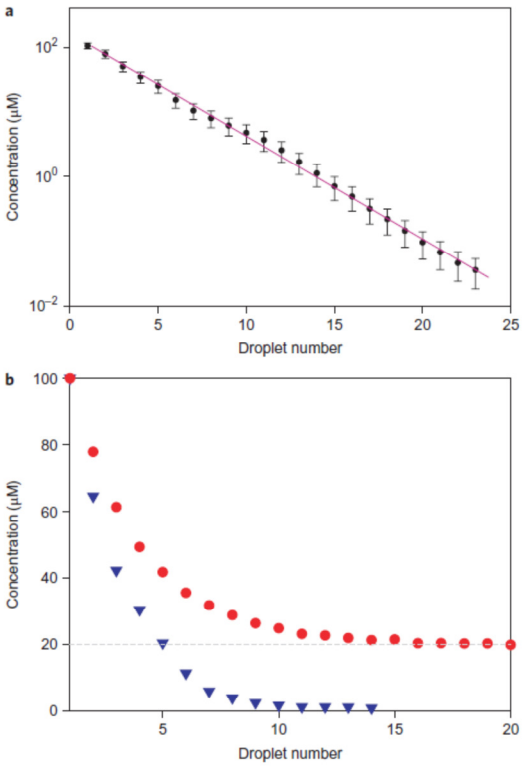


Figure 2 | Calibration of sequential dilution. a, Sequential dilution of a 6 nl mother droplet containing 100 μM fluorescein in water. The concentration of each output droplet was calculated from the recovered fluorescent signal. In this experiment, 23 output droplets accessed approximately four orders of magnitude in terms of concentration (100 μM to 36 nM). Error bars were calculated from the propagation of volume mismatches throughout the dilution process. **b**, Sequential dilution of a 100 μM fluorescein sample water droplet with different baselines. The triangles represent dilution with pure water input droplets and the circles represent dilution with aqueous input droplets composed of 20 μM fluorescein.

Careful inspection of Fig. 1b shows that during the resplitting process, fluid within the mother droplet moves in a laminar fashion with weak corner flows. This means that the newly merged droplet is kept wholly within the dilution chamber until the next droplet enters. Mixing of the newly merged droplet with the mother droplet occurs immediately after resplitting and relies on a 'moving wall' effect at the interface between the oil and the droplet. The viscous-drag force from the shearing of oil flow, $F \propto \mu h U$ (where μ is the viscosity of the aqueous phase, h is the height of the chamber and U is the average flow rate at the oil–water interface), induces circulation inside the mother droplet[28,29] and complete mixing is achieved within 500 ms at a total flow rate of 2 μl min^{-1}. Although this is slower than chaotic mixing in a droplet moving along a channel[30], a further increase in flow rate is expected to increase the mixing speed.

The dilution capability of the device was verified experimentally by forming a mother droplet with a 100 μM fluorescein solution and a sequence of smaller buffer droplets. A 488 nm excitation

© 2011 Macmillan Publishers Limited. All rights reserved.

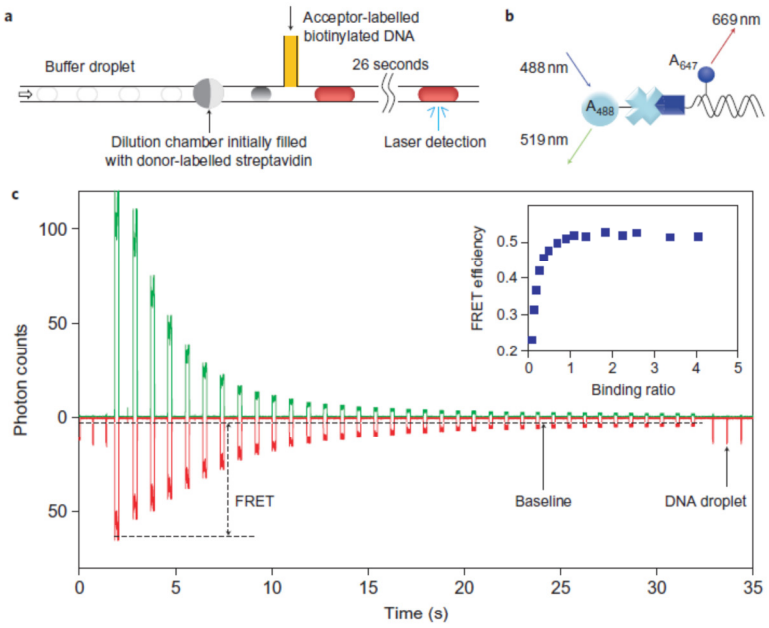


Figure 3 | Application of the droplet dilution module in a homogeneous DNA-binding assay. a, Schematic of the droplet dilution and further reaction. 100 nM streptavidin labelled with AF488 were diluted with buffer droplets that contained 100 mM Tris-HCl, 10 mM NaCl and 3 mM $MgCl_2$ at pH 8.0. The output droplets were merged with a continuous stream of AF647-labelled biotinylated oligonucleotide. The product droplet was flowed for 26 seconds through an incubation channel before optical detection. **b**, The FRET pair AF488–AF647 was brought into proximity through the biotin–streptavidin binding. **c**, Green and red fluorescent signals as detected by avalanche photodiode detectors for the donor and acceptor. Each peak represents one droplet. The baseline represents the red signal from AF647 in the absence of FRET. Its height is two-fifths of the signal of the DNA droplet alone, which correlates to the volumetric ratio between the DNA droplet and the merged droplet (DNA droplet plus buffer droplet). The red signal above the baseline corresponds to FRET events. The complete screening was performed within 30 seconds with 30 droplets. Inset: the binding curve illustrates binding ratio as a function of FRET efficiency, inferred from the fluorescence bursts.

beam was focused into the microfluidic channel at a fixed point downstream of the dilution chamber. Emitted photons were collected using a microscope objective and focused onto an avalanche photodiode detector. The analytical concentration of each droplet was calculated from the measured fluorescence intensity. Figure 2a demonstrates the excellent correspondence between the measured droplet concentrations and the designed dilution ratio (solid line). Significantly, the concentration gradient formed can cover four orders of magnitude in a single experiment and was limited only by the achievable limit of detection. Moreover, by changing the droplet size or sample concentration in the subsequent droplets, a variety of dilution ratios or baselines were achieved readily. For example, Fig. 2b shows two droplet concentration gradients formed using an identical mother droplet with either pure solvent dilution droplets or dilution droplets at 20% of the mother droplet concentration. Such operational flexibility is especially useful in screening applications where the analytical response shows a complex dependency on concentration. This flexibility is exemplified in a study of the self-quenching behaviour of carboxyfluorescein in aqueous solutions (Supplementary Figs S6,S7).

It is recognized that the majority of chemical and biological assays require the dilution of one or more reagents when characterizing parameters such as reaction kinetics, efficiency and toxicity[5]. To this end, we used a DNA-binding homogeneous assay based on fluorescence resonance energy transfer (FRET) as a model system to demonstrate the operational utility of the dilution platform and its integration with other functional components[31]. Figure 3a illustrates the fluidic scheme. Here a FRET donor (mother) droplet contains 100 nM streptavidin labelled with Alexa Fluor 488 (AF488). Initially, this mother droplet was diluted into a sequence of 3 nl droplets of decreasing concentrations. Subsequently, these droplets were merged with a continuous stream of 20 nM single-stranded DNA (ssDNA) to generate a larger merged droplet. The ssDNA was biotinylated and labelled with the FRET acceptor AF647. Each merged droplet had a volume of 4 nl, which generated an effective DNA concentration of 5 nM with an initial streptavidin concentration of 75 nM. An incubation time of 26 seconds (between the point of merging and detection) ensured complete mixing within the droplets. The fluorescence signature (in both red and green channels) occurred as the droplet transited the optical probe volume, and the spectrally resolved emission was acquired through the use of a dichroic filter and two avalanche photodiodes, as shown in Fig. 3c.

The precise concentration of the donor was inferred directly from the green fluorescence signal (originating solely from AF488) (Fig. 3c). The concentration of the acceptor was inferred from the red fluorescence signal of AF647 with no streptavidin in the droplet. FRET signals were obtained by subtracting the contribution of AF647 to the red signal from the contribution of the diluted DNA sample. This yielded the baseline above which fluorescence reports actual FRET events. Accordingly, the correspondence of the FRET signal and the binding ratio, defined as the ratio of DNA concentration to streptavidin concentration, can be determined experimentally. This binding ratio can be used to derive binding properties based on FRET efficiency[31].

© 2011 Macmillan Publishers Limited. All rights reserved.

As shown in the insert of Fig. 3c, the FRET efficiency rapidly increases as a function of binding ratio with a subsequent levelling off after a threshold value of approximately one. This behaviour indicates that the number of biotin binding sites occupied by biotinylated DNA is between one and two. This result agrees with previously published results based on the same assay[31]. After the threshold binding ratio, the FRET efficiency plateaus at 50%. This is higher than the theoretical FRET efficiency of 40% defined by equation (3) with $R_0 = 39$ Å and $R_{DA} = 41.6$ Å:

$$E_{theory} = \frac{1}{(R_{DA}/R_0)^6} \quad (3)$$

Here R_0 is the characteristic Förster distance and R_{DA} is the distance between donor and acceptor. This discrepancy can be explained by the high number of fluorophores per streptavidin (approximately five). Accordingly, this type of assay can provide high-throughput molecular information on binding-site occupancy and dye–molecule interactions. Moreover, the logarithmic nature of this dilution scheme allows the collection of many data points in the regime of extreme binding ratios. This is normally difficult to achieve using conventional continuous-flow approaches. Also, although the second inlet incorporated a continuous flow, a droplet approach can be adapted easily. Accordingly, the dilution device minimizes not only the amount of compound to be screened, but also the target molecules consumed; this provides a direct route to high-throughput screening of rare samples. The output droplets can be detected directly on-chip (as shown herein) or stored within an internal or external device for applications that require a long period of incubation, such as cell culturing or crystallization.

Conclusion

In summary, we have demonstrated a new technique for the high-throughput dilution and screening of nanolitre droplets in microfluidic channels. In contrast to conventional microfluidic-based screening methods that utilize microlitre volumes of compounds and substrates, our approach requires only nanolitres at most and (in a non-optimized format) has a similar throughput to that of state-of-the-art liquid-handling technologies. The entire screening process is performed in a passive and sequential manner, and other droplet-manipulation processes (such as droplet splitting and sorting) can be integrated with ease. Also, other routine screening applications can be performed using this platform (for example, titrations, pH screening and mapping of crystallization conditions) and we will report on these in future publications. Through parallelization, screening of large compound libraries will be facilitated, and it is expected that this inexpensive chip-level screening technology has the potential to replace current expensive high-throughput screening platforms.

Methods

Chip fabrication. The microfluidic devices used for all experiments were fabricated in poly(dimethylsiloxane) (PDMS) by single-layer soft lithography[3] and bonded to a flat layer of PDMS by plasma bonding (Harrick Plasma) for one minute. The bonded chips were ready to use after being kept in a 65 °C oven overnight.

Fluidics. A precision syringe pump (PHD 2000, Harvard) was used to generate and manoeuvre droplets along the fluidic network. The pump was used in refill mode and operated at a rate of 2 μl min^{-1}. A second pump was used to inject the DNA solution at a volumetric flow rate of 0.2 μl min^{-1}. For the initial system characterization, deionized water that contained a food dye or a binding buffer was used as the aqueous phase and FC-40 with 0.75 weight% 1H,1H,2H,2H-perfluorooctanol as the oil phase. The dilution channel was rinsed with oil for ten minutes before use.

FRET assay. AF488 streptavidin conjugate was obtained from Invitrogen. The biotinylated oligonucleotide strand had the sequence biotin-5′-CGCTAAAATTATTTATTGATCGATTTTTTTTCGGGCGCGGCGGGC-3′ (Operon). The complementary strand internally modified with AF 647 was 3′-CGCG[Alexa647]TTTTAATAAATAACTAGCTAAAAAAAAGCCCGCGCC GCCCG-5′. These two strands were hybridized to produce the FRET acceptor. Hybridization was performed using a binding buffer of 100 mM Tris–HCl, 10 mM NaCl and 3 mM $MgCl_2$ at pH 8.0, and a mixture of ssDNA (biotin-labelled DNA and Alexa 647-labelled DNA) was prepared, with a final concentration of 100 nM for both strands. The DNA mixture was hybridized using a Genius Thermal Cycler (Techne, Cambridge) by quickly ramping the temperature to 92 °C and holding it for two minutes. The temperature was then slowly decreased to 4 °C at a rate of 1.6 °C min^{-1}.

For the FRET experiments described herein, the initial concentrations of labelled streptavidin and labelled biotinylated DNA were 100 nM and 20 nM, respectively. After merging, droplets that contained DNA and streptavidin were incubated for 26 seconds with the use of a long serpentine output channel.

Optics. A continuous-wave diode laser operating at 488 nm was introduced into the microfluidic channel via a dichroic mirror (505DRLP02, Omega Optical) and ×20 objective. Fluorescence photons were collected via the same objective and an emission filter (515 EFLP, Omega Optical) was used to further filter the excitation light before it was focused to a precision pinhole (75 μm, Thor Labs, Ely, Cambridgeshire). A second dichroic mirror (630DCXR) split and directed the signal onto two avalanche photodiodes (AQR-141, EG&G, Perkin-Elmer). Both detectors were linked to a DAQ device (National Instruments, USB-6251) with 50 μs resolution per channel.

Received 21 September 2010; accepted 5 April 2011; published online 23 May 2011

References

1. Hertzberg, R. P. & Pope, A. J. High-throughput screening: new technology for the 21st century. *Curr. Opin. Chem. Biol.* **4**, 445–451 (2000).
2. Sundberg, S. A. High-throughput and ultra-high-throughput screening: solution- and cell-based approaches. *Curr. Opin. Biotechnol.* **11**, 47–53 (2000).
3. Xia, Y. N. & Whitesides, G. M. Soft lithography. *Ann. Rev. Mater. Sci.* **28**, 153–184 (1998).
4. Unger, M. A., Chou, H. P., Thorsen, T., Scherer, A. & Quake, S. R. Monolithic microfabricated valves and pumps by multilayer soft lithography. *Science* **288**, 113–116 (2000).
5. deMello, A. J. Control and detection of chemical reactions in microfluidic systems. *Nature* **442**, 394–402 (2006).
6. Thorsen, T., Maerkl, S. J. & Quake, S. R. Microfluidic large-scale integration. *Science* **298**, 580–584 (2002).
7. Gomez-Sjoberg, R., Leyrat, A. A., Pirone, D. M., Chen, C. S. & Quake, S. R. Versatile, fully automated, microfluidic cell culture system. *Anal. Chem.* **79**, 8557–8563 (2007).
8. Hansen, C. L., Skordalakes, E., Berger, J. M. & Quake, S. R. A robust and scalable microfluidic metering method that allows protein crystal growth by free interface diffusion. *Proc. Natl Acad. Sci. USA* **99**, 16531–16536 (2002).
9. Jeon, N. L. *et al.* Generation of solution and surface gradients using microfluidic systems. *Langmuir* **16**, 8311–8316 (2000).
10. Dertinger, S. K. W., Chiu, D. T., Jeon, N. L. & Whitesides, G. M. Generation of gradients having complex shapes using microfluidic networks. *Anal. Chem.* **73**, 1240–1246 (2001).
11. Chung, B. G. *et al.* Human neural stem cell growth and differentiation in a gradient-generating microfluidic device. *Lab Chip* **5**, 401–406 (2005).
12. Stone, H. A., Stroock, A. D. & Ajdari, A. Engineering flows in small devices: microfluidics toward a lab-on-a-chip. *Ann. Rev. Fluid Mech.* **36**, 381–411 (2004).
13. Makamba, H., Kim, J. H., Lim, K., Park, N. & Hahn, J. H. Surface modification of poly(dimethylsiloxane) microchannels. *Electrophoresis* **24**, 3607–3619 (2003).
14. Song, H., Chen, D. L. & Ismagilov, R. F. Reactions in droplets in microfluidic channels. *Angew. Chem. Int. Ed.* **45**, 7336–7356 (2006).
15. Thorsen, T., Roberts, R. W., Arnold, F. H. & Quake, S. R. Dynamic pattern formation in a vesicle-generating microfluidic device. *Phys. Rev. Lett.* **86**, 4163–4166 (2001).
16. Anna, S. L., Bontoux, N. & Stone, H. A. Formation of dispersions using 'flow focusing' in microchannels. *Appl. Phys. Lett.* **82**, 364–366 (2003).
17. Song, H. & Ismagilov, R. F. Millisecond kinetics on a microfluidic chip using nanoliters of reagents. *J. Am. Chem. Soc.* **125**, 14613–14619 (2003).
18. Brouzes, E. *et al.* Droplet microfluidic technology for single-cell high-throughput screening. *Proc. Natl Acad. Sci. USA* **106**, 14195–14200 (2009).
19. Link, D. R. *et al.* Electric control of droplets in microfluidic devices. *Angew. Chem. Int. Ed.* **45**, 2556–2560 (2006).
20. Prakash, M. & Gershenfeld, N. Microfluidic bubble logic. *Science* **315**, 832–835 (2007).
21. Niu, X., Gulati, S., Edel, J. B. & deMello, A. J. Pillar-induced droplet merging in microfluidic circuits. *Lab Chip* **8**, 1837–1841 (2008).
22. Niu, X. Z., Gielen, F., deMello, A. J. & Edel, J. B. Electro-coalescence of digitally controlled droplets. *Anal. Chem.* **81**, 7321–7325 (2009).

© 2011 Macmillan Publishers Limited. All rights reserved.

23. Tan, Y. C., Fisher, J. S., Lee, A. I., Cristini, V. & Lee, A. P. Design of microfluidic channel geometries for the control of droplet volume, chemical concentration, and sorting. *Lab Chip* **4**, 292–298 (2004).
24. Niu, X. Z. *et al.* Droplet-based compartmentalization of chemically separated components in two-dimensional separations. *Chem. Commun.* 6159–6161 (2009).
25. Garstecki, P., Fuerstman, M. J., Stone, H. A. & Whitesides, G. M. Formation of droplets and bubbles in a microfluidic T-junction – scaling and mechanism of break-up. *Lab Chip* **6**, 437–446 (2006).
26. Bremond, N., Thiam, A. R. & Bibette, J. Decompressing emulsion droplets favors coalescence. *Phys. Rev. Lett.* **100**, 024501 (2008).
27. Shi, W. W., Qin, J. H., Ye, N. N. & Lin, B. C. Droplet-based microfluidic system for individual *Caenorhabditis elegans* assay. *Lab on a Chip* **8**, 1432–1435 (2008).
28. Fidalgo, L. M., Abell, C. & Huck, W. T. S. Surface-induced droplet fusion in microfluidic devices. *Lab Chip* **7**, 984–986 (2007).
29. Ottino, J. M. *The Kinematics of Mixing: Stretching, Chaos, and Transport* (Cambridge Univ. Press, 1989).
30. Tice, J. D., Song, H., Lyon, A. D. & Ismagilov, R. F. Formation of droplets and mixing in multiphase microfluidics at low values of the Reynolds and the capillary numbers. *Langmuir* **19**, 9127–9133 (2003).
31. Srisa-Art, M., deMello, A. J. & Edel, J. B. High-throughput DNA droplet assays using picoliter reactor volumes. *Anal. Chem.* **79**, 6682–6689 (2007).

Acknowledgements
This work was partially supported by the Research Councils UK Basic Technology Programme (Grant EP/D048664/1) and the National Research Foundation of Korea (Grant Number R11-2009-044-1002-0K20904000004-09A050000410).

Author contributions
X.N. conceived the dilution module, X.N., F.G., J.B.E. and A.J.D. designed the experiments, X.N. and F.G. performed the experiments, X.N., J.B.E. and F.G. analysed the data, and X.N. and A.J.D. co-wrote the manuscript. All authors discussed the results and commented on the manuscript.

Additional information
The authors declare no competing financial interests. Supplementary information accompanies this paper at www.nature.com/naturechemistry. Reprints and permission information is available online at http://www.nature.com/reprints/. Correspondence and requests for materials should be addressed to J.B.E. and A.J.d.

© 2011 Macmillan Publishers Limited. All rights reserved.